The Propeller Driven Pulsar-like Spin-down and Non-thermal Emission in the Nova-like Variable Star AE Aquarii

Bosco Oruru

(MSc)

Thesis submitted in fulfillment of the requirements

for the degree

Philosophiae Doctor

in the Faculty of Natural and Agricultural Sciences,

Department of Physics

at the University of the Free State, South Africa

Promoter: **Prof. P. J. Meintjes**

April 2012

University of the Free State

P. O. Box 339, Bloemfontein 9300, South Africa

Dedicated to my late parents,

Andriano Ogwang (Apap) and *Florence Anyinge (Maa)*,

with whom I am spiritually connected. Though bereaved, I treasure accomplishing their educational hope and wish.

May the Lord rest their souls in peace.

Acknowledgements

I would like to express my sincere gratitude to Professor P. J. Meintjes for his effort to ensure quality of this work, which included innovative suggestions and positive criticisms. His continuous motivation, moral support and parental guidance have been of immense importance. I also thank the examiners for their valuable time, recommendation and suggestions.

This study was sponsored by the South African Square Kilometre Array (SKA) project, with funds from the National Research Foundation (NRF). Many thanks to the management for the conducive atmosphere and follow-ups to ensure successful completion. I am grateful to Mev Kim de Boer and Mev Rose Robertson for their on-time responses and motherly patience.

I am also grateful to the members of the UFS Physics Department for their kind hospitality. Special thanks to the HoD, Professor H. C. Swart, for his friendly leadership and the trust that enabled me to participate in the departmental activities, such as: tutoring undergraduate students and giving inspirational presentations, the experience of which are worth. I also thank my colleague postgraduate students for the valuable and constructive interactions.

I would also like to thank the Astrophysics community (in South Africa) for the warm hospitality and electing me to represent the students at the South African Institute of Physics (SAIP) from 2010 to 2012. I hope I tried my best during my term in office.

Lastly, I would like to thank my family members, relatives, friends and in-laws for their financial and moral support. In particular, I humbly document my sincere thanks to Uncle J. B. Ogwang Arip for the timely and uninterrupted effort to give me the most needed foundation, and my beloved wife, Caroline Joyce Atim, for the immense faith and trust during my university education lasting nine years. Your contributions are highly appreciated.

May the love of the Almighty God shine up on us, and may the Lord God be the alpha and omega, for he said in Jeremiah 29:11, *"I alone know the plans I have for you, plans to bring you prosperity and not disaster, plans to bring about the future you hope for."*

Kind regards,

Bosco Oruru

Abstract

The nova-like variable AE Aquarii consists of a fast rotating magnetized white dwarf, orbiting a late-type main sequence companion star. It is the most enigmatic among cataclysmic variables, and perhaps the best laboratory to study the physics of accretion and related phenomena, due to its multi-wavelength nature and unique flaring activity. The system is in an accretor-propeller state and most of its properties are associated with the propeller process.

Using data observed contemporaneously with Chandra and Swift, the UV and X-ray properties of AE Aquarii have been studied. It is shown that the X-ray emission below 10 keV is predominantly soft and characterized by flares and emission lines. The spectra can be reproduced by multi-component thermal emission models, and the time-averaged X-ray luminosity is determined to be $L_{\rm X} \sim 10^{31}$ erg s^{-1}. The thermal soft X-ray emission (below 10 keV) is modelled in terms of plasma heating at the magnetospheric radius, where accretion flow from the secondary star interacts with the magnetosphere of the white dwarf. Both UV and X-ray emission are pulsed at the spin period of the white dwarf.

The recently detected hard X-ray emission in AE Aquarii (above 10 keV), with a luminosity of $L_{\rm X,hard} \leqslant 5 \times 10^{30}$ erg s^{-1}, shows a non-thermal nature, possible synchrotron emission of high energy electrons in the white dwarf magnetosphere. It is proposed that these electrons are accelerated by large field aligned potentials of $V \geqslant 10^{12}$ V, a process common in the magnetospheres of fast rotating neutron stars, or pulsars. This places AE Aquarii in a unique category with respect to most members of cataclysmic variables. The ratio of the observed hard X-ray luminosity to the spin-down luminosity of the white dwarf in AE Aquarii lies in the range 0.01-0.1 %, which is the same as observed from young rotation-powered neutron stars in the 2-10 KeV range. In this regard, a pulsar-like model is appropriate to explain the origin of the observed non-thermal hard X-ray emission in AE Aquarii.

Key words: Binary stars: cataclysmic variables - Stars: individual (AE Aquarii) - Rotation: white dwarf - Emission: thermal - Emission: non-thermal - Radiation: Synchrotron

Abstrak

Die nova-tipe veranderlike AE Aquarii bestaan uit 'n vinnig roterende gemagnetiseerde wit dwerg, wat wentel om 'n gevorderde K3-5 hoofreeks ster. Dit is die enigmatiese onder die kataklismiese veranderlikes en dalk ook die beste laboratorium om die fisika van massa-akresie en verwante verskynsels te bestudeer weens die aard van sy multi-golflengte straling en unieke uitbarstings. Die sisteem is in 'n sogenaamde “akresie-propeller” toestand en die meeste van sy multi-golflengte eienskappe word geassosieer met die sogenaamde “propeller” proses.

Die UV en X-straal eienskappe van AE Aquarii is bestudeer deur gebruik te maak van die data van gelyktydige waarnemings tussen Chandra en Swift. Dit is bewys dat die X-strale onder 10 keV hoofsaaklik sag is en gekenmerk word deur flikkerings en stralingslyne. Die spektrum kan verklaar word deur multi-komponent termiese stralingsmodelle en die bepaalde tydsgemiddelde X-strale helderheid is $L_{\mathrm{X}} \sim 10^{31}$ erg s^{-1}. Die sagte X-strale onder 10 keV is gemoduleer in terme van plasma verhitting by die magnetosferiese radius, soos die massavloed vanaf die sekondêre ster reageer met die vinnig roterende magnetosfeer van die wit dwerg. Beide die UV en X-straal emissie toon die rotasie modulasie van die wit dwerg.

Die harde X-strale in AE Aquarii (bokant 10 keV), met 'n helderheid van $L_{\mathrm{X,hard}} \leqslant 5 \times 10^{30}$ erg s^{-1}, dui op 'n nie-termiese proses, moontlik synchrotron straling van hoë-energie elektrone in die wit dwerg magnetosfeer. Die versnelling word veroorsaak deur elektriese potensiale parallel aan die magneetvelde wat groottes van tot $V \geqslant 10^{12}$ V kan bereik, 'n proses algemeen in die omgewings van vinnig roterende neutron sterre of pulsare. Dit plaas AE Aquarii in 'n unieke kategorie met betrekking tot meeste kataklismiese veranderlikes. Die verhouding van die waargenome harde X-straal helderheid tot die totale afrem wenteling luminositeit van die wit dwerg in die AE Aquarii sisteem is tussen 0.01-0.1 %, soortgelyk as wat waargeneem word by jong rotasie-gedrewe neutron sterre tussen 2-10 KeV. In hierdie geval, is 'n pulsar-tipe model toepaslik om die oorsprong van die nie-termiese harde X-strale in AE Aquarii te verklaar.

Kernwoorde: Binêre sterre: Kataklismiese veranderlikes - Sterre: individueel (AE Aquarii) - Rotasie: wit dwerg - Straling: termies - Straling: nie-termies - Straling: Synchrotron

Contents

List of Figures

List of Tables

Chapter 1

Introduction

Since its discovery on photographic plates (Zinner 1938), the transient nature of the optical emission (Figure 1.1) of AE Aquarii has resulted in numerous follow-up observational studies in other wavelengths. Its peculiar transient nature in optical wavelengths has been verified in radio (Figure 1.2), Infrared (Tanzi, Chincarini & Tarenghi 1981), UV (Figure 1.3) and X-rays (Figure 1.4). Reports of pulsed and burst-like high energy gamma-ray emission (10^{11} eV - 10^{12} eV) were made in the 1990's (Figure 1.5 and Figure 1.6). It seems that the unique properties of AE Aquarii are associated with the interaction of a rapidly rotating, highly magnetized white dwarf with the mass transfer flow from the secondary star companion. This results in AE Aquarii being an ideal astrophysical laboratory for the study of fascinating magnetohydrodynamic (MHD) and associated thermal and non-thermal radiation processes.

AE Aquarii displays the characteristics of cataclysmic variables. However, its transient multi-wavelength nature is unique (e.g. Warner 1995). Theoretical studies (e.g. Schenker et al. 2002; Meintjes 2002) suggest that its peculiar properties may be due to an evolution different from ordinary cataclysmic variables and that it may have evolved from a SuperSoft X-ray Source (SSS). According to this model, the system passed through a violent mass transfer and accretion phase more than 10^7 years ago, during which the compact primary star, believed to be a highly magnetized white dwarf, was spun-up to a short rotation period of $P_* \sim 33$ seconds. This spin period of the white dwarf, i.e. $P_* \sim 33$ seconds, is very short compared to the system's orbital

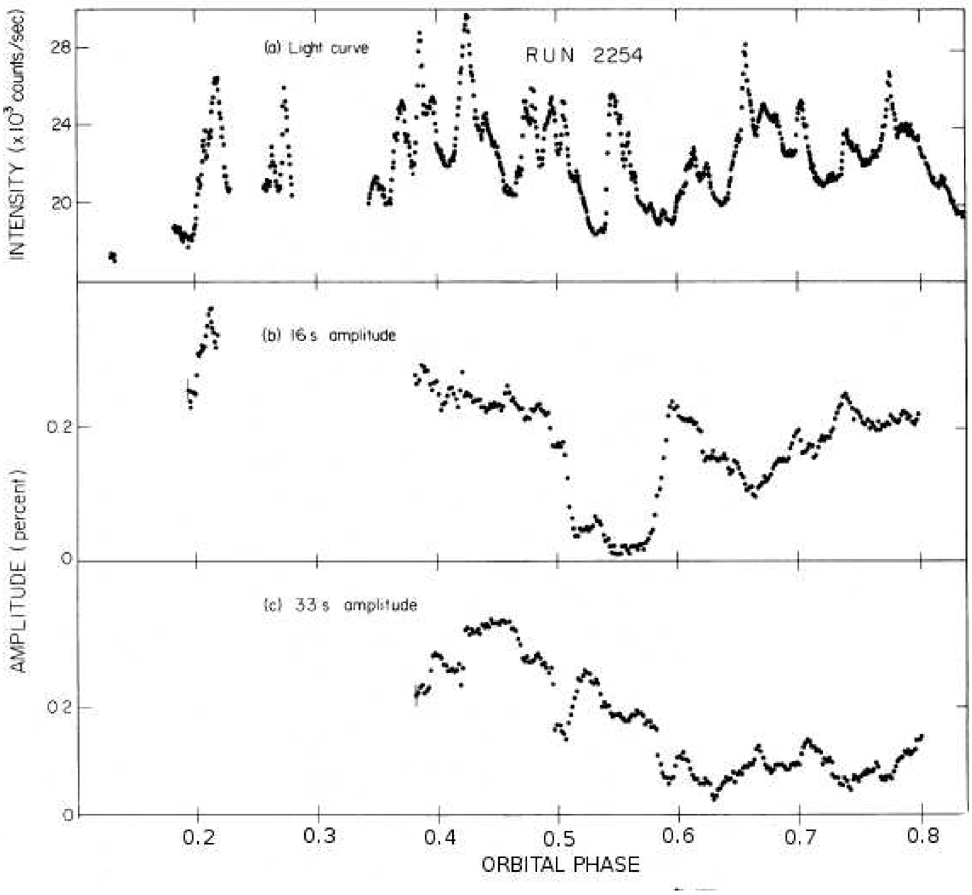

Figure 1.1: Optical light curve of AE Aquarii from the McDonald Observatory (Adapted from Patterson 1979).

period of $P_{\rm orb} \approx 9.88$ hours. The asynchronicity between these two periods may be explained by the mass transfer and accretion history. The violent phase of high mass accretion ended $\sim 10^7$ years ago (e.g. de Jager et al. 1994; Wynn, King & Horne 1997; Meintjes & de Jager 2000), leaving a rapidly rotating white dwarf interacting with a more modest mass flow resulting in a propeller ejection of matter and subsequent transient multi-wavelength emission (e.g. Wynn, King & Horne 1997; Meintjes & de Jager 2000). Had the violent mass transfer process not occurred, the spin period of the white dwarf may have remained intermediate to compare with the orbital period of the system.

The interaction between the rapidly rotating white dwarf and the modest mass flow from the secondary star results in the white dwarf spinning down, losing rotational kinetic energy at a rate $P_{\rm s-d} \sim 10^{34}$ erg s^{-1} (e.g. de Jager et al. 1994; Wynn, King & Horne 1997; Meintjes & de Jager 2000). This spin-down power, and not direct accretion with resultant luminosity $L_{\rm acc} \sim 10^{31}$ erg s^{-1} (Eracleous et al. 1994), is believed to be the driving mechanism behind the unique

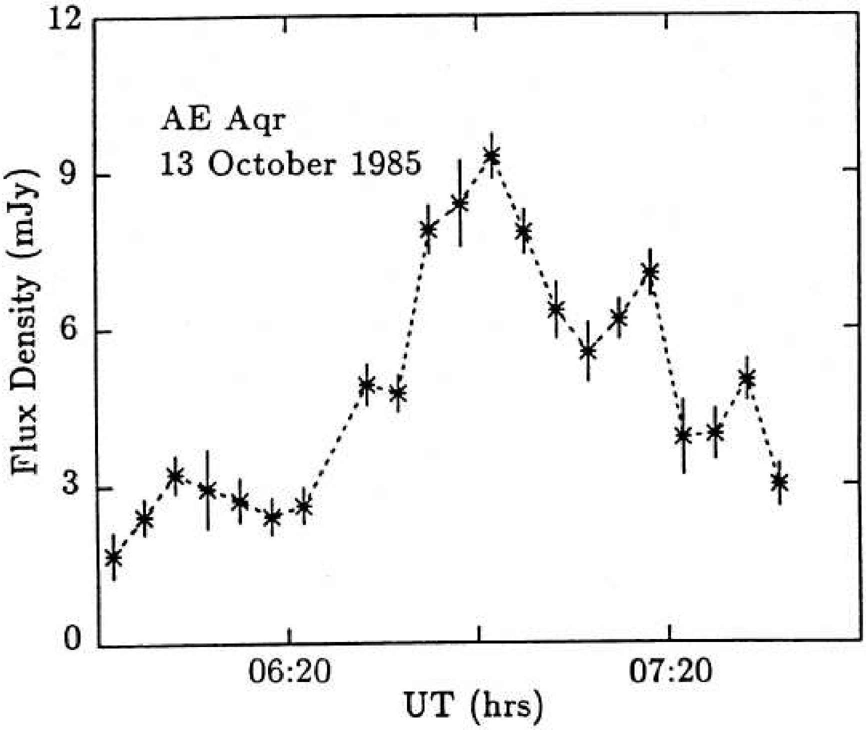

Figure 1.2: Radio light curve of AE Aquarii from VLA data (Taken from Bastian et al. 1988).

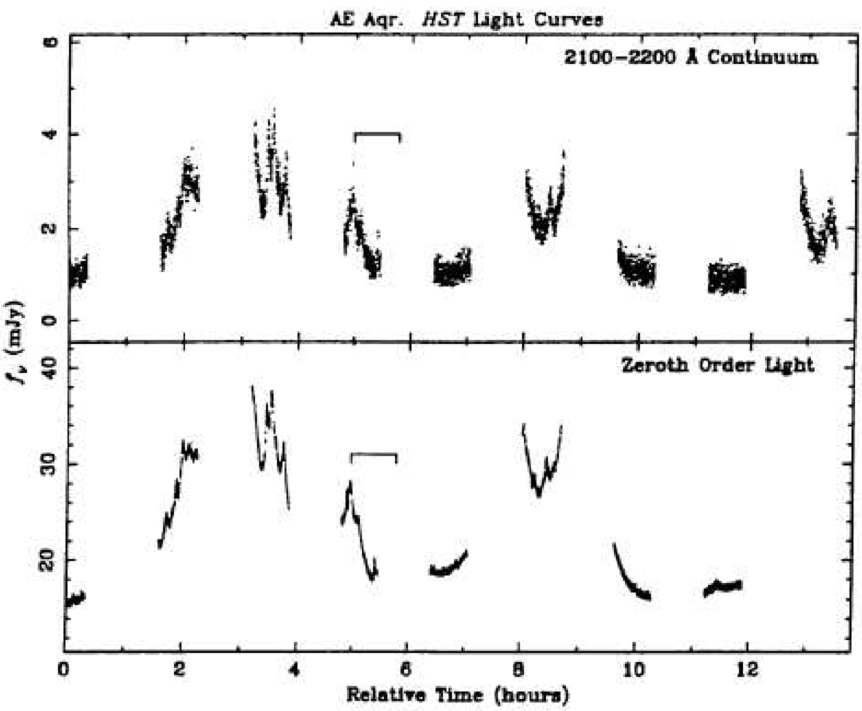

Figure 1.3: UV light curves of AE Aquarii from HST data (Taken from Eracleous et al. 1994).

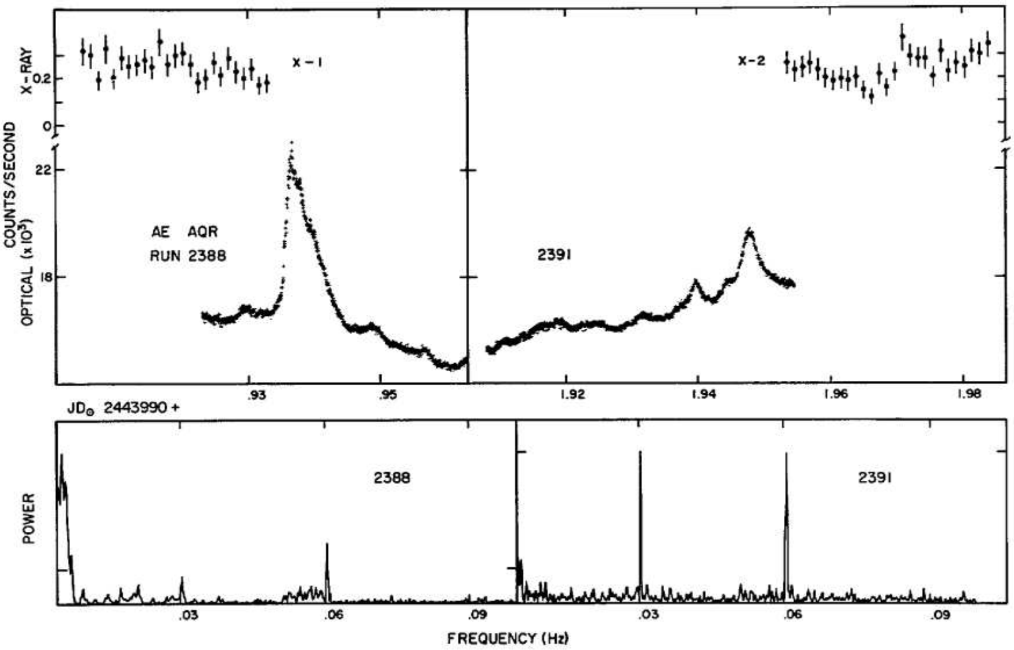

Figure 1.4: X-ray light curve of AE Aquarii from data observed with EINSTEIN (Taken from Patterson et al. 1980).

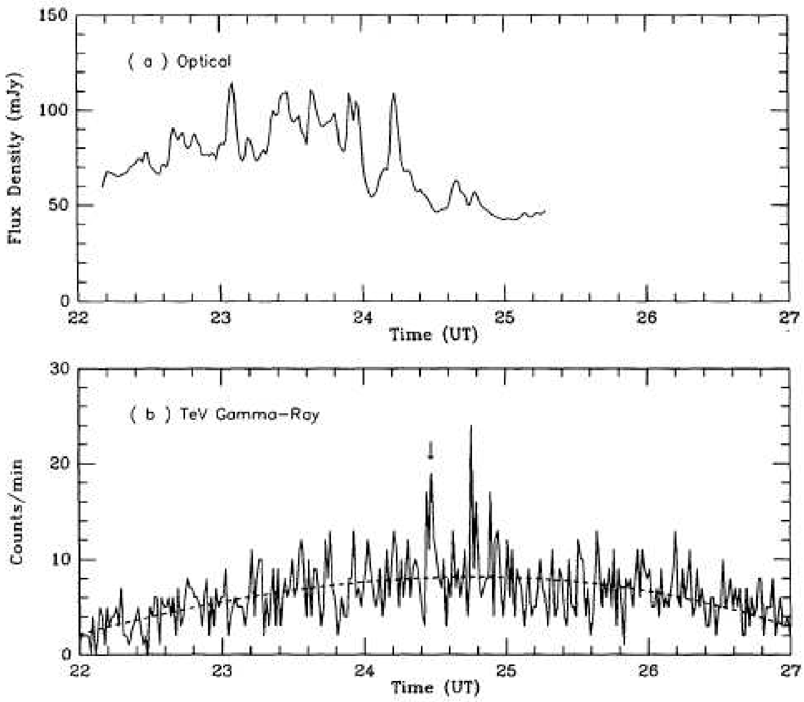

Figure 1.5: Optical and TeV γ-ray ($\epsilon_\gamma \geqslant 1$ TeV) light curves of AE Aquarii from data observed with the SAAO 30 inch Cassegrain telescope and the Nooitgedacht Mk I Cherenkov telescope respectively (Taken from Meintjes et al. 1994).

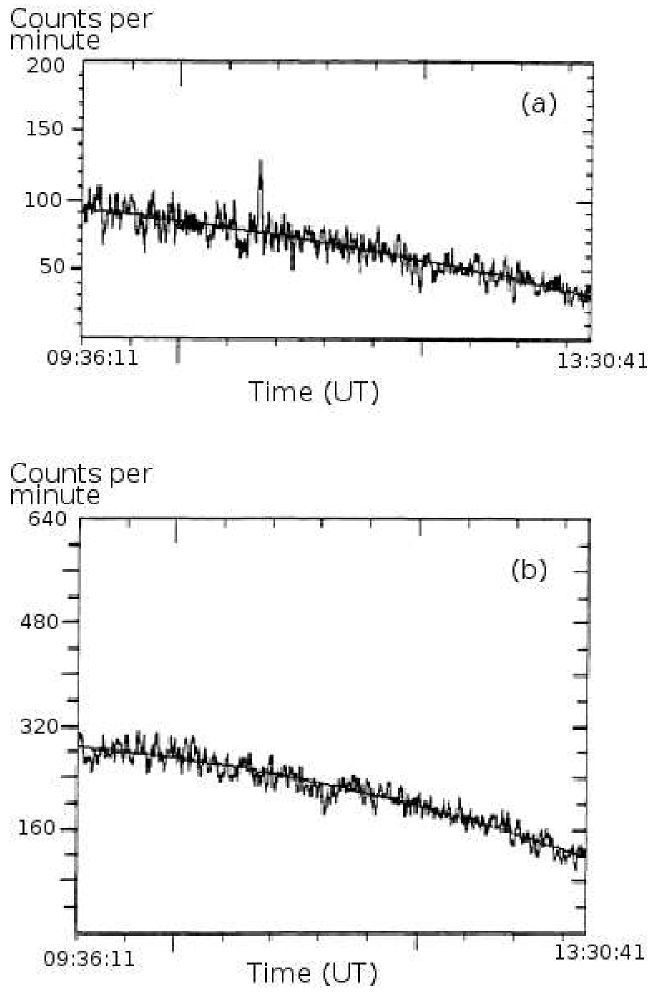

Figure 1.6: Summed light curves of AE Aquarii from data observed with Mark 3 and Mark 4 telescopes (at Narrabri) at γ-ray energies above 350 GeV. (a) Channel on-source (b) Channel off-source (Adapted from Bowden et al. 1992).

(peculiar) multi-wavelength emission properties of the system, justifying further investigation on the nature of the thermal and non-thermal emission.

Most observational studies have reported that the X-ray emission (below 10 keV) from AE Aquarii is pulsed (Figure 1.7) at the 33 s spin period of the white dwarf (e.g. Patterson et al. 1980; Choi et al. 1999; Eracleous 1999), and that the time-averaged X-ray spectra are dominated by soft X-ray emission. The spectrum shows a number of emission lines and can be described by multi-component thermal emission models, for example three-temperature VMEKAL[1] model

[1]VMEKAL model is an emission spectrum from hot diffuse gas based on the model calculations of Mewe and Kaastra with Fe L calculations by Liedahl (Mewe et al. 1985; Mewe et al. 1986; Arnaud & Rothenflug 1985). VMEKAL model includes line emissions from several elements. MEKAL model has a similar explanation.

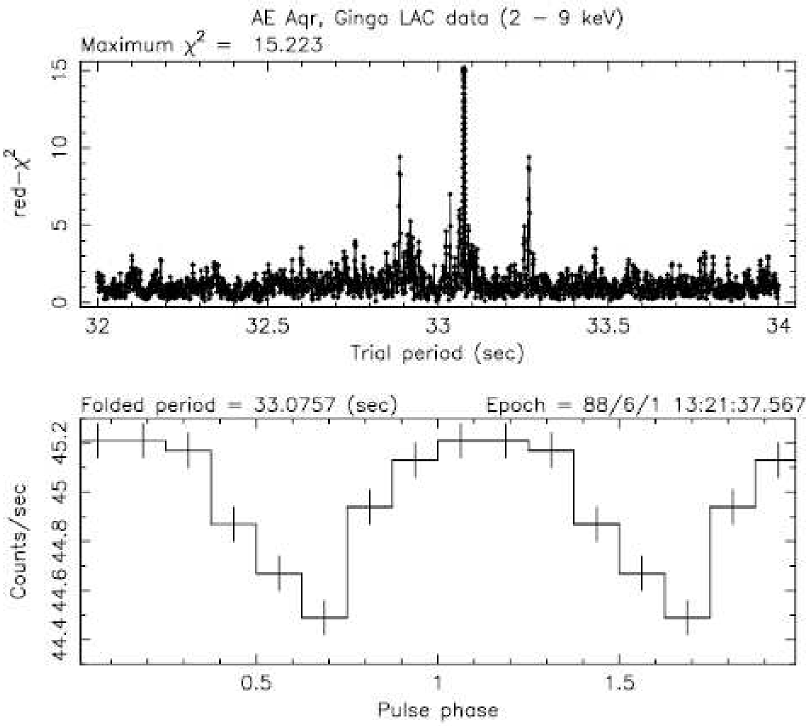

Figure 1.7: Periodograms and folded pulse profile of the Ginga LAC data (Taken from Choi et al. 1999).

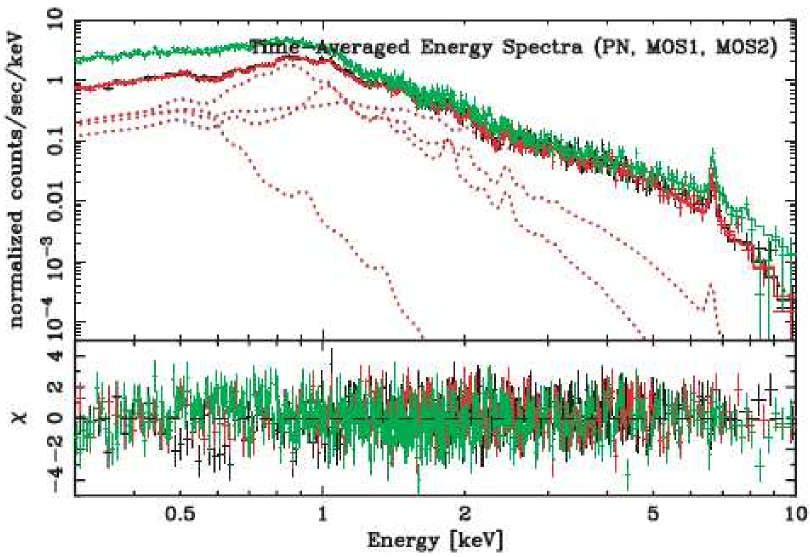

Figure 1.8: Time-averaged energy spectra of AE Aquarii from XMM-Newton data, fitted with a four-temperature VMEKAL model, showing characteristic emission lines (Taken from Itoh et al. 2006).

(Choi et al. 1999; Eracleous 1999; Itoh et al. 2006), as shown in Figure 1.8. Using an approximate distance of $\sim$ 100 pc, Eracleous (1999) computed the properties of the X-ray emitting plasma in AE Aquarii, and showed that the emission measure of a plasma, and also the cooling time,

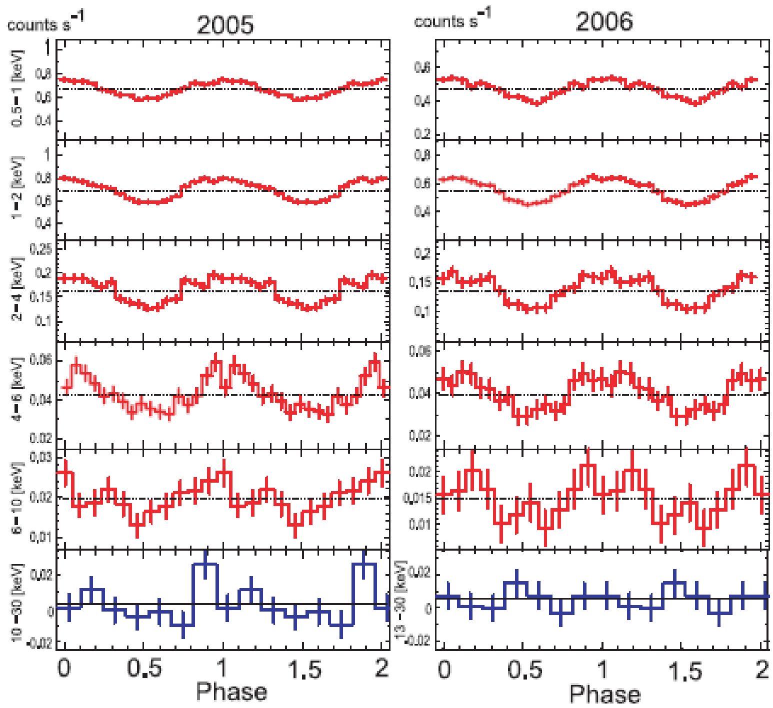

Figure 1.9: Folded energy-resolved light curves of AE Aquarii from Suzaku data. Phase 0.0 corresponds to BJD 2453673.5000 (Taken from Terada et al. 2008).

depends on its temperature, and the author suggested that X-ray flares occur close to the white dwarf. It was suggested that the conversion of the gravitational potential energy can heat the plasma to the observed temperatures.

A recent Suzaku detection has reported pulsed non-thermal hard X-ray emission (Figure 1.9) from AE Aquarii above 10 keV (Terada et al. 2008), with the associated spectrum fitted with a power-law model (Figure 1.10). This detection has motivated the detailed study of the X-ray properties of the system. The origin of the pulsed non-thermal hard X-ray emission from AE Aquarii is possibly synchrotron radiation of accelerated particles, powered by the spin-down luminosity of the rapidly rotating white dwarf. This places AE Aquarii within the realm of binary pulsars, as illustrated in Figure 1.11, where (in the figure) AE Aquarii falls in the category of the intermediate polars. A possible detection of pulsed VHE and TeV γ-ray emission (Figures 1.12, 1.13 and 1.14) from AE Aquarii (e.g. Bowden et al. 1992; Meintjes et al. 1992, 1994), may suggest sites where electrons are accelerated to relativistic energies, where the γ-rays may be produced by either upscattering soft photons from the K-type secondary star through the inverse Compton process, or a circumbinary ring that may orbit the system (e.g. Dubus et al. 2004).

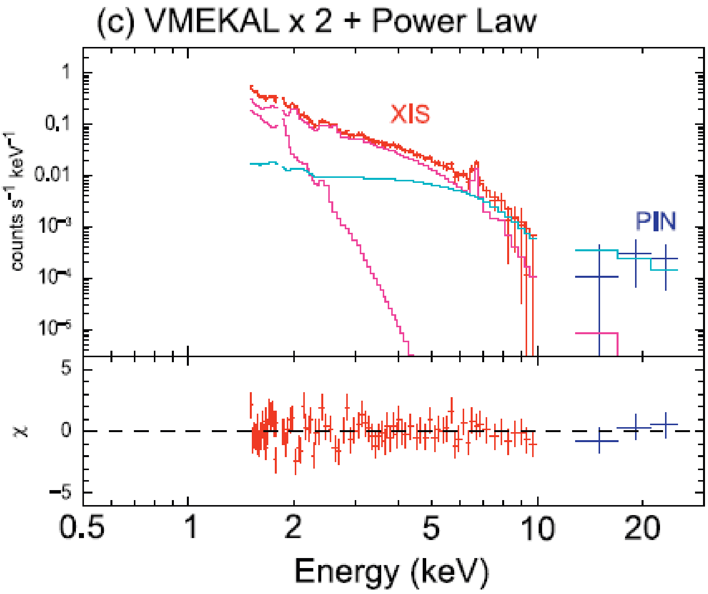

Figure 1.10: Spectrum of AE Aqr from Suzaku data, fitted with a power-law model, for $\epsilon_X > 10$ keV (Taken from Terada et al. 2008).

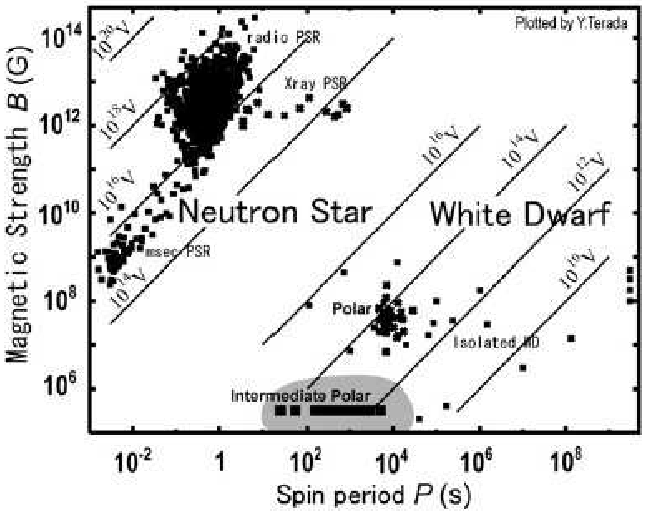

Figure 1.11: Period versus magnetic field strength for neutron stars and white dwarfs. The parallel lines show the electric potentials induced by the rotation (Taken from Terada et al. 2008).

This may provide an exciting prospect for follow-up studies using modern γ-ray telescopes.

The focus of this investigation is to verify and to constrain the properties of the thermal and the conjectured non-thermal emission from AE Aquarii. I investigate in detail the spectral properties of AE Aquarii using X-ray data from Chandra and Swift. My principal objective is to determine whether there is any non-thermal component in the emission, and if there is, to

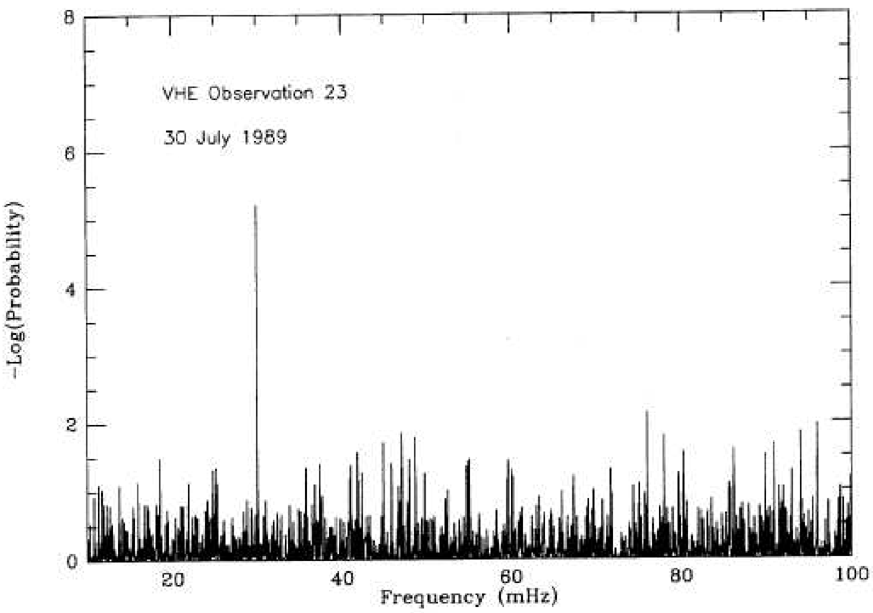

Figure 1.12: VHE power spectrum of AE Aquarii, representing pproximately 1000 independent Fourier frequencies (Taken from Meintjes et al. 1992).

isolate and constrain it. I also investigate the behaviour of the pulsed periodic UV and X-ray emission associated with the rotation of the white dwarf. In this, I make extensive use of the results of earlier studies (e.g. de Jager et al. 1994; Mauche 2006, 2009; Terada et al. 2008).

In this thesis, I summarise and present in a systematic form results that I have already reported in the following peer reviewed papers: Bosco Oruru and P. J. Meintjes, 2011, Pos (HTRS 2011) 063; B Oruru and P J Meintjes, 2011, Proceedings of SAIP 2011, ISBN: 978-86888-688-3, pages 501-506; B Oruru and P J Meintjes, 2011, Proceedings of SAIP 2011, ISBN: 978-86888-688-3, pages 507-512; B. Oruru and P. J. Meintjes, 2012, MNRAS, 421, 1557-1568. These papers are reproduced in Appendices A.1, A.2, A.3 and A.4 respectively.

I have structured this thesis as follows. In Chapter 2, I discuss cataclysmic variables in general. The purpose of this review is to put into perspective the exceptional properties of AE Aquarii. The magnetic propeller process is important in explaining the transient nature of the multi-wavelength emission of AE Aquarii. I therefore present also a detailed discussion of this process. A major part of this thesis is a study of the X-ray properties of this system. In the final part of this chapter, I thus review previous studies of the X-ray emission from AE Aquarii. I review radiation processes that are relevant to the study of AE Aquarii in Chapter 3. In Chapter 4, I

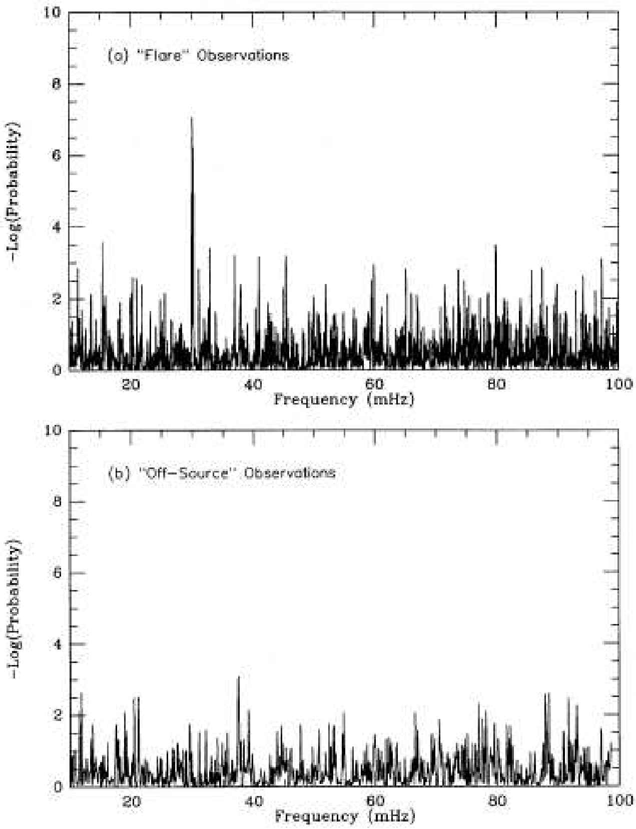

Figure 1.13: VHE power spectrum of AE Aquarii, showing on-source and off-source observations (Taken from Meintjes et al. 1992).

present results of the analysis of data observed with Chandra and made available to the public. Before this, I review the operation of the Chandra satellite, and also the different forms (or levels) of data found in the Chandra data archive. I have made use of standard processed data and used the steps outlined to process the light curves and spectra respectively. In Chapter 5, I present a similar discussion of the operation of the Swift satellite, levels of data stored in the Swift data archive, and the methods that I used to analyse the UVOT and XRT data that is made available to the public. I also review the methods of generating the Swift XRT data products by use of a web-based facility developed by the Swift team, which I have used to process the spectra. In Chapter 6, I present the Spectral Energy Distribution (SED) of AE Aquarii, plotted using the archived, published and analysed data. I also present the proposed X-ray emission models, which form the main component of this chapter. Thermal soft X-ray emission (below 10 keV), which is the dominant emission, is constrained in terms of the conversion of a fraction of gravitational potential energy (of the infalling material) to heat energy, at the magnetospheric radius of the white dwarf. On the other hand, non-thermal hard X-ray emission (above 10 keV) is constrained

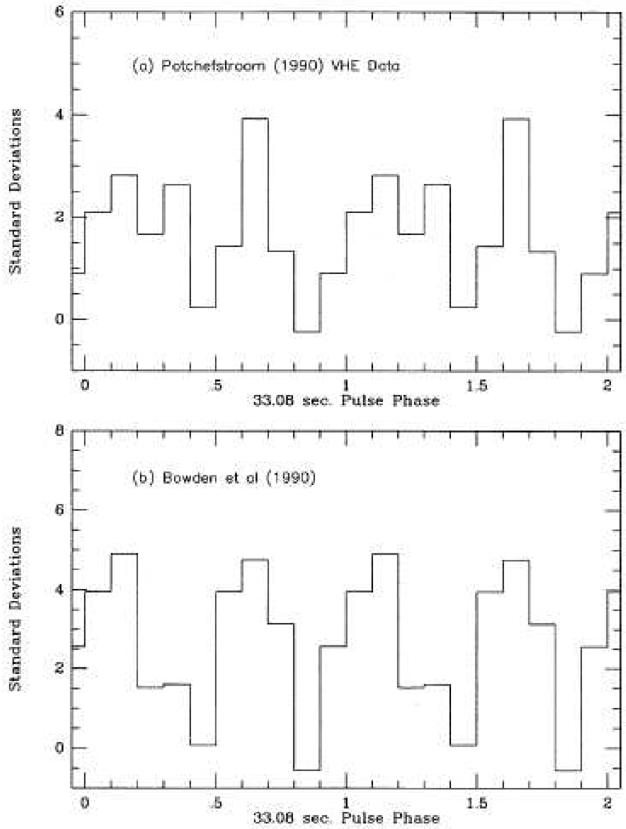

Figure 1.14: Folded light curves of AE Aquarii, for VHE observations at (a) 2.4 TeV, and at (b) 400 GeV (Taken from Meintjes et al. 1994).

in terms of synchrotron radiation of accelerated electrons, powered by the rotation of the white dwarf. Finally, in Chapter 7, I summarise the principal results of this study and discuss their implications for our understanding of AE Aquarii.

Chapter 2

Cataclysmic Variables

2.1 Introduction

Cataclysmic variables (CVs) in general display multi-wavelength emission properties that are related to the accretion disc and to the processes of mass transfer and accretion. This makes them ideal laboratories to study these processes. The system parameters, which include distance to the system, magnetic field strength, companion masses, and orbital period, can readily be determined (e.g. Abada-Simon et al. 1999, 2005). There is a large number of CVs in the Galaxy. Their variability and unpredictability make them ideal targets for both amateur and professional astronomers (e.g. Hellier 2001, page 1). About 75% of all known CVs have been discovered either due to their variability and their X-ray emission (e.g. Aungwerojwit et al. 2005). CVs are characterised by frequent outbursts, high variability in amplitude, and strong X-ray emission (e.g. Aungwerojwit et al. 2005).

The nova-like variable AE Aquarii, which is the subject of this study, is possibly the most enigmatic of all CVs. Its transient multi-wavelength emission (e.g. Patterson 1979; Bookbinder & Lamb 1987; Meintjes et al. 1992, 1994) makes it unique among the CVs. Although in this study I focus mainly on this enigmatic system, I will present in this chapter a general discussion of CVs with emphasis on the magnetic systems in order to put the properties of AE Aquarii in perspective.

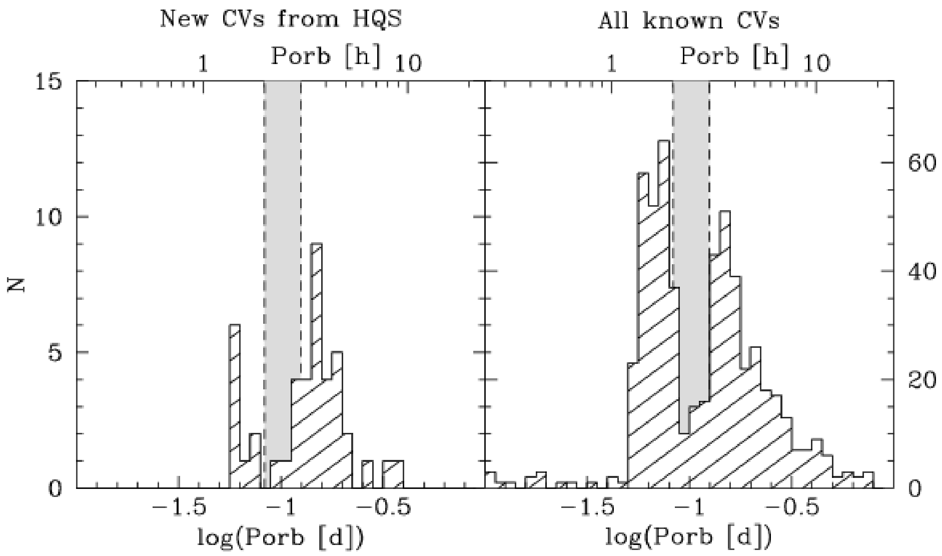

Figure 2.1: Distribution of orbital periods among CVs showing a period gap between 2 and 3 hours. HQS is the **H**amburg **Q**uasar **S**urvey (Taken from Aungwerojwit et al. 2005).

There are various classes of CVs. These include classical novae, dwarf novae, recurrent novae, nova-likes and magnetic cataclysmic variables (MCVs). See Warner (1995, pages 27-28) for an extensive review. All of these systems are modelled as an interacting binary (almost comparable in size to the Earth-Moon system) which consists of a white dwarf (WD) orbiting a low-mass, late-type main sequence companion (e.g. Eracleous & Horne 1996; Knigge et al. 2011). The companion stars orbit their common centre of mass with characteristic orbital periods ranging from 1 to 10 hours (e.g. Warner 1995, page 29; Aungwerojwit et al. 2005). Figure 2.1 shows the distribution of orbital periods among CVs. Standard models for the population of known CVs predict that the vast majority of these systems have short orbital periods, i.e. $P_{\rm orb} < 2$ hours (e.g. Aungwerojwit et al. 2005 and references therein).

Because of the close proximity of the primary star (i.e. the white dwarf), the secondary star (i.e. the companion star) is distorted by the gravitational field of the compact WD. As the secondary evolves, the binary system becomes more compact, eventually initiating mass transfer from the outer atmosphere of the secondary to the white dwarf through the inner Lagrangian point (e.g. Warner 1995, pages 30-32 ; Hellier 2001, page 20). Depending on the magnetic field strength of the primary, material transferred from the secondary may either form an accretion disc, or is channelled onto the polar caps of the primary. If the WD is a fast rotator and magnetic field is strong enough, the material transferred from the secondary may be expelled from the system.

2.2 Formation and Evolution of CVs

Stars usually form in clusters, inside giant molecular clouds. They are thought to emerge due to gravitational collapse of clumps of gas inside these clouds, triggered possibly by shock waves from nearby supernova explosions. Large clouds containing thousands and/or millions of solar masses collapse under gravity forming a whole cluster of young stars (e.g. Hellier 2001, page 45). Most of these stars form near companions and may become gravitationally bound into binaries, triples, pairs of binaries, and so forth. Stars which later evolve to become CVs emerge as binary stars of unequal masses, separated by hundreds of solar radii and orbiting one another with periods close to 10 years.

It is established that the lighter of the companion stars in such systems is less than a solar mass (e.g. Hellier 2001, page 45). The greater weight and associated higher pressure and temperature on the core of the heavier star causes it to evolve faster, leading eventually to a red giant. It then overfills its Roche lobe and transfers gas from its outer layers to the companion. To conserve angular momentum, the binary separation decreases, and also the Roche lobe size (e.g. Hellier 2001, page 45). The overfilled Roche lobe of the heavier star results in more matter being transferred to the low-mass companion. Eventually, the companion can no longer assimilate this huge influx of mass flow into its Roche lobe, resulting in the overfilling of both Roche lobes and, consequently, in the formation of a common envelope. The companion stars then orbit within the common envelope. The resultant drag drains orbital energy, resulting in a decrease of the binary separation. In approximately 1000 years, the binary expels the envelope into space, thus forming a planetary nebula (e.g. Hellier 2001, page 46). At this stage, a CV (i.e. a red dwarf - white dwarf binary system) is formed, with the low mass star (secondary star) still unevolved (e.g. Schenker & King 2002; Schenker et al. 2002).

From the instance when a CV is formed, the companion star drives the system, essentially transferring its outer layers to the white dwarf through Roche lobe overflow (or to a lesser extent, steller wind outflow) as it evolves. When the white dwarf has accumulated enough mass to become unstable, it either collapses into a neutron star (thus becoming a hard X-ray source) or else explodes as a Type Ia supernova. In the latter case, the companion star is ejected from the system.

2.3 Mass Transfer in Interacting Binaries

The importance of accretion as a source of energy was first widely recognized in the study of X-ray binaries (e.g. Frank, King & Raine 2002, page 48). Most stars are members of binary systems and, as they evolve, mass transfer takes place. In principle, the orbital separation plays a significant role since mass transfer and accretion are the result of strong tidal interactions between the compact star and its companion. Close (or interacting) binaries are binary systems in which significant interaction other than simple gravitational attraction occurs (e.g. Warner 1995, page 30).

In close binaries, the radii of the two stars are a significant fraction of their orbital separation. Interaction between the stars may be radiative (due to the heating of the face of one component by a hotter companion), or tidal, distorting both components through a combination of gravitational and centrifugal effects, which may lead to mass transfer. In CVs, the secondary star is always greatly distorted by the gravitational influence of the white dwarf primary, but the small radius of the latter leaves it immune to tidal influence (e.g. Warner 1995, page 30). Tidal interaction causes the secondary to rotate synchronously with the orbital revolution.

There are two modes through which many binaries transfer material during some stage of their evolution (e.g. Frank, King & Raine 2002, page 48):

Mode 1. One of the component stars increases in radius as it evolves, or there is a decrease in orbital separation, to an extent where the gravitational pull of the companion can remove the material from its outer layers. This case, called Roche lobe overflow, is common in CVs and low-mass X-ray binaries (LMXBs). I will discuss this case in more detail.

Mode 2. One of the stars (as it evolves) may eject most of its material in the form of a stellar wind. Some may be captured by the companion. This mode of mass transfer is common in high-mass X-ray binaries (HMXBs). I will not discuss this case further.

2.3.1 Roche Lobe Geometry

The orbital separation of close binaries is comparable to their radii. Hence their shapes are tidally distorted. For CVs and XRBs, the gravity of the compact object distorts the companion star (e.g. Frank, King & Raine 1992, page 50; Warner 1995, page 30). When the gravititational field of the secondary star fails to hold material in its outer layers, this material escapes into the potential well of the primary (e.g. Hellier 2001, page 20).

The dynamics of the infalling gas is governed by the Euler equation,

$$\rho\frac{\partial\vec{v}}{\partial t}+\rho\vec{v}\cdot\nabla\vec{v}=-\nabla P+\vec{f}, \tag{2.1}$$

where ρ and $\vec{v}$ are the density and velocity of the gas, ∇P is the pressure gradient, and $\vec{f}$ represents the force per unit volume exerted by the force fields, gravitational and electromagnetic, on the gas. In a frame rotating with the binary at angular velocity ω relative to the inertial frame of its centre of mass, the Coriolis[1] and centrifugal force terms are incorporated to give

$$\frac{\partial\vec{v}}{\partial t}+\vec{v}\cdot\nabla\vec{v}=-\nabla\Phi_{\rm R}-2(\vec{\omega}\times\vec{v})-\frac{1}{\rho}\nabla P, \tag{2.2}$$

where -$\nabla\Phi_{\rm R}$ is a term that includes the effect of gravitational and centrifugal forces, and -$2(\vec{\omega}\times\vec{v})$ is the coriolis force per unit mass (Frank, King & Raine 2002, page 50). The angular velocity vector is given by

$$\vec{\omega}=\left(\frac{GM}{a^3}\right)^{\frac{1}{2}}\hat{\rm e}, \tag{2.3}$$

where a is the orbital separation, and ê is a unit vector normal to the orbital plane. The parameter $\Phi_{\rm R}$ in Eq. 2.2 is called the Roche potential, and takes the form

$$\Phi_{\rm R}(r)=-\frac{GM_1}{|\vec{r}-\vec{r}_1|}-\frac{GM_2}{|\vec{r}-\vec{r}_2|}-\frac{1}{2}(\vec{\omega}\times\vec{r})^2, \tag{2.4}$$

where $\vec{r}_{\rm i}$ (i = 1, 2) are the position vectors of the centres of the two stars from the centre of mass, and $\vec{r}$ denotes the position vector of an arbitrary point P from the centre of mass respectively.

Figure 2.2 shows a surface representing the Roche potential for a binary system with mass ratio $q = M_2/M_1 = 0.25$. Near the centres of the stars (r_1, r_2), the equipotentials are spherical but become pear-shaped further away. Hence, the potential $\Phi_{\rm R}$ has two deep valleys centred on r_1

[1]Coriolis effect is a deflection of freely moving objects when they are viewed from a rotating frame.

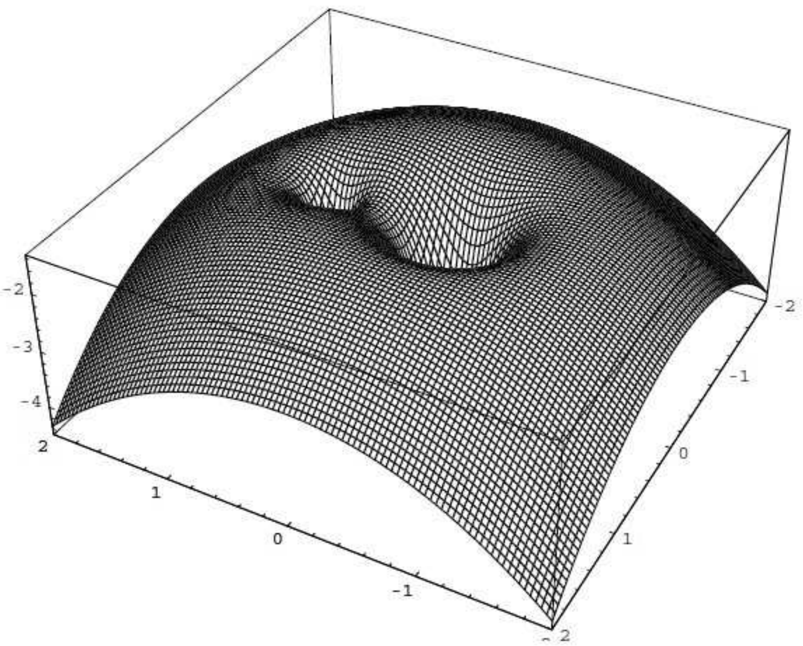

Figure 2.2: A surface representing the Roche potential. The larger well is around the more massive star (Taken from Frank, King & Raine 2002, page 51).

and r_2 (e.g. Frank, King & Raine, 2002, page 51). The downward curvature near the edges is due to the centrifugal term. Particles that attempt to corotate with the binary near these edges will experience a net outward force.

Figure 2.3 shows the equipotentials of Φ_R, also plotted for $q = 0.25$. To matter orbiting at large distances ($r \gg a$), the system appears to be a point mass concentrated at the centre of mass (CM). In other words, the equipotentials at large distances are just those of a point mass viewed from the rotating frame (e.g. Frank, King & Raine 2002, page 51). The critical feature of Figure 2.3 is the heavily marked figure-eight shape, which traces the so-called **Roche lobes** of the orbiting stars (e.g. Hellier 2001, page 20; Frank, King & Raine 2002, page 51). These critical surfaces join at the inner Lagrange point (L_1), which is a saddle point of Φ_R. Then L_1 acts like a high mountain pass between two valleys (Figure 2.2), which means that material inside one of the lobes in the vicinity of L_1 finds it much easier to pass through L_1 into the other lobe than to escape the Roche lobe altogether.

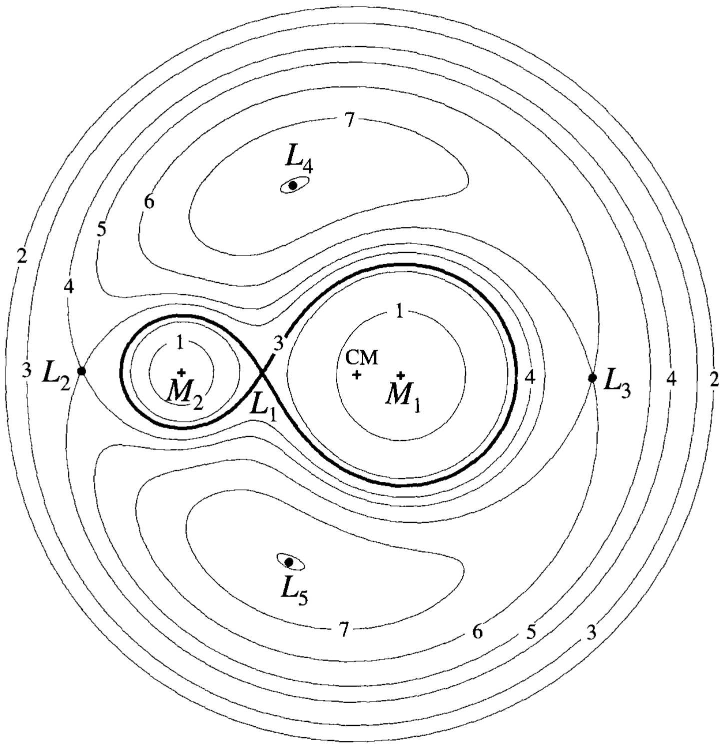

Figure 2.3: Equipotential surfaces of close binary stars, showing the Roche lobes and the Lagrangian points (Taken from Frank, King & Raine, 2002, page 52).

Figure 2.4 (on the right) illustrates three common types of binary systems. (a) In some systems, neither stars fill their Roche lobes (as in the NN Ser system). The binary is detached, and mass transfer cannot take place between the two stars by means of Roche lobe overflow. This is common among main sequence binaries. (b) In CVs and LMXBs, only one of the stars fills its Roche lobe, leading to a semi-detached system which permits mass transfer through Roche lobe overflow. In these systems, it is the red dwarf that fills its Roche lobe (Hellier 2001, page 21). (c) In cases where both stars fill their Roche lobes (e.g. W UMa star systems), a contact binary is formed (Frank, King & Raine 1992, page 50).

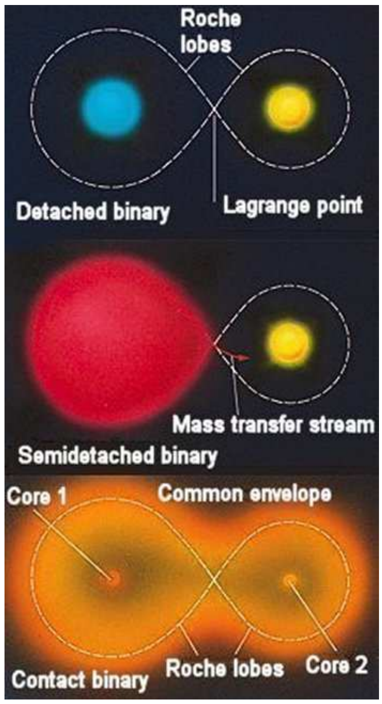

Figure 2.4: Close binary systems (www.daviddarling.info/encyclopedia/C/close_binary.html).

2.3.2 Mass Transfer Equations

Mass transfer in a binary system will change its mass ratio $q = \frac{M_2}{M_1}$, where M_1 and M_2 represent the white dwarf and secondary masses respectively, as well as the orbital separation a (e.g. Frank, King & Raine 2002, page 55). These two parameters (q, a) determine the Roche lobe geometry, and any change in their values will cause the size of the Roche lobe of the mass-losing star to change.

The angular momentum of a binary system is the sum of the individual angular momenta about their centre of mass:

$$\begin{aligned} J &= J_1 + J_2 \\ &= \frac{2\pi}{P}(M_1 r_1^2 + M_2 r_2^2), \end{aligned} \tag{2.5}$$

where the orbital velocity $v = \frac{2\pi r}{P}$, and it is assumed that the two stars are treated as point masses, each without spin. Kepler's third law for two orbiting objects gives

$$P = 2\pi\sqrt{\frac{a^3}{G(M_1 + M_2)}}, \tag{2.6}$$

which implies that

$$J = \sqrt{\frac{G(M_1 + M_2)}{a^3}}(M_1 r_1^2 + M_2 r_2^2). \tag{2.7}$$

Also for the two masses of the orbiting stars and their radial distance from the centre of mass,

$$r_1 + r_2 = a \tag{2.8}$$

$$M_1 r_1 = M_2 r_2. \tag{2.9}$$

Therefore,

$$r_1 = \frac{M_2 a}{M_1 + M_2} \tag{2.10}$$

$$r_2 = \frac{M_1 a}{M_1 + M_2}. \tag{2.11}$$

The orbital angular momentum equation then reduces to

$$J = M_1 M_2 \left(\frac{Ga}{M}\right)^{\frac{1}{2}}, \tag{2.12}$$

where $M = M_1 + M_2$, is the total mass of the binary. Logarithmic differentiation of Eq. 2.12 gives,

$$\frac{\dot{J}}{J} = \frac{\dot{M}_1}{M_1} + \frac{\dot{M}_2}{M_2} - \frac{\dot{M}}{2M} + \frac{\dot{a}}{2a}. \tag{2.13}$$

Here $\dot{M}_2$ represents the mass transfer rate from secondary star, $\dot{M}_1$ the mass accretion rate onto the surface of compact star, and $\dot{M}$ represents the mass loss rate from the binary system. For conservative mass transfer, i.e. $\dot{M} = 0$ and $\dot{M}_1 =$ - $\dot{M}_2$, it can be shown that

$$\frac{\dot{a}}{a} = 2\frac{\dot{J}}{J} + 2\frac{-\dot{M}_2}{M_2}\left(1 - \frac{M_2}{M_1}\right). \tag{2.14}$$

Conservative mass transfer is characterized by constant binary mass and angular momentum, i.e. $\dot{J} = 0$ and - $\dot{M}_2 = \dot{M}_1$ is positive (e.g. Frank, King & Raine 2002, page 56). This leads to an increase in orbital separation ($\dot{a} > 0$), provided that $M_2 < M_1$ (which is usually the case in CVs). In other words, as more matter is placed near the centre of mass (into the Roche lobe of the primary), the remaining mass of the companion should move in a wider orbit to conserve orbital angular momentum (e.g. Frank, King & Raine 2002, page 56).

The Roche lobe radius of the secondary star, e.g. Hellier (2001, page 48), is related to the mass ratio and orbital separation by,

$$\begin{aligned} R_2 &= a\left(\frac{q}{1+q}\right)^{\frac{1}{3}} \\ &= a\left(\frac{M_2}{M}\right)^{\frac{1}{3}}. \end{aligned} \tag{2.15}$$

Then, one can also show that

$$\frac{\dot{R}_2}{R_2} = \frac{\dot{a}}{a} + \frac{\dot{M}_2}{3M_2} - \frac{\dot{M}}{3M}. \tag{2.16}$$

By using Eq. 2.14 and the fact that $\dot{M} = 0$ for conservative mass transfer, it can be shown that

$$\frac{\dot{R}_2}{R_2} = 2\frac{\dot{J}}{J} + 2\frac{-\dot{M}_2}{M_2}\left(\frac{5}{6} - \frac{M_2}{M_1}\right). \tag{2.17}$$

If $\dot{J} = 0$, mass transfer from the secondary star to the primary causes the secondary's Roche lobe to increase in size, i.e. $\dot{R}_2 > 0$, provided that $q < \frac{5}{6}$. However, for stable and sustained mass transfer, angular momentum should be lost, i.e. $\dot{J} < 0$ (Hellier 2001, page 48). Continued mass transfer is then enhanced in two possible ways: (i) when the mass-losing star expands, or (ii) the binary loses angular momentum. Case (i) occurs as the secondary star evolves off the main sequence and becomes a giant or a subgiant (e.g. Frank, King & Raine 2002, page 57).

This case is confined to relatively long-period systems where the Roche lobe is large enough to accommodate such a star. Case (ii) mainly applies to short-period binaries, for example CVs, where the Roche lobe is too small to enable evolution into the red giant phase, and also the secondary has a very low mass and its main-sequence lifetime is too long compared with the Hubble time. Loss of angular momentum shrinks the orbit, and hence also the Roche lobe of the secondary star.

There are two possible mechanisms for angular momentum loss in CVs. These are: gravitational radiation and magnetic braking respectively. The former is significant in short-period systems, where relativistic effects are important (e.g. Frank, King & Raine 1992, page 53; Hellier 2001, page 47). Gravitational radiation is brought about by space warping due to the periodic orbital motion of the companion stars about their common centre of mass. Magnetic braking, on the other hand, is the result of a stellar wind and a stellar magnetic field. Charged particles in the wind move along the field lines and hence corotate with the magnetic field as the red dwarf rotates. These particles are accelerated to high speeds by the magnetic field and shot off into space, carrying with them significant quantities of angular momentum. The drain of angular momentum could brake the secondary's rotation, but due to tidal interactions (e.g. Hellier 2001, page 47), the orbit supplies angular momentum to maintain synchronism. Hence, the orbit shrinks while the mass-losing star rotates faster. The same effect is observed when low-Earth orbiting satellites lose altitude, i.e. they spin faster as their altitude decreases.

Angular momentum loss in a wind magnetically linked to the secondary is a currently favoured possibility. However, the nature of the transfer process depends on the secondary's reaction to the mass loss (e.g. Frank, King & Raine 2002, page 57). For a gentle mass loss, the star stays close to thermal equilibrium. Hence, $R_2 \propto M_2$, and hence $\dot{R}_2/R_2 = \dot{M}_2/M_2$. Then Eq. 2.17 becomes

$$-\frac{\dot{M}_2}{M_2} = \frac{-\dot{J}/J}{4/3 - q}. \tag{2.18}$$

This shows that mass transfer proceeds on the angular momentum loss time scale. The parameters a and P also decrease on similar time scales:

$$\frac{\dot{a}}{a} = \frac{2\dot{P}}{3P} = \frac{2\dot{J}/3J}{4/3 - q}, \tag{2.19}$$

for $q < \frac{4}{3}$.

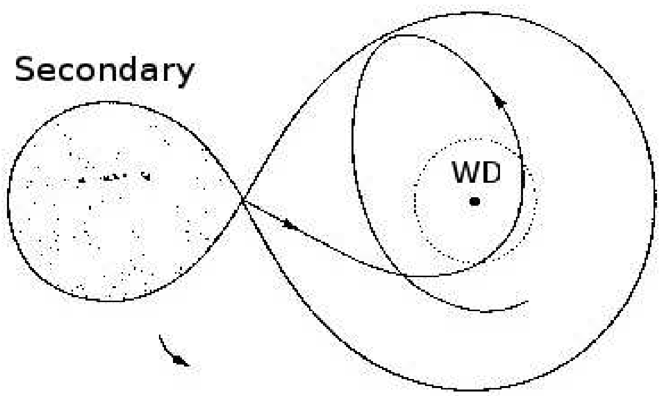

Figure 2.5: Trajectory of material from the inner Lagrangian point (L_1) in the vicinity of the white dwarf (Taken from Hellier, 2001, page 25).

2.3.3 Formation of Accretion Discs in Semi-detached Binaries

A consequence of mass transfer via Roche lobe overflow is the high load of specific angular momentum of the infalling material, inhibiting direct accretion onto the primary star (Frank, King & Raine 2002, page 58). This is illustrated in Figure 2.5. The material squirts out of L_1 at roughly sonic speed (~ 10 km s^{-1}), but L_1 itself rotates so rapidly that the gas stream appears to move almost orthogonally to the line of centres connecting the two stars (e.g. Frank, King & Raine 2002, page 59; Hellier 2001, page 23).

The gravitational attraction of the white dwarf accelerates the gas stream, which then follows a ballistic trajectory, determined largely by the Roche lobe potential and the injection velocity. The stream swings into an orbit around the white dwarf; the coriolis force causes the stream to deflect past the white dwarf (e.g. Frank, King & Raine 2002, page 59). A continuous stream along this trajectory will intersect itself with energy dissipation such that the material settles eventually into a circular orbit, i.e. the lowest energy orbit. To conserve angular momentum, the stream orbits at the so-called circularization radius ($R_{\rm circ}$), for which the orbital velocity is given by,

$$v = \left(\frac{GM_1}{R_{\rm circ}}\right)^{\frac{1}{2}}, \tag{2.20}$$

where $R_{\rm circ}v = b_1^2\omega$, with b_1 the distance of L_1 from the primary.

Dissipative processes at $R = R_{\rm circ}$ convert some energy of the orbital motion into internal energy

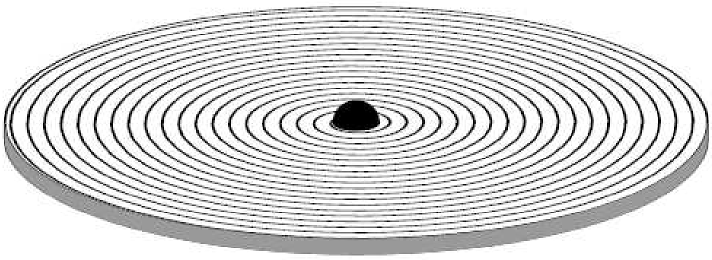

Figure 2.6: View of an idealized accretion disc around a compact object (Taken from Frank, King & Raine 2002, page 61).

(e.g. Frank, King & Raine 1992, page 57). The gas then sinks deeper into the Roche lobe of the primary, thus losing angular momentum. Due to viscous dissipation, some material moves to larger orbits. The ring of radius $R = R_{\rm circ}$ will therefore spread, with some material moving to smaller and some to larger radii. In other words, the ring spreads into a thin disc of circling material (the so-called accretion disc), where the inner edge may eventually meet the surface of the white dwarf. This is illustrated in Figure 2.6. In many magnetic systems, the inner part of the disc settles at the magnetospheric radius, where the disc's ram pressure balances the magnetospheric pressure. The outward spread of the disc is, however, limited by tidal interactions between the disc's outer edge and the secondary which soaks up angular momentum, returning it to the red dwarf's orbit (e.g. Hellier 2001, page 25).

Usually, the total mass of matter in the accretion disc is so small that its mean density is very small compared with that of the WD. Hence, the self-gravity of the disc can be ignored . The orbits of the disc's material are Keplerian, as shown in Figure 2.6; the angular velocity can be obtained by balancing the gravitational force and the centripetal force:

$$\Omega_K(R) = \left(\frac{GM_1}{R^3}\right)^{\frac{1}{2}}. \tag{2.21}$$

In a steady state, the total disc luminosity is half the accretion luminosity:

$$L_{\rm disc} = \frac{GM_1\dot{M}}{2R_1}, \tag{2.22}$$

where $\dot{M}$ is the mass accretion rate. Half of the accretion luminosity must thus go into radiation (e.g. Frank, King & Raine 1992, page 57).

Once a disc is formed, the gas stream from L_1 will hit the outer edge of the disc supersonically,

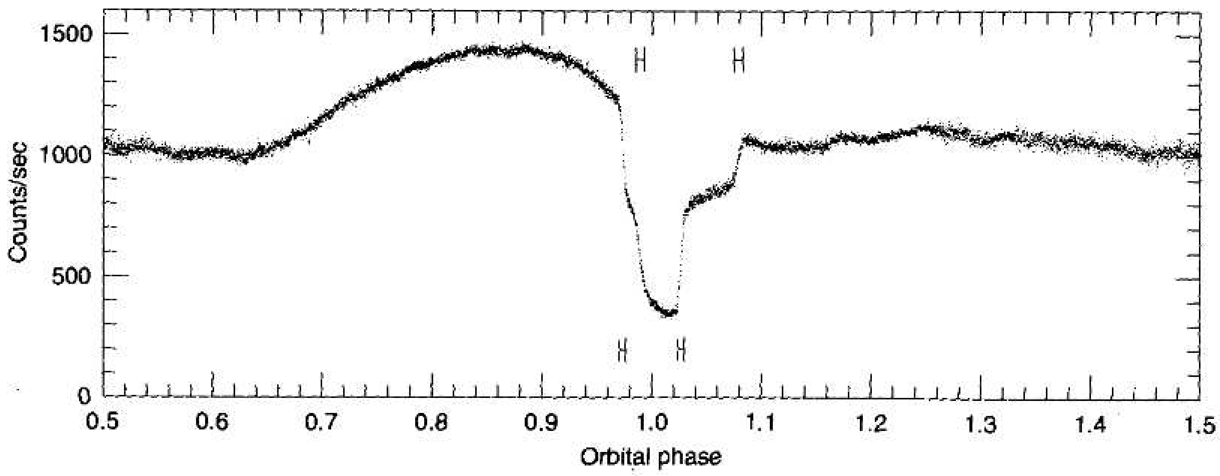

Figure 2.7: Orbital humps in the light curve of a CV. The H marks below the data locate the circumstances when the white dwarf enters and comes out of eclipse, and those above are when the bright spot enters and leaves eclipse (Taken from Hellier, 2001, page 28).

creating a shock heated area called the bright spot (Hellier 2001, page 27; Warner 1995, page 38). The turbulent encounter at the bright spot is poorly understood. Computer simulations, however, reveal that part of the stream flows over the edge due to the narrow width of the disc, and some material continues in its original trajectory. It is reported that ~ 30 % of the total light in some CVs is emitted at the bright spot. This is usually deduced through the observation of orbital humps, as shown in Figure 2.7 (Hellier 2001, page 27-28).

2.4 Magnetic Cataclysmic Variables (MCVs)

Some white dwarfs in CVs have substantial magnetospheres, i.e. the mass accretion process is controlled by the magnetic field, and may hamper the formation of an accretion disc. In non-magnetic CVs, therefore, a disc forms around the WD, resulting in some observable properties that are quite different from those of MCVs (e.g. Cropper 1990). A partially ionized gas falling towards a magnetic star will, at some point, have its motion restricted by the magnetic field. The volume within which this effect is felt defines the magnetosphere of the star (Lamb 1989 e.g. Warner 1995, page 308). The underlying principle is that the field and the matter become frozen together such that charged particles are unable to cross the field lines, but is constrained to move along them (e.g. Hellier 2001, page 109).

The dynamics of a stream of gas from the secondary star is as follows. Far from the magnetic white dwarf, the kinetic energy associated with the bulk flow of the gas greatly exceeds that associated with the interaction with the field. The flow continues as though there were no field since the field is dragged along with the flow, but is unable to affect it. But close to the white dwarf, the magnetospheric energy density greatly exceeds that of the bulk flow (e.g. Hellier 2001, page 109). In this region, the field lines are rigid and the material can only flow along them. MCVs can thus be considered consisting of an outer zone (non-magnetic) and a magnetically dominated magnetosphere that surrounds the white dwarf. The transition region between the two regimes is, however, poorly understood.

Inside the magnetosphere, material corotates with the white dwarf. The WD's spin period adjusts itself so as to balance the circular motion just inside the magnetosphere and the Keplerian motion of the material just outside. In this equilibrium situation, there is no jump in velocity at the magnetospheric boundary (e.g. Hellier 2001, page 110). For a spherically symmetric infall, the magnetic pressure balances the gas ram pressure (e.g. Davidson & Ostriker 1973). So the magnetospheric radius ($R_{\rm M}$), or the Alfvén radius, can be computed to be

$$R_{\rm M} \simeq 5 \times 10^{10} \mu_{34}^{\frac{4}{7}} M_1^{-\frac{1}{7}} \dot{M}_{17}^{-\frac{2}{7}} \ {\rm cm}, \tag{2.23}$$

where M_1 is the mass of the WD, μ_{34} is its magnetic moment in units of 10^{34} G cm^3, and $\dot{M}_{17}$ is the mass accretion rate in units of 10^{17} g s^{-1} respectively.

2.4.1 Polars and Intermediate Polars

MCVs can be divided into two classes according to the strengths of the surface magnetic field of the white dwarf (Warner 1995, page 28). The two classes are called Polars and Intermediate Polars respectively. Those having the strongest surface fields, $B_* > 10^7$ G are classified as polars (from the level of polarization of their optical emission), or AM Herculis systems. MCVs having medium-magnetic field strengths ($B_* < 10^7$ G) are classified intermediate polars, or DQ Herculis systems (in the special case when the WDs are rapidly rotating). The magnetic field strength is the principal distinguishing property between these two classes. In polars, therefore, the strength of the field forces the WD to corotate with the secondary star. The field always presents the same aspect to the incoming accretion stream (e.g. Cropper 1990).

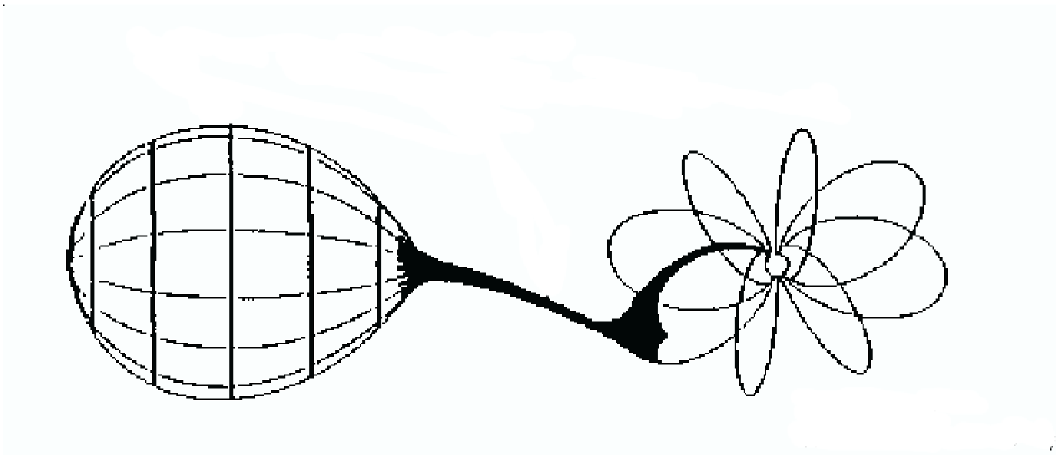

Figure 2.8: Trajectory of a gas stream in a polar. From L_1, the stream maintains its trajectory until magnetic forces begin to control its flow at $R_{\rm M}$, where it is channeled to one of the magnetic poles of the white dwarf (Adapted from Cropper 1990).

Polars are strong X-ray sources at energies $E \leqslant 0.1$ keV, and can be easily identified through the optical polarization of cyclotron emission (e.g. Frank, King & Raine 1992, page 128). These MCVs have magnetic moment (μ) $\sim 10^{34}$ G cm^3 and hence $R_{\rm M} \sim$ few $\times\ 10^{10}$ cm. This is comparable with the distance of the white dwarf from L_1. In a sense, the field lines from the primary star can readily connect with the companion to ensure synchronous rotation of the latter (e.g. Warner 1995, page 309). For $R_{\rm M} \geqslant R_{\rm L,1}$, the gas stream from the secondary star is expected to be attached to the field lines of the primary for its entire trajectory (e.g. Schneider & Young, 1980a,b). However, for $R_{\rm M} \leqslant R_{\rm L,1}$, which is the common case in Polars, the stream leaving L_1 would first follow a trajectory as in non-MCV, then upon $R = R_{\rm M}$, its motion is guided by the field and it may be shattered into small fragments due to Rayleigh-Taylor instabilities (e.g. Burnard, Lea & Arons 1983; Hameury, King & Losata 1986a). Figure 2.8 shows the trajectory of gas from L_1 in a typical AM Her system.

Intermediate polars (IPs), as the name suggests, have magnetic field strengths that combine the characteristics of non-MCVs and those of polars. They have a characteristic surface magnetic field of $B_* < 10^7$ G, not strong enough to completely disrupt the formation of a disc (e.g. Cropper 1990) and synchronise the spin period of the white dwarf with the binary orbital motion (e.g. Kuijpers et al. 1997 and references therein). IPs are characterized by a combination of multi-periodic photometric behaviour and hard X-ray spectra (Warner 1995 e.g. Harrison et al. 2006). Mass transfer in IPs involves two modes. (a) For very small primary magnetic moments, a disc is formed and magnetic accretion is restricted to the region from the inner edge of the disc down to the surface of the white dwarf. (b) If μ is sufficiently large, no accretion disc forms and mass transfer then becomes largely determined by the location of the threading region.

Short period IPs with rapidly rotating white dwarfs, i.e. DQ Herculis and AE Aquarii, lack hard X-ray emission, thought to result from the proximity of the Alfvén radius and the white dwarf surface (e.g. Warner 1995, page 412). It is believed that the white dwarfs in DQ Her systems are spun-up to short rotation periods by accretion torques. The discussions presented thus far are aimed at introducing the characteristic DQ Her system, AE Aquarii, which is the subject of this study. In the next section, therefore, this peculiar system is discussed in greater detail, focussing mainly on the propeller process which is believed to drive the highly transient multi-wavelength emission in the system, as well as the X-ray properties of AE Aquarii, which is the focus of this particular investigation.

2.5 AE Aquarii

The low mass, non-eclipsing close binary system AE Aquarii (AE Aqr) consists of a fast rotating ($P_* = 33$ s) magnetized white dwarf orbiting a late-type secondary star (e.g. Choi et al. 1999; Itoh et al. 2006) with an orbital period of 9.88 h (e.g. Welsh et al. 1993). The secondary star is a spectral type K3-5 (e.g. Welsh et al. 1995; Ikhsanov 1997; Itoh et al. 2006) red dwarf star filling its Roche lobe and hence transfers matter to the primary companion. Most CVs have M-type dwarf secondaries, indicating that the K-type secondary star in AE Aqr suggests a different evolutionary path for the system (e.g. Schenker et al. 2002). For an inclination angle of $i = 58° \pm 6°$, the masses of the white dwarf and secondary star in AE Aqr are evaluated to $M_1 = 0.79 \pm 0.16 M_\odot$ and $M_2 = 0.5 \pm 0.1 M_\odot$ respectively (e.g. Casares et al. 1996; Itoh et al. 2006). The semi-major axis of the binary system is $a \sim 1.8 \times 10^{11}$ cm.

AE Aqr has traditionally been classified as a nova-like variable (e.g. Joy 1954; Crawford & Craft 1956; de Jager 1991). Utilizing the oblique rotator model, Patterson (1979) modelled the system as a fast rotating magnetized star accreting matter from the secondary star or from an accretion disc, placing AE Aqr in the category of the DQ Herculis sub-class of magnetic cataclysmic variables (e.g. Warner 1983; Ikhsanov 1997). However, as shall be reviewed later, the formation of an accretion disc is unlikely, and most of the properties of the system are unrelated to those of most CVs with well-developed accretion discs.

AE Aqr has been detected and studied in almost all wavelength bands (e.g. de Jager 1991); in radio (e.g. Bookbinder & Lamb 1987; Bastian, Dulk & Chanmugam 1988; Abada-Simon et al. 1993), in optical (e.g. Zinner 1938; Patterson 1979; Chincarini & Walker 1981; Eracleous & Horne 1996), in X-rays (e.g. Patterson et al. 1980; Clayton & Osborne 1995), and VHE & TeV γ-rays (e.g. Bowden et al. 1992; Meintjes et al. 1992, 1994; Chadwick et al. 1995). The system has a visual magnitude ranging from 10 to 12, and was discovered in the optical in 1938 (Zinner 1938). In quiescence, the optical emission is dominated by the contribution from the secondary ($\sim$ 95 %), with the remaining 5 % coming from the primary component (e.g. Bruch 1991). The visible brightness of the system (e.g Beskrovnaya et al. 1996) varies approximately 3 magnitudes in the U-passband on time scales from minutes to hours. Patterson (1979) observed a 33 s coherent oscillation in the optical light, which was later observed in other wavelengths (e.g. Patterson et al. 1980; de Jager et al. 1994; Eracleous et al. 1994; Meintjes et al. 1992, 1994). The characteristics of the observed radio flares, which are reportedly distinct from optical, UV, and X-ray flares (e.g. Abada-Simon et al. 1995) are associated with transient non-thermal emission processes resembling Cyg X-3 in a high state (Bookbinder & Lamb 1987), justifying VHE - TeV follow-up studies of this enigmatic object.

Most of the observed properties of AE Aqr contribute to the uniqueness of this source, justifying a thorough investigation on the nature of the primary star and the mode of mass transfer in the system (Ikhsanov 1997). Schenker et al. (2002) have suggested that AE Aqr recently evolved from the common envelope phase. With an orbital period of 9.88 h (e.g. Joy 1954; Patterson 1979), which is rather long for a typical CV, a large binary separation would be implied. Although an accretion disc is expected for such a long orbital period, the spectral profile of the H_α emission line is single-peaked, with its centroid velocity inconsistent with the white dwarf orbit but lags behind the secondary orbit by some 70° - 80°, and the spectral widths of the Balmer emission lines are highly variable (e.g. Itoh et al. 2006, and references). Itoh et al. (2006) also noted that the maximum temperature of the X-ray emission ($\sim$ 3 keV) is much less than the temperature of the hard X-ray emission at the post-shock accretion columns in magnetic cataclysmic variables.

The primary star is considered to be a white dwarf, having a spin period of 33 s which was deduced from the superimposed 33 s modulation of the optical and X-ray light curves (e.g. Patterson 1979, Patterson et al. 1980; de Jager et al. 1994). The great difference between the white dwarf spin period and the system's orbital period makes AE Aqr one of the most asynchronous known cataclysmic variables (e.g. Abada-Simon et al. 1993; 1999). It is believed that, at some stage during its evolution, AE Aqr underwent a run-away mass transfer process, causing a large spin-up of the WD (e.g. Meintjes 2002). The spin period of the white dwarf, as well as the relatively strong surface magnetic field of $B_* \sim 10^6$ G (e.g. Meintjes & de Jager 2000), combined with the non-thermal nature of the recently detected pulsed hard X-ray emission above 10 keV (Terada et al. 2008), makes AE Aqr unique among most cataclysmic variables.

The most unique characteristic of AE Aqr is perhaps its rapid flaring in almost all wavelengths (e.g. Ikhsanov et al. 2004, and references therein). Large optical flares and flickering (e.g. Patterson 1979), large radio flares (e.g. Bastian et al. 1988) and TeV γ-ray emission (e.g. Meintjes et al. 1994) have contributed to the system's branding as "enigmatic"(e.g. Itoh et al. 2006). In radio (e.g. Bastian et al. 1988; Abada-Simon et al. 1993) and possibly TeV γ-rays (e.g. de Jager 1994; Meintjes et al. 1994), AE Aqr reveals itself as a powerful non-thermal variable source (Figs. 1.2 & 1.5), resembling Cyg X-3 (a microquasar) rather than any of the presently known CVs (e.g. Ikhsanov 1997). Besides, a similar radio brightness has never been observed in any of the other CVs. Bowden et al. (1991, 1992), de Jager (1991), Meintjes et al. (1992, 1994) reported a 33 s modulation in TeV emission from AE Aqr (Figs. 1.12, 1.13 & 1.14), with a luminosity $\sim 1.5\times10^{32}$ erg s^{-1}. The observed luminosity of the strongest TeV flare is $\sim 10^{34}$ erg s^{-1}, which corresponds to the inferred spin-down power of the white dwarf. In the remaining parts of the spectrum, the emission is predominantly thermal (Figs. 1.1, 1.3 & 1.8). Figure 2.9 shows the UV spectrum of AE Aqr with emission lines, which is characteristic of emission from hot optically thin plasma. A recent Suzaku detection (Terada et al. 2008), however, has reported non-thermal hard X-ray emission from AE Aqr above 10 keV (Figs. 1.9 & 1.10). This detection has motivated the detailed study of the X-ray properties of the system, which is the main focus of this study.

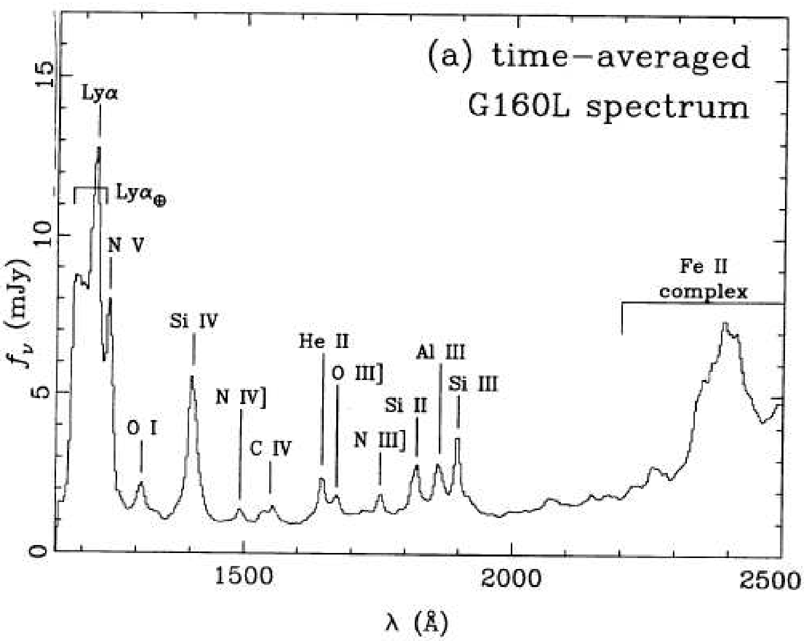

Figure 2.9: Time-averaged UV spectrum of AE Aqr from HST data (Taken from Eracleous et al. 1994).

2.5.1 The Spin-down of the Primary Star

A study related to the stability of the 33 s spin period of the white dwarf in AE Aqr, using a data set spanning $\sim$ 14 years (de Jager et al. 1994) showed that the white dwarf is spinning down at a rate of $\dot{P} \sim 5.64{\times}10^{-14}$ s s^{-1}. Adopting a white dwarf moment of inertia of $I \sim 10^{50}$ g cm^2, the spin-down translates to a luminosity (i.e. rate of change of rotational kinetic energy) of

$$\begin{aligned} L_{\text{s-d}} &= -\frac{dE_{\text{rot}}}{dt} \\ &\simeq 6\times 10^{33}\left(\frac{\dot{P}}{5.64\times 10^{-14}\ \text{s s}^{-1}}\right)\left(\frac{P}{33\ \text{s}}\right)^{-3}\ \text{erg s}^{-1}, \end{aligned} \tag{2.24}$$

where $E_{\text{rot}} = \frac{1}{2}I\Omega^2$ and $\Omega = \frac{2\pi}{P}$. A follow-up study utilizing optical and Chandra data (Mauche 2006) revealed a spin-down rate slightly higher ($\sim$ 3.5 %) than reported earlier by de Jager et al. (1994). Either way, the spin-down luminosity of the white dwarf exceeds the observed UV and X-ray luminosities of the system, i.e. $L_{\text{UV}} = L_{\text{X}} \sim 10^{31}$ erg s^{-1} (e.g. Eracleous et al. 1991, 1994; Reinsch et al. 1995), by more that two orders of magnitude. Besides, $L_{\text{s−d}}$ exceeds the system's total bolometric luminosity of $L_{\text{bol}} \sim 10^{33}$ erg s^{-1} (e.g. van Paradijs et al. 1989; Beskrovnaya et al. 1996), by more than a factor of 5. It has been noted that the spin-down luminosity dominates the total energy budget of the system (e.g. Ikhsanov 1997).

A detailed study of the spectral line behaviour utilizing the data from the Hubble Space Telescope (HST) revealed transient line emission and velocities exceeding typical Keplerian velocities in disc accreting systems (e.g. Eracleous & Horne 1996). To explain the line emission, a mass outflow rate of $\dot{M}_{\rm out} \sim 3\times10^{17}$ g s^{-1} is required (e.g. Eracleous & Horne 1996). This mass outflow rate corresponds remarkably well with the current thermal time scale mass transfer rate from the secondary star, i.e. $\dot{M}_2 \sim$ few $\times10^{17}$ g s^{-1} (e.g. Meintjes & de Jager 2000; Meintjes 2002; Meintjes 2004). This would imply that the spin-down of the white dwarf in AE Aqr is possibly associated with a propeller/ejector phase where the fast rotating white dwarf ejects the vast majority of the mass flow from the secondary star (e.g. Wynn, King & Horne 1997; Meintjes & de Jager 2000). This would explain the low X-ray luminosity of $L_{\rm X} \sim 10^{31}$ erg s^{-1}, implying a mass accretion rate onto the WD's surface of only $\dot{M}_* \sim$ few $\times10^{14}$ g s^{-1}.

2.5.2 The Magnetic Propeller in AE Aquarii

Although AE Aqr is a member of the DQ Her systems (e.g. Meintjes & de Jager 2000), its relatively low X-ray luminosity of $L_{\rm X} \sim 10^{31}$ erg s^{-1} (e.g. Choi et al. 1999), and the structure of the $\rm H_\alpha$ Doppler tomogram (e.g. Wynn, King & Horne 1997) argue against the possibility of the mass transfer flow from the secondary being accreted onto the surface of the white dwarf, with or without an accretion disc. Wynn & King (1995) and Wynn, King & Horne (1997) have proposed a model which suggests that most of the accretion outflow is ejected from the system by the fast rotating magnetosphere of the WD, the so-called propeller action. It is suggested that the mass ejection takes place before the gas can penetrate into the magnetosphere deeper than the radius, $R_{\rm mag} \sim 10^{10}$ cm (e.g. Meintjes & de Jager 2000), which correlates with the so-called magnetospheric (Alfvén) radius, i.e. where the magnetospheric pressure starts to dominate the gas ram pressure. Since the magnetospheric propeller process is inherently the driving mechanism behind the unique multi-wavelength emission in AE Aqr, a detailed discussion is presented. The discussion follows the discussions presented by Wynn, King & Horne (1997), Meintjes & Venter (2005) and Venter & Meintjes (2007):

The first attempt to model the magnetospheric propeller effect utilized the physical interaction between a rotating magnetosphere and large diamagnetic blobs (e.g. Wynn & King 1995; Wynn, King & Horne 1997). In this approach, the blobs experienced a surface drag from the rotating magnetospheric field sweeping across it, transmitting mechanical energy to blobs on a time scale

$$t_{\rm mag} \simeq \frac{c_{\rm A}\rho_{\rm b}l_{\rm b}}{B^2}\frac{|v_\perp|}{|(v-v_{\rm f})_\perp|}, \tag{2.25}$$

where $\rho_{\rm b}$ and $l_{\rm b}$ denote the density and length scale of the blobs, $c_{\rm A}$ is the Alfvén speed in the interblob fluid, v and $v_{\rm f}$ are the blob and fluid velocities, and the components perpendicular to the field are taken. In terms of the magnetospheric drag model, a blob will follow a ballistic trajectory which is modified by the drag term (e.g. Wynn, King & Horne 1997):

$$g_{\rm mag} = -k(v-v_{\rm f})_\perp, \tag{2.26}$$

where $k \sim \frac{1}{t_{\rm mag}}$ is the drag coefficient. The velocity difference introduces $P_{\rm spin}$ into the magnetic acceleration ($g_{\rm mag}$), so that $P_{\rm spin}$ directly influences the magnetospheric gas flow (Wynn, King & Horne 1997). Thus, blobs may either be accreted or ejected, depending on $P_{\rm spin}$ and k.

Meintjes & de Jager (2000) have explained the magnetic propeller in AE Aqr in terms of the interaction between the WD magnetosphere and a clumpy ring at the circularization radius ($R_{\rm circ}$), in which angular momentum is transferred from the rotating magnetic field to the ring. Hence shearing of magnetic field will occur at $R_{\rm circ}$ where strong MHD instabilities are excited causing the field lines to mix with the gas (e.g. Wang & Robertson 1985). This results in a propeller-like expulsion of the gas stream, which also triggers both thermal and non-thermal outbursts. In this model, Meintjes & de Jager (2000) considered the twisting of the magnetic field into outward floating loops, transferring angular momentum to the orbiting gas. As these flux tubes expand and unravel (e.g. Wang & Robertson 1985), the angular momentum flux will centrifugally propel the gas. The sheared field lines generate currents that flow along the flux tubes, which also result in huge field-aligned potential drops (or double layers) that develop to sustain the current.

The flow pattern of the accretion stream in the magnetospheric propeller process in AE Aqr is depicted in Figure 2.10. At the radius of closest approach, most of the material of the stream is ejected, with escape velocity of $v_{\rm esc} \sim 1500$ km s^{-1} (e.g. Meintjes & Venter 2005; Venter & Meintjes 2007). As the blobs gain orbital angular momentum traversing the magnetosphere, the WD spins down. The energetics of the interaction between the diamagnetic blobs and the

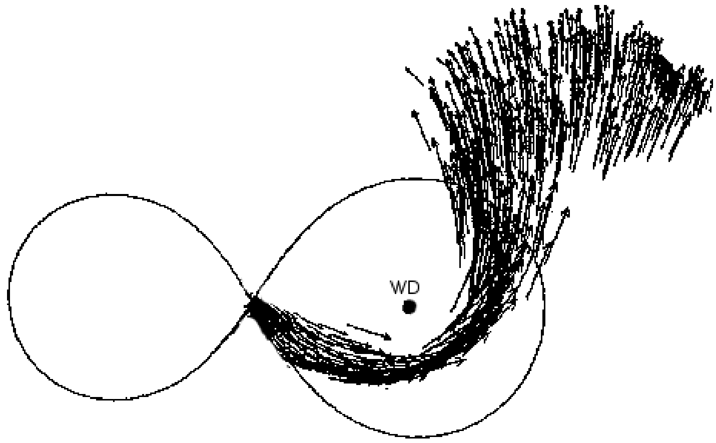

Figure 2.10: The magnetic propeller in AE Aqr. The distance of closest approach of the stream to the white dwarf is $\sim 10^{10}$ cm (Adapted from Wynn, King & Horne 1997).

magnetosphere is explained by the Poynting theorem (e.g. Meintjes & Venter 2005):

$$\frac{d}{dt}(u_{\mathrm{mech}} + u_{\mathrm{field}}) = -\nabla \cdot \left[\frac{c}{4\pi}(\vec{E} \times \vec{B})\right], \tag{2.27}$$

where u_{mech} is the mechanical energy density, u_{field} the field energy density, and the $\vec{E} \times \vec{B}$ term is the Poynting flux ($\vec{S}$) respectively. Integrating over the volume occupied by a conducting fluid interacting with the magnetosphere, and using the Gauss divergence theorem:

$$\int_V (\nabla \cdot \vec{F}) dV = \oint_S \vec{F} \cdot d\vec{S}, \tag{2.28}$$

$$\frac{d}{dt}(U_{\mathrm{mech}} + U_{\mathrm{field}}) = -\int \frac{c}{4\pi} \nabla \cdot (\vec{E} \times \vec{B}) dV = -\int \frac{c}{4\pi}(\vec{E} \times \vec{B}) \cdot d\vec{A}. \tag{2.29}$$

From standard MHD theory,

$$\vec{E}_{\perp} = -\frac{\vec{v}}{c} \times \vec{B} \left(1 + \left(\frac{1}{R_{\mathrm{m}}}\right)\left(\frac{\vec{L}v}{c}\right)\left(\frac{\nabla \times \vec{B}}{\vec{B} \times \vec{v}/c}\right)\right), \tag{2.30}$$

where $R_{\mathrm{m}} \gg 1$ is the magnetic Reynold's number (e.g. Meintjes & Venter 2005). Thus, considering that the velocity of the field relative to the flow velocity is perpendicular to the poloidal magnetic field,

$$\vec{E}_{\perp} = -\frac{1}{c}(\vec{v}_{\mathrm{rel},\perp} \times \vec{B}), \tag{2.31}$$

resulting in the Poynting flux transmitted into the flow given by

$$\vec{S} = \frac{1}{4\pi}(\vec{B} \times (\vec{v}_{\mathrm{rel},\perp} \times \vec{B})) = \frac{1}{4\pi} B^2 \vec{v}_{\mathrm{rel},\perp}. \tag{2.32}$$

Since the azimuthal velocity of the corotating magnetosphere at the radius of closest approach of the stream exceeds the free-fall velocity of the flow significantly (Meintjes & Venter 2005), the propeller process increases the mechanical energy of the material due to power transferred from the magnetosphere to the stream. The azimuthal acceleration of blobs of different masses may also explain the transient nature of the optical emission (flares) as blobs of different speeds ram into one another upon interaction with the magnetospheric field (Beardmore & Osborne 1997).

2.5.3 X-Ray Emission from AE Aqr

AE Aqr is a relatively bright X-ray source ($L_{\mathrm{X}} \sim 10^{31}$ erg s^{-1}; Choi et al. 1999), and coupled with its close proximity to the earth ($D \sim 100$ pc; Welsh et al. 1993), it has been observed on a regular basis. The first successful attempt was with the EINSTEIN satellite (e.g. Patterson et al. 1980). Later, Eracleous et al. (1991) also obtained data with the same satellite. Many other observations were made, for example, EXOSAT (e.g. Osborne 1990), Ginga (e.g. Choi et al. 1999), ROSAT (e.g. Reinsch et al. 1995; Clayton & Osborne 1995), ASCA (e.g. Choi et al. 1999; Eracleous 1999), and XMM-Newton (e.g. Itoh et al. 2006).

Data analysed from ASCA, EINSTEIN and ROSAT have revealed that at low X-ray energies, the spectrum can be described by either a single thermal bremsstrahlung model or a two-temperature emission model (Figs. 2.11 & 2.12). Analysis by Clayton & Osborne (1995) has indicated that both quiescent and flare spectra in the energy range 0.1-2.5 keV can be reproduced by a two-temperature optically thin emission model, showing that a single-temperature bremsstrahlung model is insufficient to reproduce the observed quiescent spectra (e.g. Choi et al. 1999).

Following the discovery of periodic oscillations in the optical light curve of AE Aqr (Patterson 1979), at the time interpreted as rapid rotation of the accreting magnetized white dwarf, a search has been conducted for pulsed X-ray emission (Patterson et al. 1980) using data from the EINSTEIN X-ray satellite. These authors discovered a coherent 33 s X-ray pulse (Figure 2.13), and also found agreement in the arrival times of the optical and X-ray pulses, proposing thermal blackbody emission from a hot spot on the white dwarf. Patterson et al. (1980) further noted that the similarity between the pulsed and unpulsed spectra would require temperatures in

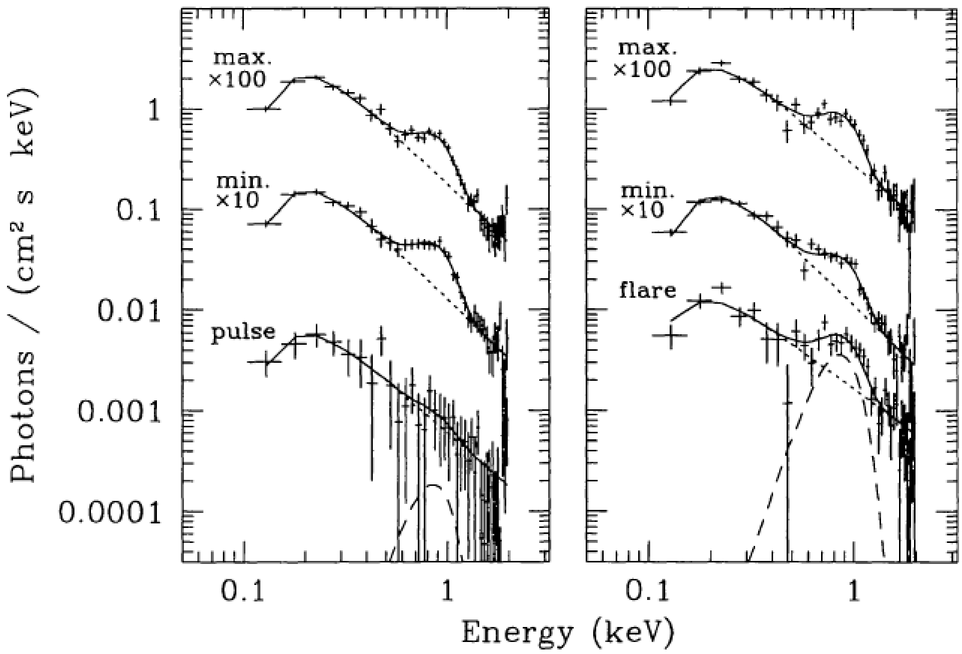

Figure 2.11: X-ray spectrum of AE Aqr from ROSAT data, fitted with the simplest model, power-law plus an emission line feature centred at 0.85 keV (Taken from Reinsch et al. 1995). The authors noted that similar results can be obtained with a two-component optically thin thermal model.

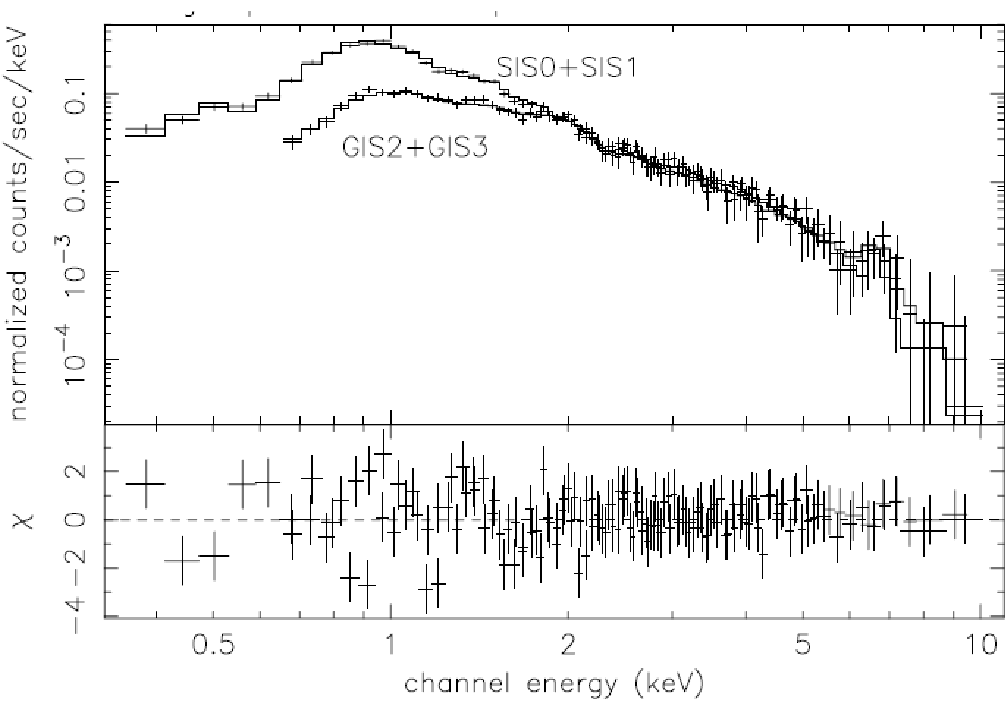

Figure 2.12: Time-averaged energy spectrum of AE Aqr from ASCA data, fitted with a two-temperature MEKAL model (Taken from Choi et al. 1999).

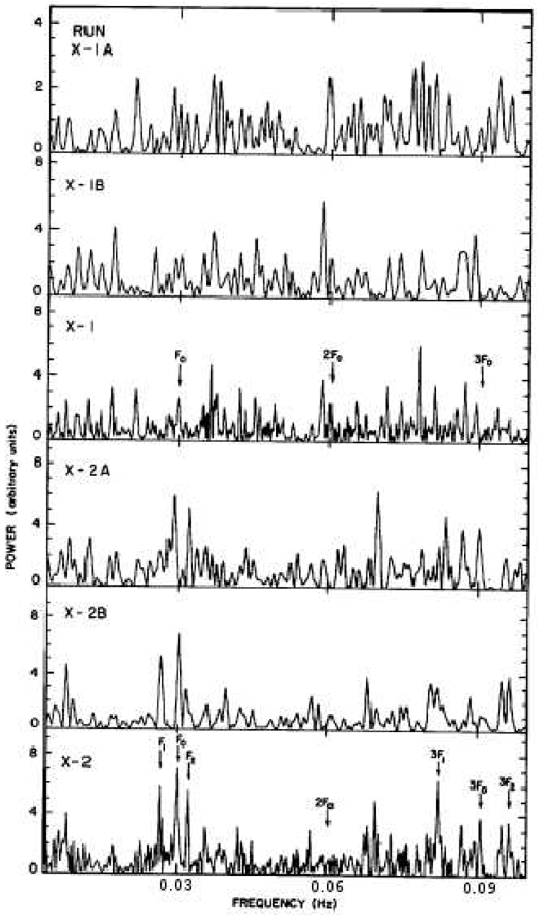

Figure 2.13: Power spectrum of AE Aqr from EINSTEIN data. F_0 is the fundamental period obtained in the optical data (Adapted from Patterson et al. 1980).

excess of 10^6 K, regardless of whether a blackbody or bremsstrahlung origin is assumed. Thus, a significant fraction of the pulsed X-ray flux must emerge from a location with $T > 10^6$ K. Using the Ginga data, Choi et al. (1999) also detected the 33 s pulsations in the X-ray light curve (Figure 1.7), which have also been seen in other observations (e.g. Mauche 2006, 2009; Terada et al. 2008).

The time-averaged energy spectra of AE Aqr obtained from ASCA data (Figure 2.12), ROSAT data (Figure 2.11) and XMM-Newton data (Figure 2.14) are dominated by soft X-ray emission and show a number of H-like or He-like K_α emission line features (e.g. Choi et al. 1999; Eracleous 1999; Itoh at al. 2006). These features (e.g. Choi et al. 1999; Itoh et al. 2006) imply an optically thin X-ray emitting plasma with a continuous energy distribution in the range $kT \simeq$ 0.1-10 keV. A recent detection of pulsed non-thermal hard X-rays (above 10 keV) by Terada et al. (2008),

Table 2.1: Emission Measures (EM) and Cooling Times Computed for X-ray Emission from AE Aqr (Taken from Eracleous 1999).

Component	Temperature (keV)	Emission Meassure (cm^{-3})	Cooling Time (s)
1	0.15	5.0×10^{52}	150
2	0.83	1.4×10^{53}	360
3	3.2	5.0×10^{53}	700

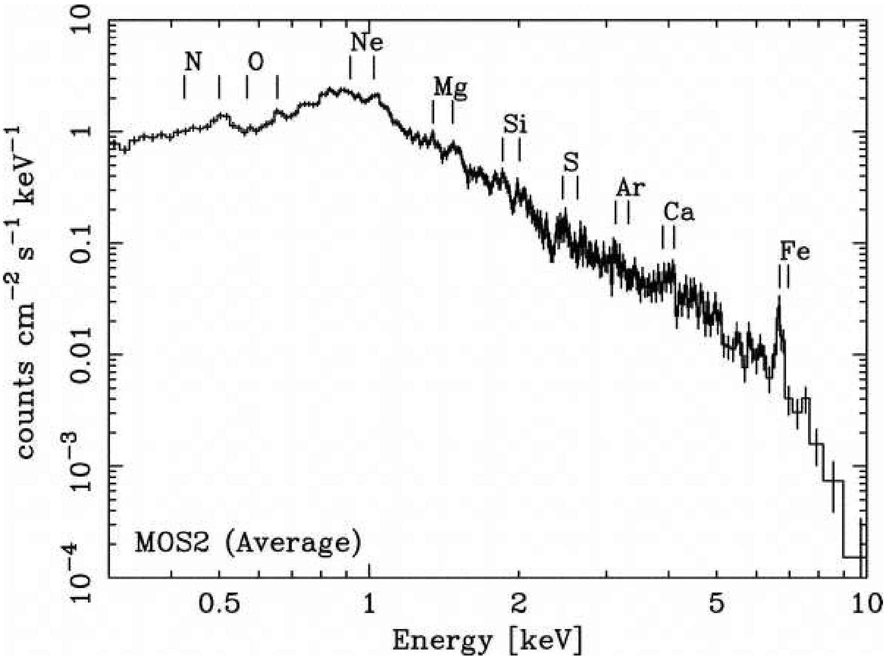

Figure 2.14: Time-averaged energy spectrum of AE Aqr from XMM-Newton data, with characteristic emission lines (Taken from Itoh et al. 2006).

using the Japanese-USA Suzaku satellite (Figure 1.8), may indicate a different mechanism for the hard X-ray emission, and this forms the basis for the intense study of the system in soft and hard X-rays, through data analysis and theoretical modelling, which are presented in this thesis.

Using an approximate distance to AE Aqr of $\sim$ 100 pc (e.g. Welsh et al. 1993), Eracleous (1999) computed the properties of the X-ray emitting plasma summarized in Table 2.1. From these properties, the bolometric luminosity of the X-ray source in AE Aqr is then obtained from the sum of the contributions of the different components:

$$L_{\rm bol} = 4.8 \times 10^{29} \sum_{i=1}^{n} \left(\frac{kT_{\rm i}}{1\ {\rm keV}}\right)^{1/2} \left(\frac{EM_{\rm i}}{10^{53}\ {\rm cm}^{-3}}\right)\ {\rm erg\ s}^{-1}, \tag{2.33}$$

where $T_{\rm i}$ and $EM_{\rm i}$ are the temperature and emission measure of component i respectively. For a known plasma density (n), the plasma cooling time is given by

$$\tau_{\rm cool} \sim 410 \left(\frac{kT}{1\ {\rm keV}}\right)^{1/2} \left(\frac{n}{10^{12}\ {\rm cm}^{-3}}\right)\ {\rm s}. \tag{2.34}$$

Assuming that the accretion flow is made up of blobs with size comparable to the white dwarf (e.g. Wynn, King & Horne 1997), a reasonable assumption (for an estimated plasma density) is that X-ray flares originate from shocked blobs. In this case,

$$n \sim \left(\frac{EM}{V}\right)^{1/2} \sim 10^{12} \left(\frac{EM}{10^{53}\ {\rm cm}^{-3}}\right)^{1/2} \left(\frac{r}{R_*}\right)^{-3/2}\ {\rm cm}^{-3}, \tag{2.35}$$

where V and r are the volume and radius of the plasma blob respectively. Since EM increases with increasing temperature (Table 2.1), flares are associated with significant plasma heating. Blobs heated to such high temperatures by the shock result in temperatures that relate to the shock velocity as

$$kT \sim 1.8 \left(\frac{v}{1000\ {\rm km\ s}^{-1}}\right)^2\ {\rm keV}, \tag{2.36}$$

which implies that a shock of velocity of $v \sim 1000$ km s^{-1} is required to produce the observed plasma temperature. Incidentally, this velocity is comparable with the velocity of free fall of the blobs at their closest approach to the white dwarf, suggesting that the blobs are shocked at this phase of their inflow from L_1 region. It appears that the heating occurs the instant the blobs are propelled, due to the apparent coincidence of the optical and X-ray flares (Osborne et al. 1995; Eracleous 1999). A scenario is considered where the blobs from the companion crash into a fast rotating magnetic barrier at their closest approach to the white dwarf, releasing some of the bulk kinetic energy in the form of heat and associated UV and X-ray emission (Eracleous & Horne 1996).

The flux of non-pulsed X-ray emission may be the result of magnetospheric emission (e.g. Choi et al. 1999). Energy is liberated at the rate,

$$L_{\rm th} = 1.3 \times 10^{33} f \left(\frac{\dot{M}}{10^{17}\ {\rm g\ s}^{-1}}\right) \left(\frac{M}{M_\odot}\right) \left(\frac{r_{\rm c}}{10^{10}\ {\rm cm}}\right)^{-1}\ {\rm erg\ s}^{-1}, \tag{2.37}$$

where $r_{\rm c}$ is the radius of closest approach of the blobs to the white dwarf, and f is the fraction of the potential energy liberated through the interaction with the magnetic field. $L_{\rm th}$ may well explain the quiescent X-ray luminosity. The maximum blob temperature is

$$T_{\rm max} \leqslant 10 \left(\frac{M}{M_\odot}\right) \left(\frac{r_{\rm c}}{10^{10}\ {\rm cm}}\right)^{-1}\ {\rm keV}. \tag{2.38}$$

Choi et al. (1999) have explained that the magnetospheric emission in AE Aqr may be related to its less intense emission measure, which is 1-3 orders of magnitude smaller than the typical emission measure of IPs. This indicates that the physical conditions driving the X-ray emission in AE Aqr differ substantially from other MCVs, contributing to its enigmatic nature.

The X-ray pulsations, as detected from the timing analysis of the Ginga and ASCA data of AE Aqr at quiescence, are characterized by single-peaked sinusoidal pulses. These make them quite different from UV and optical pulsations (e.g. Choi et al. 1999), exhibiting sinusoidal double-peaked pulse profiles (e.g. Eracleous et al. 1994), which correspond to the emission from the two magnetic poles. It has been noted that the large amplitude UV pulses could be due to some material accreting onto the white dwarf magnetic poles with the resultant UV emission coming from the accretion column above the polar caps. From the propeller point of view, matter is being expelled from the system (e.g. Wynn, King & Horne 1997). However, it is possible that some material remains attached to the field lines through plasma instabilities (e.g. the K-H instabilities) allowing some mass accretion onto the magnetic poles (e.g. Choi et al. 1999). Matter attached to the field lines can gradually drift towards the polar cap regions, cooling radiatively with dominant emission in the UV near the surface. In this picture, X-ray emission occurs in the magnetospheric boundary, hence the emitting plasma can not be occulted by the white dwarf.

The temporal nature of the X-ray emission is consistent with observations in other wavelengths. Choi et al. (1999) noted that the amplitude of the 33 s pulsations is the same in both flare and quiescent states. Also, the unpulsed quiescent component is ~ 30 % that of the unpulsed component in the flare state. Based upon these results, they argued against the flares coming from the polar cap regions on the surface of the magnetic white dwarf, instead suggesting a location far from the surface. In this context, the flare site is associated with the magnetospheric boundary, which coincides with the site of persistent emission. This was supported by the fact that the energy spectrum remained unchanged during the quiescent and flare states (e.g. Choi et al. 1999). The flares (with emission measure of $EM \sim 10^{54}$ cm^{-3}) are then viewed as resulting from a sudden increase in the emission in the magnetosphere due to sporadic mass flow from the companion star. It is suggested (e.g. Choi et al. 1999) that the size of the plasma emission region responsible for the flares is roughly the size of the magnetosphere ($\sim 2{\times}10^{10}$ cm), with plasma number density $n \sim 2\times10^{11}$ cm^{-3}. In this scenario, excess mass is unable to accrete onto the white dwarf due to the propeller mechanism. This is supported by the fact that the pulse amplitude of the UV pulsations remains more or less constant during quiescence or flares (e.g. Eracleous et al. 1994).

The average number density of electrons ($n_{\rm e}$) deduced by Itoh et al. (2006) from XMM-Newton data is $\sim 10^{11}$ cm^{-3}. This value is several orders of magnitude less than the conventional estimate in the postshock accretion column of typical MCVs of $n_{\rm e} \sim 10^{16}$ cm^{-3} (e.g. Frank, King & Raine 2002). From $n_{\rm e} \sim 10^{11}$ cm^{-3}, Itoh et al. (2006) have calculated the linear scale of the plasma components with kT_i = 0.2-0.3 keV to be $l_{\rm p} = (EM/n_{\rm e}^2)^{1/3} \approx$ (2-3)$\times10^{10}$ cm. The inferred linear scale is larger than the radius of the white dwarf ($R_* \sim 10^9$ cm) by more than an order of magnitude. From these results, Itoh et al. (2006) have concluded that the X-ray emitting plasma in AE Aqr cannot be a product of mass accretion onto the WD.

For the estimated maximum plasma temperature of $kT_{\rm max}$ = 4.6 keV (e.g. Itoh et al. 2006), the accretion material is accelerated to at least the thermal velocity of $v_{\rm th} = (3kT_{\rm max}/\mu m_{\rm H})^{1/2}$ $\approx$ 1500 km s^{-1} within the gravitational potential well of the white dwarf. This agrees well with the predictions from theoretical calculations of $\rm H_\alpha$ Doppler tomograms (e.g. Wynn, King & Horne 1997; Welsh et al. 1998). The high temperature is expected to arise due to the release of gravitational energy at a thermalization radius estimated from,

$$\frac{3}{2}kT_{\rm max} \sim \frac{GM_1}{r_{\rm th}}\mu m_{\rm H}, \tag{2.39}$$

resulting in $r_{\rm th} \sim 10^{10}$ cm. This agrees with the fact that the X-ray emission originates in the the propeller zone which correlates with the Alfvén radius (e.g. Wynn, King & Horne 1997; Ikhsanov et al. 2004). At $r_{\rm th}$, the magnetospheric corotation velocity, $v_{\rm cor} \sim 1.9\times10^9$ cm s^{-1}, is more than an order of magnitude higher than the Keplerian velocity, $v_{\rm K} \sim 1.0\times10^8$ cm s^{-1}. Hence, any plasma heated at $r \sim r_{\rm th}$ can be expelled rapidly by the rotating magnetosphere of the WD. The widths of the observed emission lines from X-ray to optical suggest that the plasma blobs are heated to $T_{\rm max}$ and then cool through adiabatic expansion (e.g. Itoh et al. 2006). The broad lines are expected to be emitted in the course of the cooling. The manifestation of flares in the emission lines from optical to X-rays support the prediction that they have a common origin, namely, the interaction between the white dwarf magnetosphere and the accretion stream.

The recent detection of non-thermal hard X-rays ($\epsilon_{\rm X} \geqslant 10$ keV) from AE Aqr with Suzaku (Terada et al. 2008) re-afirm the unique nature of the source. Hard X-ray emission from MCVs, in general, originates close to the white dwarf surface from the postshock plasma, with the temperature of the postshock plasma reaching a few tens of keV (Itoh et al. 2006). For AE Aqr, the ratio of the hard X-ray luminosity to the spin-down power, $\alpha \approx \frac{10^{31}}{10^{34}} \sim 0.1$ %, similar to that observed in young spin-powered pulsars (Becker & Trümper 1997; Terada et al. 2008). The fact that a fraction of the spin-down power of the white dwarf is channelled into particle acceleration and associated non-thermal emission (Meintjes & de Jager 2000) opens up possibilities for future multi-wavelength campaigns, from radio to TeV γ-rays.

Chapter 3

Radiation Processes

In the previous chapters, I reviewed the multi-wavelength emission properties of AE Aqr, and showed that the emission is due to a number of different thermal and non-thermal processes. To provide a framework for analysing and understanding the emission, I will review in this Chapter the theory underlying those radiation processes that are most relevant to the emission from AE Aqr. In this study, I am interested in the mechanisms associated with the production of the soft X-rays detected by Chandra and Swift which are predominantly of thermal origin, and in the hard ($\epsilon_{\rm X} \geqslant 10$ keV) X-ray emission detected by Suzaku (e.g. Terada et al. 2008). I will therefore discuss both thermal and non-thermal X-ray emission processes. Thermal X-ray emission is produced principally by blackbody radiation and thermal bremsstrahlung. Non-thermal hard X-ray emission is most likely the result of synchrotron radiation process.

3.1 Thermal Radiation

The soft X-ray emission ($\epsilon_{\rm X} \leqslant 10$ keV) displays a spectral behaviour that is characteristic of those thermal processes associated with both optically thick and optically thin hot plasmas. These are responsible for blackbody radiation and bremsstrahlung respectively. I will therefore review these processes in some detail.

3.1.1 Blackbody Radiation

Blackbody radiation is one which is in thermal equilibrium, i.e. the emitting medium is in thermal equilibrium with the radiation field (See Rybicki & Lightman 2004, pages 15 and 16 for a detailed discussion).

The spectral specific intensity of the emission from a blackbody is given by the Planck spectrum (e.g. Rybicki & Lightman 2004, page 19):

$$B_\nu(T) = \frac{2h\nu^3/c^2}{e^{\frac{h\nu}{kT}} - 1}, \tag{3.1}$$

where ν is the frequency of the radiation, and T is the temperature of the medium. An alternative form of the Planck law can be written in the form of wavelength:

$$B_\lambda(T) = \frac{2hc^2/\lambda^5}{e^{\frac{hc}{\lambda kT}} - 1}. \tag{3.2}$$

Figure 3.1 shows a plot of Planck spectrum as a funtion of frequency. The major properties of the Planck law are the following:

1. For $h\nu \ll kT$, it reduces to

$$B_\nu^{'}(T) = I_\nu^{\mathrm{RJ}}(T) \simeq \frac{2\nu^2}{c^2}kT, \tag{3.3}$$

   which is the Rayleigh-Jeans law, which applies at low frequencies (e.g. radio band).

2. For $h\nu \gg kT$,

$$B_\nu^{'}(T) = I_\nu^{\mathrm{W}}(T) \simeq \frac{2h\nu^3}{c^2}\exp(-h\nu/kT), \tag{3.4}$$

   which is Wien's law, which applies at high frequencies ($\nu > \nu_{\mathrm{max}}$). This implies that the brightness decreases rapidly with frequency from ν_{max} and beyond (Figure 3.1).

3. At a given temperature, the frequency at which the Planck function peaks (ν_{max}) can be obtained by differentiating the function to obtain the frequency when the gradient is zero. It can be shown that

$$\frac{h\nu_{\mathrm{max}}}{kT} = 2.82. \tag{3.5}$$

   This is Wien's displacement law (e.g. Rybicki & Lightman 2004, page 24).

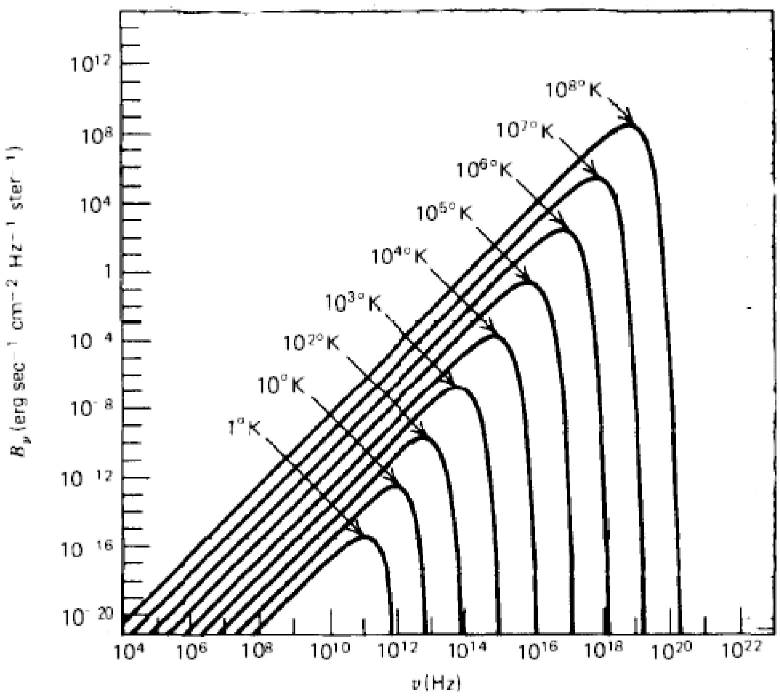

Figure 3.1: Spectrum of blackbody radiation at various temperatures. Maximum frequency increases with temperature (Adapted from Rybicki & Lightman 2004).

The total brightness of a blackbody emitter can be obtained by integrating the Planck function over all frequencies:

$$
\begin{aligned}
B(T) &= \int_0^\infty B_\nu(T) d\nu \\
&= \int_0^\infty \frac{2h\nu^3/c^2}{e^{\frac{h\nu}{kT}} - 1} d\nu \qquad (3.6)
\end{aligned}
$$

Using the substitution $x = \frac{h\nu}{kT}$, it can be shown (e.g. Rybicki & Lightman 2004, page 25) that

$$
\begin{aligned}
B(T) &= \frac{2\pi^4 k^4}{15c^2h^3} T^4 \\
&= \frac{ac}{4\pi} T^4, \qquad (3.7)
\end{aligned}
$$

where

$$a = \frac{8\pi^5 k^4}{15c^3h^3}. \qquad (3.8)$$

The total energy radiated per unit surface area of a blackbody per unit time, i.e. the blackbody emissive power (P') is given by

$$
\begin{aligned}
P'(T) &= \pi B(T) \\
&= \sigma T^4 \text{ erg cm}^{-2} \text{ s}^{-1}, \qquad (3.9)
\end{aligned}
$$

where

$$\sigma = \frac{ac}{4}, \tag{3.10}$$

is Stefan's constant.

3.1.2 Bremsstrahlung

Bremsstrahlung (or free-free radiation; e.g. Ryibicki & Lightman 2004, page 155) is the process in which a charged particle (e.g., an electron) is accelerated in the Coulomb field of another charged particle (e.g., a proton or an ion). The accelerated particle emits energy at the expense of its kinetic energy, hence the name *bremsstrahlung* which is German for *braking radiation.*

In astrophysical plasmas, electrons are accelerated in the Coulomb field of protons. The protron is very much heavier than the electron and so undergoes negligible acceleration in the encounter. The electron undergoes a substantial acceleration and so is the primary source of radiation (Rybicki & Lightman 2004, page 155). This process is shown systematically in Figure 3.2.

In astrophysics, the term bremsstrahlung is used in a wide range of phenomena, involving radiation from accelerated electrons. It is used to describe radio emission from compact regions of ionized hydrogen, and X-ray emission from binary systems and intergalactic gas. I have based the following discussion of the spectral properties associated with bremsstrahlung on Longair (2011) and Rybicki & Lightman (2004).

Consider an electron (e^-), with velocity $\vec{v}$, passing a charge consisting of Z protons and total charge Ze^+. The electron is accelerated during its interaction with the charge. In the rest frame of the electron, the acceleration generally has components given by

$$a_\parallel(t) = \frac{\gamma Z e^2 v t}{4\pi\varepsilon_0 m_e [b^2 + (\gamma v t)^2]^{3/2}} \tag{3.11}$$

$$a_\perp(t) = \frac{\gamma Z e^2 b}{4\pi\varepsilon_0 m_e [b^2 + (\gamma v t)^2]^{3/2}}, \tag{3.12}$$

where b is the impact parameter (e.g. Longair 2011, page 163). In the following derivation, I will use a system of units in which $4\pi\varepsilon_0$ has value one. The Fourier transforms of the components

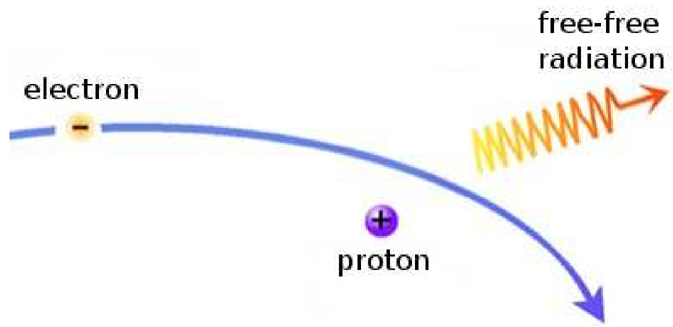

Figure 3.2: Bremsstrahlung, or free-free radiation of an electron accelerated in the electrostatic field of a proton (www.astro.wisc.edu/∼bank/index.html).

are

$$a_{\parallel}(\omega) = \frac{1}{\sqrt{2\pi}}\int_{-\infty}^{+\infty}\frac{\gamma Ze^2 vt}{m_e[b^2+(\gamma vt)^2]^{3/2}}\exp(i\omega t)dt \tag{3.13}$$

$$a_{\perp}(\omega) = \frac{1}{\sqrt{2\pi}}\int_{-\infty}^{+\infty}\frac{\gamma Ze^2 b}{m_e[b^2+(\gamma vt)^2]^{3/2}}\exp(i\omega t)dt. \tag{3.14}$$

Using the substitution $bx = \gamma vt$, one can show that

$$a_{\parallel}(\omega) = \frac{1}{\sqrt{2\pi}}\frac{Ze^2}{m_e}\frac{1}{\gamma bv}I_1(y), \tag{3.15}$$

where

$$I_1(y) = \int_{-\infty}^{+\infty}\frac{x}{(1+x^2)^{3/2}}\exp(iyx)dx,$$

and $y = \omega b/\gamma v$. Using integration by parts, it can be shown that

$$I_1(y) = 2iy\int_0^{+\infty}\frac{1}{(1+x^2)^{1/2}}e^{iyx}dx. \tag{3.16}$$

From Abramovitz & Stegun (1972),

$$I_1(y) = 2iyK_0(y), \tag{3.17}$$

where

$$K_0(y) = \int_0^{+\infty}\frac{1}{(1+x^2)^{1/2}}e^{iyx}dx \tag{3.18}$$

is the modified Bessel function of order zero. Therefore,

$$\begin{aligned} a_{\parallel}(\omega) &= \frac{1}{\sqrt{2\pi}}\frac{Ze^2}{m_e}\frac{1}{\gamma bv}2iyK_0(y) \\ &= \frac{1}{\sqrt{2\pi}}\frac{Ze^2}{m_e}\frac{2i\omega}{\gamma^2 v^2}K_0\left(\frac{\omega b}{\gamma v}\right). \end{aligned} \tag{3.19}$$

In a similar fashion,

$$a_{\perp}(\omega) = \frac{1}{\sqrt{2\pi}} \frac{Ze^2}{m_e} \frac{1}{bv} I_2(y), \tag{3.20}$$

where

$$\begin{aligned} I_2(y) &= \int_{-\infty}^{+\infty} \frac{1}{(1+x^2)^{3/2}} \exp(iyx)dx \\ &= 2yK_1(y), \end{aligned} \tag{3.21}$$

and $K_1(y) =$ - $K_0'(y)$ is the first order modified Bessel function. Then,

$$\begin{aligned} a_{\perp}(\omega) &= \frac{1}{\sqrt{2\pi}} \frac{Ze^2}{m_e} \frac{1}{bv} 2yK_1(y) \\ &= \frac{1}{\sqrt{2\pi}} \frac{Ze^2}{m_e} \frac{2\omega}{\gamma v^2} K_1\left(\frac{\omega b}{\gamma v}\right). \end{aligned} \tag{3.22}$$

It can readily be shown (Longair 2011, page 162) that the spectral intensity of a radiating particle is given by

$$I(\omega) = \frac{4e^2}{3c^3} |\vec{a}(\omega)|^2. \tag{3.23}$$

The acceleration can be decomposed into parallel and perpendicular components, i.e. $\vec{a} = a_{\parallel}\hat{i}_{\parallel}$ + $a_{\perp}\hat{i}_{\perp}$. Using the components of the acceleration derived in equations (3.19) and (3.22), it can be shown that the intensity spectrum from a single collision with impact parameter b is given by

$$I(\omega) = \frac{8Z^2e^6}{3\pi c^3 m_e^2} \frac{\omega^2}{\gamma^2 v^4} \left[\frac{1}{\gamma^2} K_0^2\left(\frac{\omega b}{\gamma v}\right) + K_1^2\left(\frac{\omega b}{\gamma v}\right)\right]. \tag{3.24}$$

It can be seen that the intensity along the particle's path decreases as $\frac{1}{\gamma^2}$. In this case, the radiation spectrum is dominated by the impulse perpendicular to the direction of motion of the electron. The limiting cases are defined by:

$$K_0(y) = -\ln(y) \tag{3.25}$$

$$K_1(y) = \frac{1}{y}, \tag{3.26}$$

for $y \ll 1$, and

$$K_0(y) = K_1(y) = \left(\frac{\pi}{2y}\right)^{1/2} \exp(-y), \tag{3.27}$$

for $y \gg 1$. An exponential cut-off occurs at high frequencies (Figure 3.3),

$$\begin{aligned} I(\omega) &= \frac{8Z^2e^6}{3\pi c^3 m_e^2} \frac{\omega^2}{\gamma^2 v^4} \left[\frac{1}{\gamma^2}\left(\frac{\pi}{2y}\right) \exp(-2y) + \left(\frac{\pi}{2y}\right) \exp(-2y)\right] \\ &= \frac{4Z^2e^6\omega}{3c^3 m_e^2 v^3 \gamma b} \left[\frac{1}{\gamma^2} + 1\right] \exp\left(-\frac{2\omega b}{\gamma v}\right). \end{aligned} \tag{3.28}$$

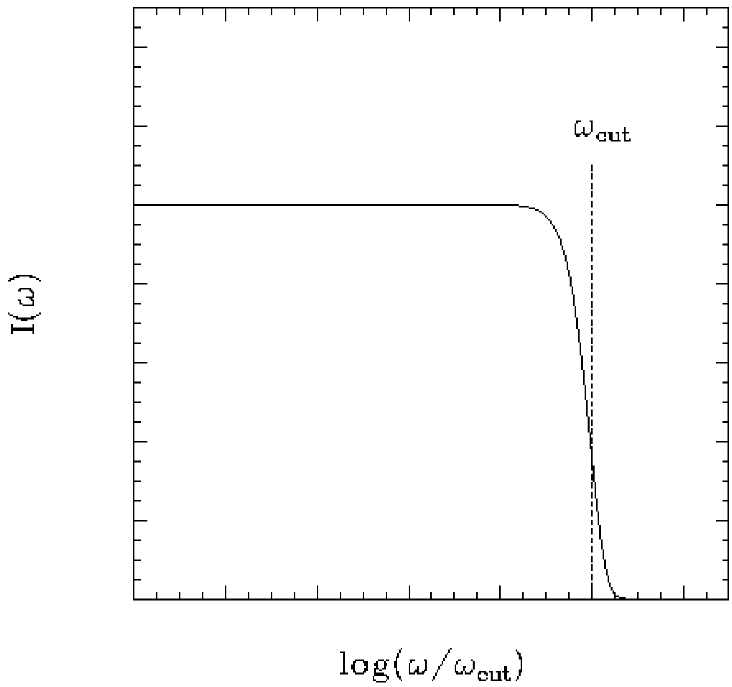

Figure 3.3: Spectrum of bremsstrahlung showing a flat spectrum up to a cut-off frequency $\omega_{\rm cut}$, then falling off exponentially at $\omega > \omega_{\rm cut}$ (www.astro.utu.fi/∼cflynn/astroII/l3.html).

The duration of a relativistic collision, $\tau \sim \frac{2b}{\gamma v}$, and the dominant Fourier component of the radiation spectrum must correspond to

$$\nu \simeq \frac{1}{\tau} = \frac{\gamma v}{2b}, \tag{3.29}$$

or $\omega = \frac{\pi\gamma v}{b}$. To order of magnitude, $\frac{\omega b}{\gamma v} \approx 1$. The exponential cut-off then reveals little power being radiated at $\omega > \frac{\gamma v}{b}$. In the low frequency approximation ($y = \frac{\omega b}{\gamma v} \ll 1$), the intensity is constant (Figure 3.3), i.e.

$$\begin{aligned} I(\omega) &= \frac{8Z^2e^6}{3\pi c^3 m_e^2 b^2 v^2}\left[1+\frac{1}{\gamma^2}\left(\frac{\omega b}{\gamma v}\right)^2\left(-\ln\left[\frac{\omega b}{\gamma v}\right]\right)^2\right] \\ &\approx \frac{8Z^2e^6}{3\pi c^3 m_e^2 b^2 v^2} \\ &= K. \end{aligned} \tag{3.30}$$

If the electron is moving at a relativistic speed, the observed nuclear number density is enhanced by γ, due to length contraction (e.g. Longair 2011, page 166). Then, in the rest frame (K′) of the moving electron, the space density of target nuclei is

$$N^{'} = \gamma N, \tag{3.31}$$

where N is the space nuclear number density in the laboratory frame. The total number of encounters per second is $N'v$. In the frame of the electron, the radiation spectrum becomes

$$\begin{aligned} j(\omega') &= \int_{b'_{\min}}^{b'_{\max}} 2\pi b'\gamma N v K db' \\ &= \frac{16Z^2e^6\gamma N}{3c^3m_e^2 v}\ln\left(\frac{b'_{\max}}{b'_{\min}}\right). \end{aligned} \tag{3.32}$$

It should be mentioned that the validity of the last equation in the limit $y = \frac{\omega b}{\gamma v}$ is based upon the fact that $I(\omega) = K$ (Constant), which is a relativistic invariant. For non-relativistic particles, γ tends to 1, and the dashes on $b_{\min}$ and $b_{\max}$ can be neglected, as well as any further possible relativistic factors. In the non-relativistic regime, the frequency spectrum becomes

$$j(\omega) = \frac{16Z^2e^6N}{3c^3m_{\mathrm{e}}^2 v}\ \ln\Lambda, \tag{3.33}$$

with

$$\Lambda = \frac{b_{\max}}{b_{\min}}. \tag{3.34}$$

By imposing appropriate limits on $b_{\min}$ and $b_{\max}$ (Longair 2011, page 166), it can be shown that

$$\Lambda = \frac{2m_{\mathrm{e}}v^3}{Ze^2\omega} \qquad \text{[low velocities]} \tag{3.35}$$

$$\Lambda = \frac{2m_{\mathrm{e}}v^2}{\hbar\omega} \qquad \text{[high velocities]} \tag{3.36}$$

To find the total energy loss rate of a high energy particle, the spectral intensity relation can be integrated from $\omega = 0$ to $\omega_{\max}$, where $\omega_{\max}$ corresponds to the cut-off frequency, $\hbar\omega \sim \frac{1}{2}m_{\mathrm{e}}v^2$. This results in

$$\begin{aligned} -\left(\frac{dE}{dt}\right)_{\mathrm{br}} &= \int_0^{\omega_{\max}} j(\omega)d\omega \\ &= \int_0^{\omega_{\max}} \frac{16Z^2e^6N}{3c^3m_{\mathrm{e}}^2v}\ \ln\Lambda\ d\omega \\ &= \frac{16Z^2e^6N}{3c^3m_{\mathrm{e}}^2v}\ \ln\Lambda \int_0^{\omega_{\max}} d\omega \\ &= \frac{16Z^2e^6N}{3c^3m_{\mathrm{e}}^2v}\ \ln\Lambda\ \tfrac{1}{2}\frac{m_{\mathrm{e}}v^2}{\hbar} \\ &= \frac{16Z^2e^6Nv}{6c^3m_{\mathrm{e}}\hbar}\ \ln\Lambda \\ &= BZ^2Nv, \end{aligned} \tag{3.37}$$

where Λ depends weakly on ω, and

$$B = \frac{16e^6}{6c^3m_{\mathrm{e}}\hbar}\ \ln\Lambda. \tag{3.38}$$

Since the kinetic energy of a particle $\varepsilon_{\mathrm{k}} = \frac{1}{2}m_{\mathrm{e}}v^2$, one can show that

$$v = \sqrt{2\ \frac{\varepsilon_{\mathrm{k}}}{m_{\mathrm{e}}}}. \tag{3.39}$$

Hence, the energy loss rate,

$$-\left(\frac{dE}{dt}\right)_{\mathrm{br}} \propto \varepsilon_{\mathrm{k}}^{\frac{1}{2}}. \tag{3.40}$$

The preceding analysis was based upon the assumption of constant target density. For thermal plasmas, this is not the case, where the number density follows a thermal Maxwellian distribution, given by

$$N_e(v)dv = 4\pi N_e \left(\frac{m_e}{2\pi kT}\right)^{3/2} v^2 \exp\left(-\frac{m_e v^2}{2kT}\right) dv. \tag{3.41}$$

The radiation spectrum (e.g. Eq. 3.33),

$$j(\omega) = \frac{16Z^2e^6N}{3c^3m_e^2v}\ln\Lambda, \tag{3.42}$$

is integrated over this distribution, i.e.,

$$J(\omega) = \frac{16Z^2e^6N}{3c^3m_e^2}\int_0^\infty \ln\Lambda\frac{1}{v}N_e(v)dv. \tag{3.43}$$

In the low frequency approximation, $\Lambda = \frac{2m_e v^3}{Ze^2\omega}$, and for $v = \left(\frac{3kT}{m_e}\right)^{1/2}$,

$$\Lambda = \frac{2m_e}{Ze^2\omega}\left(\frac{3kT}{m_e}\right)^{3/2}. \tag{3.44}$$

The intensity spectrum becomes

$$\begin{aligned}
J(\omega) &= \frac{16Z^2e^6NN_e}{3c^3m_e^2}4\pi\left(\frac{m_e}{2\pi kT}\right)^{3/2}\ln\left[\frac{2m_e}{Ze^2\omega}\left(\frac{3kT}{m_e}\right)^{3/2}\right]\int_0^\infty ve^{-\frac{m_e v^2}{2kT}}dv \\
&= \frac{16Z^2e^6NN_e}{3c^3m_e^2}\left(\frac{2}{\pi}\right)^{1/2}\left(\frac{m_e}{kT}\right)^{1/2}\ln\left[\frac{2m_e}{Ze^2\omega}\left(\frac{3kT}{m_e}\right)^{3/2}\right] \\
&= \frac{16Z^2e^6NN_e}{3\sqrt{3}c^3m_e^2}\left(\frac{m_e}{kT}\right)^{1/2}g(\omega,T),
\end{aligned} \tag{3.45}$$

where $\int_0^\infty ve^{-\frac{m_e v^2}{2kT}}dv = \frac{kT}{m_e}$, and $g(\omega, T)$ is a velocity averaged Gaunt factor (e.g. Rybicki & Lightman 2004).

At high frequencies, there is an exponential cut-off in the spectrum, i.e. $e^{-\hbar\omega/kT}$, which is due to the electrons in the high energy tail of the Maxwellian distribution ($\hbar\omega >$ kT). The total energy loss rate in this case is

$$-\left(\frac{dE}{dt}\right) = \int_0^{\frac{kT}{\hbar}} \frac{16Z^2e^6NN_e}{3\sqrt{3}c^3m_e^2}\left(\frac{m_e}{kT}\right)^{1/2} g(\omega,T)d\omega. \tag{3.46}$$

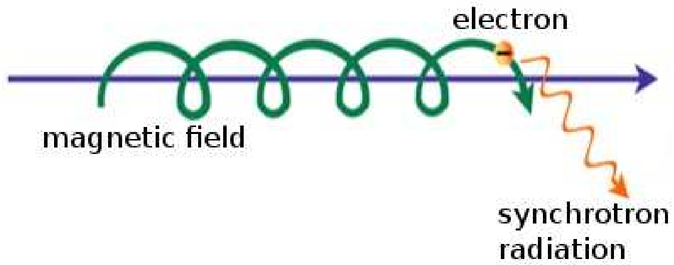

Figure 3.4: Synchrotron radiation of an electron accelerated in a magnetic field. The magnetic field line shown points in the z-direction (www.astro.wisc.edu/∼bank/index.html).

From detailed calculations (e.g. Longair 2011, page 168), the spectral emissivity of the plasma is given by

$$\kappa_\nu = \frac{64\pi}{3}\left(\frac{\pi}{6}\right)^{1/2}\frac{Z^2e^6}{c^3m_e^2}\left(\frac{m_e}{kT}\right)^{1/2} g(\nu,T)NN_e e^{-\frac{h\nu}{kT}}, \tag{3.47}$$

where N_e is the number density of the electrons, and N is the number density of the nuclei. The Gaunt factor has only a logarithmic dependence on frequency, and in X-ray wavelengths,

$$g(\nu,T) = \frac{\sqrt{3}}{\pi}\ln\left(\frac{kT}{h\nu}\right). \tag{3.48}$$

3.2 Non-thermal Synchrotron Radiation

The recent Suzaku results above $\epsilon_\mathrm{X} \geqslant 10$ keV (Terada et al. 2008) revealed non-thermal power-law spectral properties in the X-ray emission resembling that of rotation-powered X-ray pulsars, where the emission is dominated by the synchrotron process. This process is the direct result of the emission from relativistic particles in magnetic fields (Figure 3.4). The relevance of this process for AE Aqr therefore justifies a detailed discussion. The discussion follows presentations by Rybicki & Lightman (1979, 2004) and Longair (1994, 2011).

The equation of motion describing the motion of a relativistic particle in a magnetic field is

$$\frac{d}{dt}(\gamma m\vec{v}) = q\left(\frac{\vec{v}\times\vec{B}}{c}\right), \tag{3.49}$$

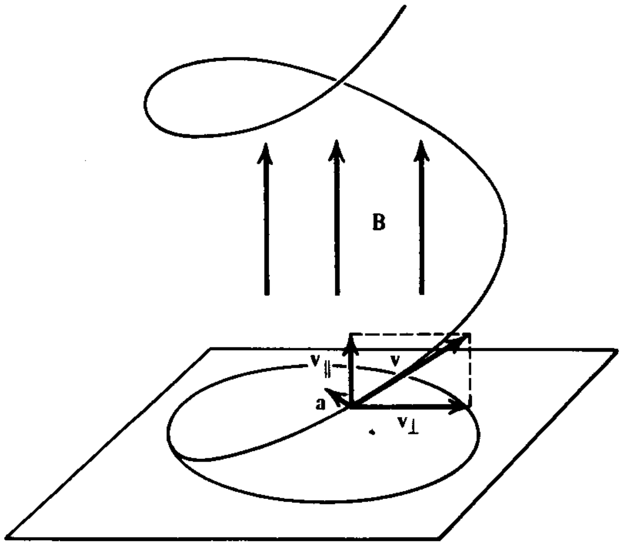

Figure 3.5: Helical motion of a charged particle in a magnetic field (Taken from Rybicki & Lightman 1979, page 169).

where $\gamma = \left(1 - \frac{v^2}{c^2}\right)^{-\frac{1}{2}}$ is the Lorentz factor. Equation (3.49) simplifies to

$$m\gamma\frac{d\vec{v}}{dt} + m\gamma^3\vec{v}\left(\frac{\vec{v}\cdot\vec{a}}{c^2}\right) = q\left(\frac{\vec{v}\times\vec{B}}{c}\right). \tag{3.50}$$

For motion in a magnetic field, $\vec{v}\cdot\vec{a} = 0$ since the vectors are perpendicular to each other (e.g. Longair 1994, page 331). Therefore,

$$m\gamma\frac{d\vec{v}}{dt} = q\left(\frac{\vec{v}\times\vec{B}}{c}\right). \tag{3.51}$$

If the pitch angle (angle between the velocity and the magnetic field) is θ, then

$$\begin{aligned} \gamma m\frac{d\vec{v}}{dt} &= \frac{qvB\sin\theta}{c}\hat{n} \\ \vec{a} &= \frac{qvB\sin\theta}{c\gamma m}\hat{n}, \end{aligned} \tag{3.52}$$

where $\hat{n}$ is a unit vector in the direction of $\vec{a}$. The motion of the particle is illustrated in Figure 3.5. For a typical gyromotion, $a_{\|} = 0$, hence

$$a_{\perp} = \frac{qvB\sin\theta}{c\gamma m}. \tag{3.53}$$

Using the radiation loss rate formula for a relativistic particle (e.g. Rybicki & Lightman 2004, page 140):

$$\begin{aligned} P &= \frac{2q^2\gamma^4}{3c^3}\left[{a_\perp}^2 + \gamma^2 {a_\parallel}^2\right] \\ &= \frac{2q^2\gamma^4}{3c^3}{a_\perp}^2 \\ &= \frac{2q^4\gamma^2 v^2 B^2 \sin^2\theta}{3c^5 m^2} \\ &= 2\left(\frac{8\pi q^4}{3m^2c^4}\right)\frac{v^2}{c^2}\frac{B^2}{8\pi}c\gamma^2 \sin^2\theta. \end{aligned} \tag{3.54}$$

For an electron,

$$P = 2\gamma^2\beta^2\sigma_T c U_B \sin^2\theta, \tag{3.55}$$

where, $\beta = v/c$, $U_B = \frac{B^2}{8\pi}$ is the magnetic energy density, and $\sigma_T = \frac{8\pi e^4}{3m^2c^4} \sim 6.65 \times 10^{-25}$ cm^2 is the Thomson cross-section. Averaging over the entire solid angle ($d\Omega$), and assuming an isotropic distribution of pitch angles, for which $< \sin^2\theta > = \frac{\int \sin^2\theta d\Omega}{\int d\Omega} = \frac{2}{3}$, it can be shown that the total power radiated is

$$P = \frac{4}{3}\sigma_T c\beta^2\gamma^2 U_B. \tag{3.56}$$

Synchrotron radiation fields appear to be concentrated in a narrow set of directions about the particle's velocity. This is due to "relativistic beaming", which applies for $\gamma \gg 1$. The observer usually sees the emission confined within a small cone of half-opening angle $\sim 1/\gamma$ (Rybicki & Lightman 2004, page 169; Vietri 2008, page 136). The illustration is shown in Figure 3.6. The distance along the path (Δs) is given by,

$$\Delta s = a\Delta\theta = \frac{2a}{\gamma}, \tag{3.57}$$

where a is the radius of curvature. From the equation of motion of the particle, i.e.

$$\gamma m \frac{\Delta\vec{v}}{\Delta t} = \frac{q}{c}\vec{v} \times \vec{B}, \tag{3.58}$$

with $|\Delta\vec{v}| \approx v\Delta\theta$, and $\Delta t = \Delta s/v$, it can be shown that

$$\frac{\Delta\theta}{\Delta s} = \frac{qB \sin\alpha}{\gamma mcv}, \tag{3.59}$$

where

$$a = \frac{v}{\omega_B \sin\alpha}. \tag{3.60}$$

Equation (3.57) then simplifies to

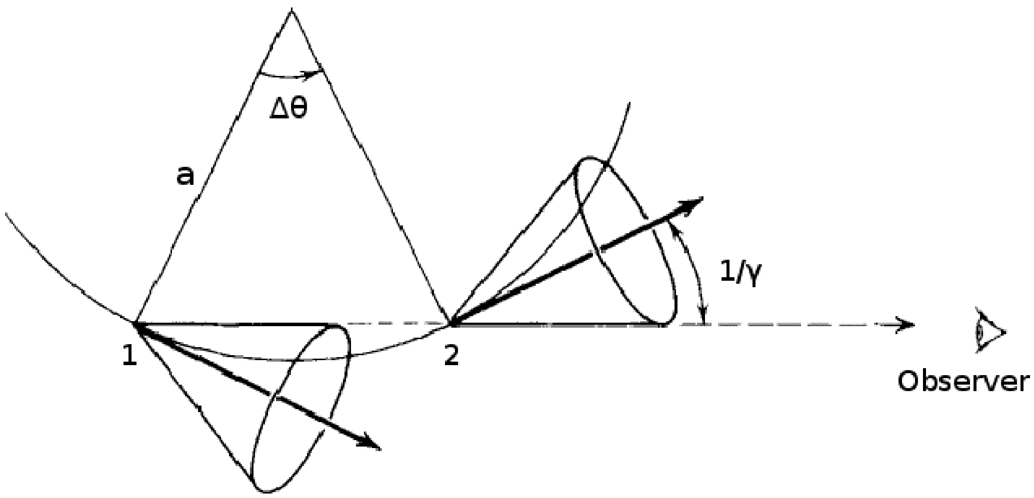

Figure 3.6: Synchrotron radiation cones, observed at various points as a particle traverses a helical path around a magnetic field (Adapted from Rybicki & Lightman 2004, page 170).

$$\Delta s = \frac{2v}{\gamma \omega_B \sin \alpha}. \tag{3.61}$$

The time interval between the points 1 and 2, for the passage of the particle, is given by

$$\begin{aligned} t_2 - t_1 &= \frac{\Delta s}{v} \\ \Delta t &= \frac{2}{\gamma \omega_B \sin \alpha}. \end{aligned} \tag{3.62}$$

However, the arrival times of the radiation, at the observer (t_1^A and t_2^A), differ by

$$\Delta t^A = \frac{2}{\gamma \omega_B \sin \alpha} \left(1 - \frac{v}{c}\right), \tag{3.63}$$

where (1 - v/c) is the Doppler factor, which can be shown (for relativistic speeds) to be $\approx (2\gamma^2)^{-1}$ (e.g. Rybicki & Lightman 2004, page 171; Longair 2011, page 201). Therefore,

$$\Delta t^A = \frac{1}{\gamma^3 \omega_B \sin \alpha}. \tag{3.64}$$

To derive the formulae related to the radiation spectrum of an arbitrary moving electron, we use the Liénard-Wiechert potentials:

$$\begin{aligned} \vec{A}(\vec{r}, t) &= \frac{1}{c^2 r} \left(\frac{q\vec{v}}{1 - \frac{\vec{v} \cdot \hat{n}}{c}} \right)_{\text{ret}} \\ \phi(\vec{r}, t) &= \frac{1}{r} \left(\frac{q}{1 - \frac{\vec{v} \cdot \hat{n}}{c}} \right)_{\text{ret}}, \end{aligned} \tag{3.65}$$

where $\hat{n} = \frac{\vec{R}}{|\vec{R}|}$ is the unit vector from the particle to the point of observation (e.g. Longair 1994, page 240; Longair 2011, page 202), and the subscript *ret* denotes evaluation at retarded times (t'). From the radiation formula (e.g. Longair 2011, page 162):

$$I(\omega) = \frac{4e^2}{3c^3}|\vec{a}(\omega)|^2, \tag{3.66}$$

where, under a Fourier transform,

$$\vec{a}(\omega) = \frac{1}{\sqrt{2\pi}}\int_{-\infty}^{+\infty}\vec{a}(t)e^{i\omega t}dt. \tag{3.67}$$

Then, when there is no net motion of the particle,

$$I(\omega) = \frac{2e^2}{3\pi c^3}\left|\int_{-\infty}^{+\infty}\vec{a}(t)e^{i\omega t}dt\right|^2. \tag{3.68}$$

However, for a moving particle,

$$\frac{dI(\omega)}{d\Omega} = \frac{e^2}{4\pi^2 c}\left|\int_{-\infty}^{+\infty}\left\{\hat{n}\times\left[\left(\hat{n}-\frac{\vec{v}}{c}\right)\times\frac{\dot{\vec{v}}}{c}\right]\kappa^{-3}\right\}_{\text{ret}} e^{i\omega t}dt\right|^2, \tag{3.69}$$

where $\kappa = 1 - \frac{\vec{v}\cdot\hat{n}}{c}$ (e.g. Longair 1994, page 240; Longair 2011, page 202). If $t' = t$ - $\frac{R(t')}{c}$ (where $R(t') = |\vec{r}|$ - $\vec{n}\cdot\vec{r_0}(t')$, and $\vec{r_0}(t')$ describes the position of the particle relative to an origin at $\vec{r}$), then it can be shown (e.g. Longair 2011, page 203) that $dt = \kappa dt'$. Assume that $\vec{r} > \vec{r_0}(t')$, then

$$\frac{dI(\omega)}{d\Omega} = \frac{e^2}{4\pi^2 c}\left|\int_{-\infty}^{+\infty}\hat{n}\times\left[\left(\hat{n}-\frac{\vec{v}(t')}{c}\right)\times\frac{\dot{\vec{v}}(t')}{c}\right]\kappa^{-2}\text{exp}\left[i\omega\left(t'-\frac{\hat{n}\cdot\vec{r_0}(t')}{c}\right)\right]dt'\right|^2. \tag{3.70}$$

Note that the identities,

$$\hat{n}\times\left[\left(\hat{n}-\frac{\vec{v}(t')}{c}\right)\times\frac{\dot{\vec{v}}(t')}{c}\right]\kappa^{-2} = \frac{d}{dt'}\left\{k^{-1}\left[\hat{n}\times\left(\hat{n}\times\frac{\vec{v}}{c}\right)\right]\right\}, \tag{3.71}$$

and $\vec{a}\times(\vec{b}\times\vec{c}) = (\vec{a}.\vec{c})\vec{b}$ - $(\vec{a}.\vec{b})\vec{c}$, will lead to

$$\frac{dI(\omega)}{d\Omega} = \frac{e^2}{4\pi^2 c}\left|\int_{-\infty}^{+\infty}\frac{d}{dt'}\left\{k^{-1}\left[\hat{n}\times(\hat{n}\times\vec{v}/c)\right]\right\}\exp\left[i\omega\left(t'-\frac{\hat{n}\cdot\vec{r_0}(t')}{c}\right)\right]dt'\right|^2. \tag{3.72}$$

Then, integrating by parts, it can be shown that

$$\frac{dI(\omega)}{d\Omega} = \frac{e^2\omega^2}{4\pi^2 c}\left|\int_{-\infty}^{+\infty}i\omega\left[\hat{n}\times(\hat{n}\times\vec{v}/c)\right]\exp\left[i\omega\left(t'-\frac{\hat{n}\cdot\vec{r_0}(t')}{c}\right)\right]dt'\right|^2. \tag{3.73}$$

In a co-ordinate system described by the unit vectors $\vec{\epsilon}_{\parallel}$ and $\vec{\epsilon}_{\perp}$, where $\vec{\epsilon}_{\parallel}$ lies in the plane containing $\hat{n}$ and the direction of $\vec{B}$, with $\vec{\epsilon}_{\perp}$ along the y-axis,

$$\hat{\epsilon}_{\parallel} = \hat{n}\times\hat{\epsilon}_{\perp}. \tag{3.74}$$

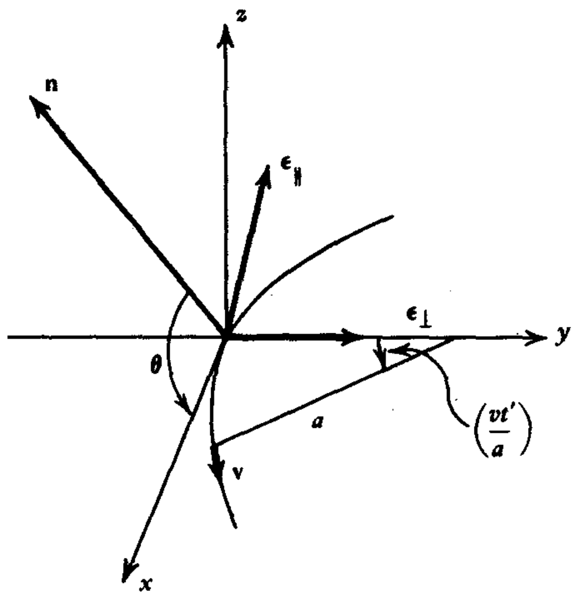

Figure 3.7: Geometry for evaluating the intensity and polarisation properties of synchrotron radiation (Taken from Rybicki & Lightman 2004, page 175).

The components $\hat{\epsilon}_{\parallel}$ and $\hat{\epsilon}_{\perp}$ are parallel and perpendicular to $\vec{B}$ respectively, illustrated in Figure 3.7. Now, write down the co-ordinates of the electron in ($\hat{n}$, $\hat{\epsilon}_{\parallel}$, $\hat{\epsilon}_{\perp}$) and take $t' = 0$ at $x = y = z = 0$.

Geometrically,

$$\begin{aligned} \vec{v} &= |\vec{v}| \left[\cos\left(\frac{vt'}{a}\right) \hat{i}_x + \sin\left(\frac{vt'}{a}\right) \hat{\epsilon}_{\perp} \right] \\ &= |\vec{v}| \left[\cos\theta \cos\left(\frac{vt'}{a}\right) \hat{n} - \sin\theta \cos\left(\frac{vt'}{a}\right) \hat{\epsilon}_{\parallel} + sin\left(\frac{vt'}{a}\right) \hat{\epsilon}_{\perp} \right], \end{aligned} \tag{3.75}$$

where θ is the angle between $\hat{n}$ and the $x - y$ plane. Thus, it can be shown that,

$$\hat{n} \times (\hat{n} \times \vec{v}) = |\vec{v}| \left[\sin\theta \cos\left(\frac{vt'}{a}\right) \hat{\epsilon}_{\parallel} - \sin\left(\frac{vt'}{a}\right) \hat{\epsilon}_{\perp} \right], \tag{3.76}$$

where the following cross product rules hold:

$$\begin{aligned} \hat{n} \times \hat{\epsilon}_{\parallel} &= \hat{\epsilon}_{\perp} \\ \hat{\epsilon}_{\parallel} \times \hat{\epsilon}_{\perp} &= \hat{n} \\ \hat{\epsilon}_{\perp} \times \hat{n} &= \hat{\epsilon}_{\parallel} \\ \hat{n} \times \hat{n} &= 0. \end{aligned}$$

Also from Figure 3.7,

$$\vec{r}_0(t') = 2a\,\sin\left(\frac{vt'}{2a}\right)\left[\cos\theta\,\cos\left(\frac{vt'}{2a}\right)\hat{n} - \sin\theta\,\cos\left(\frac{vt'}{2a}\right)\hat{\epsilon}_{\parallel} + \sin\left(\frac{vt'}{2a}\right)\hat{\epsilon}_{\perp}\right], \tag{3.77}$$

implying that

$$\hat{n}\cdot\vec{r}_0(t') = 2a\,\cos\theta\,\sin\left(\frac{vt'}{2a}\right)\cos\left(\frac{vt'}{2a}\right) = a\,\cos\theta\,\sin\left(\frac{vt'}{a}\right) \tag{3.78}$$

$$t' - \frac{\hat{n}\cdot\vec{r}_0(t')}{c} = t' - \frac{a}{c}\cos\theta\,\sin\left(\frac{vt'}{a}\right). \tag{3.79}$$

The radiation is strongly beamed in the direction of motion. Then, considering small pitch angles such that

$$\begin{aligned}
\sin\theta &= \theta - \frac{\theta^3}{3!} + \frac{\theta^5}{5!} + \ldots \\
\cos\theta &= 1 - \frac{\theta^2}{2!} + \frac{\theta^4}{4!} + \ldots,
\end{aligned} \tag{3.80}$$

and ignoring higher orders,

$$\begin{aligned}
t' - \frac{\hat{n}\cdot\vec{r}_0(t')}{c} &= t' - \frac{a}{c}\left(1 - \frac{\theta^2}{2}\right)\left(\frac{vt'}{a} - \frac{v^3t'^3}{6a^3}\right) \\
&= t' - \frac{vt'}{c} + \frac{v^3t'^3}{6ca^2} + \frac{v\theta^2t'}{2c} - \frac{v^3t'^3}{12ca^2} \\
&= t'\left(1 - \frac{v}{c}\right) + \frac{v}{c}\frac{\theta^2}{2}t' + \frac{v^3}{6ca^2}t'^3.
\end{aligned} \tag{3.81}$$

Recall that for $v \sim c$, 1 -$\frac{v}{c} = \frac{1}{2\gamma^2}$. Then, it can be shown that

$$t' - \frac{\hat{n}\cdot\vec{r}_0(t')}{c} = \frac{1}{2\gamma^2}\left[t'\left(1+\gamma^2\theta^2\right) + \frac{c^2\gamma^2t'^3}{3a^2}\right]. \tag{3.82}$$

Also,

$$\begin{aligned}
\hat{n}\times\left(\hat{n}\times\frac{\vec{v}}{c}\right) &= \frac{|\vec{v}|}{c}\left[\left\{\left(\theta - \frac{\theta^3}{6}\right)\left(1 - \frac{v^2t'^2}{2}\right)\right\}\hat{\epsilon}_{\parallel} - \left(\frac{vt'}{a} - \frac{v^3t'^3}{6a^3}\right)\hat{\epsilon}_{\perp}\right] \\
\hat{n}\times\left(\hat{n}\times\frac{\vec{v}}{c}\right) &\simeq \left(\theta\hat{\epsilon}_{\parallel} - \frac{vt'}{a}\hat{\epsilon}_{\perp}\right).
\end{aligned} \tag{3.83}$$

Then, equations (3.82) and (3.83) into equation (3.73), with the components separated, give

$$\frac{dI_{\parallel}(\omega)}{d\Omega} = \frac{e^2\omega^2\theta^2}{4\pi^2c}\left|\int_{-\infty}^{+\infty}\exp\left\{\frac{i\omega}{2\gamma^2}\left[t'\left(1+\gamma^2\theta^2\right) + \frac{c^2\gamma^2t'^3}{3a^2}\right]\right\}dt'\right|^2, \tag{3.84}$$

$$\frac{dI_{\perp}(\omega)}{d\Omega} = \frac{e^2\omega^2}{4\pi^2c}\left|\int_{-\infty}^{+\infty}\frac{ct'}{a}\exp\left\{\frac{i\omega}{2\gamma^2}\left[t'\left(1+\gamma^2\theta^2\right) + \frac{c^2\gamma^2t'^3}{3a^2}\right]\right\}dt'\right|^2. \tag{3.85}$$

Now, the following substitutions are used:

$$
\begin{aligned}
\theta_\gamma^2 &= 1+\gamma^2\theta^2 \\
y &= \frac{\gamma c}{a\theta_\gamma}t' \\
dt' &= \frac{a\theta_\gamma}{\gamma c}dy \\
\eta &= \frac{\omega a\theta_\gamma^3}{3c\gamma^3} \\
\omega &= \frac{3c\gamma^3}{a\theta_\gamma^3}\eta
\end{aligned}
$$

Eventually,

$$
\begin{aligned}
\frac{dI_\parallel(\omega)}{d\Omega} &= \frac{e^2\omega^2\theta^2}{4\pi^2 c}\left|\int_{-\infty}^{+\infty}\exp\left\{\frac{i3c\gamma^3\eta}{2\gamma^2 a\theta_\gamma^3}\left[\frac{a\theta_\gamma y}{\gamma c}\theta_\gamma^2+\frac{c^2\gamma^2}{3a^3}\frac{a^3\theta_\gamma^3 y^3}{\gamma^3 c^3}\right]\right\}\frac{a\theta_\gamma}{\gamma c}dy\right|^2 \\
&= \frac{e^2\omega^2\theta^2}{4\pi^2 c}\left(\frac{a\theta_\gamma}{\gamma c}\right)^2\left|\int_{-\infty}^{+\infty}\exp\left[\frac{i3\eta}{2}\left(y+\frac{y^3}{3}\right)\right]dy\right|^2. \qquad (3.86)
\end{aligned}
$$

Similarly,

$$
\begin{aligned}
\frac{dI_\perp(\omega)}{d\Omega} &= \frac{e^2\omega^2}{4\pi^2 c}\left(\frac{a\theta_\gamma}{\gamma c}\right)^2\left|\int_{-\infty}^{+\infty}\frac{c}{a}\frac{a\theta_\gamma}{\gamma c}y\,\exp\left[\frac{i3\eta}{2}\left(y+\frac{y^3}{3}\right)\right]dy\right|^2 \\
&= \frac{e^2\omega^2}{4\pi^2 c}\left(\frac{a\theta_\gamma^2}{\gamma^2 c}\right)^2\left|\int_{-\infty}^{+\infty}y\,\exp\left[\frac{i3\eta}{2}\left(y+\frac{y^3}{3}\right)\right]dy\right|^2. \qquad (3.87)
\end{aligned}
$$

The exponential part can be expanded in a similar way as

$$e^{ix} = \cos \mathrm{x} + i\,\sin \mathrm{x}. \qquad (3.88)$$

So,

$$\exp\left[\frac{i3\eta}{2}\left(y+\frac{y^3}{3}\right)\right] = \cos\left[\frac{3\eta}{2}\left(y+\frac{y^3}{3}\right)\right]+i\,\sin\left[\frac{3\eta}{2}\left(y+\frac{y^3}{3}\right)\right]. \qquad (3.89)$$

Since most of the radiation is beamed in the direction of motion of the radiating particle, the real part is taken for the parallel component, and the imaginary part for the perpendicular component respectively. Then,

$$
\begin{aligned}
\frac{dI_\parallel(\omega)}{d\Omega} &= \frac{e^2\omega^2\theta^2}{4\pi^2 c}\left(\frac{a\theta_\gamma}{\gamma c}\right)^2\left|\int_{-\infty}^{+\infty}\cos\left[\frac{3\eta}{2}\left(y+\frac{y^3}{3}\right)\right]dy\right|^2 \\
&= \frac{e^2\omega^2\theta^2}{\pi^2 c}\left(\frac{a\theta_\gamma}{\gamma c}\right)^2\left|\int_{0}^{+\infty}\cos\left[\frac{3\eta}{2}\left(y+\frac{y^3}{3}\right)\right]dy\right|^2, \qquad (3.90) \\
\frac{dI_\perp(\omega)}{d\Omega} &= \frac{e^2\omega^2}{4\pi^2 c}\left(\frac{a\theta_\gamma^2}{\gamma^2 c}\right)^2\left|\int_{-\infty}^{+\infty}y\,\sin\left[\frac{3\eta}{2}\left(y+\frac{y^3}{3}\right)\right]dy\right|^2 \\
&= \frac{e^2\omega^2}{\pi^2 c}\left(\frac{a\theta_\gamma^2}{\gamma^2 c}\right)^2\left|\int_{0}^{+\infty}y\,\sin\left[\frac{3\eta}{2}\left(y+\frac{y^3}{3}\right)\right]dy\right|^2. \qquad (3.91)
\end{aligned}
$$

Then, the following relations, presented by Abramovitz and Stegun (1965), are used to express the integrals (e.g Longair 2011, page 206):

$$\int_0^{+\infty} \cos\left[\frac{3\eta}{2}\left(y+\frac{y^3}{3}\right)\right] dy = \frac{1}{\sqrt{3}} K_{1/3}(\eta) \tag{3.92}$$

$$\int_0^{+\infty} y \sin\left[\frac{3\eta}{2}\left(y+\frac{y^3}{3}\right)\right] dy = \frac{1}{\sqrt{3}} K_{2/3}(\eta), \tag{3.93}$$

where $K_{1/3}$ and $K_{2/3}$ are the modified Bessel functions of orders 1/3 and 2/3 respectively. It follows that

$$\frac{dI_{\parallel}(\omega)}{d\Omega} = \frac{e^2\omega^2\theta^2}{3\pi^2 c}\left(\frac{a\theta_\gamma}{\gamma c}\right)^2 K^2{}_{1/3}(\eta), \tag{3.94}$$

$$\frac{dI_{\perp}(\omega)}{d\Omega} = \frac{e^2\omega^2}{3\pi^2 c}\left(\frac{a\theta_\gamma^2}{\gamma^2 c}\right)^2 K^2{}_{2/3}(\eta). \tag{3.95}$$

Most of the radiation is emitted within a very small angle with respect to the pitch angle of the electron. Thus, it can be assumed that, for one period of gyration of the electron about the magnetic field direction, the angle over which the integral is to be taken is $2\pi \sin\alpha \, d\theta$ (see Longair 2011, page 206 for detailed discussion). Then,

$$I_{\parallel}(\omega) = \frac{2e^2\omega^2 a^2 \sin\alpha}{3\pi c^3\gamma^2}\int_{-\infty}^{+\infty} \theta_\gamma^2\theta^2 K^2{}_{1/3}(\eta) d\theta \tag{3.96}$$

$$I_{\perp}(\omega) = \frac{2e^2\omega^2 a^2 \sin\alpha}{3\pi c^3\gamma^4}\int_{-\infty}^{+\infty} \theta_\gamma^4 K^2{}_{2/3}(\eta) d\theta. \tag{3.97}$$

Then, the following standard solutions by Westfold (1959) and by Le Roux (1961) are considered (e.g. Longair 2011, pages 206-207):

$$\int_{-\infty}^{+\infty} \theta_\gamma^2\theta^2\gamma^2 K^2{}_{1/3}\left(\frac{x}{2}\theta_\gamma^3\right) d\theta = \frac{\pi}{\sqrt{3}\gamma x}\left[\int_x^\infty K_{5/3}(z)dz - K_{2/3}(x)\right] \tag{3.98}$$

$$\int_{-\infty}^{+\infty} \theta_\gamma^4 K^2{}_{2/3}\left(\frac{x}{2}\theta_\gamma^3\right) d\theta = \frac{\pi}{\sqrt{3}\gamma x}\left[\int_x^\infty K_{5/3}(z)dz + K_{2/3}(x)\right]. \tag{3.99}$$

By comparison, $\eta = \frac{x}{2}\theta_\gamma^3$. But $\eta = \frac{\omega a\theta_\gamma^3}{3c\gamma^3}$, so $x = \frac{2\omega a}{3c\gamma^3}$. One can write

$$F(x) = x\int_x^{+\infty} K_{5/3}(z)dz, \tag{3.100}$$

$$G(x) = xK_{2/3}(x). \tag{3.101}$$

Then,

$$\begin{aligned} I_{\parallel}(\omega) &= \frac{2e^2\omega^2 a^2 \sin\alpha}{3\pi c^3\gamma^4}\frac{\pi}{\sqrt{3}\gamma x^2}\left[x\int_x^\infty K_{5/3}(z)dz - xK_{2/3}(x)\right] \\ &= \frac{2e^2\omega^2 a^2 \sin\alpha}{3\pi c^3\gamma^4}\frac{\pi}{\sqrt{3}\gamma}\frac{9c^2\gamma^6}{4\omega^2 a^2}\left[F(x) - G(x)\right] \\ &= \frac{\sqrt{3}e^2\gamma \sin\alpha}{2c}\left[F(x) - G(x)\right]. \end{aligned} \tag{3.102}$$

Similarly,

$$I_{\perp}(\omega) = \frac{\sqrt{3}e^2\gamma \sin\,\alpha}{2c}\left[F(x) + G(x)\right]. \tag{3.103}$$

Equations (3.102) and (3.103) are expressions defining the energy emitted in the two polarizations in one period of the electron's orbit. Define $\omega_c = 3c\gamma^3/2a$ such that $x = \frac{\omega}{\omega_c}$. With reference to the guiding centre of the particle's trajectory, the radius of curvature, $a = \frac{v}{\omega_r\,\sin\,\alpha}$. Thus,

$$\omega_c = \frac{3c\gamma^3}{2v/\omega_r\,\sin\,\alpha} = \frac{3}{2}\gamma^3\omega_r\,\sin\,\alpha, \tag{3.104}$$

where $\omega_r = \frac{eB}{\gamma m_e}$, and $v \sim c$.

$$\nu_c = \frac{\omega_c}{2\pi} = \frac{3}{2}\gamma^2\left(\gamma\frac{\omega_r}{2\pi}\right)\,\sin\,\alpha. \tag{3.105}$$

The non-relativistic gyrofrequency, $\nu_g = \gamma\nu_r = \frac{eB}{2\pi m_e}$. The orbital period of the electron is $T_r = \frac{1}{\nu_r} = \frac{2\pi\gamma m_e}{eB}$. Emissivity in each polarization is,

$$j_{\parallel}(\omega) = \frac{I_{\parallel}(\omega)}{T_r} = \frac{\sqrt{3}e^3B\,\sin\,\alpha}{4\pi c m_e}\left[F(x) - G(x)\right], \tag{3.106}$$

$$j_{\perp}(\omega) = \frac{I_{\perp}(\omega)}{T_r} = \frac{\sqrt{3}e^3B\,\sin\,\alpha}{4\pi c m_e}\left[F(x) + G(x)\right]. \tag{3.107}$$

For a single electron, the total emissivity, also called the spectral energy density is,

$$\begin{aligned} j(\omega) &= j_{\parallel}(\omega) + j_{\perp}(\omega) \\ &= \frac{\sqrt{3}e^3B\,\sin\,\alpha}{2\pi c m_e}F(x). \end{aligned} \tag{3.108}$$

The total energy loss rate is,

$$\begin{aligned} -\frac{dE}{dt} &= \int_0^\infty j(\omega)d\omega \\ &= \frac{\sqrt{3}e^3B\,\sin\,\alpha}{2\pi c m_e}\int_0^\infty F(x)d\omega. \end{aligned} \tag{3.109}$$

For $x = \frac{\omega}{\omega_c}$, $d\omega = \omega_c dx$. Then,

$$-\frac{dE}{dt} = \frac{\sqrt{3}e^3B\omega_c\,\sin\,\alpha}{2\pi c m_e}\int_0^\infty F(x)dx. \tag{3.110}$$

From,

$$\nu_c = \frac{3}{2}\gamma^2\nu_g\,\sin\,\alpha \tag{3.111}$$

$$\omega_c = 2\pi\nu_c = \frac{3}{2}\gamma^2\omega_g\,\sin\,\alpha = \frac{3}{2}\gamma^2\frac{eB}{m_e}\,\sin\,\alpha. \tag{3.112}$$

Then, it can be shown that

$$-\frac{dE}{dt} = \frac{9\sqrt{3}}{4\pi}\sigma_T c U_B \gamma^2 \sin^2 \alpha \int_0^\infty F(x)dx. \tag{3.113}$$

Then, the standard integrals (e.g. Rybicki and Lightman 2004, page 180):

$$\int_0^\infty x^\mu F(x)dx = \frac{2^{\mu+2}}{\mu+1}\Gamma\left(\frac{\mu}{2}+\frac{7}{3}\right)\Gamma\left(\frac{\mu}{2}+\frac{2}{3}\right) \tag{3.114}$$

$$\int_0^\infty x^\mu G(x)dx = 2^\mu\Gamma\left(\frac{\mu}{2}+\frac{4}{3}\right)\Gamma\left(\frac{\mu}{2}+\frac{2}{3}\right), \tag{3.115}$$

are used, where $\Gamma(\zeta)$ is the gamma function of argument ζ. Comparing, $\mu = 0$. Then,

$$\int_0^\infty F(x)dx = \Gamma\left(\frac{7}{3}\right)\Gamma\left(\frac{2}{3}\right). \tag{3.116}$$

So,

$$\begin{aligned} -\frac{dE}{dt} &= \sigma_T c U_B \gamma^2 \sin^2 \alpha \frac{9\sqrt{3}}{4\pi}\Gamma\left(\frac{7}{3}\right)\Gamma\left(\frac{2}{3}\right) \\ &= 2\sigma_T c U_B \gamma^2 \sin^2\alpha, \end{aligned} \tag{3.117}$$

where (e.g. Longair 2011, page 209)

$$\frac{9\sqrt{3}}{4\pi}\Gamma\left(\frac{7}{3}\right)\Gamma\left(\frac{2}{3}\right) = 2. \tag{3.118}$$

3.2.1 The Spectrum for a Power-law Energy Distribution

In most astrophysical environments, the acceleration of particles is associated with a power-law energy distribution,

$$N(E)dE = KE^{-p}dE, \tag{3.119}$$

where $N(E)dE$ is the number density of electrons in the energy interval E to $E + dE$. The spectrum of synchrotron radiation is quite sharply peaked near the critical frequency, ν_c (Figure 3.8). The energy radiated in the frequency range ν to $\nu + d\nu$ can be attributed to electrons with energies in the range E to $E + dE$ (e.g. Longair 2011, page 212). Now consider electrons at a fixed pitch angle. The contributions of the electrons to the intensity is integrated at angular frequency ω. Recall that,

$$x = \frac{\omega}{\omega_c} = \frac{\omega}{\frac{3}{2}\gamma^2\omega_g \sin\alpha} = \frac{2\omega m_e^2 c^4}{3E^2\omega_g \sin\alpha} = \frac{A}{E^2}. \tag{3.120}$$

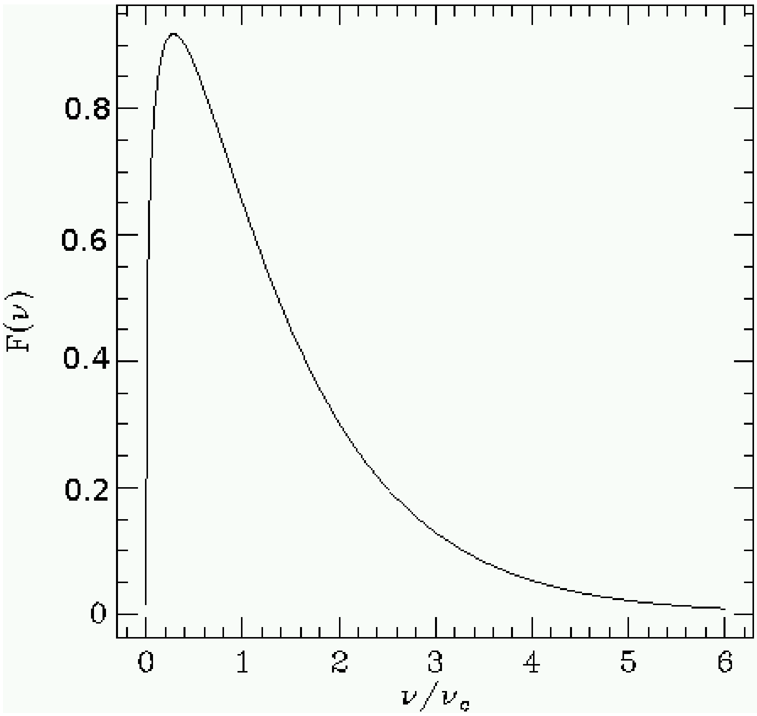

Figure 3.8: Spectrum of synchrotron radiation showing the characteristic peak emission at $0.29\nu_{\rm c}$ (www.astro.utu.fi/∼cflynn/astroII/l4.html).

The emissivity per unit volume is,

$$J(\omega) = \int_0^{\infty} j(x) K E^{-p} dE. \tag{3.121}$$

But, from equation (3.120),

$$E = A^{\frac{1}{2}} x^{-\frac{1}{2}} \tag{3.122}$$

$$dE = -\frac{A^{\frac{1}{2}}}{2} x^{-\frac{3}{2}} dx. \tag{3.123}$$

Ignoring the negative sign resulting from the change of variables, since $J(\omega) = |J(\omega)|$, the emissivity is

$$\begin{aligned} J(\omega) &= \int_0^{\infty} j(x) K \left(\frac{A}{x}\right)^{-\frac{p}{2}} \frac{1}{2} A^{\frac{1}{2}} x^{-\frac{3}{2}} dx \\ &= \frac{K}{2A^{\frac{(p-1)}{2}}} \int_0^{\infty} j(x) x^{\frac{(p-3)}{2}} dx \\ &= \frac{\sqrt{3} e^3 B K \sin\alpha}{4\pi c m_e A^{\frac{(p-1)}{2}}} \int_0^{\infty} F(x) x^{\frac{(p-3)}{2}} dx. \end{aligned} \tag{3.124}$$

Consider the standard integral,

$$\int_0^{\infty} x^{\mu} F(x) dx = \frac{2^{\mu+1}}{\mu} \Gamma\left(\frac{\mu}{2} + \frac{7}{3}\right) \Gamma\left(\frac{\mu}{2} + \frac{2}{3}\right), \tag{3.125}$$

which, by comparison, μ = (p-3)/2. Hence,

$$\int_0^{\infty} F(x)x^{\frac{(p-3)}{2}}dx = \frac{2^{\frac{(p-1)}{2}}}{(p+1)}\Gamma\left(\frac{p}{4}+\frac{19}{12}\right)\Gamma\left(\frac{p}{4}-\frac{1}{12}\right) \tag{3.126}$$

Then, it can be shown that

$$J(\omega) = \frac{\sqrt{3}e^3BK\,\sin\alpha}{2\pi cm_e(p+1)}\left(\frac{\omega m_e^3c^4}{3eB\,\sin\alpha}\right)^{-\frac{(p-1)}{2}}\Gamma\left(\frac{p}{4}+\frac{19}{12}\right)\Gamma\left(\frac{p}{4}-\frac{1}{12}\right). \tag{3.127}$$

Finally, integrate equation 3.127 over α, considering isotropic distribution of pitch angles such that the probability distribution of α is $\frac{1}{2}\sin\alpha\, d\alpha$ (e.g. Longair 2011, page 213),

$$\begin{aligned} J(\omega) &= \frac{\sqrt{3}e^3BK}{2\pi cm_e(p+1)}\left(\frac{\omega m_e^3c^4}{3eB}\right)^{-\frac{(p-1)}{2}}\Gamma\left(\frac{p}{4}+\frac{19}{12}\right)\Gamma\left(\frac{p}{4}-\frac{1}{12}\right) \\ &\quad\times\int_0^{\pi}\sin^{\frac{(p+1)}{2}}\alpha\frac{1}{2}\sin\alpha\, d\alpha \\ &= \frac{\sqrt{3}e^3BK}{2\pi cm_e(p+1)}\left(\frac{\omega m_e^3c^4}{3eB}\right)^{-\frac{(p-1)}{2}}\Gamma\left(\frac{p}{4}+\frac{19}{12}\right)\Gamma\left(\frac{p}{4}-\frac{1}{12}\right) \\ &\quad\times\frac{1}{2}\int_0^{\pi}\sin^{\frac{(p+3)}{2}}\alpha\, d\alpha. \end{aligned} \tag{3.128}$$

Then, consider the standard integral (e.g. Longair 1994, page 251; Longair 2011, page 213):

$$\frac{1}{2}\int_0^{\pi}\sin^{\frac{(p+3)}{2}}\alpha\;\mathrm{d}\alpha = \frac{\sqrt{\pi}\Gamma\left(\frac{p+5}{4}\right)}{2\Gamma\left(\frac{p+7}{4}\right)}. \tag{3.129}$$

Thus,

$$J(\omega) = \frac{\sqrt{3\pi}e^3BK}{2\pi cm_e(p+1)}\left(\frac{\omega m_e^3c^4}{3eB}\right)^{-\frac{(p-1)}{2}}\frac{\Gamma\left(\frac{p}{4}+\frac{19}{12}\right)\Gamma\left(\frac{p}{4}-\frac{1}{12}\right)\Gamma\left(\frac{p}{4}+\frac{5}{4}\right)}{\Gamma\left(\frac{p}{4}+\frac{7}{4}\right)} \tag{3.130}$$

$$J(\omega) \propto KB^{\frac{(p+1)}{2}}\omega^{-\frac{(p-1)}{2}}. \tag{3.131}$$

This relation gives the spectral emissivity of a population of relativistic particles in a magnetic field, displaying a typical power-law relation. It should be noted that the photon power-law index (α) relates to the power-law index of the relativistic electron population (p) by

$$\alpha = \frac{p-1}{2}. \tag{3.132}$$

In this Chapter, a brief review of just the most appropriate aspects related to the thermal and non-thermal emission properties relevant to the spectral nature of the soft ($\epsilon_{\rm X} \leqslant$ 10 keV) and hard ($\epsilon_{\rm X} \geqslant$ 10 keV) X-ray emission from AE Aqr were presented. In the next two Chapters, the Chandra and Swift observations and analyses are discussed respectively.

Chapter 4

Reduction and Analysis of Chandra Data

4.1 The Chandra X-ray Observatory (CXO)

The Chandra X-ray Observatory (e.g. Brissenden 2001; Weisskopf et al. 2002; Weisskopf 2003), formerly called the Advanced X-ray Astrophysics Facility (AXAF), was launched on July 23, 1999 by the Space Shuttle Columbia. It has since been NASA's flagship mission for X-ray astronomy, hence one of NASA's "Great Observatories" alongside the Hubble Space Telescope (HST; 1990-) and the Compton Gamma-Ray Observatory (CGRO), with the latter already decommissioned (1991-2000). Following its launch and orbital insertion, Chandra underwent a 2 month Orbital Activation and Checkout phase before starting Guaranteed Time Observations (GTOs) in September 1999 (e.g. Brissenden 2001).

Chandra provides unprecedented capabilities for sub-arcsecond imaging, spectroscopic imaging, and high resolution dispersive spectroscopy over the energy band 0.08-10 keV (15-0.12 nm; Weisskopf et al. 2002; Weisskopf 2003). The observatory contains a high resolution ($0.5''$) X-ray telescope, and a complementary set of imaging and spectroscopic instruments (e.g. Brissenden 2001). These capabilities have enabled observations of a wide range of high energy phenomena in a broad range of astronomical objects (e.g. Weisskopf 2003), with scientific data constantly provided to the international community.

The CXO is the product of the efforts of many institutions in the US and Europe. These include: the NASA Marshall Space Flight Center, which manages the Chandra program (e.g. Brissenden 2001); science and mission operations for the Chandra program are done at the Chandra X-ray Center (CXC) and the Operations Control Center (OCC), using facilities of the Smithsonian Astrophysical Observatory (SAO) and the Massachusetts Institute of Technology (MIT). Observing time is awarded through an annual group review, for which selected targets are scheduled in weekly segments. Subsequently, telemetry and data are downlinked in 8 hour intervals, monitored at the OCC and passed to the CXC for processing, archiving, and distribution to the scientific community.

4.1.1 Orbital Insertion and Activation

Approximately 8 hours after its launch (e.g. Weisskopf 2003), Chandra was deployed, together with its attached two-stage Inertial Upper Stage (IUS) monitor, into a low Earth orbit at an altitude of $\sim$ 240 km. Subsequently, the IUS propelled the observatory's flight system into a highly elliptical transfer orbit (e.g. Weisskopf et al. 2002). Then, over a period of days, its Internal Propulsion System (IPS), via a series of firings, placed the observatory into its initial operational orbit, i.e. 140,000 km apogee and 10,000 km perigee (e.g. Brissenden 2001; Weisskopf et al. 2002), with Keplerian orbital parameters shown in Table 4.1. Once the final orbit was attained, the systems of the spacecraft were activated over several weeks (e.g. Brissenden 2001), followed by activation of the pointing system. The first X-rays were eventually observed on 12 August 1999 (e.g. Weisskopf et al. 2002).

The highly elliptical orbit of Chandra yields a high observing efficiency. The fraction of the sky occulted by the Earth is small, hence more than 70 % of the observing time is useful, and observations exceeding 2 days are possible. Chandra was designed for a minimum lifetime of 5 years. However, the quantity of the gas that maneuvers the spacecraft can allow operation for more than 10 years. Therefore, the satellite has been productive for more than a decade.

Table 4.1: Keplerian orbital parameters of the Chandra X-ray observatory at its initial operational orbit (Taken from Brissenden 2001).

Parameter	Symbol	Value and unit
Semi major axis	a	80,798.5 km
Eccentricity	e	0.802
Inclination	i	28.5°
Right Ascension of Ascending Node	Ω	194.1°
Argument of Perigee	ω	271.1°
True Anomaly	ν	180.1°
Period	P	63.491 hr

4.1.2 The Chandra Systems

The Chandra X-ray observatory consists of many systems and subsystems. These are shown in Figure 4.1. The major systems include: the telescope system and the science instruments. Other systems are: the Command, Control and Data Management (CCDM) system, the Pointing, Control and Aspect (Attitude) Determination (PCAD) system, the Thermal Power, Thermal Control and Propulsion systems respectively. I will review some of these components, following the descriptions by Brissenden (2001), Weisskopf et al. (2002) and Weisskopf (2003). More detailed descriptions are found in the Chandra Proposers' Observatory Guide (POG; http://cxc.harvard.edu/proposer/POG/).

I. The Telescope System

The principal elements (or components) of the telescope system are the High Resolution Mirror Assembly (HRMA) and the Optical Bench Assembly (OBA). The system does provide mounts and mechanisms for Chandra's two Objective Transmission Gratings (OTGs). One of the components of the telescope system, the Aspect Camera Assembly (e.g. Weisskopf et al. 2002, and reference therein), attaches to, and is coupled with the HRMA through a transfer system, which maps the X-ray focal plane onto the sky.

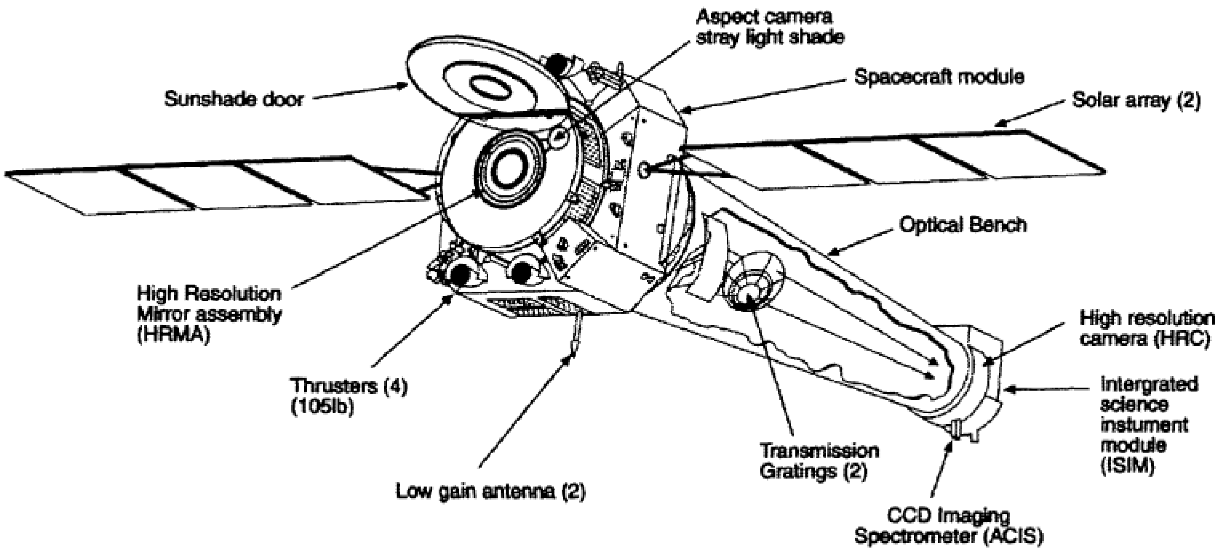

Figure 4.1: Components of the Chandra X-Ray Observatory in its deployed configuration. The telescope system and the science instruments constitute the major components of the observatory's systems (Taken from Brissenden 2001).

(i) The Integrated Science Instrument Module (ISIM)

The ISIM or the Science Instrument Module (SIM; Skinner & Jordan 1997) includes mechanisms for focusing and translating the satellite's focal plane instruments. Detail related to these instruments will follow in §4.1.2 (II-3).

(ii) The Electron Proton Helium Instrument (EPHIN)

The EPHIN is a particle detector mounted on the spacecraft and it consists of an array of six silicon detectors. It is sensitive to electrons in the energy range of 250 keV to 10 MeV, and for the isotopes of hydrogen and helium it is between 5-53 MeV per nucleon. EPHIN monitors the local charged particle environment so as to protect the focal plane instruments from particle radiation damage (Weisskopf et al. 2002).

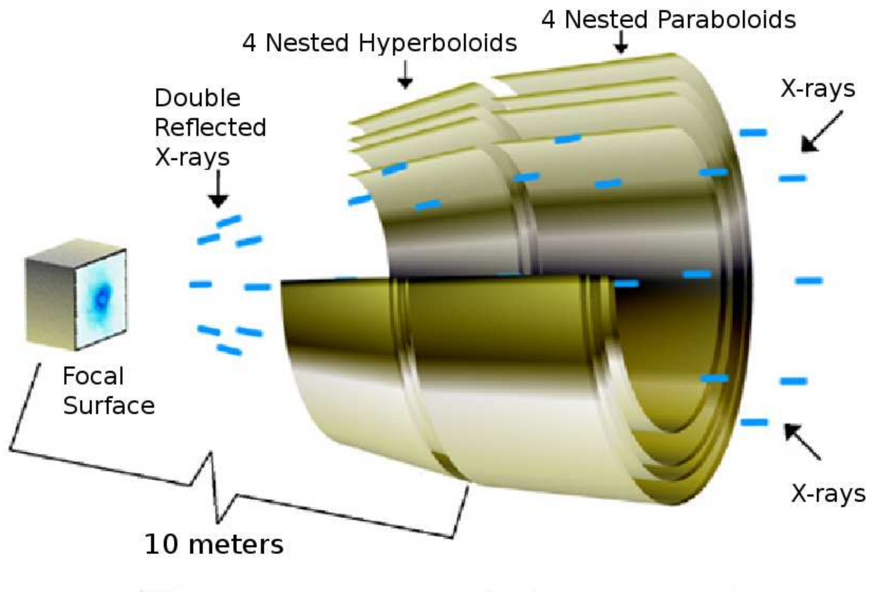

Figure 4.2: X-ray reflections in the High Resolution Mirror Assembly. The mirror elements are 0.8 m long and 0.6-1.2 m in diameter. The FoV on the focal surface is ±5 deg (Adapted from http://chandra.harvard.edu/resources/illustrations/teleSchem.html).

II. X-ray Subsystems

Two of the X-ray subsystems have already been mentioned, i.e. the HRMA and the OTGs. The third component consists of the focal plane science instruments. Each of these subsystems will be discussed briefly below, and for in-depth discussion, the reader is referred to the Chandra Proposers' Observatory Guide (POG), and references therein.

1. The High Resolution Mirror Assembly (HRMA)

This consists of four pairs of grazing incidence Wolter Type I mirrors (e.g. Brissenden 2001), coated with iridium for high X-ray reflectivity and chemical stability (e.g. Weisskopf et al. 2002). The Eastman Kodak Company (Rochester, New York) aligned and assembled the mirrors into the 10 m focal length HRMA. The mirror assembly has an effective area of 800, 400 and 100 cm^2 at 0.25, 5 and 8 keV respectively, and provides a FoV of 30 arcmin diameter. The optics of the HRMA is shown in Figure 4.2.

2. The Objective Transmission Gratings (OTGs)

Mounted behind the HRMA are the Chandra's two OTGs (e.g. Weisskopf et al. 2002): the Low Energy Transmission Grating (LETG) and the High Energy Transmission Grating (HETG). Essentially, either OTG is inserted into the converging beam by positioning mechanisms, where the X-ray radiation is dispersed onto the focal plane.

The LETG is a collaborative effort of the Space Research Institute of the Netherlands (SRON; Utrecht, Netherlands) and the Max-Planck-Institüt für extra-terrestrische Physik (MPE; Garching, Germany). It has 540 grating facets, mounted three per module, which lie tangent to the focal plane. LETG provides high resolution spectroscopy from 0.08 to 2 keV (15-0.6 nm).

The HETG, on the other hand, was designed and fabricated by the Massachusetts Institute of Technology (MIT; Cambridge, Massachusetts). It has two types of grating facets, each with a different period, mounted on the same structure: the Medium Energy Gratings (MEGs) which are mounted behind the two outermost shells of the HRMA, and the High Energy Gratings (HEGs), mounted behind the two innermost shells of the HRMA. The HETG provides high resolution spectroscopy from 0.4 to 4 keV (3-0.3 nm) for MEG, and 0.8 to 8 keV (1.5 - 0.15 nm) for HEG respectively.

The Chandra's Objective Transmission Gratings allow measurements with resolving power of $\lambda/\Delta\lambda$ (or $E/\Delta E$) > 500 for $\lambda > 0.4$ nm (or $E < 3$ keV), as shown in Figure 4.3.

3. The Focal Plane Science Instruments

Chandra's two science instruments, the High Resolution Camera (HRC) and the Advanced CCD Imaging Spectrometer (ACIS), are housed in the ISIM. Each of these instruments provides an Imaging detector (I) and a Spectroscopy detector (S), the latter designed to serve as a readout for dispersed photons from the transmission gratings. X-rays are focused onto one of the selectable instruments which are optimized for higher and lower portions of the energy range respectively (e.g. Brissenden 2001).

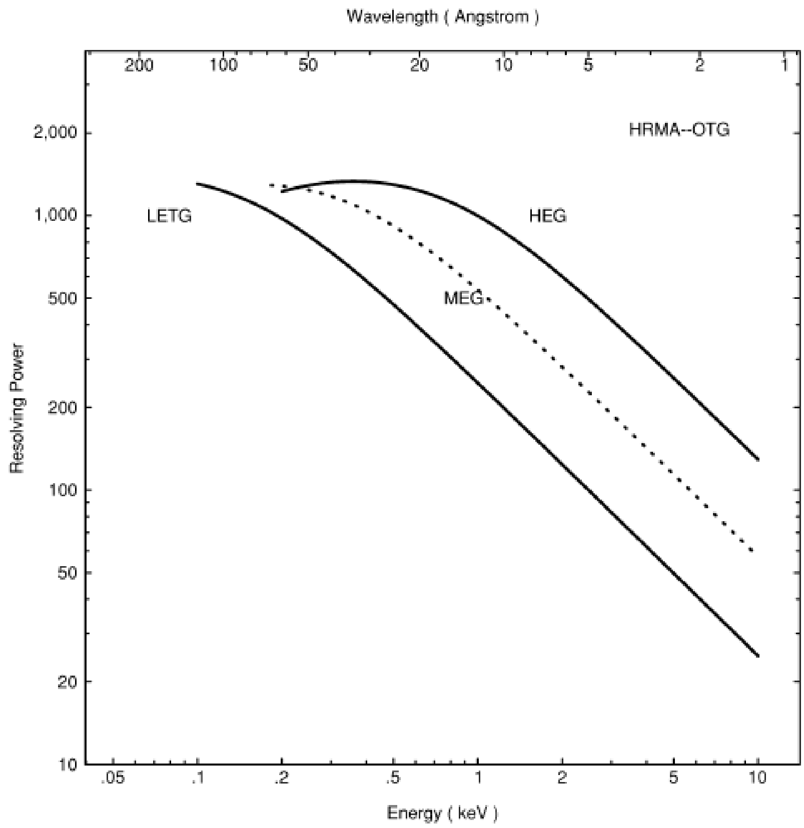

Figure 4.3: Spectral resolving power of the Chandra's OTGs (Taken from Weisskopf et al. 2002).

The High Resolution Camera (HRC; Murray et al. 2000) was designed and fabricated by the Smithsonian Astrophysical Observatory (SAO). Both the imaging and spectroscopy detectors of the HRC are coated with a cesium-iodide photocathode, and covered with aluminized-polyimide UV/ion shields (e.g. Weisskopf et al. 2002; Weisskopf 2003). The HRC-I is made up of a single 10 cm^2 microchannel plate, and provides high resolution imaging over a 31 arcmin square FoV. The HRC-S, however, consists of 3 rectangular segments (3 cm $\times$ 10 cm each), mounted end to end along the dispersion direction of the OTG. It is the primary readout detector for the LETG.

The Advanced CCD Imaging Spectrometer (ACIS) was designed and fabricated by the Pennsylvania State University (PSU; University Park, Pennsylvania) and the MIT. The ACIS-I is made of a 2 $\times$ 2 array of large-format front-illuminated (FI), 2.5 cm^2 CCDs. It provides high resolution spectroscopic imaging over a 17 arcmin square FoV (e.g. Weisskopf et al. 2002). Image data from the ACIS CCD chips are acquired and processed on-board by the ACIS software (e.g. Brissenden 2001). The ACIS-S, on the other hand, has a 1 $\times$ 6 array of FI CCDs and two back-illuminated (BI) CCDs, mounted along the OTG dispersion direction, both serving as the primary detector for the HETG. Both the ACIS detectors are covered with aluminized-polyimide optical blocking filters.

4.2 Observation of AE Aquarii

AE Aquarii was observed by Chandra (ObsID 5431) on August 30, 2005 at 06:37 UT for ~ 80 ks (Mauche 2006; Mauche 2009), using the Advanced CCD Imaging Spectrometer (ACIS) detector and the High Energy Transmission Grating (HETG). Each of these detection instruments was described explicitly in the previous section. Standard data processing was done at the Chandra X-ray Center (CXC), and the archived data became public on September 7, 2006. Data were acquired through the High Energy Astrophysics Science Archive Research Center (HEASARC) on-line service, provided by the NASA's Goddard Space Flight Center (GSFC).

4.2.1 Description of the Data Products

In this subsection, I give a short description on the data products, based on the contents of the files downloaded from the CXC archive. This may also provide a general picture for all the archived data observed by Chandra, and more information on these products may be obtained from the Chandra Analysis Basic Guide (e.g. May 18-22, 2009), edited by Marilena Caramazza (http://www.astropa.unipa.it/ScuolaX2009/manuals/chandra_analysis_basic_guide.pdf).

The Observation Identification (ObsID) directory is the top level directory in the directory tree. This directory contains the observation index file (oif.fits) which provides a summary of the data products associated with the observation, then two sub-directories, i.e. the primary and secondary directories respectively. The primary directory contains all data product files necessary for most of the analyses. The most important of these include: the level 2 event file (evt2.fits), which is created from the level 1 event list by filtering the good time intervals (GTIs) and status bits; the bad pixels file (bpix1.fits), which contains a list of pixels identified as bad and criteria for flagging a pixel. Any tool reading this latter file will exclude the bad pixels from further analysis. Then, there is also the orbit ephemeris file (eph1.fits) which contains the orbit ephemeris information, and the aspect solution file (pcad_asol1.fits) that describes the orientation of the telescope. The detected position of an event and the corresponding telescope aspect are combined for accurate determination of the celestial position of an event.

In the secondary directory, the following files are placed: the Verification and Validation (V&V) report file, which is a pdf file containing a summary of the V&V report by a CXC scientist (after checking all data products to ensure data quality and to investigate the cause of any exposure losses or other anomalies). Scientists are supposed to review the information in the V&V report before embarking on their analyses. Then, there is the level 1 event file (evt1.fits) which contains all the events recorded for the observation. Many of these events have a status bit set to flag them as bad, but none of the information has been removed. This file is filtered on GTIs and status bit. Therefore, the evt1.fits file is the starting point for reprocessing the data. In addition, there is also a filter file (e.g., flt1.fits, for ACIS) containing the GTI information. This information includes the start and stop times of all accepted time intervals. When the event is filtered, the GTIs are stored as extensions of the data file. Finally, the parameter block file (pbk0.fits) is needed when creating a new bad pixel list. It is used to determine observational parameters, such as active CCDs, the readmode and datamode respectively. This file is required for observations done with the ACIS only.

4.3 Data Reduction and Analysis

I installed the Chandra Interactive Analysis of Observations (ciao) version 4.2 software and used it to process the light curves and spectra. In both cases, I utilized the level 2 event file, processed at the Chandra X-ray Center from the level 1 event list using the standard pipeline processing, and archived together with other data products which I explained in §4.2.1. In this section, I present the procedures followed to generate the light curves and the spectra, as well as the results of the analyses.

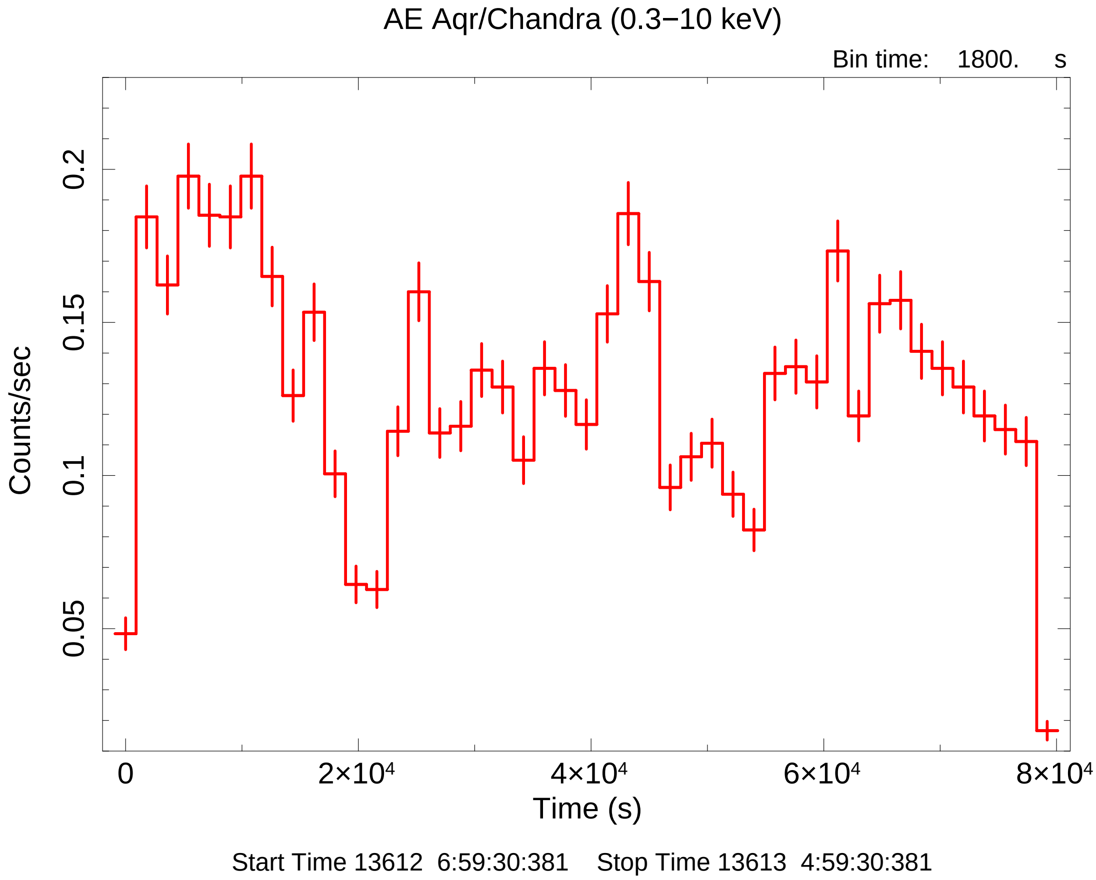

Figure 4.4: Background subtracted light curve for the energy band 0.3-10 keV.

4.3.1 Light curves

The event times in the level 2 event file were converted from Terrestrial Time (TT) to Barycentric Dynamical Time (TDB) by applying the axbary tool using the orbit ephemeris file. Then, energy filtering was applied to the barycentric corrected data. For each of the filtered data set, I created a source region and a background region in DS9 (an astronomical imaging and data visualization application), then determined the chip (CCD_ID) being used. From these, background subtracted binned light curves were created.

Figure 4.4 shows the background subtracted light curve for the energy range 0.3-10 keV, with a bin time of 1800 s. The well established highly variable nature of AE Aqr is seen in the light curve, characterized by flaring (e.g. Patterson 1979; Bookbinder & Lamb 1987; Mauche 2009). The light curves and hardness ratio for the energy bands 0.3-2 keV and 2-10 keV are presented in Figure 4.5, where it can be seen that most of the X-ray emission is in the lower energy range

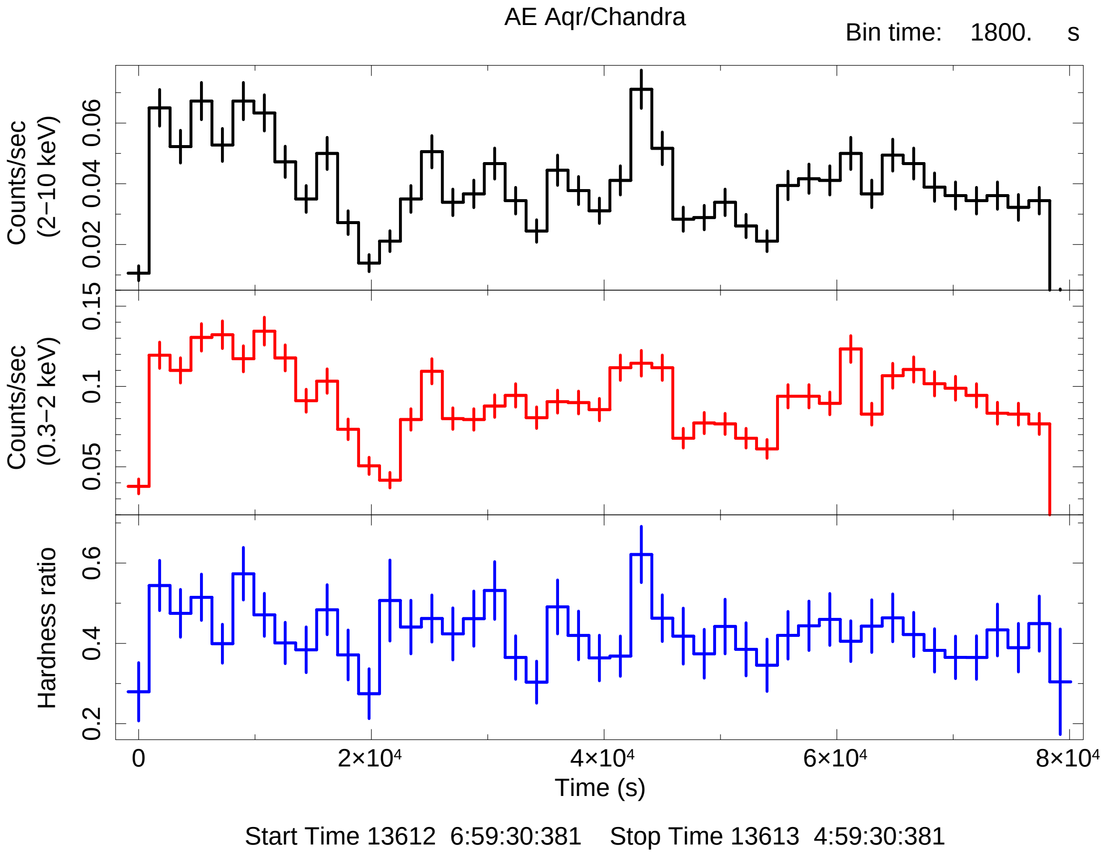

Figure 4.5: Light curves and hardness ratio for the energy bands: 2-10 and 0.3-2 keV.

(0.3-2 keV), i.e. the hardness ratio (HR), defined by the hard X-ray count rate divided by the soft X-ray count rate, is less than unity.

4.3.2 Pulse timing

I carried out a search for periodicities in the light curve using epoch folding method, where the light curve was folded with a large number of periods around an approximate value, and the best period obtained from chi squared maximization. An estimated pulse period of 33.0775 s was determined from the power spectrum of the light curve (Figure 4.6). Since, this period is near the spin period of the white dwarf determined from a long baseline of optical data (e.g. de Jager et al. 1994), I adopted the latter and used it to fold the light curve. Figure 4.7 shows the pulse period determined from the epoch folding search. The default Fourier period resolution (FPR) is $P^2/2T \sim 6.75 \times 10^{-3}$ s, where P is the folding period and T is the length of observation ($\sim$ 80 ks). To indicate the exact location of the period, the resulting peak was fitted with a gaussian

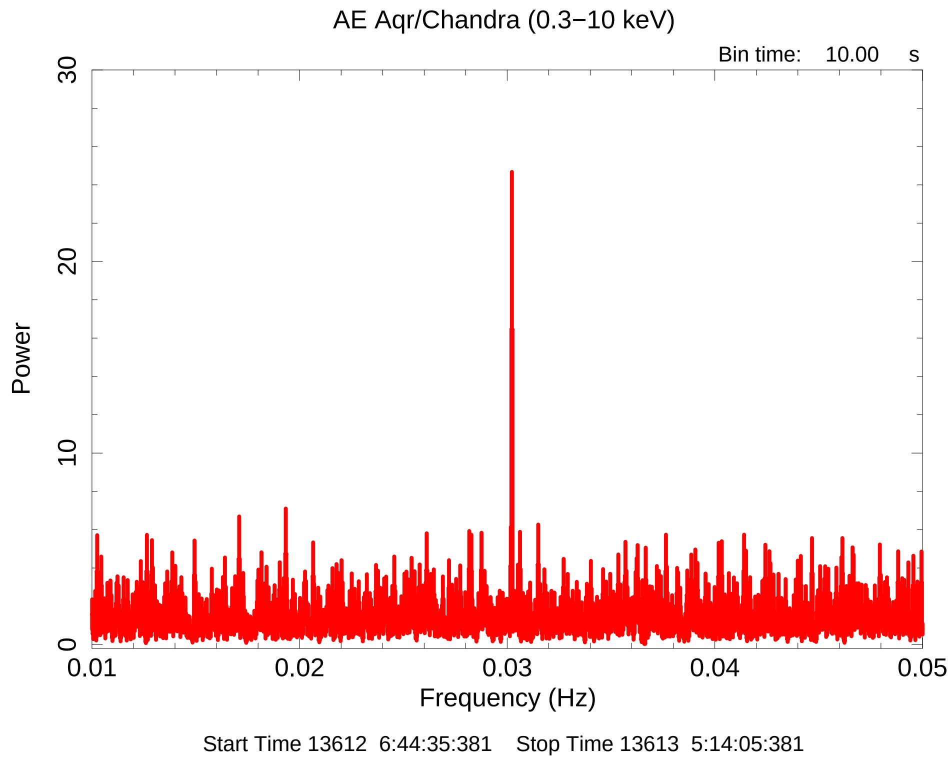

Figure 4.6: Power spectrum, showing the highest power at 0.030232±0.000021 Hz ($P \approx 33.0775$ s).

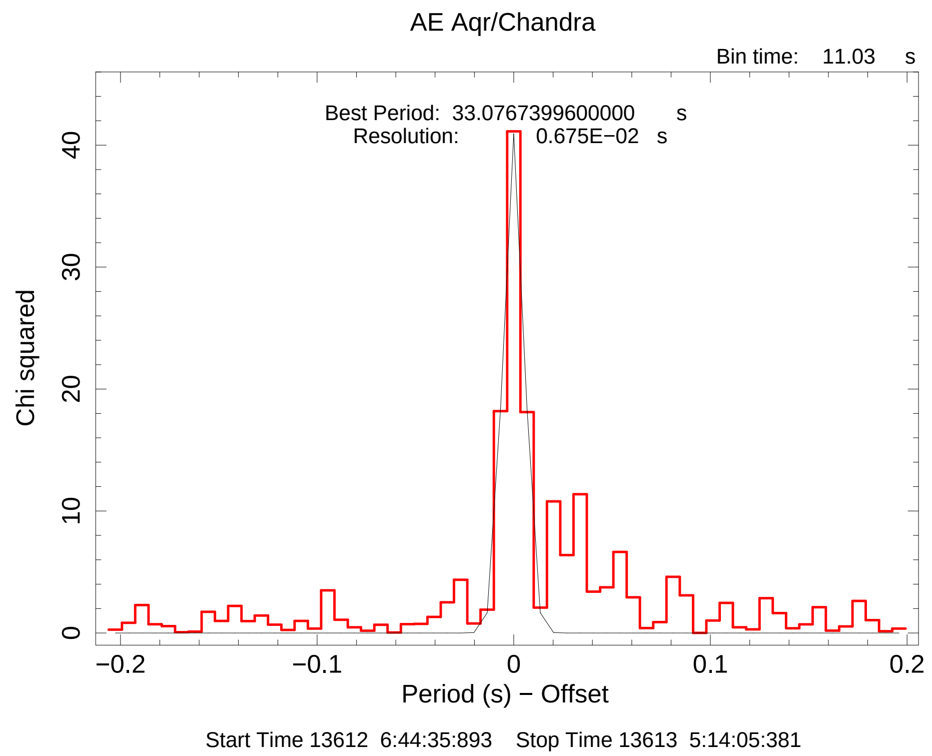

Figure 4.7: Pulse period determined from epoch folding search. The best period obtained from a chi-squared fit corresponds to $P \approx 33.0767$ s.

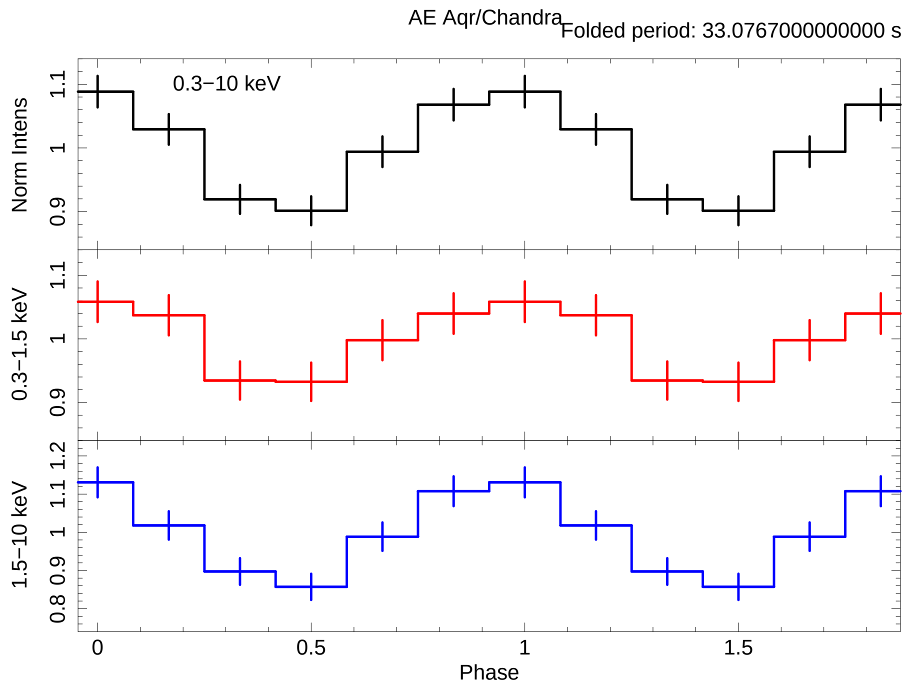

Figure 4.8: Pulse profiles for 0.3-10, 0.3-1.5, and 1.5-10 keV. Phase 0 corresponds to BJD 2453673.5.

and its central value used to indicate the exact pulse period of $P_{\rm pulse} = 33.0767{\pm}0.0068$ s. Using the pulse period obtained, phase profiles were determined using the epoch of BJD 2453673.5 (Terada et al. 2008). The profiles are shown in Figure 4.8. These are characterized by small amplitude, single-peaked and broad sinusoidals, with the pulse maximum of the 33 s spin period of the white dwarf consistent with that obtained from the Suzaku data (Terada et al. 2008).

4.3.3 Spectra

Utilizing the level 2 event file, I extracted a spectrum file (pha2.fits). This was then split into single spectrum files with respect to the order of the spectrum (diffraction order) and the spectral component (grating arm), which were determined from the spectrum block of the pha2 file. Then, for each of the single spectra, I created a response matrix file (RMF) and used it alongside the event and pha2 files to create the corresponding ancilliary response file (ARF). Finally, a background subtracted spectrum was plotted for each diffraction order and grating arm, and models fitted using sherpa, one of the packages in the ciao software.

Figures 4.9 and 4.10 show the MEG energy and wavelength spectra for m = -1, fitted with

Table 4.2: Best fit parameters for each grating arm and diffraction order. Elemental abundances are fixed to those obtained by Itoh et al. (2006); see also Choi & Dotani (2006): N = 3.51, O = 0.74, Ne = 0.43, Mg = 0.70, Si = 0.81, S = 0.73, Ar = 0.21, Ca = 0.19, Fe = 0.47, and Ni = 1.27.

	Best fit values			
Parameter	MEG (m=-1)	MEG (m=+1)	HEG (m=-1)	HEG (m=+1)
$N_{\rm H}$ (10^{20} cm^{-2}).........	3.59 (fixed)	3.59 (fixed)	3.59 (fixed)	3.59 (fixed)
kT_1 (keV)..................	$0.19^{+0.05}_{-0.04}$	$0.17^{+0.06}_{-0.06}$	—	—
Norm$_1$ (10^{-3})............	0.87±0.26	1.37±1.00	—	—
kT_2 (keV)..................	$0.64^{+0.02}_{-0.02}$	$0.61^{+0.05}_{-0.01}$	$0.63^{+0.04}_{-0.04}$	$0.62^{+0.05}_{-0.05}$
Norm$_2$ (10^{-3})............	2.15±0.16	2.07±0.18	2.54±0.33	$2.28^{+0.35}_{-0.36}$
kT_3 (keV)..................	$3.14^{+0.35}_{-0.33}$	$3.10^{+0.32}_{-0.27}$	$3.19^{+0.51}_{-0.44}$	$3.05^{+0.51}_{-0.37}$
Norm$_3$ (10^{-3})............	3.70±0.20	3.84±0.20	3.44±0.34	3.57±0.36
χ^2_ν (dof)......................	2.23 (137)	1.83 (123)	0.90 (130)	0.68 (107)
	Absorbed flux (10^{-12} erg cm^{-2} s^{-1})			
0.5-1.0 keV..................	3.45	3.70	2.80	2.62
1.0-2.0 keV..................	2.28	2.27	2.29	2.24
2.0-4.0 keV..................	1.50	1.52	1.42	1.43
4.0-8.0 keV..................	1.02	1.04	0.97	0.94
0.5-10 keV....................	8.40	8.67	7.61	7.36

a three-temperature vmekal model of temperatures (kT) of $0.19^{+0.05}_{-0.04}$ keV, $0.64^{+0.02}_{-0.02}$ keV and $3.14^{+0.35}_{-0.33}$ keV respectively. The corresponding spectra for the order m = +1, also fitted with a three-temperature model, are shown in Figures 4.11 and 4.12, respectively. The HEG spectra, on the other hand, are fitted with two-temperature vmekal models. The energy and wavelength spectra are shown in Figures 4.13 and 4.14 for m = -1, and Figures 4.15 and 4.16, for m = +1 respectively. The best fit parameters for each of the grating arms and diffraction orders, are given in Table 4.2.

Noticeable from the spectra are emission lines, most of which are in the lower energy range ($\leqslant$ 2 keV). Some of the prominent lines are labelled (e.g. Mauche 2009). The energy fluxes at the identified prominent lines are given in Table 4.3, for each grating arm and diffraction order respectively. Figure 4.17 shows the high-resolution spectrum obtained by Mauche (2009),

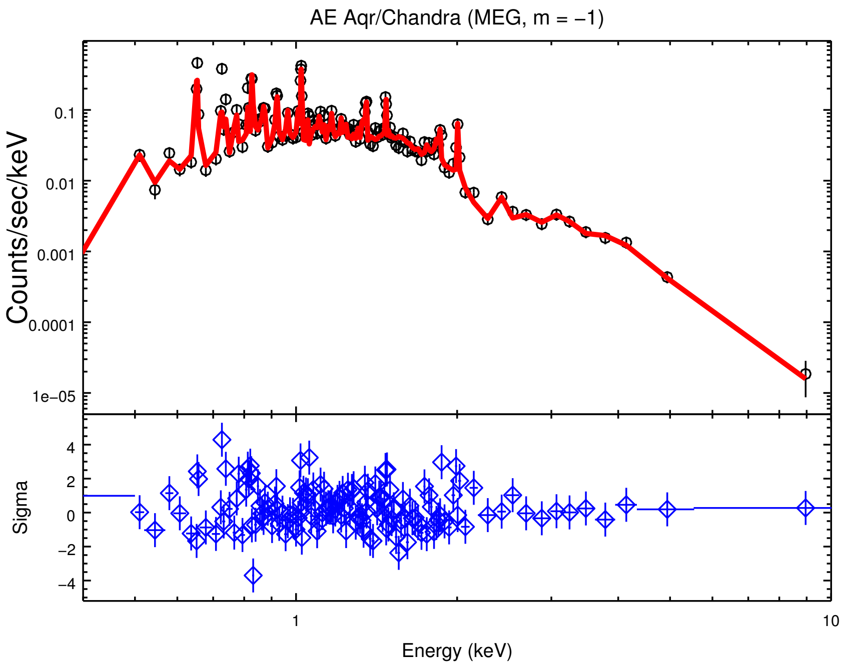

Figure 4.9: MEG energy spectrum for order m = -1, fitted with a three-temperature vmekal model.

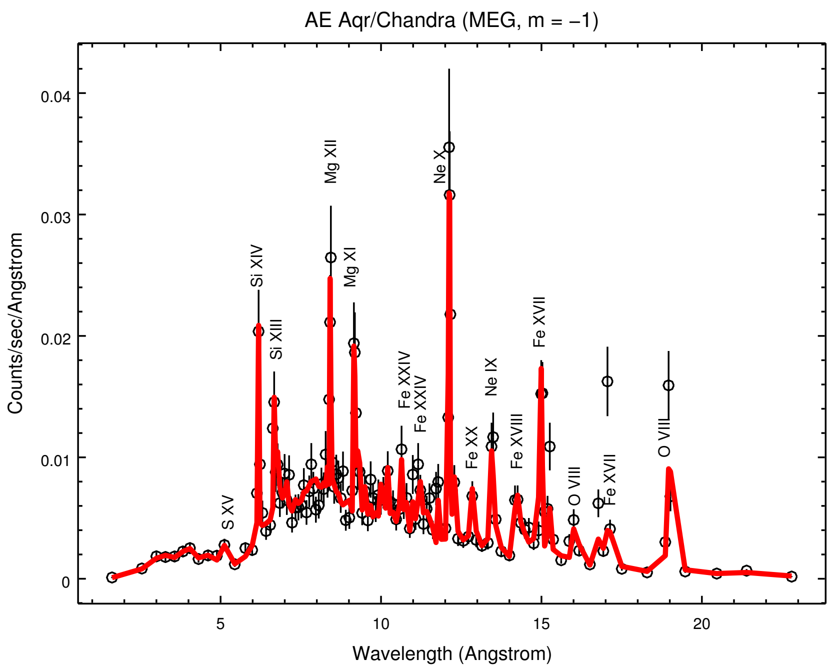

Figure 4.10: MEG wavelength spectrum for m = -1, fitted with a three-temperature vmekal model. Here, the low energy range is expressed in units of wavelength ($\mathring{A}$).

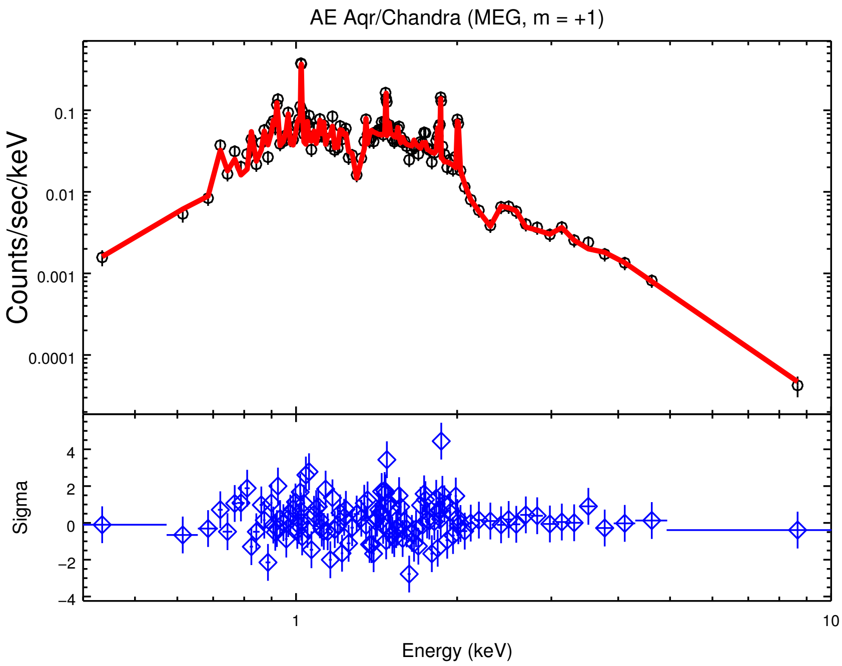

Figure 4.11: MEG energy spectrum for order $m = +1$, fitted with a three-temperature vmekal model.

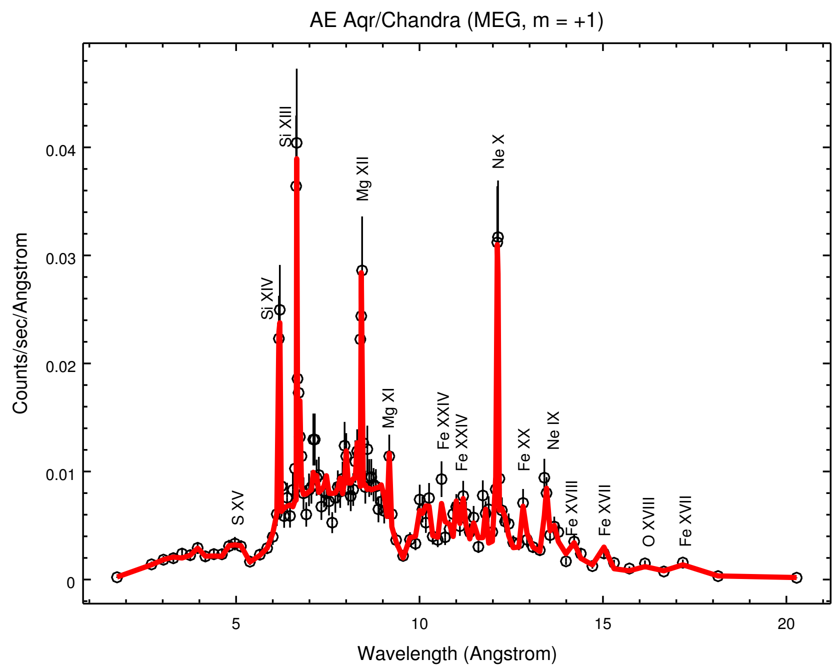

Figure 4.12: MEG wavelength spectrum for $m = +1$, fitted with a three-temperature vmekal model. Here, the low energy range is again expressed in units of wavelength ($\mathring{A}$).

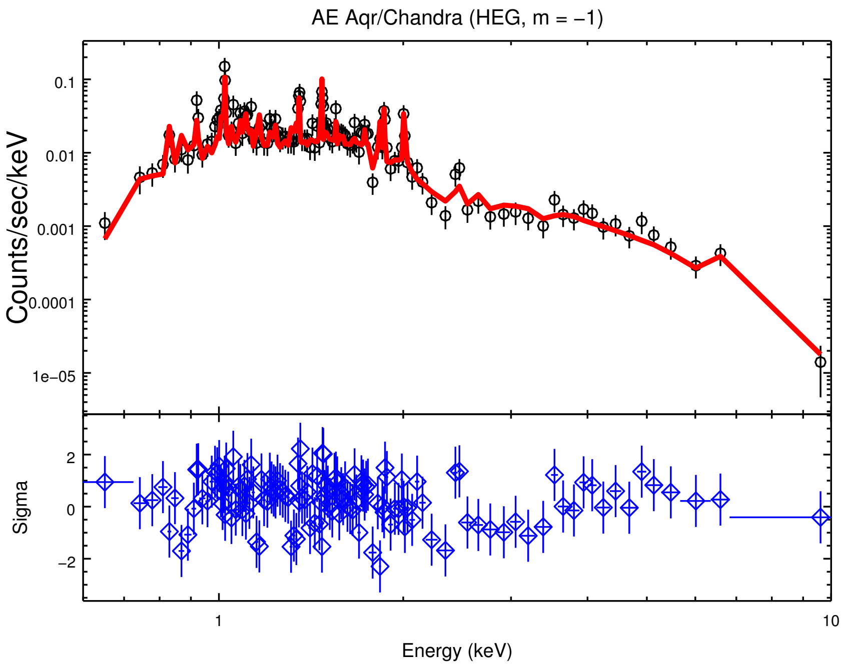

Figure 4.13: HEG energy spectrum for order m = -1, fitted with a two-temperature vmekal model.

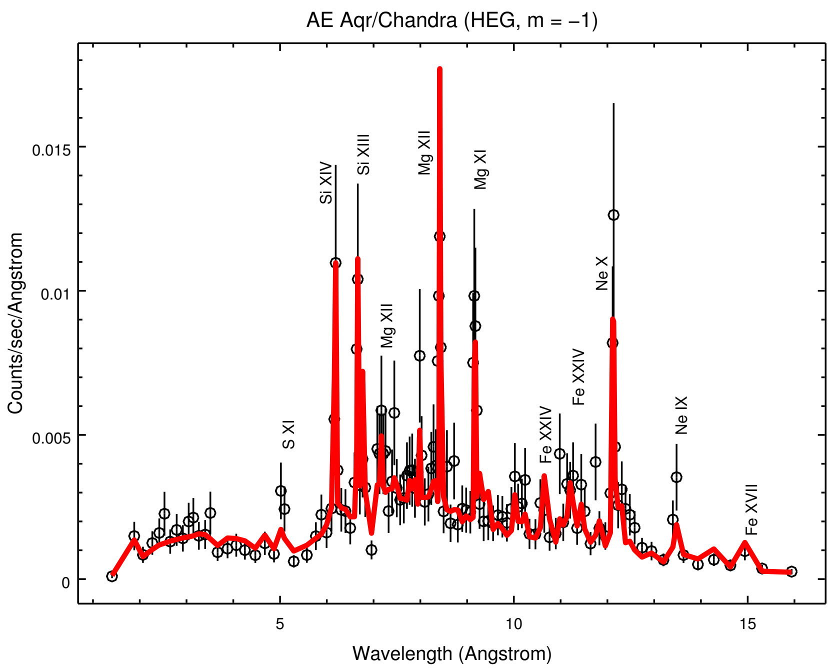

Figure 4.14: HEG wavelength spectrum for order m = -1, fitted with a two-temperature vmekal model, expressed in units of wavelength ($\AA$).

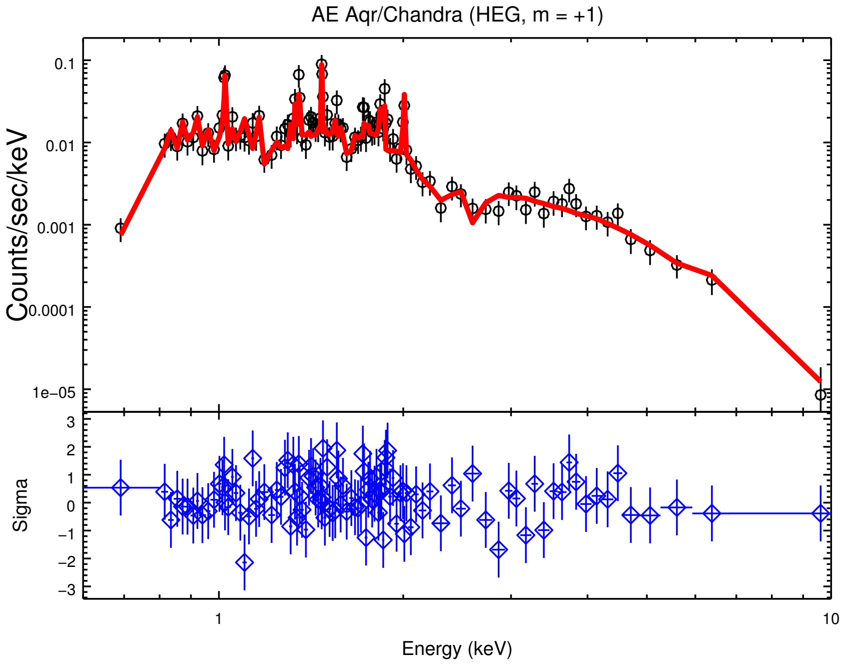

Figure 4.15: HEG energy spectrum for order $m = +1$, fitted with a two-temperature vmekal model.

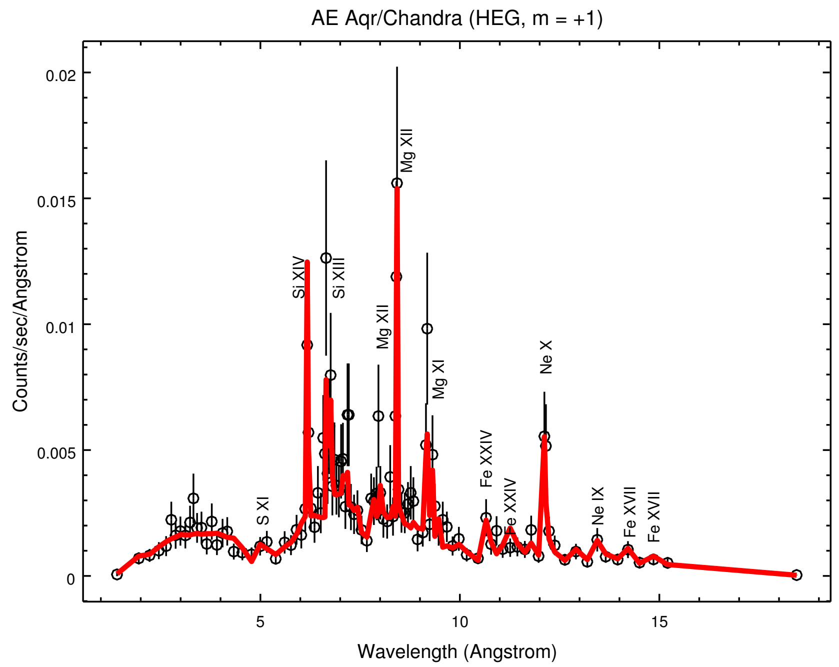

Figure 4.16: HEG wavelength spectrum for $m = +1$, fitted with a two-temperature vmekal model, expressed in units of wavelength ($\mathring{A}$).

Table 4.3: Energy fluxes determined for prominent emission lines from the Chandra spectra.

			MEG		HEG	
			m=-1	m=+1	m=-1	m=+1
Line	$<\lambda>$ (Å)	$<kT>$ (keV)	Flux $\times 10^{-13}$ erg cm^{-2} s^{-1}			
Si XIV	6.2	2.0	1.2	1.2	1.1	1.1
Si XIII	6.7	1.9	1.4	1.3	1.4	1.4
Mg XII	8.4	1.5	1.1	1.1	1.1	1.0
Mg XI	9.2	1.4	1.0	1.0	1.0	1.0
Ne X	12.1	1.0	1.5	1.5	1.7	1.6
Ne IX	13.5	0.9	1.7	1.6	1.8	1.6
Fe XVII	15.0	0.8	2.2	2.3	2.5	–
O VIII	19.0	0.7	3.8	–	–	–

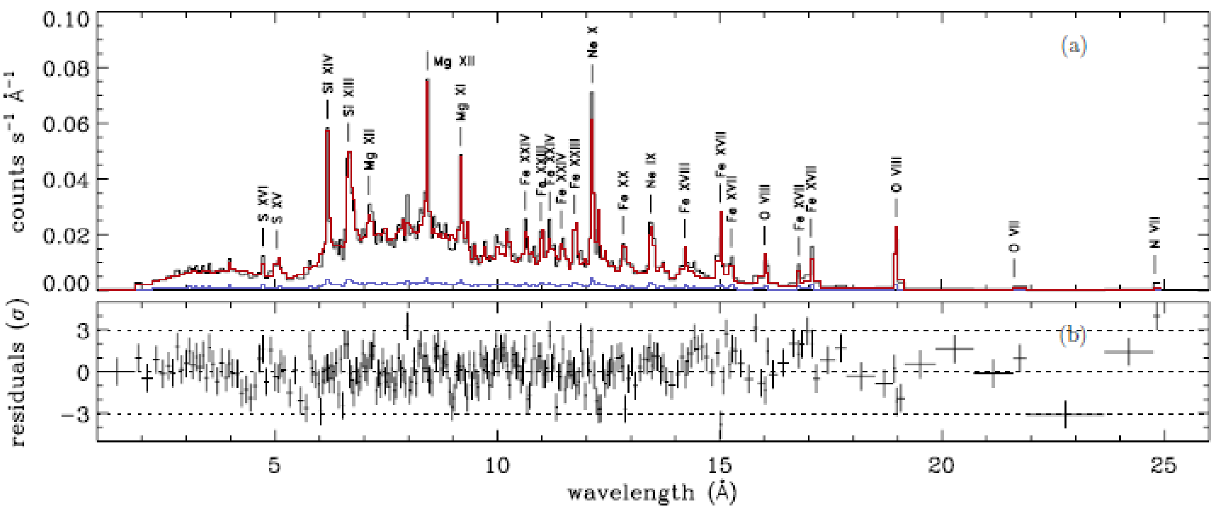

Figure 4.17: High resolution count spectrum of AE Aqr from Chandra data (MEG + HEG), showing characteristic emission lines (Taken from Mauche 2009).

for the combined MEG and HEG data, which is similar to the independent analysis done in this study. The time-averaged X-ray flux ($F_{\rm X}$) determined in the energy range 0.5-10 keV is 8.54×10^{-12} erg cm^{-2} s^{-1} for MEG and 7.49×10^{-12} erg cm^{-2} s^{-1} for HEG respectively (Table 4.2). These translate to $L_{\rm X} \sim 9.7\times10^{30}$ erg s^{-1} for MEG and 8.5×10^{30} erg s^{-1} for HEG respectively, considering a source distance of 100 pc (e.g. Welsh et al. 1993), i.e. $L = 4\pi D^2 F$.

Chapter 5

Reduction and Analysis of Swift UVOT and XRT Data

5.1 The Swift Gamma-Ray Burst Explorer

The most energetic phenomena in the universe recorded since the Big Bang are Gamma-ray Bursts. These flashes of γ-rays are observed approximately once per day. Since their discovery, Gamma-ray Bursts (GRBs; e.g. Klebesadal et al. 1973) have been known to occur with energies which are many orders of magnitude higher than supernova explosions (e.g. Mészáros & Rees 1992). They can shine as brightly as a billion galaxies ($E \sim 10^{53}$ ergs). Scientists originally believed GRBs came from within our galaxy, but a sky map from the Burst And Transient Source Experiment (BATSE) instrument on the Compton Gamma Ray Observatory (CGRO; e.g. Meegan et al. 1996) showed that GRBs are uniformly distributed throughout the sky, and must be at cosmological distances. This notion is further supported by the detection of GRB 970228, with a redshift of $z = 0.835$ (e.g. Roming et al. 2005, and references therein). Following from the BATSE detection, two populations of GRBs, distinguished on the basis of their duration, are known (e.g. Meegan et al. 1996). Short bursts with duration $t < 2$ s, and long bursts with $t > 2$ s respectively. Proposed progenitors of GRBs are: neutron stars in the Milky Way galaxy, NS-NS and NS-BH mergers, and failed supernovae (e.g. Roming et al. 2005

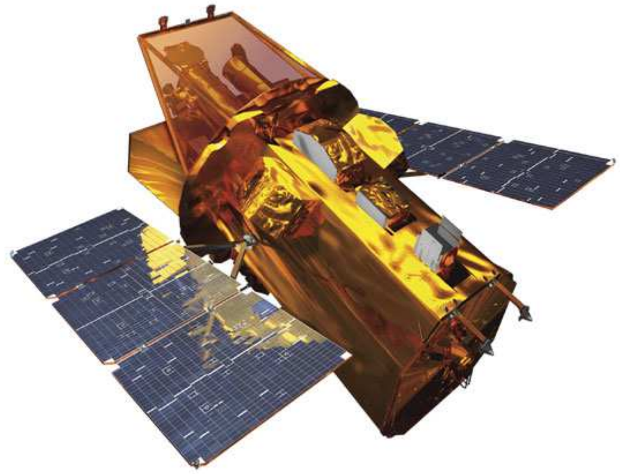

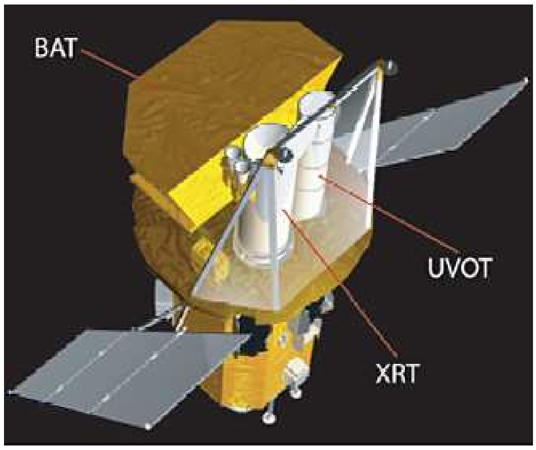

Figure 5.1: External view of Swift (http://no.wikipedia.org/wiki/Fil:Nasa_swift_satellite.jpg), with instruments on-board (http://home.cc.umanitoba.ca/∼umbarkm4/swift_telescope.html).

and references therein).

The Swift GRBs Explorer (e.g. Gehrels et al. 2004), shown in Figure 5.1, was launched on 20 November 2004 (e.g. Burrows et al. 2005; Pagani et al. 2006) with the main goal of discovering and studying the origin of GRBs and their afterglows, as well as using these to probe the early universe (e.g. Gehrels et al. 2004; Goad et al. 2007). The characteristics of the satellite are summarized in Table 5.1. Since its launch, Swift has routinely observed hundreds of GRBs on time scales ranging from minutes to hours and days. Swift is a NASA facility whose hardware was developed by a team from the US, UK and Italy, with additional scientific involvement from Denmark, France, Germany, Spain and South Africa (e.g. Gehrels et al. 2004). Since the discovery of GRBs in the late 1960s (e.g. Klebesadel et al. 1973), Swift has revolutionalized the current understanding of GRBs (e.g. Evans et al. 2009).

The three instruments flying on-board Swift are the Burst Alert Telescope (BAT, e.g. Barthelmy et al. 2005), the X-Ray Telescope (XRT, e.g. Burrows et al. 2005), and the Ultraviolet/Optical Telescope (UVOT, e.g. Roming et al. 2005). They combine to make a powerful multi-wavelength observatory capable of rapid position determination of GRBs, and the ability to measure both the light curves and the redshifts of the bursts and their afterglows (e.g. Burrows et al. 2005). Swift is the first mission to cover the near-UV part of the spectrum, and the wavelength coverage of the three instruments corresponds to 0.2-150 keV and 170-600 nm (e.g. Roming et al. 2005)

Table 5.1: Sample characteristics of Swift satellite (Adapted from Gehrels et al. 2004; Barthelmy et al. 2005).

Parameter	Value
Orbit	Low Earth, 600 km altitude
Inclination	22°
Slew rate	50° in < 75 s
Launch vehicle	Delta 7320-10 with 3 m firing
Mass	1450 kg
Power	1040 W
Mission life	2 yrs
Orbital lifetime	> 5 yrs

respectively. The BAT searches the sky for new GRBs, upon which an autonomous spacecraft slew is triggered to bring the bursts in the fields of view of the XRT and the UVOT respectively.

The BAT is a highly sensitive, large field of view (FoV), coded-aperture instrument designed to search for GRBs in the sky. It provides the burst trigger with 1-4 arcmin position accuracy (e.g. Barthelmy et al. 2005), used to slew the spacecraft to point the XRT and the UVOT for follow-up observations. When the BAT triggers on a newly discovered GRB, the Swift satellite performs an autonomous slew to the GRB position determined on-board, allowing prompt follow-up observations with the XRT and the UVOT (e.g. Pagani et al. 2006). BAT has a large dynamical range and trigger capabilities in order to study GRBs with a variety of intensities and duration (e.g. Gehrels et al. 2004). Both the UVOT and the XRT are narrow-FoV instruments and are co-aligned (e.g. Gehrels et al. 2004).

Besides GRBs, Swift has also routinely observed a number of non-GRBs' sources, with the XRT data being crucial to the science goals of the observations (e.g. Evans et al. 2009). Most of these sources are Pre-Planned Targets (PPTs) or Targets of Opportunities (ToOs), in which the observations are planned on the ground and uploaded to Swift. This is the category in which AE Aquarii was observed. While detecting GRBs, BAT also performs an all-sky hard X-ray survey and monitors hard X-ray transients (e.g. Barthelmy et al. 2005). In the next two sections, details of the operation of the two narrow-FoV science instruments will be reviewed.

5.2 The Swift Ultraviolet/Optical Telescope (UVOT)

The Swift UVOT (e.g. Roming et al. 2005) is designed to capture the early UV and optical photons from the afterglow of GRBs, and the long term observations of these afterglows, utilizing UV and optical broadband filters and grisms[1] (e.g. Roming et al. 2005). Essentially, it has a modified Ritchey-Chrétien configuration with a 30 cm primary mirror and an f-number[2] of 12.7. The characteristics of the telescope are listed in Table 5.2. The UVOT has two detectors, which are micro-channel plate intensified CCDs (MICs), each positioned behind one of the identical 11-position filter wheels. Incoming light beam from the telescope is directed to any one of the detectors by a 45 degree mirror.

The functional units of the UVOT are shown in Figure 5.2. Essentially, they are: the telescope module (TM) which consists of the UV/optical telescope and other systems which are listed in the next paragraph; there are also two digital electronics modules (DEMs), each containing a data processing unit (DPU) and an instrument control unit (ICU). Finally, there are two

Table 5.2: Characteristics of the Ultraviolet/Optical Telescope (Taken from Roming et al. 2005).

Telescope	Modified Ritchey-Chrétien
Aperture	30 cm diameter
f-number	12.7
Filters	11
Wavelength range	170-600 nm
Detector	MCP intensified CCD
Detector operation	Photon counting
Sensitivity	$m_{\mathrm{B}} = 24.0$ in white light in 1000 s
FoV	17 arcmin $\times$ 17 arcmin
Detector element	256 $\times$ 256 (pixels)
Pixel scale	0.5 arcsec
PSF	0.9 arcsec FWHM at 350 nm

[1] A grism is also called a grating prism

[2] f-number of an optical system is the ratio of its focal length to the effective aperture diameter. It is sometimes called the focal ratio (f-ratio).

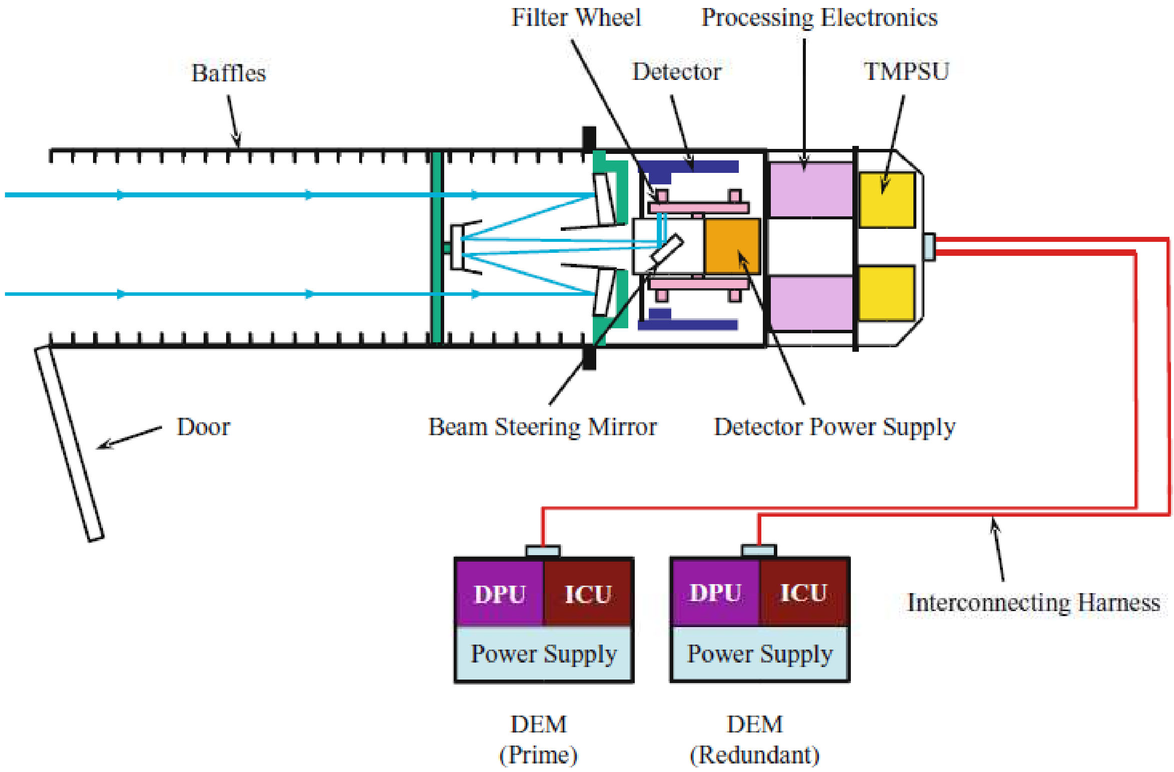

Figure 5.2: Schematic of the Swift UVOT layout, which is a 30 cm Ritchey-Chrétien telescope. The path of light through the telescope is denoted by arrows (Taken from Roming et al. 2005).

interconnecting harness units that connect the TM and the DEMs. The DEMs are mounted separately from the TM on a radiator bracket on the Swift optical bench. These modules are designed to minimize cosmic radiation.

The main sections of the TM (in sequential order) are the external baffle, the telescope tube, the detector module tube (DMT), and the power supply tube (PST). The telescope door was closed during launch and early orbit of the satellite to protect the telescope optics. The primary and secondary mirrors are mounted inside the telescope tube, and their separation is controlled using Invar[3] metering rods and heaters. The DMT contains the rest of the optical system, i.e. a beam steering mirror, two filter wheel systems, and photon counting detectors respectively.

[3]Invar is a nickel steel alloy notable for its uniquely low coefficient of thermal expansion, $\alpha \sim 1.2\times10^{-6}$ K^{-1}.

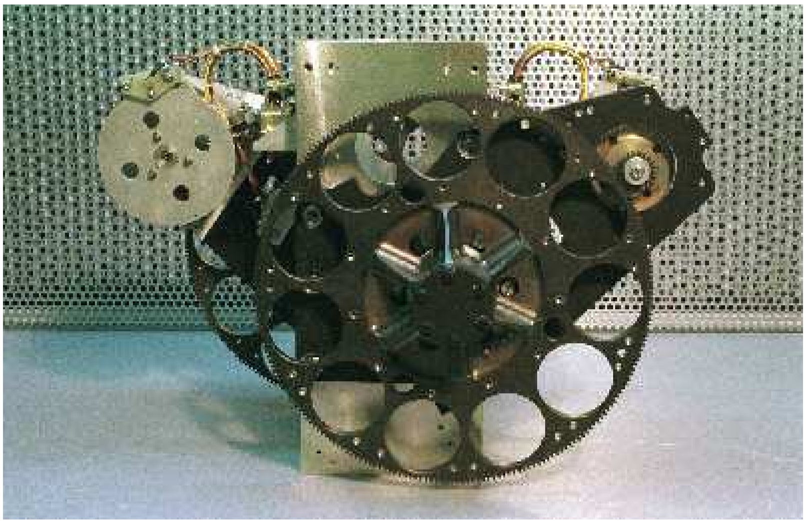

Figure 5.3: UVOT Filter Wheel Assembly with the detector, a copy of the XMM-Newton/OM's MIC detectors (http://heasarc.nasa.gov/docs/swift/about_swift/uvot_desc.html).

5.2.1 The Filter Wheel Mechanisms

Each of the two identical filter wheels rotates on a stab axle mounted to a base plate, and is driven by a motor with a gear ratio of 11:1, corresponding to the eleven optical elements placed at equal angles around each of the filter wheels, as illustrated in Figure 5.3. Each of the filter wheels contains the UV and optical grisms, a 4× magnifier, broadband colour filters, a white light filter, and a blocking filter. Before light enters the detector, it passes through a filter. The filter and magnifier characteristics are listed in Table 5.3. The fourth and fifth columns list the 50 % encircled energy radius calculated from data obtained during instrument ground calibration for channels A and B respectively. The responses of the filters are shown in Figure 5.4. The magnifier offers a 4× increase in the image scale increasing the f-ratio to f/54 in the blue. On the other hand, the grisms provide a low spectral resolution.

5.2.2 The UVOT Detectors

A typical Swift UVOT detector assembly is shown in Figure 5.5. Incoming photons from the beam steering mirrors (through a filter) enter the detector's window and strike the photocathode where electrons are discharged and driven onto micro-channel plates (MCPs) by a bias voltage, which are then amplified into an electron cloud. This cloud strikes the phosphor screen, creating

Table 5.3: Characteristics of the UVOT lenticular colour filters, magnifier, and white-light filter (Taken from Roming et al. 2005).

Filter	λ_c (nm)	FWHM (nm)	EE_{A-ch} (arsec)	EE_{B-ch} (arsec)
V	544	75.0	0.62	0.59
B	439	98.0	0.66	0.70
U	345	87.5	0.64	0.76
UVW1	251	70.0	0.80	0.83
UVM2	217	51	0.82	0.88
UVW2	188	76.0	0.87	0.88
WHITE	385	260.0	0.53	0.56

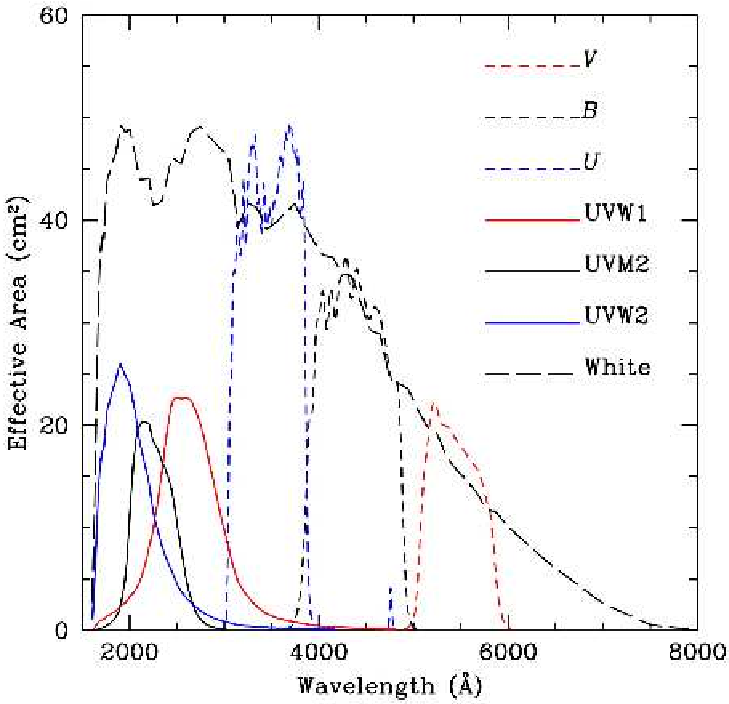

Figure 5.4: Effective area curves for the broadband UVOT filters; square centimetres versus Angstroms (http://heasarc.nasa.gov/docs/swift/about_swift/uvot_desc.html).

photons which are directed to, and registered by the CCD. The combination of the MCPs and the CCD provide an amplification of $\sim 10^6$ of the original signal. In order to protect the UVOT detector from damage due to bright sources and charged particles, high voltages are turned down, and no observations are carried out during slew or South Atlantic Anomaly (SAA) passages.

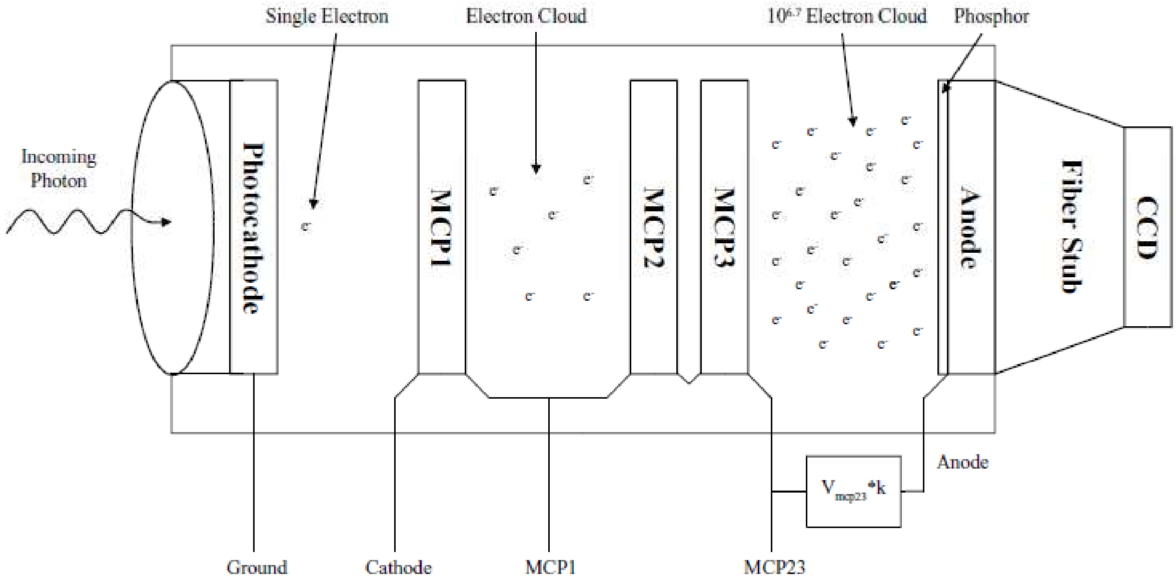

Figure 5.5: Swift UVOT Detector Assembly (Taken from Roming et al. 2005).

5.2.3 The UVOT Data Modes

The basic modes of UVOT data are the image and event data modes respectively (e.g. Immler et al. 2008). The event mode provides both the positional and time information for each of the recorded events. The image mode, on the other hand, does not provide the arrival time for the individual events, but a two-dimensional sky map with a start and stop time for the exposure.

The Swift public data can be downloaded from the HEASARC, and the UVOT data modes may populate the archive in three different levels. Typical representations of the data modes and levels are shown in Table 5.4.

Level I: This contains the raw data. Both the image and the event data are stored in raw detector coordinates.

Level II: This contains reduced data, i.e. when the UVOT reduction pipeline has been performed on the image and event tables. Images are stored in sky coordinates, and the event data have been screened for standard bad times, such as an SAA passage. Most scientists will perform their analysis from this level, unless there has been great improvements in the instrument calibration.

Table 5.4: Selected UVOT files. The characters in square brackets stand for the level of the data (Taken from Immler et al. 2008).

Filename	Description
Directory: uvot/image	
sw00000001001uuu_rw.img	U images in raw units (pixels) [I]
sw00000001001uuu_sk.img	U images in sky units (RA, Dec) [II]
sw00000001001uuu_ex.img	U images exposure maps [II]
Directory: uvot/event	
sw00000001001uvvpo_uf.evt	Unscreened V filter event tables [I]
sw00000001001uvvpo_cl.evt	Screened V filter event tables [II]
Directory: uvot/product	
sw00000001001u_sk.img	Co-added sky images (all filters) [III]
sw00000001001u_ex.img	Co-added exposure maps [III]
Directory: uvot/auxil	
sw00000001001sat.fits	Attitude history file [I]
sw00000001001sao.fits	Orbit and attitude filter data [I]

Level III: This contains quick-and-dirty representations of the high level products such as time-averaged images, light curves, and spectra. They are not meant for publication but can be used as a guide during analysis.

5.3 The Swift X-Ray Telescope (XRT)

5.3.1 Basic Structure and Characteristics

The Swift XRT (e.g. Burrows et al. 2005) is a sensitive, flexible and autonomous X-ray imaging spectrometer designed to measure fluxes, spectra and light curves of GRBs and their afterglows over a wide range covering more than 7 orders of magnitude in flux. The XRT begins observing a GRB in approximately 100 s after the trigger, and usually follows it for several days, and

Table 5.5: X-ray Telescope characteristics (Adapted from Burrows et al. 2005; Capalbi et al. 2005).

Telescope	Wolter I (3.5 m focal length)
Detector	E2V CCD-22
Pixel size	40 μm $\times$ 40 μm
Pixel scale	2.36 arcseconds/pixel
FoV	23.6 $\times$ 23.6 arcminutes
PSF	18 arcseconds HPD at 1.5 keV
	22 arcseconds HPD at 8.1 keV
Energy range	0.2 - 10 keV
Energy resolution	140 eV at 5.9 keV (at launch)
Position accuracy	3 arcseconds
Effective area	135 cm^2 at 1.5 keV
	20 cm^2 at 8.1 keV
Sensitivity	2×10^{-14} erg cm^{-2} s^{-1} in 10^4 s

occasionally for months (e.g. Evans et al. 2007). It uses a grazing incidence Wolter I telescope to focus X-rays onto a CCD detector, which is thermoelectrically cooled (e.g. Burrows et al. 2005; Capalbi et al. 2005; Gehrels et al. 2004). The main characteristics of the Swift XRT are listed in Table 5.5.

The design and block structures of the XRT are shown in Figures 5.6 and 5.7 respectively. It is mounted on an aluminium Optical Bench Interface Flange (OBIF), from which stretch a forward telescope tube (that supports the star trackers and the XRT Door Module) and an aft (that supports the Focal Plane Mirror Assembly). The OBIF also supports the mirror module, the electron deflector, and the Telescope Alignment Monitor (TAM) optics and the camera. The detailed description of each of the components mentioned above are found in the original publication by Burrows et al. (2005). The total mass of the Swift XRT is $\sim$ 198.1 kg.

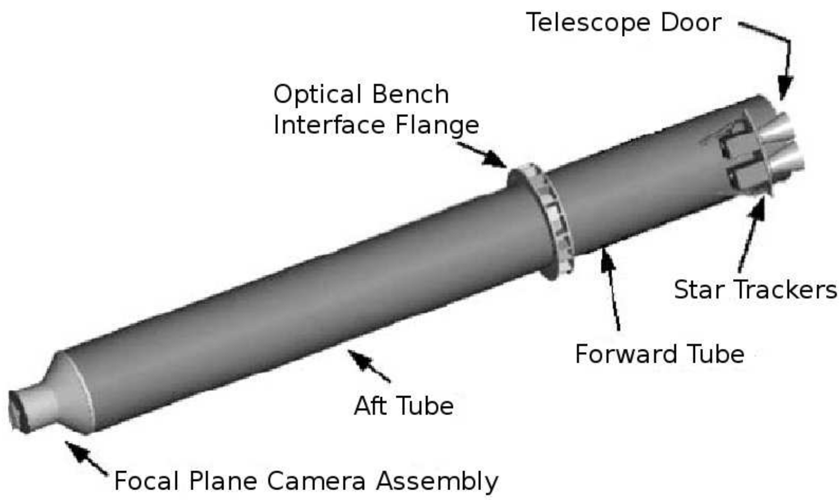

Figure 5.6: Design of the Swift XRT. Overall, it is 4.67 m long (Taken from Burrows et al. 2005).

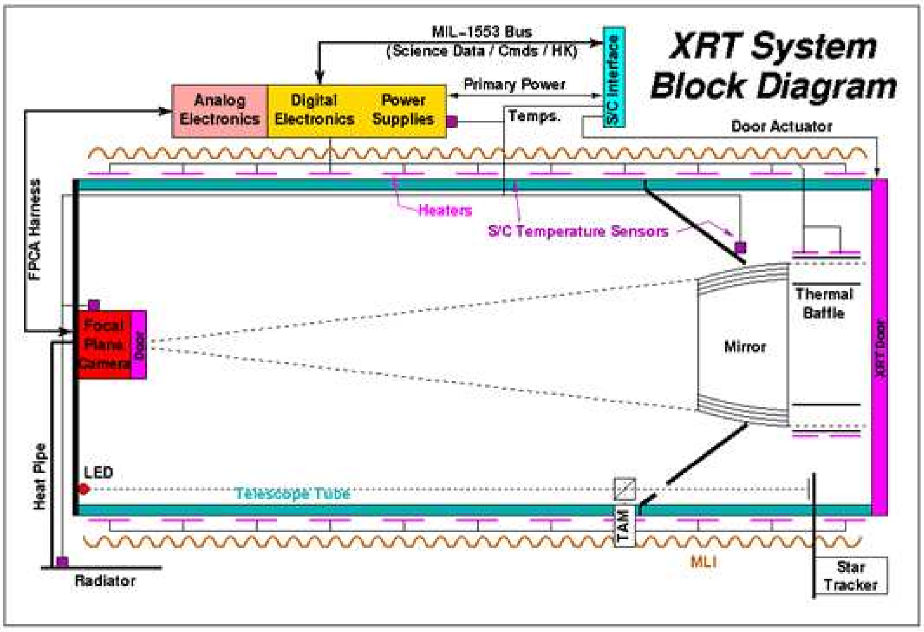

Figure 5.7: Block Diagram of Swift XRT (From www.swift.psu.edu/xrt/techDescription.html).

5.3.2 X-Ray Telescope Modes

There are two basic operational states of the XRT, the Auto and Manual states (e.g. Capalbi et al. 2005). In the Auto state, the readout mode is selected automatically according to the source count rate. The Manual state is used for calibration purposes, thus for a given observation, the science mode can be commanded. The XRT is designed for an autonomous operation, switching between the different readout modes, depending on the source intensity (e.g. Hill et al. 2004;

Evans et al. 2007). In the next paragraph, a brief description of each of these modes will be presented. However, the reader may refer to Burrows et al. (2005) and Capalbi et al. (2005), for a full review.

The XRT can operate in the following four modes:

Photodiode (PD) mode: Designed for very bright sources and high time resolution. It alternately clocks the parallel and serial clocks pixel by pixel, resulting in a very rapid clocking of each pixel across any given point on a CCD. Charge is accumulated in the serial register during each parallel transfer, with the result that each digitized pixel contains charge integrated from the entire field of view (although not simultaneously). This mode does not have spatial information but does produce a high time resolution light curve and spectrum. Data can be telemetered in either the Low rate (LR) mode, where only pixels above the lower level discriminator threshold are sent down, or the Piled-up (PU) mode, where all pixels in the pseudo-frame are sent down resulting in a more efficient telemetry format.

Image (IM) mode: Used by the XRT to obtain rapid position of a new GRB, i.e. if the spacecraft slews to a new source, the XRT captures an image and processes it on-board to determine the position of the burst. The CCD is operated like an optical CCD, collecting the accumulated charge on the detector and reading it out without any X-ray event recognition. Typically, the image will be highly piled-up and produces no spectroscopic data, but it can be used to derive accurate position and good flux estimate. Only pixels exceeding the lower discriminator are sent down or telemetered.

Windowed Timing (WT) mode: This mode uses a 200 column window covering the central 8 arcmin of the field of view, i.e. it is obtained by binning 10 rows in a serial register (or compressing 10 rows into a single row), then reading out only the central 200 columns of the CCD. It preserves one dimensional imaging information. Data in this mode are bias-subtracted on-board, and only pixels above the lower level discriminator threshold are telemetered. Since the setting only takes care of the central 200 columns, the calibration sources are not included; the event reconstruction is performed on the ground.

Photon Counting (PC) mode: This is the mode that retains full imaging and spectroscopic

Table 5.6: Characteristics of the XRT readout modes (Taken from Capalbi et al. 2005).

Mode	Image capability	Spectral capability	Time resolution	Cal sources in FOV	On-board Event reconstruction
PD (PU, LR)	no	yes	0.14 ms	yes	no, on ground
WT	1D	yes	1.7 ms	no	no, on ground
PC	2D	yes	2.5 s	-	yes
IM	2D	no	0.1 s (short) 2.5 s (long)	yes	not applicable

resolution, but timing resolution is limited to 2.5 s. A full FoV is accumulated every 2.5 s and the CCD operates in the frame transfer (normal) mode, in which each CCD frame is rapidly transferred into a frame store area, then read out by clocking the frame store one row at a time into the serial register. The pixels are processed on-board where the bias is subtracted and the events are reconstructed. For each valid event, a 3×3 matrix is telemetered. Calibration sources are included in the data when the window is set to the full FoV, and these are removed on the ground when screening the data. The advantage in this mode is that the background is approximately constant (e.g. Evans et al. 2007).

Table 5.6 gives a summary of the characteristics of the XRT science modes. During observations of an Automatic Target (AT), i.e. a new GRB, the XRT schedules the different science modes automatically, first taking an image in the IM mode to calculate the on-board source position, and afterwards running in sequence the PD, WT and PC modes, switching automatically between these modes depending on the source intensity. This same sequence is also followed for a PPT, except that the IM mode is not scheduled. At high count rates, the XRT operates in the WT mode, and at low count rates it operates in the PC modes respectively. Initially, the XRT was designed to operate in the PD mode for higher count rates than the WT mode, but the former mode was disabled following a catastrophe when the XRT was hit by a micrometeoroid on May 27, 2005 (e.g. Abbey et al. 2005; Evans et al. 2007).

5.3.3 The XRT Data Files

The XRT data contain the following files: the event files, image files, house keeping (hk) files, and filter files. In this subsection, I give a brief description of each of these files with emphasis to the levels in the event and image files respectively. An attempt is made to illustrate each file with the standard naming convention.

Event and Image Files

These are the essential files from which high level data products can be generated, which are in turn important for scientific analysis. The archived files may be of two or three levels, as described below.

Level 1 and Level 1a Files. There is one Level 1 file for each observation, in each of the readout modes. The level 1 event and image files are produced during standard processing by a task that reformats the telemetry into Flexible Image Transport System (FITS) files (e.g. Capalbi et al. 2005). There is, in addition to the Level 1 file, an intermediate Level 1a file in the PD and WT modes. This file is required in these modes to associate the proper arrival time with the events, and to reconstruct the events (e.g. Capalbi et al. 2005).

Level 2 Files. This level is the product of the standard calibration and screening of the Level 1 and Level 1a files, thus ready for use to extract high level products (e.g. images, spectra, and light curves), depending on the science goals. In the image mode, the level 2 image files are calibrated and the sky coordinates included in the header.

Conventionally, the event and image files are named as below:

"sw[obsid]x[mm][ww][pp]_[lev].[ext]",

where:

- **sw** denotes the swift mission.
- The [**obsid**] contains an 11 digit number to identify the observation.
- **x** is the instrument (XRT) identity.

Table 5.7: Window settings of the XRT CCD in PC and WT modes (Taken from Capalbi et al. 2005).

wN	Photon Counting	Windowed Timing
w1	490 × 490 pixel	100 columns
w2	500 × 500 pixel	200 columns
w3	600 × 600 pixel	300 columns
w4	480 × 480 pixel	400 columns
w5	-	500 columns

-[mm] a two letter string that identifies the XRT operation mode, e.g., pc and wt for Photon Counting and Windowed Timing modes respectively.

- [ww]. This either identifies the window setting of the CCD in the PC and WT modes, or it identifies whether the bias has been subtracted on-board (or not) in the PD mode. Examples of the window settings for PC and WT modes are given in Table 5.7.

- [pp] identifies whether data were taken with the XRT in pointing mode (*po*), or during slew (*sl*), or during a settling phase (*sd*).

- [lev] is a two or four letter string that identifies the level of the file. It is *uf* for Level 1, *ufre* for Level 1a, and *cl* for Level 2 respectively.

- [ext] is the file extension, which can be set to *evt* for the event files, or *img* for the image files.

Other Relevant Files

Housekeeping Files. These files contain information stored in the header and trailer of the science packet data, and the engineering values. The conventional naming of the housekeeping files is denoted by:

"sw[obsid]x[hh].hk",

where **[hh]** is set to *hd*, or *tr*, or *en* for the header, trailer, and engineering respectively. Of these, the header file is used in the XRT data reduction software.

The Filter File. This file is also called mkf file, and generated on ground by the task *makefilter*.

It contains a subset of housekeeping, orbit and attitude information, which are useful during screening of data. For example, an mkf file containing the attitude is denoted by:

"sw[obsid]sat.fits".

The file that contains the orbit ephemeris information, required to correct for the photons' arrival time, is conventionally of the form:

"sw[obsid]sao.fits".

5.3.4 XRT Data Products' Generation

The observing schedule of the Swift satellite is planned on a daily basis, and each day's observation of a given target has a particular Observation Identification (ObsID) and event list (e.g. Evans et al. 2007). Swift is unable to observe most targets continuously since it is a low-Earth orbit observatory ($\sim$ 600 km). In this case, any given ObsID may be made up of multiple target visits (or snapshots). The standard pipeline processing of Swift data ensures that the sky coordinates for each event are correct.

A web-based facility has been developed by the Swift team which allows for the creation of X-ray light curves, spectra and enhanced positions of any object observed by the Swift XRT. The detail surrounding the production of these products have been discussed by Evans et al. (2007, 2009). The raw Swift XRT data are processed at the Swift Science Data Center at NASA's Goddard Space Flight Center (GSFC) using standard Swift software. Before any of these products are created, the data for recent bursts are first reprocessed using the latest release of the xrtpipeline tool. In the next subsection, I present a summary of the products' generation procedures for the light curves and spectra. For more detail, one can refer to Evans et al. (2007, 2009).

For Automatic Targets (ATs), i.e. the GRBs for which Swift was launced, the light curves, spectra, and enhanced positions are created automatically. These targets also trigger the BAT automatically. However, for Targets of Opportunities (ToOs) or Pre-Planned Targets (PPTs), which include all non-GRBs' sources, the products can only be created by manually registering the information of the desired source (s). Either way, the same criteria are followed to create these products, which are given below for the light curves and spectra respectively. Also, the descriptions presented below are mainly for PC mode data, since only the data obtained in this mode were relevant to the study of AE Aqr.

Spectra

To create a spectrum for a source, each of the observations is sub-divided into snapshots. A search is quickly made for the times where the count rate (within a radius of 30 pixels centred on the source) exceeds 0.6 counts s^{-1}. This may indicate a pile-up of source photons. Pile-up occurs when two photons are incident upon the same or adjacent CCD pixels, and are registered as a single event during read-out. To check for this, a Point Spread Function (PSF) profile of the source is obtained and compared with the calibrated Swift PSF (e.g. Moretti et al. 2005). More description of the pile-up search will be presented when discussing the light curve generation procedures. If the source is not piled-up, a circular extraction region is used to extract the source data, otherwise an annular extraction region with an inner radius $r_{\rm p}$ is used, where $r_{\rm p}$ is the radius out to which pile-up is a factor.

Once the data have been divided into time intervals, each with a source extraction region whose radius was chosen such as to maximize the signal-to-noise ratio, a source spectrum for each time interval is generated. In addition, a source event list, as well as a full frame event list are also created. An exposure map is created from the full frame event list, which in turn, is used in combination with the source spectrum to create an Ancillary Response File (ARF). The source event lists are combined to give a single source spectrum. Similarly, the ARFs are combined to give a single ARF. Note that the ARF contains a correction factor (Q) that harmonizes the measured counts ($C_{\rm m}$) with the true number of counts ($C_{\rm t}$) from the source. For example, for multiple snapshots of observations (e.g. Evans et al. 2009),

$$C_{\rm t} = \sum C_{\rm m} \times \frac{\sum (C_{\rm m} Q)}{\sum C_{\rm m}}. \tag{5.1}$$

Also for each observation, a background spectrum is generated from an annulus of inner radius of ~ 60 pixels and outer radius of ~ 120 pixels, centred on the source. Also, the background spectra for the individual observations are combined to give a single background spectrum.

The combined source and background spectra, and also the ARF created above are then used to plot the spectrum of the source in xspec. However, to enable spectral fitting, an additional file, the Response Matrix File (RMF) is needed. This can be obtained from the calibration database (CALDB; http://swift.gsfc.nasa.gov/docs/heasarc/caldb/swift/). The web-based software automatically models the spectra with an absorbed power law. The results are posted online in postscript and gif formats, together with a tar archive for download. The tar file contains the source and background spectral files, and the ARF file for the users to plot the data and fit their desired models.

Light curves

There are three phases involved in the creation of light curves, i.e. the preparation phase, the production phase, and the presentation phase respectively. The products of the preparation phase provide the input to the production phase, and the products of the latter phase are used in the presentation phase, which is the final stage where the desired light curves are produced. Important detail of the first two phases are discussed below.

I. *The Preparation phase*:
As the name suggests, this phase gathers together all the observations of a target, defines appropriate source and background regions, and creates summed source and background event lists respectively. As the first steps, a list of ObsIDs is created; the position, trigger time, and name of the source is found from the metadata file. From here, an image is created from the first PC mode event list and a more accurate source position is obtained. Then centred on this position, a source region (circular) and background region (annular) are defined in almost the same way as done for the spectra generation.

Each event list is taken in turn and sub-divided into snapshots, each with a mean count rate that is used to determine the source dimension. From uniform time bins, times with counts above 0.6 counts s^{-1} are investigated for pile-up. Technically, a PSF profile is found for such times, and the wing (from $\sim 25''$ outwards) is fitted with a King function, which is of the form:

$$K(r) = S_0 \left(1 + (r/r_{\rm p})^{-2}\right)^{-\alpha}, \tag{5.2}$$

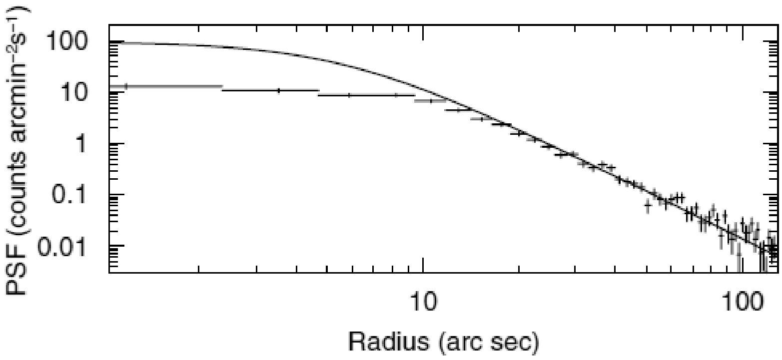

Figure 5.8: The PSF of GRB 061121 showing pile-up from within the central $10''$ radius of the source (Taken from Evans et al. 2007).

where S_0 is a normalization constant, α (always > 1) is an index (or exponent), and $r_{\rm p}$ is a characteristic radius (as defined for spectra above). The fit is extrapolated to the core of the PSF to determine the extent to which the model exceeds the data. If it is by more than the 1-σ error on the data, the source is said to be piled-up, as illustrated in Figure 5.8. Then, the source region is replaced with an annular region. The inner region of the annulus is chosen such that the model PSF and the data agree to within 1-σ of the data.

In the final steps of the preparation phase, the region files are used to create the source and background events for a given snapshot, and thus for every snapshot in an observation. The event lists are then merged to form one source event list and the corresponding background event list for the observation. And then, the source and background event lists for the individual observations are combined.

II. *The Production phase*

This phase involves the screening of the products of phase I. Only events in the energy range 0.3-10 keV, and having grades from 0 to 12 are accepted. This process occurs three times in parallel: once on the entire data set, once binning only the soft photons (0.3-1.5 keV), and then only the hard photons (1.5-10 keV). In each case, the data are binned and background subtracted. In the process, the count rates are corrected for losses due to pile-up, dead times, and source photons falling outside the source extraction region.

The final steps in this phase involves writing the data to ASCII files. Information saved for each bin include, among others:

(1) time in seconds (with error), and the bin time is defined in terms of photon arrival time. The BAT trigger time corresponds to the origin, t=0 s.

(2) the corrected and background subtracted source count rate in counts s^{-1} (with error). The detection significance (σ), which is also among the information saved, is calculated before any corrections are performed. The quantity σ is a measure of the likelihood that the measured (and not the corrected) counts were caused by a fluctuation in the background level.

The output of the production phase mentioned above is used in the presentation phase where light curves are eventually produced. Like in the case of spectra, these are posted on-line, and the users can also plot the appropriate light curves manually. For more detail on the presentation phase, one can refer to the original paper by Evans et al. (2007).

5.3.5 How to Use the Swift XRT Products' Generator

The on-line products are generated by filling in a form, for which the object detail section is mandatory. In this form, the desired products to be created must also be specified, and each contains an additional form where the detail of the products are filled. When all the detail are correctly entered, the form is then submitted by clicking on the *Build products* button. What follows is a short outline of how each section of the products' generator form is handled, and in particular, paying attention only to light curves and spectra.

Object Detail. The most sensitive aspect in this part of the form is the name of the source. The *Find* button can then use the object name to determine its RA, DEC, ID and start time, all of which could otherwise be entered manually. If the name of the target can be resolved, its coordinates are taken from SIMBAD, but if not, the values from the spacecraft pointing information are reflected. Apart from these aspects, there are two others that can be specified. First, the choice on whether the software should attempt to centroid on the source, for which the *yes* option is normal so as to obtain the best position in the XRT astrometric frame. Secondly, if this previous option is selected, the search radius (in arcminutes) around the RA and DEC must be supplied. The brightest source therein is assumed to be the target of interest. Up to these aspects, one can then proceed to specify the products to be generated.

Light curve Detail. The first field here is the binning method to select, and the possible choices are: bins defined by the elapsed time (the default option), or the number of counts (mainly for GRBs), or whether to produce one bin per snapshot or observation. Then, depending on the binning method, the remaining fields change accordingly. For most applications, and in particular non-GRBs, binning by time is more appropriate. The bin length for the hardness ratio may be made to be the same as that of the main light curve. After a gap in the data (e.g. between snapshots), a new bin begins at the start of the next Good Time Interval (GTI). The software uses Gaussian statistics to calculate the uncertainty after background subtraction. If there are fewer than 15 counts in a bin, this may not be accurate. It is important that the user chooses a bin size that ensures sufficient number of counts.

Spectrum Detail. Three options are presented for the user's selection here: whether every observation is to be used to build the spectrum, or a list of ObsIDs entered (separated by commas), or any ObsID beginning within 12 hours of the first one. The latter case is usually the default option, and the number of hours may be defined according to the user's need. All data within the selected observations are included in building up the spectrum by default. The user may, however, choose to enter up to at least four time ranges, rather than creating a single time-averaged spectrum. A name must be supplied for each time interval specified.

5.4 Observation of AE Aquarii

The Swift GRBs' explorer observed AE Aquarii (target ID = 30295) between August 30 and September 2, 2005 for a total on-source duration of $\sim$ 10.5 ks. Ten (10) observations were scheduled, with ObsIDs 00030295001, 00030295002, $\cdots$, 00030295010. The BAT trigger was at 18:56:01.298 UT on 2005 August 30, and follow-up observations started about 164 s later. Data were archived in September 2005. Standard processing was performed later at the UK Swift Science Data Centre (SDC) in April 2007. I acquired data, available for public use, through

Table 5.8: Observing log of AE Aqr with Swift satellite. Data acquired through HEASARC on-line service.

Observation Identification	Date and time of observation	XRT exposure (seconds)	UVOT exposure (seconds)	BAT exposure (seconds)
00030295001	2005-08-30 18:56:02	3519	3293	3745
00030295002	2005-08-31 00:54:01	0	0	300
00030295003	2005-08-31 01:20:01	14	0	300
00030295004	2005-08-31 18:51:02	12	0	1003
00030295005	2005-08-31 00:56:42	1804	1751	1398
00030295006	2005-08-31 18:53:08	4264	4142	3344
00030295007	2005-08-31 23:45:01	0	0	0
00030295008	2005-09-01 23:59:01	21	0	600
00030295009	2005-09-02 00:02:02	1104	1313	696
00030295010	2005-09-02 01:40:02	62	0	300

HEASARC on-line service, provided by the NASA's GSFC. Table 5.8 contains a summary of the observing log, with each instrument's exposure time shown. For data reduction and analysis, I used the High-Energy Astrophysics Software (heasoft) version 6.11, which I had installed.

5.5 Analysis of Swift UVOT Data

5.5.1 Light curves

My main objective was to obtain the UV fluxes for use in plotting the Spectral Energy Distribution (SED) of AE Aqr. However, the system's brightness and nature of the light curve were also established. I extracted the source counts from the level II image files. I ran the heasoft script (uvotmaghist) that calls all image extensions in a UVOT file, in sequence, then converts source count rates to magnitudes and fluxes. Although the downloaded data already had the level II image files, I first recreated fully calibrated (level II) images from raw (level I) images, assuming that the UVOT calibration may have changed significantly since the pipeline

Table 5.9: UVW1 (λ = 251 nm) magnitudes and count rates, for the ObsIDs 00030295001 & 00030295005.

TIME (s)	Time Err (s)	MAG (mag) (mag)	MAG ERR (mag)	Count Rate (cnts s^{-1})	Rate Err (cnts s^{-1})
ObsID = 00030295001					
5238.3	225.5	12.5	0.050	96.1	8.8
5865.2	227.0	12.1	0.046	138.2	11.9
6496.0	225.5	12.0	0.050	161.1	14.9
11276.6	175.5	12.6	0.051	93.5	8.7
11765.8	177.0	12.1	0.047	145.2	12.6
12258.0	175.5	12.0	0.051	150.3	14.2
17345.9	275.2	11.1	0.140	356.4	9.2
17418.7	252.3	11.2	0.059	338.3	7.4
ObsID = 00030295005					
21755.5	127.3	11.2	0.050	341.3	15.6
23594.6	203.1	11.8	0.048	184.1	8.1
27722.7	252.6	12.0	0.047	150.5	6.5

processing of the archive data. Essentially, quality maps for each level I image were created and used to minimize noise in the image. These were done for individual images of the ObsIDs (0003029001, 00030295005, 00030295006 & 00030295009), then source counts, magnitudes and fluxes were extracted.

Tables 5.9 and 5.10 are extracts of the variation of count rate and magnitude with time for the respective ObsIDs. The corresponding plots are shown in Figures 5.9 and 5.10 respectively. Combining the results from all the ObsIDs, the average UV (λ = 251 nm) magnitude and count rate were found to be approximately 12.1 mag and 157.9 counts s^{-1} (Figures 5.11 and 5.12). The light curves and magnitudes illustrate the highly variable nature of AE Aqr, also characterized by flaring. The time-averaged UV flux obtained is $\sim 1.05 \times 10^{-10}$ erg cm^{-2} s^{-1}. Then the near-UV luminosity translates to $L_{\rm UV,near} \sim 10^{32}$ erg s^{-1} ($D \sim 100$ pc), about an order of magnitude higher than the usual UV luminosity of $L_{\rm UV} \sim 10^{31}$ erg s^{-1} (e.g. Eracleous et al. 1994).

Table 5.10: UVW1 ($\lambda = 251$ nm) magnitudes and count rates, for the ObsIDs 00030295006 & 00030295009.

TIME (s)	Time Err (s)	MAG (mag) (mag)	MAG ERR (mag)	Count Rate (cnts s^{-1})	Rate Err (cnts s^{-1})
ObsID = 00030295006					
96856.0	470.6	13.3	0.047	48.7	2.1
102762.6	559.0	12.3	0.047	120.9	5.2
108585.8	556.2	12.2	0.047	135.2	5.8
112560.3	218.5	12.6	0.053	90.0	4.4
114259.1	445.7	13.0	0.048	60.6	2.6
ObsID = 00030295009					
191403.2	212.4	11.9	0.019	177.2	3.1
195333.0	337.9	12.4	0.048	107.6	4.7
197313.0	337.9	12.4	0.048	104.2	4.6

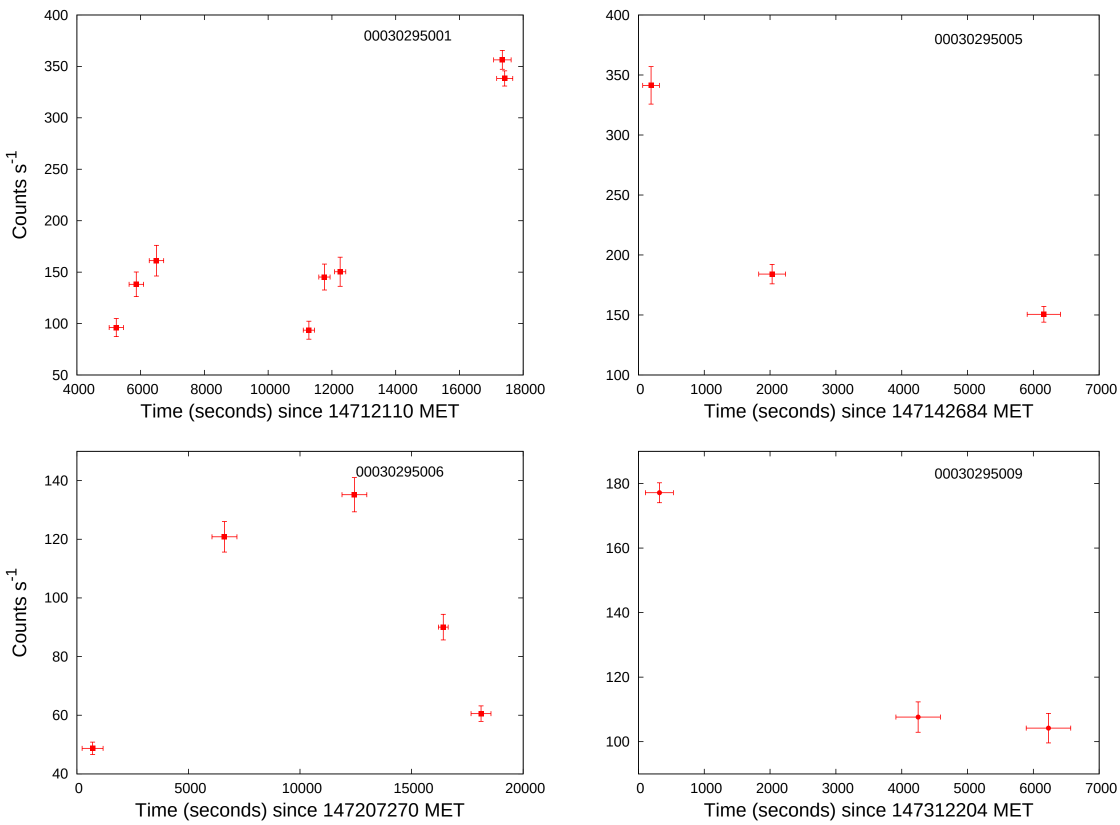

Figure 5.9: UV ($\lambda = 251$ nm) light curves plotted for individual ObsIDs, showing the variability in each case.

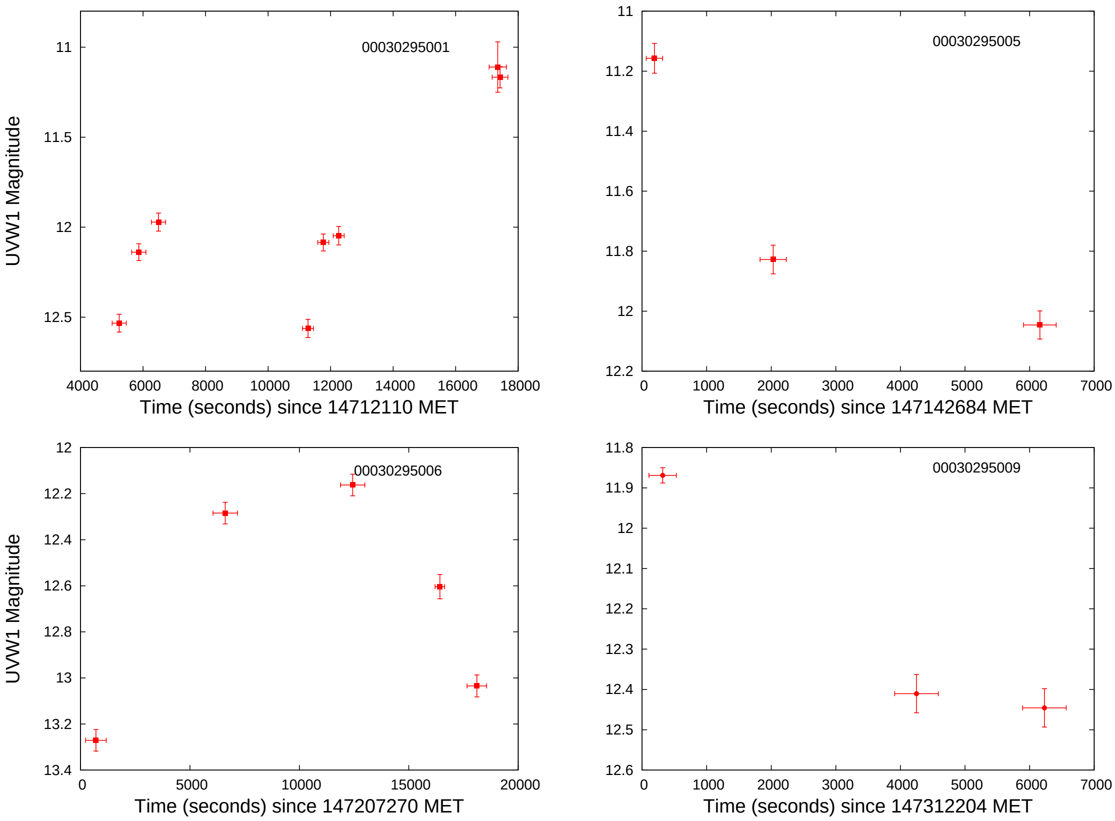

Figure 5.10: UV ($\lambda = 251$ nm) magnitudes plotted for individual ObsIDs, showing the variability in each case.

5.5.2 Pulse Analysis

In this analysis, I used the level I event file, i.e. the unscreened event data. Then, I screened the events using time-tagged quality information both internal and external to the file, by running the *uvotscreen* task with the event file as input file, and the orbit ephemeris file. A level II event data file was then created, with the photon arrival times corrected. From the level II event file, I created a source region file and used it to generate a light curve necessary for pulse timing.

I made an independent search for periodicities with the UVOT data using epoch[4] folding method. See Larsson (1996) for detailed discussion on epoch folding method. The light curve, in this case, was folded with large number of periods where 64 periods were searched with a phase bin of 16 per period, using the default epoch of the light curve of 13613 and the ephemeris of de Jager et al. (1994). I used a period resolution of of 2.98×10^{-5} s which was an oversampling of the default Fourier period resolution. The most probable pulse period, obtained by fitting a gaussian to the

[4]Epoch is the reference point with respect to what the light curve is folded.

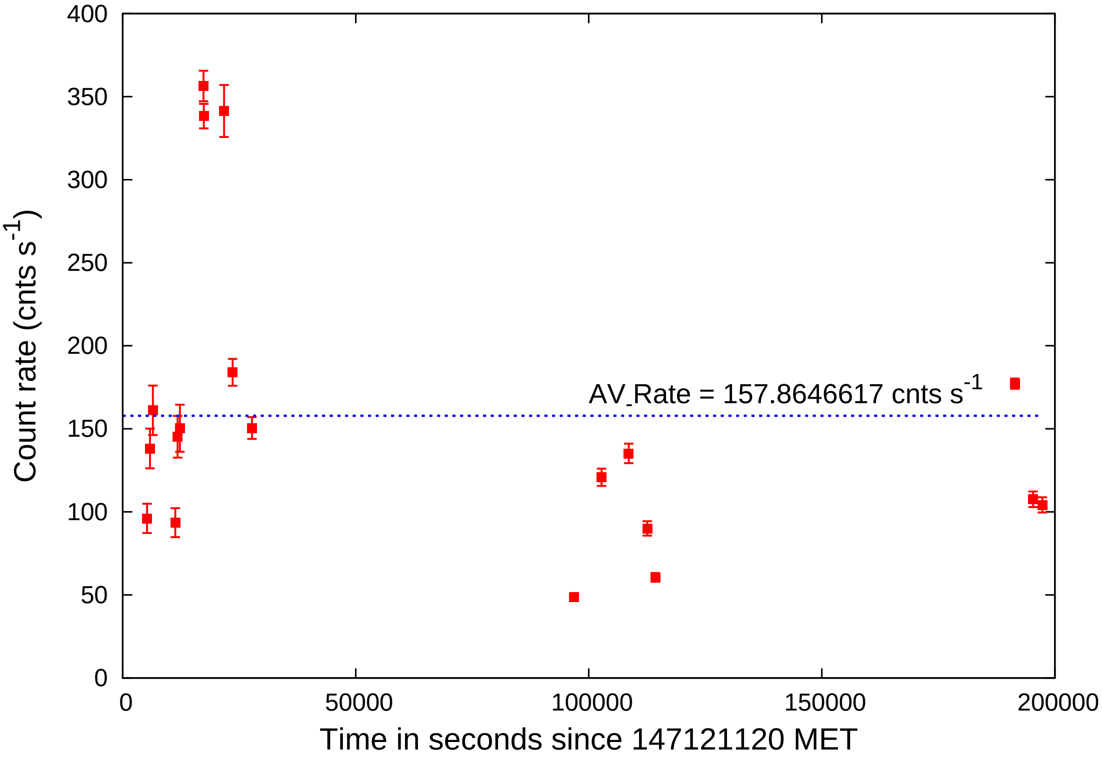

Figure 5.11: UV (λ = 251 nm) light curve for all datasets. The average count rate is $\sim$ 157.9 counts s^{-1}.

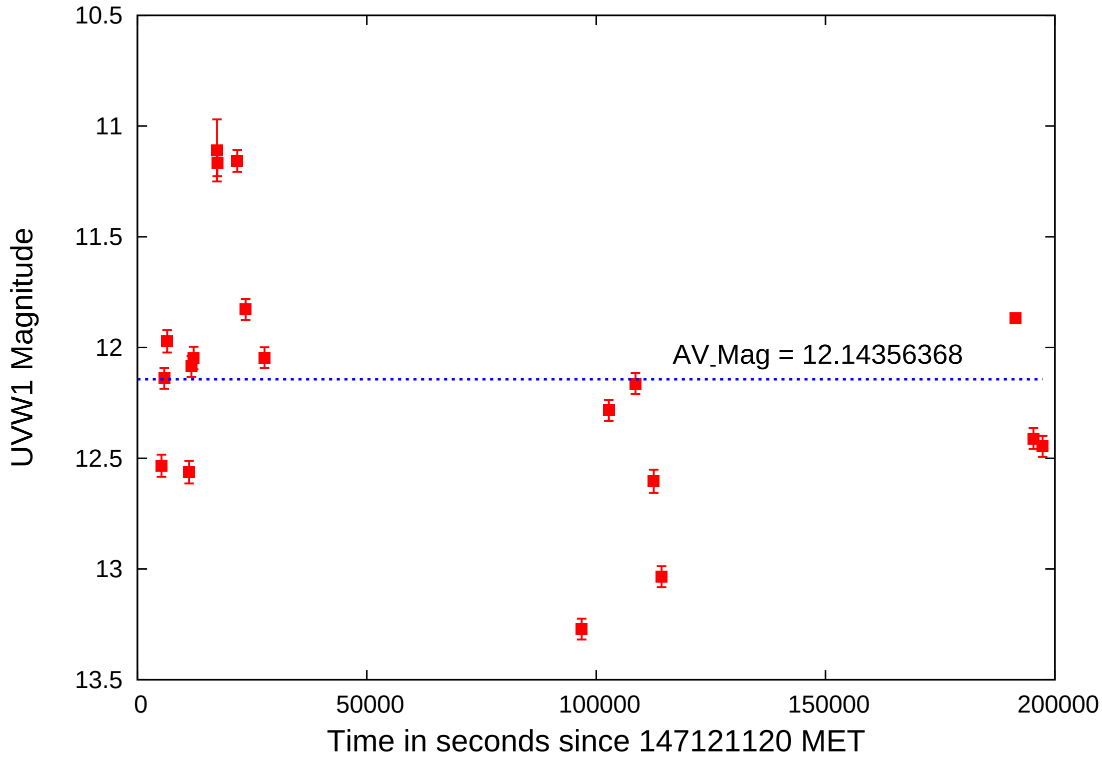

Figure 5.12: UV (λ = 251 nm) magnitude for all datasets. The average magnitude is $\sim$ 12.1.

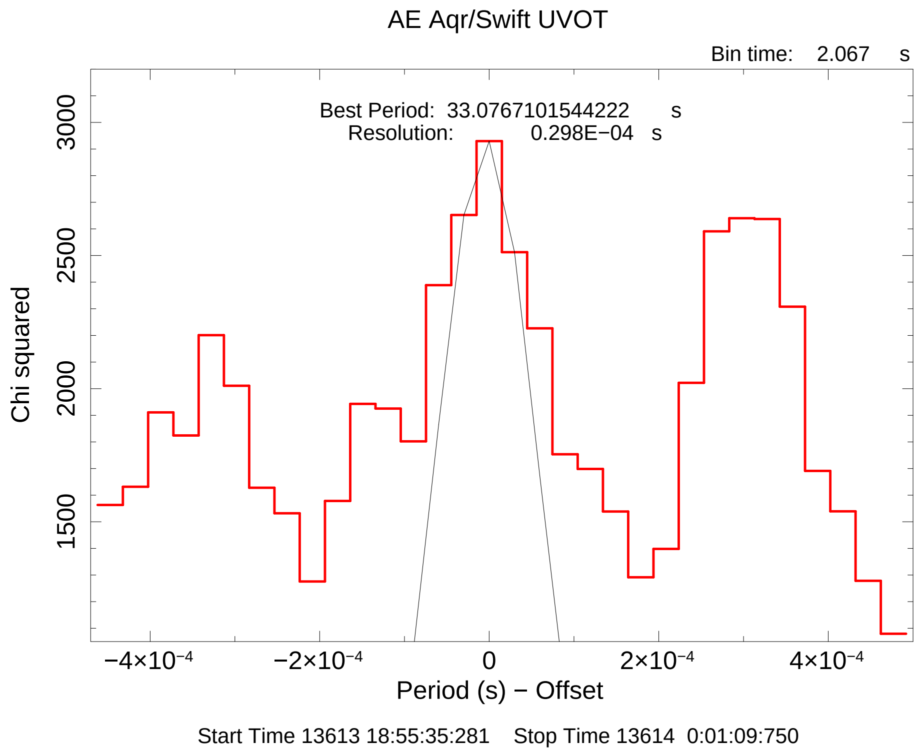

Figure 5.13: UV pulse period determined using a time resolution of 2.98×10^{-5} s is ~ 33.0767 s.

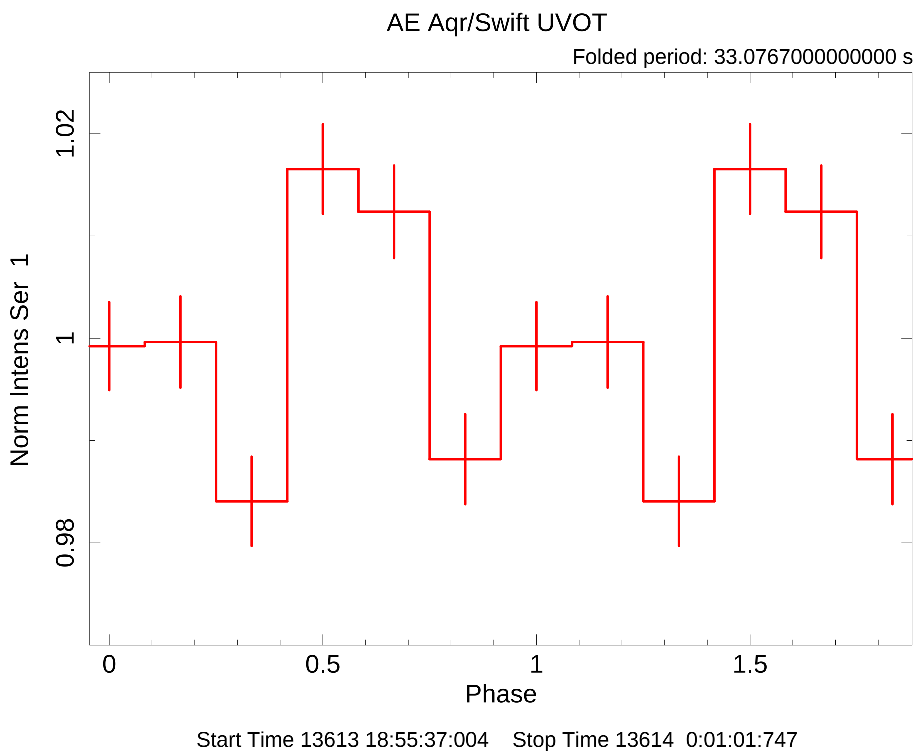

Figure 5.14: UV pulse profile for the 33.0767 s pulse period, using the default epoch of the light curve. The data was folded using the de Jager et al. (1994) ephemeris.

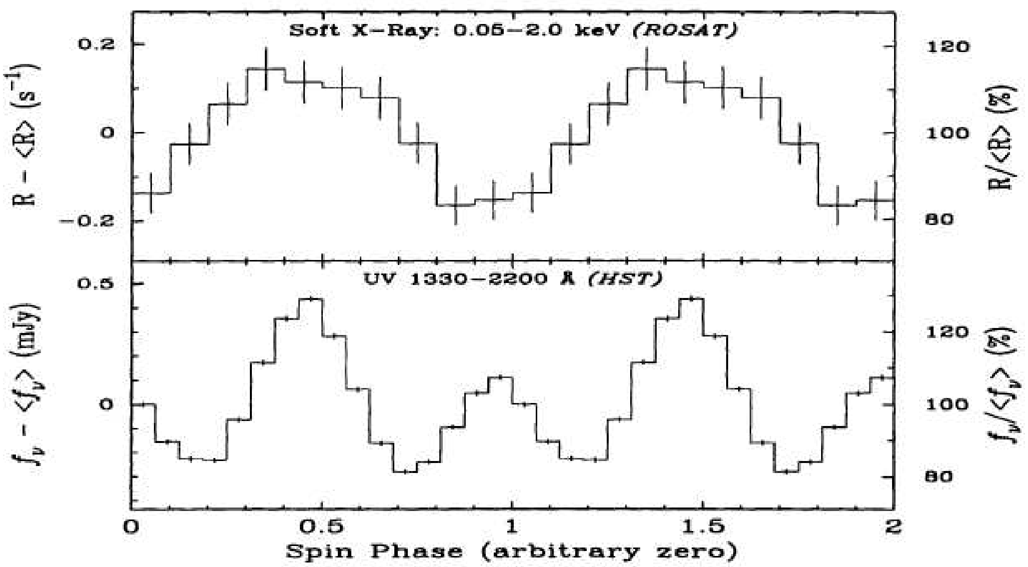

Figure 5.15: A comparison of the 33 s pulse profiles of AE Aqr in the UV and X-ray bands (Taken from Eracleous et al. 1995).

peak of the period-chi squared plot, shown in Figure 5.13, is 33.0767±0.0032 s. Then, using this period I plotted the pulse profile of the UVOT light curve (Figure 5.14). The resultant profile shows two peaks per cycle, which is consistent with ealier studies by Eracleous et al. (1994) and Eracleous et al. (1995), shown in Figure 5.15. The two peaks imply that the UV emission is from the two magnetic poles at the surface, or close to the surface of the white dwarf (e.g. Eracleous et al. 1995; Choi et al. 1999).

5.6 Analysis of Swift XRT Data

The results I shall present here (for both light curves and spectra) are based on data collected when the XRT was operating in the Photon Counting (PC) mode. The descriptions of the XRT science modes were given in §5.3.2, i.e. in the PC mode, full imaging and spectroscopic resolutions are retained, but timing resolution is limited to 2.5 s.

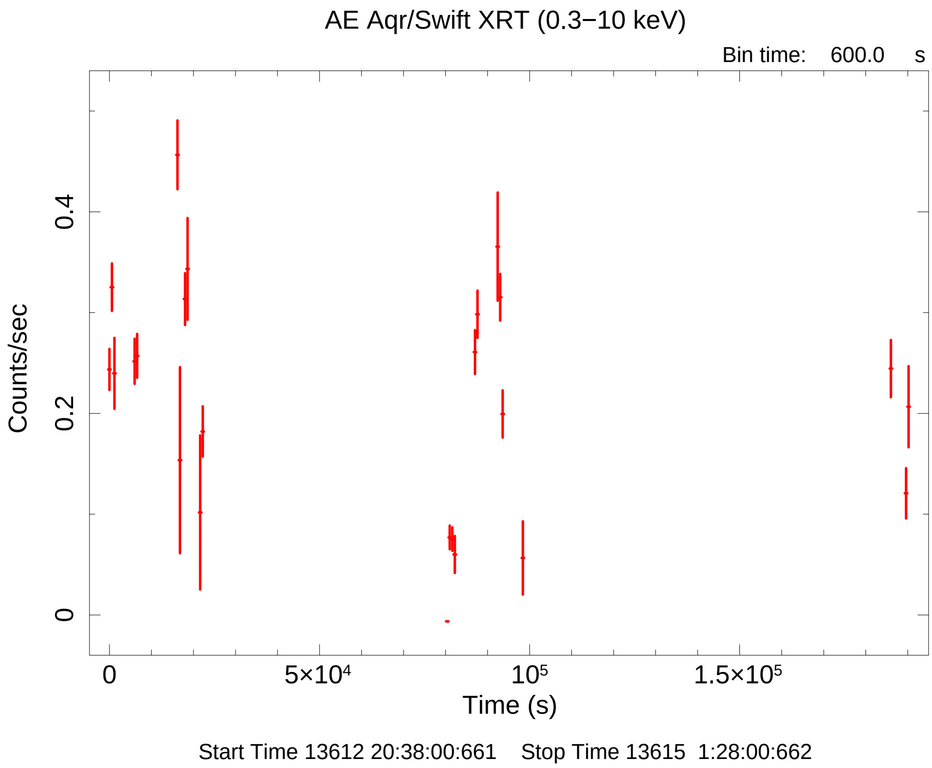

Figure 5.16: Background subtracted light curve from the combined data.

5.6.1 Light curves

To construct light curves, I used the level 2 event file for each of the scheduled observations, processed at the UK SDC. I applied a barycentric correction to each of these files, utilizing the multi-mission barycentric correction tool (barycorr) with the ascii version of the clock file (swco.dat), and the orbit file for the particular observation. Then, a grade filtering (0-12) was applied to the barycentric corrected data. The data from the individual observations were then combined. From each of the observations and the combined data, source and background regions were created in DS9, from which source and background events were generated. Then, energy filtering was applied to the source and background events, and finally binned background subtracted light curves were created.

Figure 5.16 shows the background subtracted light curve for all the observations combined, created with a bin time of 600 s. The light curves and hardness ratio for the default Swift XRT soft X-rays (0.3-1.5 keV) and hard X-rays (1.5-10 keV) are shown in Figure 5.17. Since Swift is a low-Earth orbit satellite, the light curves are interrupted as a result of Earth occultation, hence

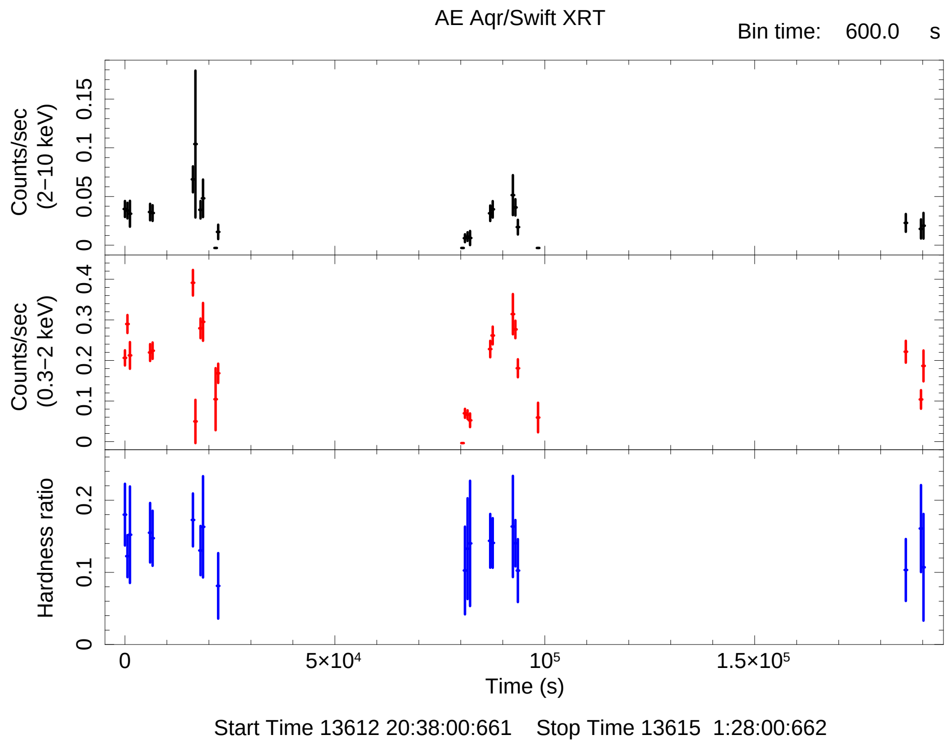

Figure 5.17: Light curves and hardness ratio for the combined data.

continuous observation of a target is not possible, but only snapshot observations. However, the highly variable (flaring) nature of AE Aqr is noticeable, with the soft X-rays dominating the emission since the hardness ration, $HR \ll 1$. The light curves for the individual observations (OBsIDs) are shown in Figures 5.18-5.21 respectively.

5.6.2 Pulse Analysis

I also made another independent search for periodicities with the XRT data using epoch folding method. The light curve, in this case, was folded with large number of periods (64 periods searched with a phase bin of 3 per period) using the ephemeris of de Jager et al. (1994). The default Fourier period resolution (FPR), $P^2/2T \sim 2.87 \times 10^{-3}$ s. Since the Swift data, as a result of the data gaps, does not lend itself to periodic analysis in the same way as the Chandra data, a search was carried out with an oversampling of 10 steps per Independent Fourier Spacing (IFS). The most probable pulse period, obtained by fitting a gaussian to the resulting peak of the period-chi squared plot (shown in Figure 5.22), is 33.0767±0.0030 s. This period is fully consistent with the pulse period obtained utilizing the same technique as the Chandra data, as

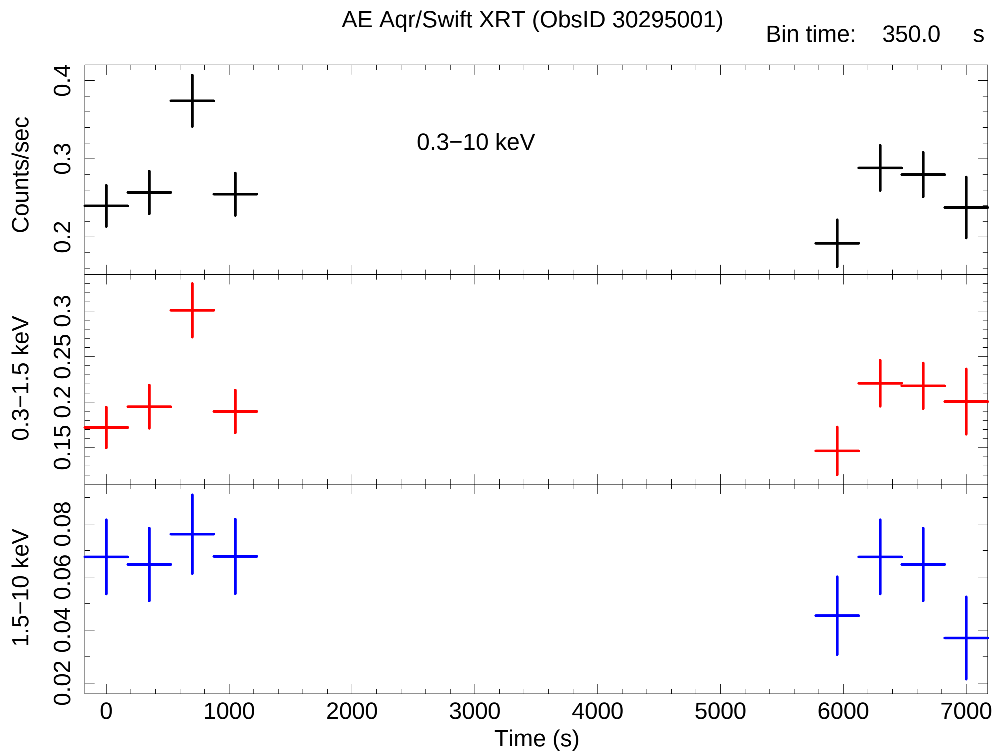

Figure 5.18: Light curves for the ObsID 30295001 with a bin time of 350 s.

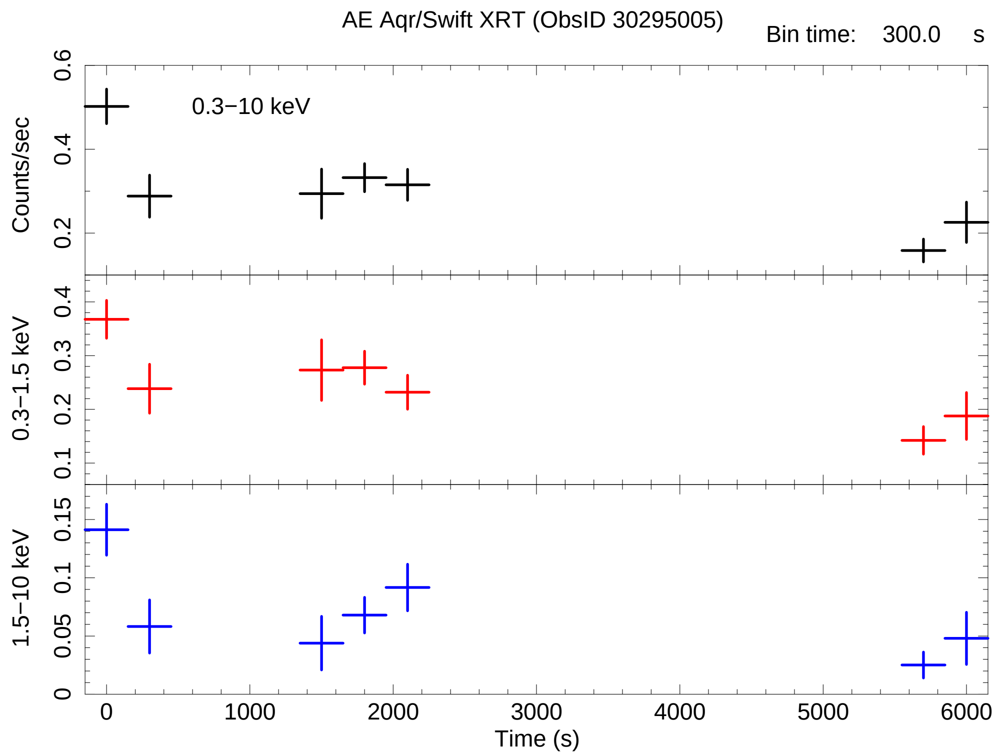

Figure 5.19: Light curves for the ObsID 30295005 with a bin time of 300 s.

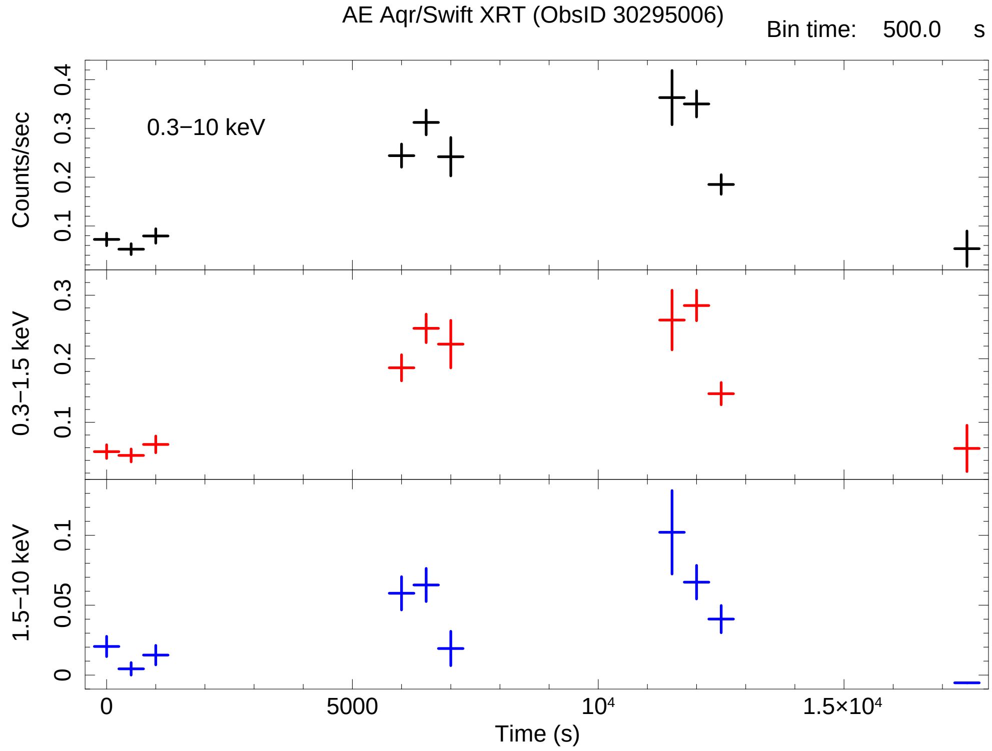

Figure 5.20: Light curves for the ObsID 30295006 with a bin time of 500 s.

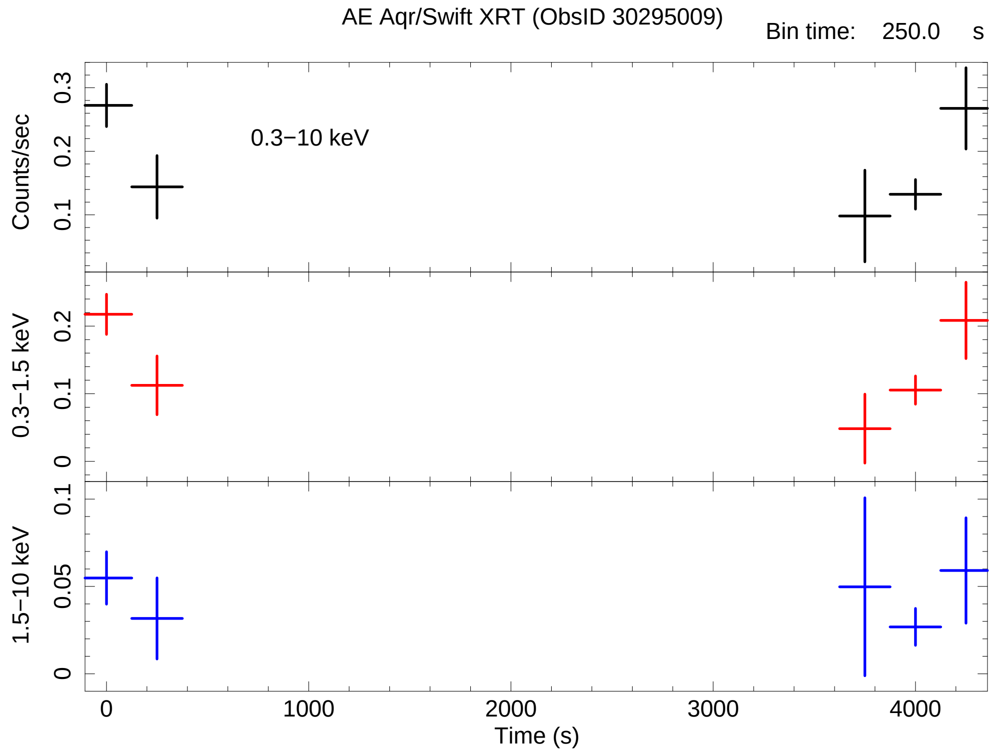

Figure 5.21: Light curves for the ObsID 30295009 with a bin time of 250 s.

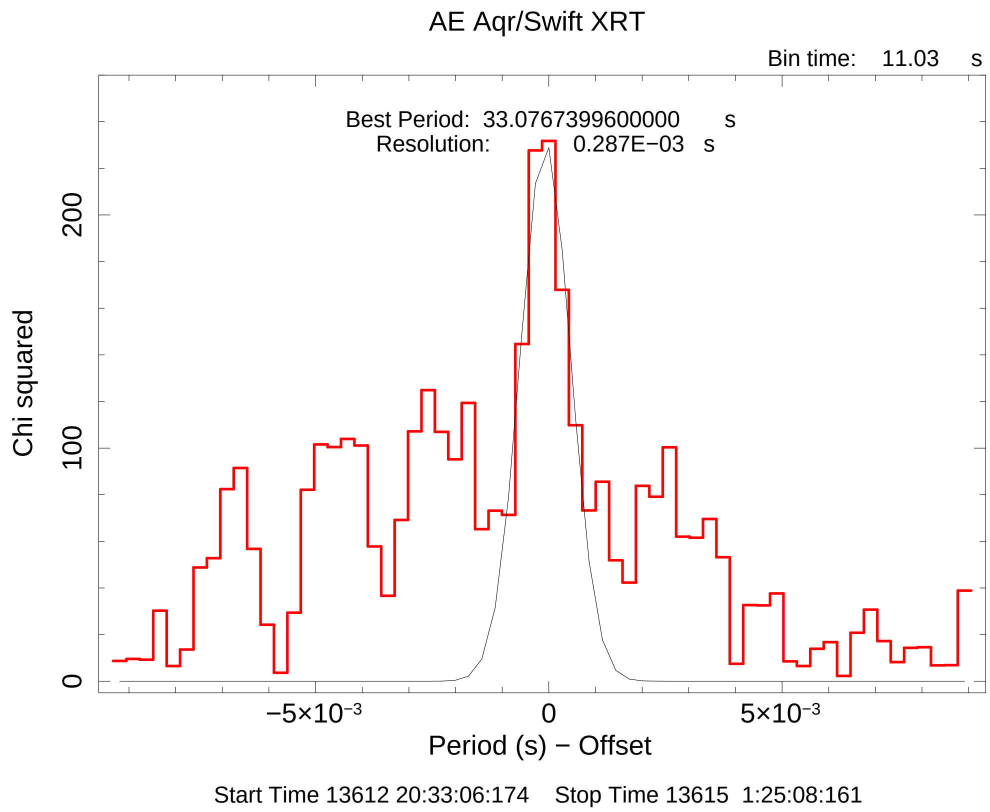

Figure 5.22: Period determined with a time resolution of 2.87×10^{-4} s.

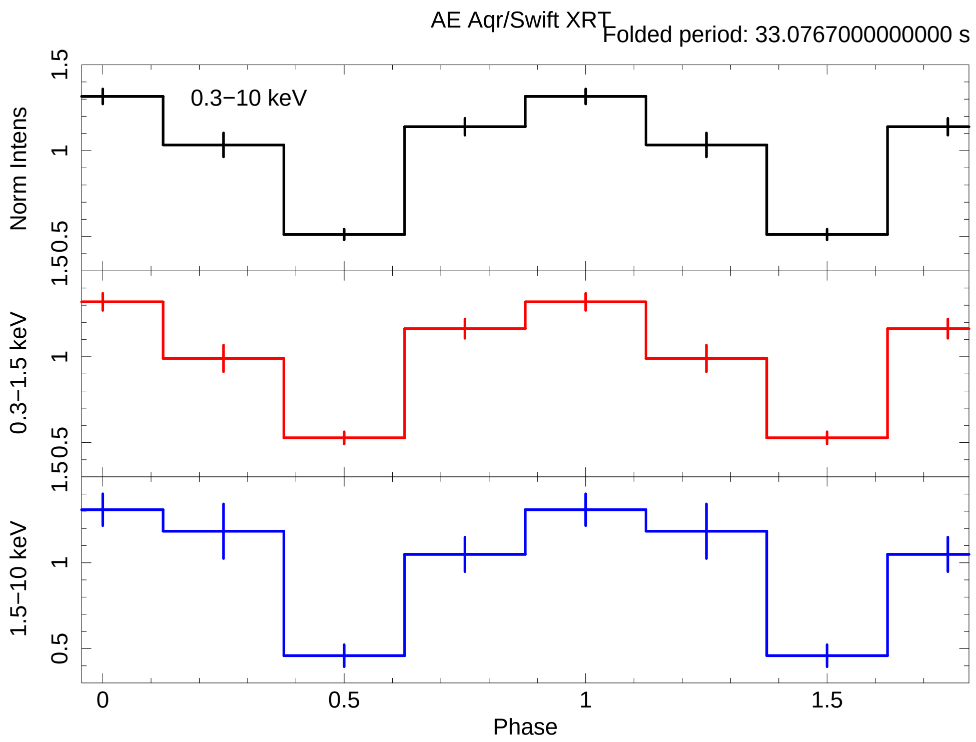

Figure 5.23: Profiles for different energy bands. Phase 0 corresponds to BJD 2453673.5 (Terada et al. 2008).

well as earlier studies by de Jager et al. (1994), Mauche (2006, 2009) and Terada et al. (2008). The aliases noticeable in the figure are introduced by the gaps in the data. Using this period, a pulse profile was determined with the epoch of Terada et al. (2008). The pulse shapes are shown in Figure 5.23, which are also characterized by broad single-peaked sinusoidals. The pulse profile of the X-ray emission, as deduced from the Chandra and Swift XRT data (Figures 4.8 & 5.23), is different from the double-peaked pulse profile of the UV emission (Figure 5.14).

5.6.3 Spectral Analysis

I obtained the spectral data files on-line, using the on-demand software (developed by the Swift team). The detail of how the spectral files are generally created were described in §5.3.4, following from the original paper by Evans et al. (2009). I then read the source and background files into xspec (which is part of the heasoft package), as well as the response matrix files. I used the c-statistic[5] for fitting, where the resulting parameters were obtained with 90 % confidence for which the fit was repeatedly done until the c-statistic had worsened by 2.706 compared with the best fitting value. Figure 5.24 shows the spectrum of data plotted against instrument channel, fitted with a three-temperature vmekal model of temperatures (kT) of $0.4^{+0.07}_{-0.07}$ keV, $0.92^{+0.12}_{-0.10}$ keV and $3.95^{+0.94}_{-0.42}$ keV respectively. Figures 5.25 and 5.26 are the corresponding spectra of data plotted against channel energy, and the unfolded vmekal model plotted with the data. Elemental abundances, relative to the solar photospheric values, were also fixed to those obtained by Itoh et al. (2006), i.e. N = 3.51, O = 0.74, Ne = 0.43, Mg = 0.70, Si = 0.81, S = 0.73, Ar = 0.21, Ca = 0.19, Fe = 0.47, and Ni = 1.27 respectively. The spectra, similar to the Chandra data, are characterized by emission line features (Figure 5.27).

The unabsorbed X-ray flux obtained in the range 0.5-10 keV is $7.98^{+0.29}_{-0.44}\times 10^{-12}$ erg cm^{-2} s^{-1}, which translates to a luminosity of $L_{\rm X} \sim 9\times10^{30}$ erg s^{-1} (estimated source distance is 100 pc; Welsh et al. 1993), consistent with the time-averaged soft X-ray luminosity ($L_{\rm X} \sim 10^{31}$ erg s^{-1}) previously reported (e.g. Itoh et al. 2006), and higher than the hard X-ray luminosity of $L_{\rm X,hard} \leqslant 5 \times 10^{30}$ erg s^{-1} (e.g. Terada et al. 2008).

[5]c-statistic is a measure of how well a model can discriminate between observations at different levels of the outcome, i.e. the discriminative power of the logistic equation (LaValley 2008).

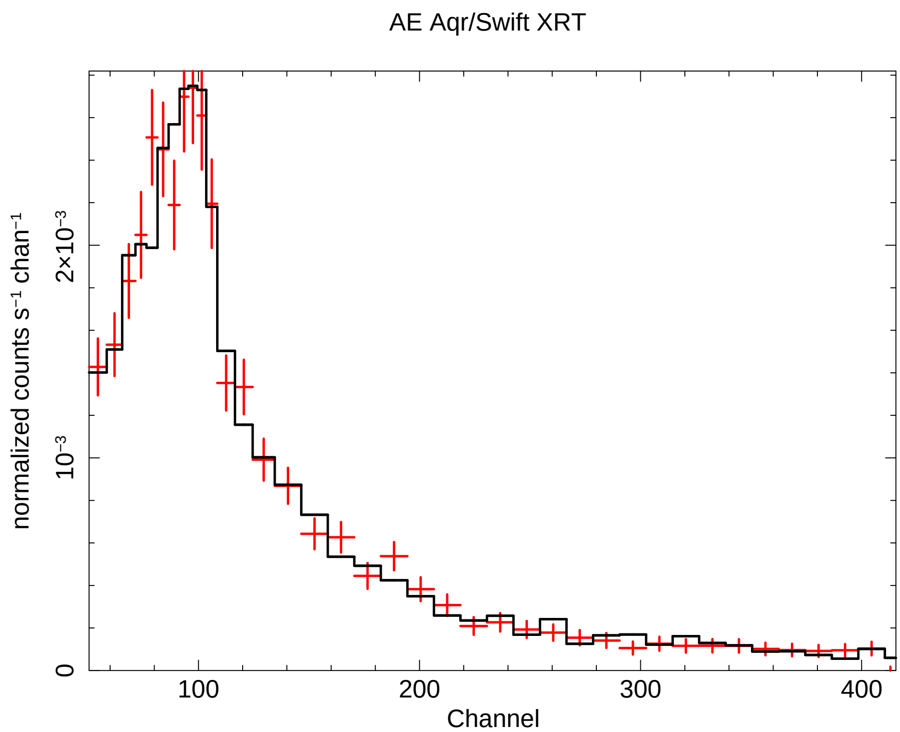

Figure 5.24: Spectrum showing data plotted against instrument channel, fitted with a three-temperature vmekal model.

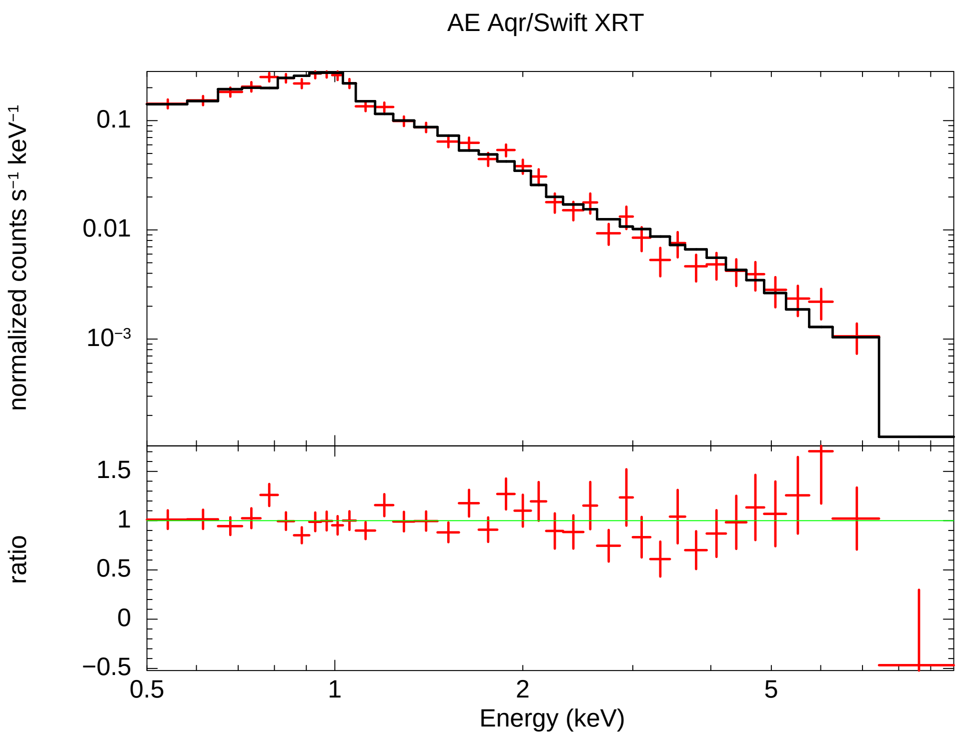

Figure 5.25: Spectrum showing data plotted against channel energy, fitted with a three-temperature vmekal model.

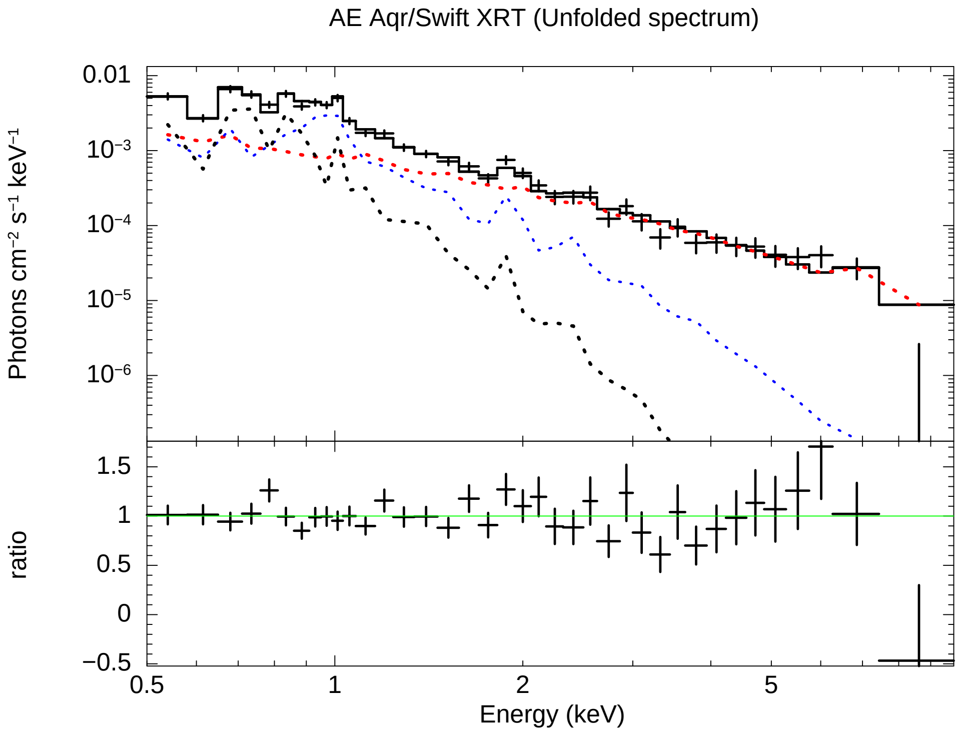

Figure 5.26: Unfolded three-temperature vmekal model plotted with data.

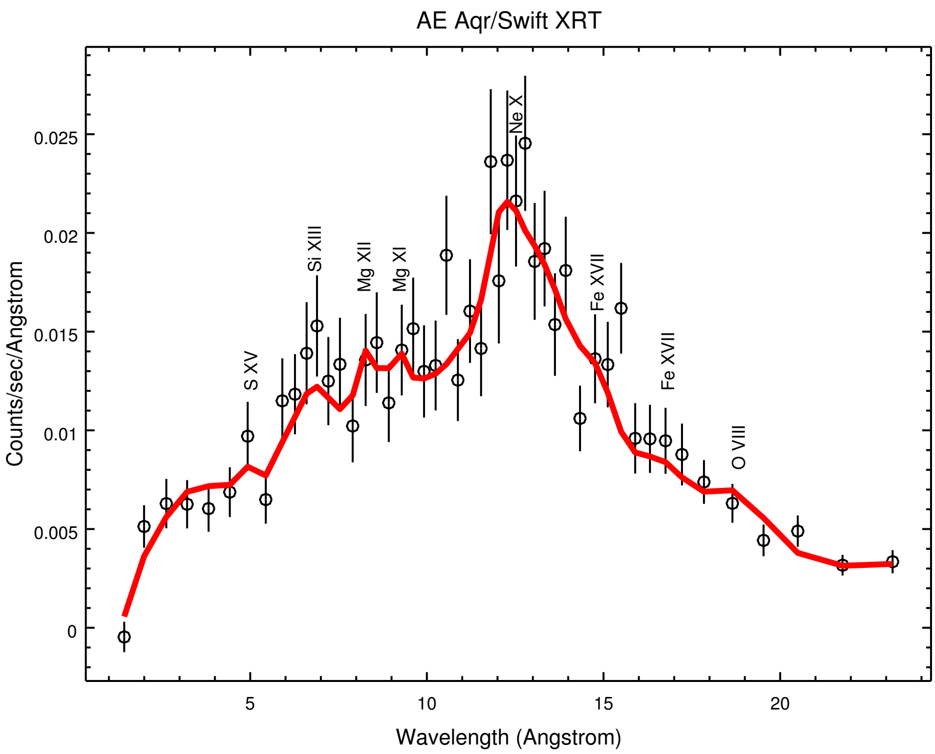

Figure 5.27: Wavelength spectrum, fitted using sherpa (ciao 4.2), with a three-temperature vmekal model.

Chapter 6

Spectral Energy Distribution of AE Aqr: X-ray Models

6.1 Introduction

The broad-band multi-wavelength emission from AE Aqr distinguishes it from other cataclysmic variables and most accretion driven X-ray binaries. This is perhaps the reason why AE Aqr has been studied intensively from radio to TeV γ-rays (e.g. Bastian et al. 1988; Patterson 1979; Meintjes et al. 1992, 1994; Chadwick et al. 1995; Dubus et al. 2004). The Spectral Energy Distribution (SED) of the system is plotted to illustrate the peculiar multi-wavelength emission characteristics of AE Aqr. Since this study focuses mainly on the X-ray characteristics of AE Aqr, I investigate possible emission models in order to constrain the underlying thermal soft X-rays below 10 keV and non-thermal hard X-rays above 10 keV.

6.2 The SED of AE Aqr

Two sets of data were used to plot the SED (or energy spectrum), i.e. catalogue (archive/published) and analysed (Chandra/Swift) data. For the catalogue data, I made extensive use of the Vizier

Table 6.1: Radio data, taken from the 1.4 GHz NRAO VLA Sky Survey (Condon et al. 1998), and Radio emission from stars at 250 GHz (Altenhoff et al. 1994).

Frequency ν (GHz)	Error in ν (GHz)	Flux density S (mJy)	Error in S (mJy)	Flux, F (erg cm^{-2} s^{-1})	Error in F (erg cm^{-2} s^{-1})
1.4	0.75	3.5	0.6	4.9×10^{-17}	8.4×10^{-18}
250	200	24.0	4.0	6.0×10^{-14}	1.0×10^{-14}

Table 6.2: Near IR data, taken from the 2MASS All-Sky Catalog of Point Sources (Skrutskie et al. 2006). The J, H, and K bands have wavelength ranges of 1000-1500, 1500-2000, and 2000-3000 nm respectively.

Band	Frequency ν (Hz)	Error in ν (Hz)	Magnitude $M_{\rm v}$	Error in $M_{\rm v}$	Flux, F (erg cm^{-2} s^{-1})	Error in F (erg cm^{-2} s^{-1})
J	2.40×10^{14}	1.00×10^{14}	9.46	0.02	6.00×10^{-10}	2.64×10^{-11}
H	1.82×10^{14}	5.00×10^{13}	8.92	0.03	4.84×10^{-10}	2.18×10^{-11}
K	1.36×10^{14}	5.00×10^{13}	8.77	0.02	2.61×10^{-10}	1.22×10^{-11}

Table 6.3: Optical data, taken from TASS Mark III Photometric Survey (Richmond et al. 2000). The V, R, and I have wavelength ranges of 500-600, 600-750, and 750-1000 nm respectively.

Band	Frequency ν (Hz)	Error in ν (Hz)	Magnitude $M_{\rm v}$	Error in $M_{\rm v}$	Flux, F (erg cm^{-2} s^{-1})	Error in F (erg cm^{-2} s^{-1})
V	5.45×10^{14}	1.00×10^{14}	11.36	0.11	5.94×10^{-10}	1.23×10^{-10}
R	4.29×10^{14}	1.00×10^{14}	10.74	0.02	6.26×10^{-10}	2.57×10^{-11}
I	3.33×10^{14}	1.00×10^{14}	10.23	0.12	6.06×10^{-10}	1.30×10^{-10}

on-line service to search for data in all wavelengths. These are shown in Tables 6.1-6.4, spanning the radio, near-IR, optical, and X-ray wavelengths respectively. I used the on-line magnitude-to-flux conversion tool to calculate fluxes for the near-IR and optical data. For the X-ray fluxes, I considered the satellites' conversion factors. For example, for ROSAT and EINSTEIN, the conversion factors are 2×10^{-11} erg cm^{-2} count^{-1} (e.g. Chisholm et al. 1999) and 3×10^{-11} erg cm^{-2} count^{-1} (e.g. Burstein et al. 1997) respectively. Figure 6.1 shows the distribution of energy fluxes across the spectrum, for the data shown in Tables 6.1-6.4.

For the analysed data, the near-UV and soft X-ray data were obtained from Swift UVOT and

Table 6.4: X-ray data, taken from ROSAT All-Sky Bright Source Catalogue (Voges et al. 1999) and the 2E Catalogue (Harris et al. 1994) respectively. Errors are shown in the brackets.

Satellite	Frequency ν (Hz)	Energy E (keV)	Count rate (Cnts s^{-1})	Energy flux F ($erg/cm^2/s$)
EINSTEIN	$4.84\ (10.4)\times10^{17}$	2.01(4.31)	$2.24(0.08)\times10^{-1}$	$6.73(0.25)\times10^{-12}$
ROSAT	$2.41(4.60)\times10^{17}$	1.00(1.91)	$6.10(0.82)\times10^{-1}$	$1.22(0.16)\times10^{-11}$

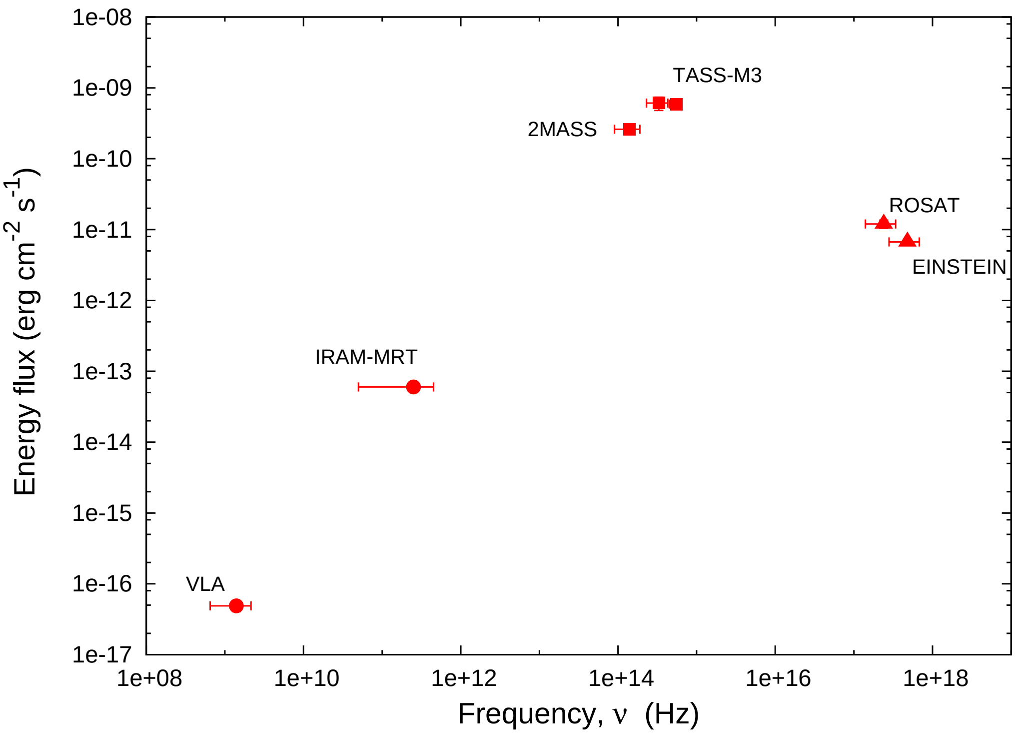

Figure 6.1: The SED of AE Aqr from catalogue data. IRAM-MRT is the 30 m **M**illimeter **R**adio **T**elescope on Pico Veleta, of the **I**nstitute for **R**adio **A**stronomy in the **M**illimeter Range; 2MASS is the **T**wo **M**icron **A**ll **S**ky **S**urvey; and TASS-M3 is **T**he **A**mateur **S**ky **S**urvey-**M**ark **III** Photometric Survey.

Chandra respectively. Chandra data is shown as part of Table 6.5. Since a full energy spectrum of AE Aqr is required, additional data were obtained in other wavelengths from published results/papers. For example, the radio data were taken from Abada-Simon et al. (2005), the IR and optical data were taken from Dubus et al. (2004), the UV data (Table 6.5) were taken from Eracleous et al. (1994) and Froning et al. (2012), and the hard X-ray data (Table 6.6) were taken from Terada et al. (2008). These data were combined with the reported, but yet unconfirmed, VHE γ-ray and TeV γ-ray emission (Chadwick et al. 1995; Meintjes et al. 1992, 1994), shown in Table 6.7.

Table 6.5: UV and X-ray fluxes. The UV data were taken from Eracleous et al. (1994) and Froning et al. (2012). The X-ray fluxes were obtained from the analysis of Chandra data.

UV Data				X-ray Data		
Frequency ν (Hz)	Energy E (eV)	Energy flux (erg cm^{-2} s^{-1})		Frequency ν (Hz)	Energy E (keV)	Energy flux (erg cm^{-2} s^{-1})
1.28×10^{15}	5.29	5.63×10^{-11}		3.63×10^{17}	1.50	3.16×10^{-12}
1.53×10^{15}	6.28	3.33×10^{-11}		6.05×10^{17}	2.51	1.18×10^{-12}
1.95×10^{15}	8.06	4.53×10^{-11}		1.09×10^{18}	4.52	4.88×10^{-13}
2.63×10^{15}	10.87	6.62×10^{-10}		1.57×10^{18}	6.51	5.78×10^{-13}
2.86×10^{15}	11.82	1.41×10^{-9}		1.81×10^{18}	7.50	2.68×10^{-13}
3.13×10^{15}	12.93	9.98×10^{-10}		-	-	-

Table 6.6: Hard X-ray fluxes (Adapted from Terada et al. 2008.

X-ray Data		
Frequency ν (Hz)	Energy E (keV)	Energy flux (erg cm^{-2} s^{-1})
3.16×10^{18}	13.09	6.67×10^{-14}
4.60×10^{18}	19.06	2.00×10^{-13}
7.26×10^{18}	30.08	1.60×10^{-13}

Table 6.7: VHE and TeV fluxes (Adapted from Chadwick et al. 1995; Meintjes et al. 1992; Meintjes et al. 1994).

VHE Data				TeV Data		
Frequency ν (Hz)	Energy E (GeV)	Energy flux (erg cm^{-2} s^{-1})		Frequency ν (Hz)	Energy E (TeV)	Energy flux (erg cm^{-2} s^{-1})
8.47×10^{25}	351	7.84×10^{-11}		4.84×10^{26}	2.01	7.04×10^{-10}
8.47×10^{25}	351	5.60×10^{-9}		4.81×10^{26}	1.99	8.82×10^{-11}
8.47×10^{25}	351	4.09×10^{-10}		4.81×10^{26}	1.99	8.00×10^{-9}
8.47×10^{25}	351	1.12×10^{-10}		-	-	-

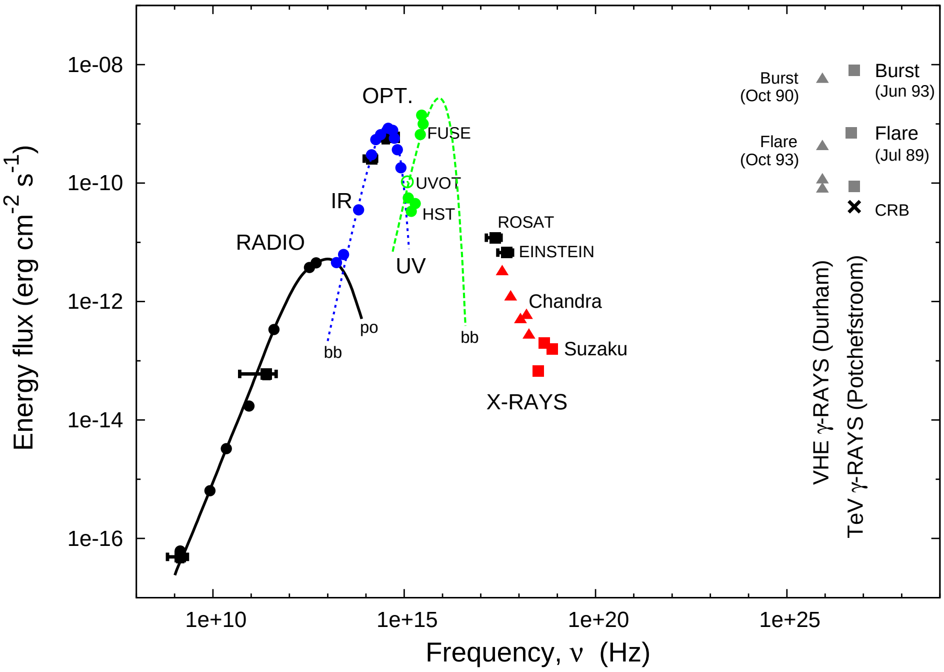

Figure 6.2: Spectral Energy Distribution (SED) of AE Aquarii with the best fitting models. Catalogue data are the black filled squares with errorbars, and the published/analysed data are the rest of the points. FUSE is **F**ar **U**ltraviolet **S**pectroscopic **E**xplorer (e.g. Froning et al. 2012). States of bursts and flares are indicated in the VHE γ-ray and TeV γ-ray regimes.

Figure 6.2 is the SED of AE Aqr, from radio to TeV γ-rays, constructed using both catalogue (archive), published and analysed data. The radio and far-IR data have been fitted with a power-law model (po). The emission in this wavelength band is attributed to synchrotron radiation of expanding magnetized blobs of relativistic electrons (e.g. Bastian et al. 1988; Meintjes & Venter 2003) which become optically thin (and hence the electrons follow a power-law distribution), and release the observed non-thermal radiation. The near-IR and optical data are fitted with a thermal black body model (bb) of temperature of $T_{\rm bb} \simeq 4.65 \times 10^3$ K, and the emission is associated with the K3-5 secondary companion star. The UV data is fitted with another thermal black body model (bb) of temperature of $T_{\rm bb} \simeq 10^5$ K, from an emission region of size $\sim 3 \times 10^8$ cm, comparable with the radius of the white dwarf. The UV emission is associated with emission from the two magnetic poles of the white dwarf, due to the drifting of material attached to the field lines at the magnetospheric radius. Proposed models of the X-ray emission follow in the next section. It has been shown (Meintjes & de Jager 2000) that the VHE and TeV γ-ray emission is most probably the result of burst-like particle acceleration events associated with the magnetospheric propeller process, i.e. exploding double layers and magnetic reconnection. The multi-wavelength emission from AE Aqr is generally the result of a combination of processes. Some of the relevant radiation processes were discussed in Chapter 3.

6.3 X-ray emission Models

The observed characteristics of the X-ray emission from AE Aqr (e.g. §2.5.3) tend to distinguish it from most cataclysmic variables which are mainly accretion driven (e.g. Warner 1995). The nature of soft X-rays ($E_{\rm X} \leqslant 10$ keV) and hard X-rays ($E_{\rm X} \geqslant 10$ keV) may best be understood within the framework of a very effective magnetospheric propeller process in the system, with the hard X-ray component suggesting a different mechanism, possibly driven by the loss of rotational kinetic energy from the fast rotating white dwarf (e.g. Cheng et al. 1998). In this section, possible models are investigated to constrain the observed characteristics.

6.3.1 Soft X-ray Emission: Gravitational Heating

Accretion in AE Aqr may be compared to the scenario in accreting X-ray pulsars, which are considered rapidly rotating magnetized neutron stars accreting gas from a binary companion star (e.g. Bildsten et al. 1997). The neutron star (NS) accretes matter from the companion star either by stellar wind capture or through a Roche lobe overflow process. Cheng et al. (2006) have suggested that the major contribution to thermal X-ray emission from accreting pulsars could emerge from their polar cap regions. The classification scheme according to Lipunov (1992) suggests that the accretion process can occur either in the phase of accretor or in the phase of propeller, depending on the rotation period and surface magnetic field of the NS. Either way, the accretion material can penetrate below the light cylinder radius ($R_{\rm lc}$) of the NS.

In the accretor scenario, most of the material will fall onto the surface creating small heated regions. In principle, the accretion flow is channelled by the magnetic field into a columnar geometry onto the magnetic poles, where gravitational energy is released in the form of radiation (e.g. Becker & Wolff 2007). The geometry of such a scenario is shown in Figure 6.3. Bednarek (2009) has explained that the accretion scenario physically corresponds to the flow of a mixture

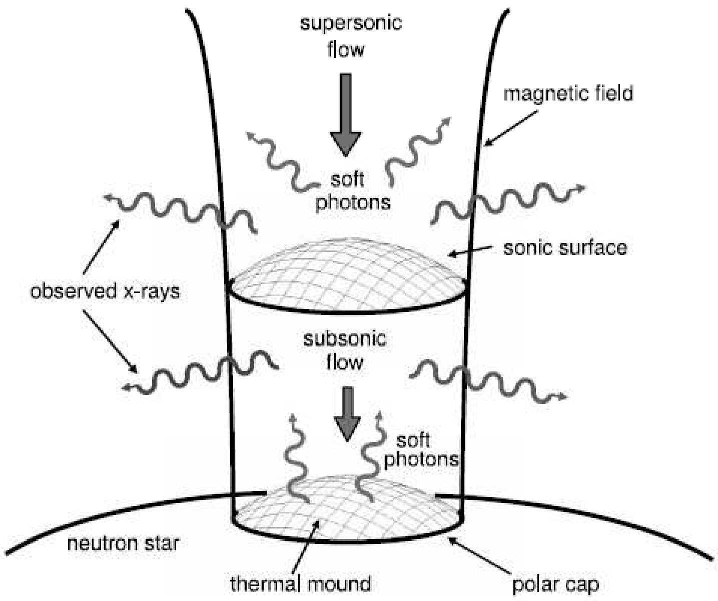

Figure 6.3: Schematic picture of gas accreting onto the magnetic polar cap. Photons are created throughout the column via bremsstrahlung and cyclotron emission respectively (Taken from Bednarek 2009).

of gas and radiation inside a magnetic pipe, sealed with respect to the gas but transparent with respect to the radiation. However, for AE Aqr, the bulk of the material is ejected at a radial distance $r \sim 10^{10}$ cm, casting doubt whether shock heated gas at the polar caps of the white dwarf is responsible for the bulk of the X-ray emission with a single-peaked pulse profile.

For typical mass accretion rates of $\dot{M}_* \sim 10^{17}$ g s^{-1}, associated with magnetic cataclysmic variables, the accretion luminosity is given by

$$L_{\rm acc} = \frac{GM_*\dot{M}_*}{R_*} \simeq 1.3\times10^{34}\left(\frac{M_*}{M_\odot}\right)\left(\frac{\dot{M}_*}{10^{17}\ \rm g\ s^{-1}}\right)\times\left(\frac{R_*}{10^9\ \rm cm}\right)^{-1}\ \rm erg\ s^{-1}, \qquad (6.1)$$

where M_* and R_* are the mass and radius of the white dwarf. Assuming that M_* and R_* are constant, then the accretion luminosity depends on the mass accretion rate only. The temperature of a black body radiating this luminosity can be estimated by

$$\begin{aligned} T_{\rm eff} &= \left(\frac{L_{\rm acc}}{A_{\rm cap}\sigma_{\rm SB}}\right)^{1/4} \\ &\simeq 3.27\times10^5\left(\frac{M_*}{M_\odot}\right)^{1/4}\left(\frac{\dot{M}}{10^{17}\ \rm g\ s^{-1}}\right)^{1/4}\left(\frac{R_*}{10^9\ \rm cm}\right)^{-1}\left(\frac{P}{33\ \rm s}\right)^{1/4}\ \rm K, \qquad (6.2)\end{aligned}$$

where $A_{\rm cap} = \pi(\Omega R_*/{\rm c})R_*^2$ is the area of the polar cap and $\sigma_{\rm SB}$ is the Stefan-Boltzmann constant. The observed soft X-ray luminosity of AE Aqr of $L_{\rm X,soft} \sim 10^{31}$ erg s^{-1} is 3 orders of magnitude less than $L_{\rm acc}$. Besides, the inferred temperature of $T_{\rm X} \geqslant 10^6$ K associated with the observed thermal X-rays, is probably not reconcilable with the inferred low accretion rate of $\dot{M}_* \sim 10^{14}$ g s^{-1} (detailed calculation of $\dot{M}_*$ will be shown later), corresponding to $L_{\rm X} \sim 10^{31}$ erg s^{-1}. An alternative source, leading to the X-ray emission in AE Aqr, may be the conversion of gravitational potential energy to heat energy of the ballistic stream plunging into the Roche lobe of the white dwarf from the inner Lagrangian point. A qualitative discussion, aiming to illustrate the energetics involved, is presented below.

Assume matter is accreted onto the magnetosphere of the white dwarf, then expelled centrifugally (e.g. King & Cominsky 1994). The captured matter has little angular momentum (e.g. King 1991) and consequently, gas falls inward with velocity

$$v_{\rm ff} = \left(\frac{2GM_*}{R}\right)^{1/2}, \tag{6.3}$$

where R is the distance from the centre of the white dwarf. The ram pressure of the infalling gas is given by

$$P_{\rm g} = \rho v_{\rm ff}^2 = \frac{\dot{M}_2(2GM_*)^{1/2}}{4\pi R^{5/2}}, \tag{6.4}$$

where the mass accretion rate ($\dot{M}_2$) is obtained from the continuity equation,

$$\dot{M}_2 = 4\pi R^2 v_{\rm ff}\rho. \tag{6.5}$$

For AE Aqr, the mass transfer from the secondary star occurs on the thermal time scale at a rate $\dot{M}_2 \sim 10^{17}$ g s^{-1}. The magnetic pressure at the distance R is given by

$$P_B = \frac{\mu^2}{8\pi R^6}, \tag{6.6}$$

where $\mu = B_* R_*^3$ is the magnetic moment of the white dwarf with surface magnetic field B_*. At the magnetospheric radius (the so-called Alfvén radius), the distance at which the magnetic field starts to dominate the accretion matter dynamics, the gas ram pressure balances the magnetic pressure. Hence, the Alfvén radius is given by

$$\begin{aligned} R_{\rm M} &= \left(\frac{\mu^2}{2\dot{M}_2(2GM_*)^{1/2}}\right)^{2/7} \\ &\simeq 1.8\times 10^{10}\left(\frac{\mu}{10^{33}\ {\rm G\ cm^3}}\right)^{4/7}\left(\frac{M_*}{M_\odot}\right)^{-1/7}\left(\frac{\dot{M}_2}{10^{17}\ {\rm g\ s^{-1}}}\right)^{-2/7}\ {\rm cm}. \end{aligned} \tag{6.7}$$

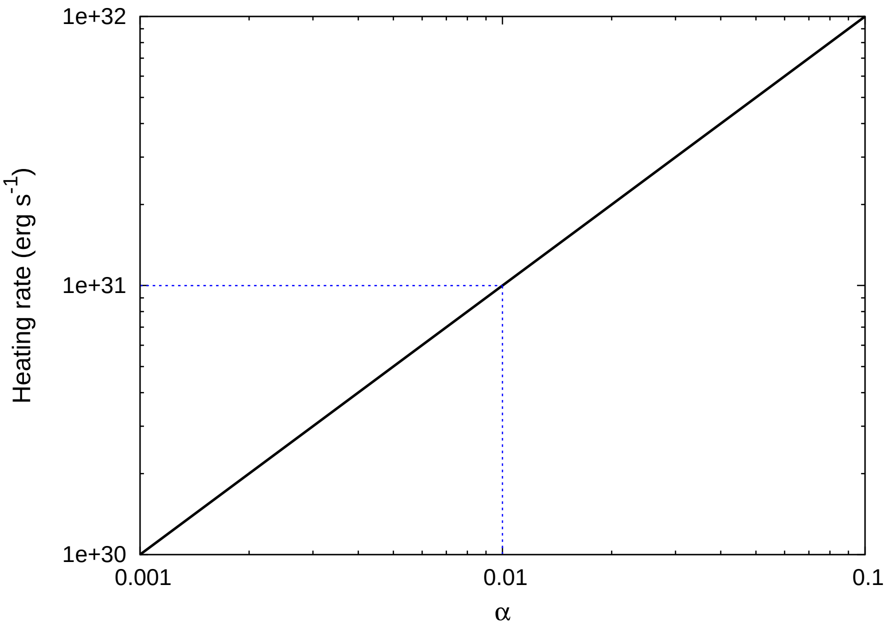

Figure 6.4: $\dot{E}_{\rm th}$ calculated for different values of α at the Alfvén radius for $\dot{M}_2 = 10^{17}$ g s^{-1} and $B_* = 10^6$ G.

If a fraction α of the accretion power liberated at the magnetospheric radius is converted to plasma heating, the resultant heating rate is

$$\begin{aligned}\dot{E}_{\rm th} &= \frac{\alpha G M_* \dot{M}_2}{R_{\rm M}} \\ &\simeq 10^{31}\left(\frac{\alpha}{0.01}\right)\left(\frac{\mu}{10^{33}\ {\rm G\ cm^3}}\right)^{-4/7}\left(\frac{M_*}{M_\odot}\right)^{8/7}\left(\frac{\dot{M}_2}{10^{17}\ {\rm g\ s^{-1}}}\right)^{9/7}\ {\rm erg\ s^{-1}}. \end{aligned} \tag{6.8}$$

For $\alpha \sim 0.01$, $\dot{E}_{\rm th} \sim L_{\rm X,soft}$ (Figure 6.4.). The rate of conversion of gravitational potential energy to thermal energy occurs on the free-fall timescale, which is of the order of $t_{\rm ff} \sim 1000$ s. The resultant increase in the thermal energy is then

$$\begin{aligned}\triangle E_{\rm th} &= \dot{E}_{\rm th} t_{\rm ff} \\ &\simeq 10^{34}\left(\frac{\dot{E}_{\rm th}}{10^{31}\ {\rm erg\ s^{-1}}}\right)\left(\frac{t_{\rm ff}}{1000\ {\rm s}}\right)\ {\rm erg}. \end{aligned} \tag{6.9}$$

The total thermal energy density at the Alfvén radius due to the dissipation of gravitational potential energy is of the order of

$$\begin{aligned}\triangle u_{\rm th} &= \frac{\triangle E_{\rm th}}{r^3} \\ &\simeq 1500\left(\frac{E_{\rm th}}{10^{34}\ {\rm erg}}\right)\left(\frac{r}{R_{\rm M}}\right)^{-3}\ {\rm erg\ cm^{-3}}. \end{aligned} \tag{6.10}$$

The increase in energy density is sufficient to heat the plasma. If $n_{\rm p}$ is the plasma density, then gravitational heating leads to the temperatures of the order of

$$\begin{aligned} kT &\approx \frac{\triangle u_{\rm th}}{n_{\rm p}} \\ &\simeq 10 \left(\frac{\triangle u_{\rm th}}{1500 \text{ erg cm}^{-3}}\right) \left(\frac{n_{\rm p}}{10^{11} \text{ cm}^{-3}}\right)^{-1} \text{ keV}, \end{aligned} \tag{6.11}$$

which is sufficient to explain the observed soft X-ray emission in AE Aqr below 10 keV.

In the propeller state, most of the matter is expelled from the vicinity of the compact object. However, it is still possible that some matter can accrete onto the surface due to gradual accumulation of the matter close to the transition region (e.g. Bednarek 2009). As a consequence, the pressure of the matter can overcome the pressure from the rotating magnetosphere. Hence, the accumulated matter is channelled onto the surface by the magnetic field.

The corotation radius ($R_{\rm co}$), at which gravitational and centrifugal forces balance, is given by

$$R_{\rm co} = \left(\frac{GM_*}{\Omega^2}\right)^{1/3} \simeq 1.55 \times 10^9 \left(\frac{M_*}{M_\odot}\right)^{1/3} \left(\frac{P}{33 \text{ s}}\right)^{2/3} \text{ cm}, \tag{6.12}$$

where P is the spin period of the white dwarf. The radius of the light cylinder of the white dwarf at which the rotational velocity of a particle approaches the speed of light is

$$R_{\rm lc} = \frac{c}{\Omega} \simeq 1.58 \times 10^{11} \left(\frac{P}{33 \text{ s}}\right) \text{ cm}. \tag{6.13}$$

One can see from Eqs. 6.7, 6.12 & 6.13 that $R_{\rm co} < R_{\rm M} < R_{\rm lc}$, i.e. the radius of the transition region lies inside the light cylinder radius.

At the Alfvén radius, the magnetosphere rotates with a velocity given by

$$\begin{aligned} v_{\rm rot} &= \frac{2\pi R_{\rm M}}{P} \\ &\simeq 3 \times 10^9 P_{33}^{-1} \left(\frac{\mu}{10^{33} \text{ G cm}^3}\right)^{4/7} \left(\frac{M_*}{M_\odot}\right)^{-1/7} \left(\frac{\dot{M}_2}{10^{17} \text{ g s}^{-1}}\right)^{-2/7} \text{ cm s}^{-1}. \end{aligned} \tag{6.14}$$

On the other hand, the Keplerian velocity of the accreting matter at this distance is

$$\begin{aligned} v_{\rm K} &= \left(\frac{GM_*}{R_{\rm M}}\right)^{1/2} \\ &\simeq 10^8 \left(\frac{\mu}{10^{33} \text{ G cm}^3}\right)^{-2/7} \left(\frac{M_*}{M_\odot}\right)^{4/7} \left(\frac{\dot{M}_2}{10^{17} \text{ g s}^{-1}}\right)^{1/7} \text{ cm s}^{-1}. \end{aligned} \tag{6.15}$$

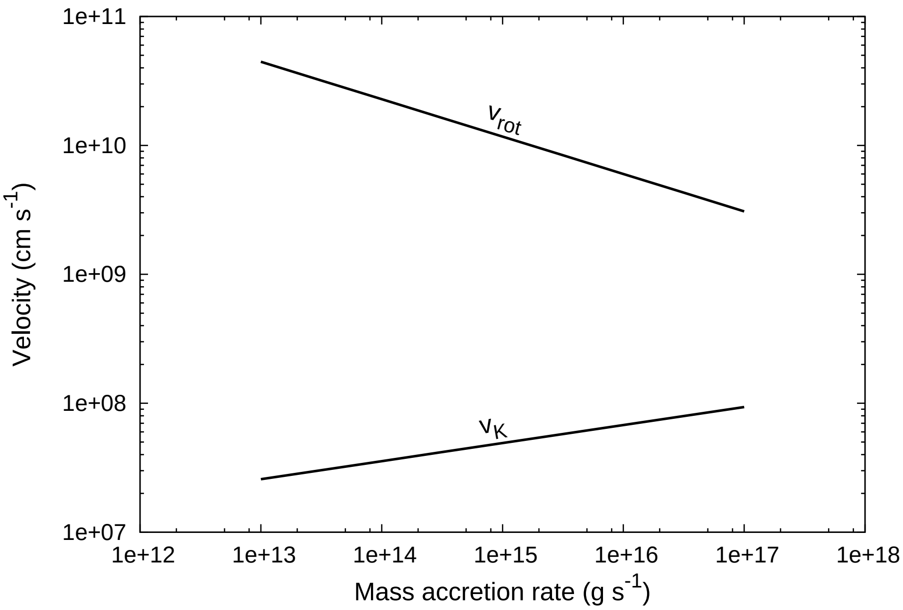

Figure 6.5: A comparison between the rotational velocity of the magnetosphere of the white dwarf and the Keplerian velocity of the gas, at the magnetospheric radius, for $\dot{M}_2 \leqslant 10^{17}$ g s^{-1}.

For $\dot{M}_2 \leqslant 10^{17}$ g s^{-1}, $v_{\rm rot} > v_{\rm K}$, as shown in Figure 6.5, and is an important result that can be used to explain the accretion dynamics in AE Aqr. The high rotational velocity of the magnetosphere with respect to the orbiting gas supports the centrifugal expulsion of material from the binary (e.g. Wynn et al. 1997; Meintjes & de Jager 2000; Ikhsanov et al. 2004).

If the mass transfer flow is converted to radiation in the propeller zone, the resulting luminosity is given by

$$\begin{aligned} L_{\rm mag} &= \frac{GM_*\dot{M}_2}{R_{\rm M}} \\ &\simeq 5\times 10^{33}\left(\frac{M_*}{M_\odot}\right)\left(\frac{\dot{M}_{2,17}}{4}\right)\left(\frac{R_{\rm M}}{10^{10}\ {\rm cm}}\right)^{-1}\ {\rm erg\ s^{-1}}, \end{aligned} \tag{6.16}$$

where $\dot{M}_{2,17}$ is the mass transfer rate in the units of 10^{17} g s^{-1}. The luminosity in Eq. 6.16 is sufficient to drive the optical emission associated with flares. The inferred accretion luminosity from UV - X-ray data is $L_{\rm acc} \sim 10^{31}$ erg s^{-1}, which implies an accretion rate of

$$\begin{aligned} \dot{M}_* &= \frac{L_{\rm acc}}{\left(\frac{GM_*}{R_*}\right)} \\ &\simeq 10^{14}\left(\frac{L_{\rm acc}}{10^{31}\ {\rm erg\ s^{-1}}}\right)\left(\frac{M_*}{M_\odot}\right)^{-1}\left(\frac{R_*}{10^{9}\ {\rm cm}}\right)\ {\rm g\ s^{-1}}. \end{aligned} \tag{6.17}$$

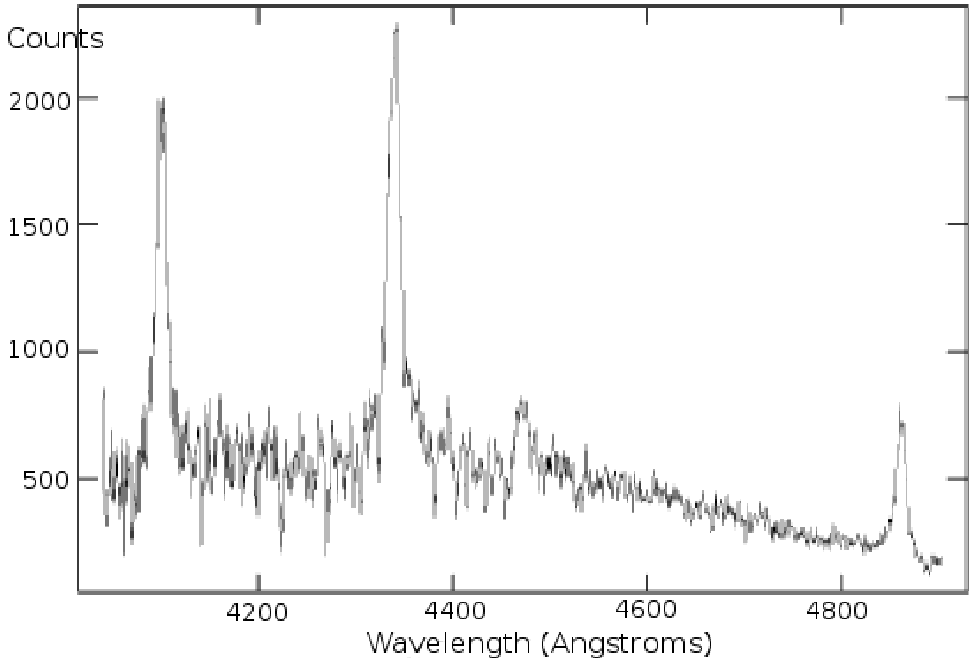

Figure 6.6: Optical spectrum of AE Aqr obtained with the grating spectrograph on the SAAO 1.9 m telescope during September 2011. The spectrum displays some broad Balmer lines.

This is significantly lower that the inferred mass transfer rate of $\dot{M}_2 \sim 10^{17}$ g s^{-1}, associated with the thermal timescale mass transfer in AE Aqr and magnetic cataclysmic variables in general. This suggests that the majority of the mass flow from the secondary star is ejected from the binary, indicating an efficient magnetospheric propeller process. The medium in the propeller zone is turbulent and highly magnetized (e.g. Bednarek 2009), providing favorable conditions for particle acceleration and associated radiation (e.g. Meintjes & de Jager 2000).

The propeller driven outflow conjecture is consistent with the widths of the Balmer lines (Figures 6.6 and 6.7). The velocity dispersions are not compatible with thermal broadening of a 10^4 - 10^5 K thermal plasma. The expected velocity dispersion due to thermal broadening of a line emitting gas at temperature $T \sim$ few $\times 10^4$ K is approximately $\triangle v \leqslant 30(T/10^4 K)^{1/2}$ km s^{-1}, several factors less than the observed velocity dispersion visible in the H_α line, which is of the order of $\triangle v \sim 2000$ km s^{-1} (Figure 6.8). This can satisfactorily be explained in terms of high velocity gas being propelled out of the system due to a magnetospheric propeller process.

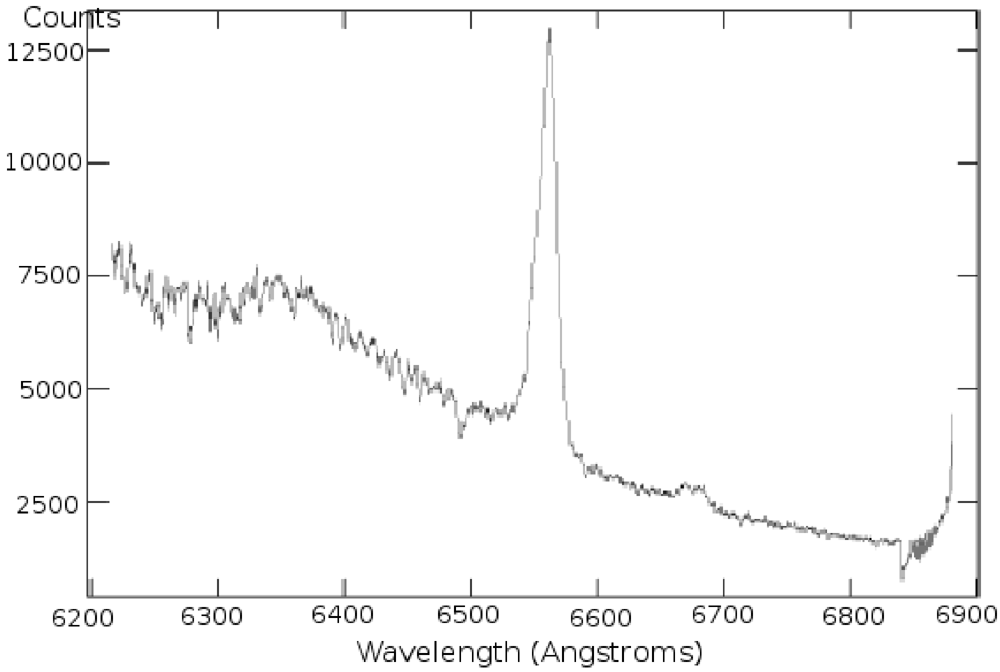

Figure 6.7: Optical spectrum of AE Aqr obtained with the grating spectrograph on the SAAO 1.9 m telescope showing broad H_α line.

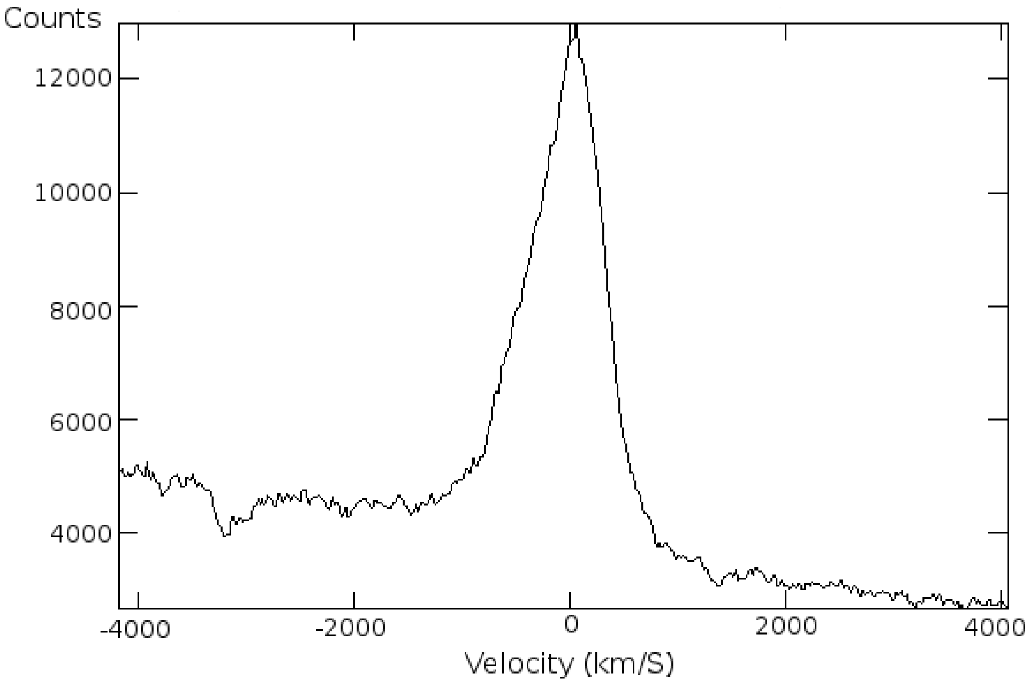

Figure 6.8: The velocity dispersion visible in the H_α line.

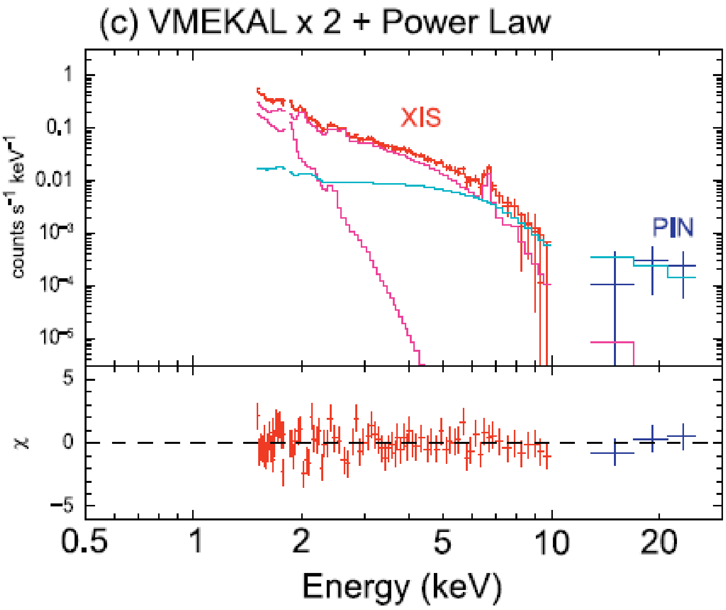

Figure 6.9: Spectrum of AE Aqr from Suzaku data, fitted with a two-temperature vmekal model (for $\epsilon_X \leqslant 10$ keV) and a power-law model, for $\epsilon_X > 10$ keV (Taken from Terada et al. 2008).

6.3.2 Non-thermal Hard X-ray Emission: Pulsar Model

Non-thermal radiation from relativistic particles in magnetized plasmas is a common phenomenon in high-energy astrophysics (e.g. Del Zanna et al. 2006), with strong shocks in relativistic flows providing a natural site for particle acceleration. For high-energy electrons and positrons spiraling in strong magnetic field lines, synchrotron radiation is an effective cooling mechanism. Cheng et al. (2006) have considered non-thermal X-ray emission from pulsars in terms of synchrotron radiation in their magnetospheres, and in shocked regions resulting from the interaction of pulsar winds with the binary companions, or the surrounding interstellar medium.

The recent Suzaku observations of AE Aqr (Terada et al. 2008) reveal a pulsed non-thermal hard X-ray component ($\epsilon_X \geqslant 10$ keV), with a power-law index of $\Gamma \sim 1.16$ (Figure 6.9), compatible with the power-law index of $\Gamma \sim 1.4$ of young rotation-powered pulsars (e.g. Gotthelf 2003). Since AE Aqr contains a rapidly rotating, highly magnetic white dwarf, which are key factors in the energetics of pulsar emission (e.g. Ikhsanov 1998), a pulsar-like process provides an attractive theoretical framework to explain the origin of the observed non-thermal hard X-ray emission from AE Aqr. Additionally, the ratio of the observed hard X-ray luminosity to the spin-down luminosity of the white dwarf in AE Aqr lies in the range 0.01-0.1 %, which is the same as

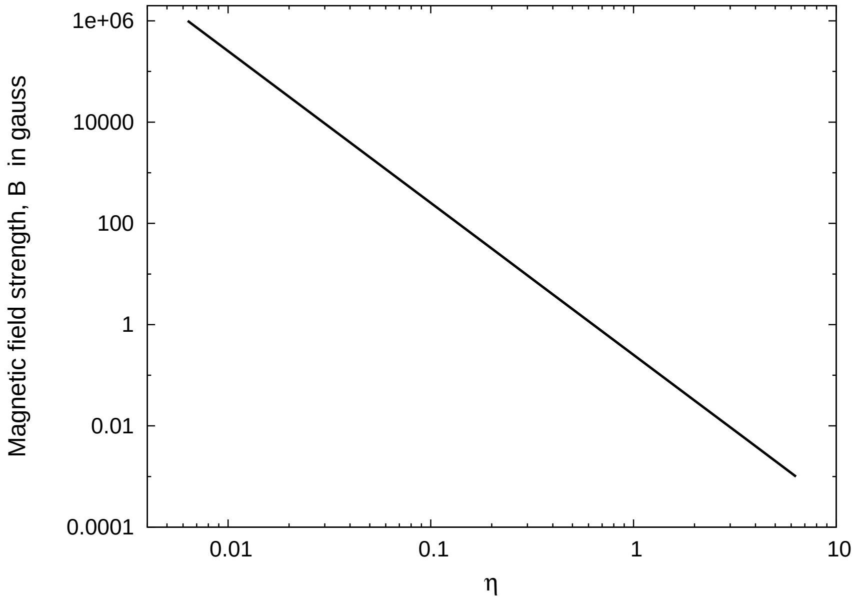

Figure 6.10: Dependence of magnetic field strength (B) on radius (r). The scaling is $B \propto 1/r^3$.

observed from young rotation-powered neutron stars in the 2-10 KeV range (e.g. Terada et al. 2008; Becker & Trümper 1997). A qualitative analysis of the energetics of particle acceleration and accompanying synchrotron radiation of accelerated electron will follow.

The process of particle acceleration in rapidly rotating magnetospheres, and the accompanying radiation, have been discussed extensively (e.g. Leung et al. 1993; Usov 1988, 1993; Ikhsanov & Biermann 2006). The lack of substantial mass accretion onto the surface of the white dwarf in AE Aqr (e.g. Wynn et al. 1997) may result in the white dwarf rotating in a region of low particle density. As a result, an electric field $E_{\|}$ may exist along the magnetic field, i.e. $E_{\|} = (\mathbf{E} \cdot \mathbf{B})/B$. Close to the surface, the electric field force ($e\mathbf{E}$) will drive charged particles away from the surface, forming a magnetosphere whose particle density is given by

$$n_{\rm GJ} = \frac{\mathbf{\Omega}_* \cdot \mathbf{B}}{2\pi ce} \simeq 2 \times 10^3 \left(\frac{B_*}{10^6 \text{ G}}\right) \left(\frac{P}{33 \text{ s}}\right)^{-1} \left(\frac{R_*}{r}\right)^3 \text{ cm}^{-3}, \tag{6.18}$$

where $n_{\rm GJ}$ is the Goldreich-Julian particle density (e.g. Goldreich & Julian 1969) and B is the magnetic field strength at a distance $r > R_*$, i.e. B scales as r^{-3}. Figure 6.10 shows the variation of B with r ($\eta = r/R_{\rm lc}$), from the surface of the WD to the vicinity of the light cylinder radius. The field component $E_{\|}$ can be evaluated for $s > R$, where $r = R + s$ (e.g. Arons & Scharlemann 1979):

$$E_{\|} = E_{\rm AS}^{\|} \sqrt{2R_*/r}, \tag{6.19}$$

where

$$E^{\parallel}_{\rm AS} = \frac{1}{8\sqrt{3}}\left(\frac{\Omega R_*}{c}\right)^{5/2} B_*. \tag{6.20}$$

Then, it can be shown that

$$E_{\parallel} \simeq 3\times 10^{8}\left(\frac{P}{33\ {\rm s}}\right)^{-5/2}\left(\frac{\mu}{10^{33}\ {\rm G\ cm^3}}\right) r^{-1/2}\ {\rm V\ m^{-1}}, \tag{6.21}$$

which translates to

$$E_{\parallel} \simeq 10^{3}\left(\frac{P}{33\ {\rm s}}\right)^{-5/2}\left(\frac{\mu}{10^{33}\ {\rm G\ cm^3}}\right)\left(\frac{r}{1.6\times 10^{11}\ {\rm cm}}\right)^{-1/2}\ {\rm V\ m^{-1}}, \tag{6.22}$$

where the field is evaluated in the vicinity of the light cylinder radius ($R_{\rm lc} \sim 1.6\times 10^{11}$ cm).

A thermal plasma exposed to an electric field in excess of the so-called Dreicer field, $E_{\rm D} \sim 6\times 10^{-6}\,(n_{\rm e}/T_{\rm eff})\,{\rm V\ m^{-1}}$ (Dreicer 1959, e.g. Meintjes & de Jager 2000), will accelerate freely without experiencing the inhibiting effect of particle-particle collisions. For AE Aqr, the Dreicer field is of the order of

$$E_{\rm D} \sim 0.1\left(\frac{n_{\rm e}}{10^{11}\ {\rm cm^{-3}}}\right)\left(\frac{T_{\rm eff}}{10^{7}\ {\rm K}}\right)^{-1}\ {\rm V\ m^{-1}}, \tag{6.23}$$

where $n_{\rm e}$ and $T_{\rm eff}$ are the particle number density and temperature respectively. One can see that $\delta = \frac{E_{\parallel}}{E_D} \sim 10^4$, implying that the electric fields along the magnetic fields are large enough to effectively accelerate the electron population to high energies.

The electric potential in the region of the polar cap is given by,

$$V_{\rm pc}(r) = \int_{R_*}^{r} E_{\parallel} ds.$$

Then, using Eqs. 6.19 and 6.20, one can show that

$$V_{\rm pc}(r) \simeq 2\times 10^{11}\left(\frac{P}{33\ {\rm s}}\right)^{-5/2}\left(\frac{\mu}{10^{33}\ {\rm G\ cm^3}}\right) R_{*,9}^{\frac{1}{2}}\left[\left(\frac{r}{R_*}\right)^{1/2} - 1\right]\ {\rm Volt}. \tag{6.24}$$

Figure 6.11 shows the variation of electric potential with distance from the white dwarf, Figure 6.12 represents the plot of electric potential as a function of the magnetic field strength. Close to the surface of the WD, there is a potential well ($V = 0$). However, V increases to values of

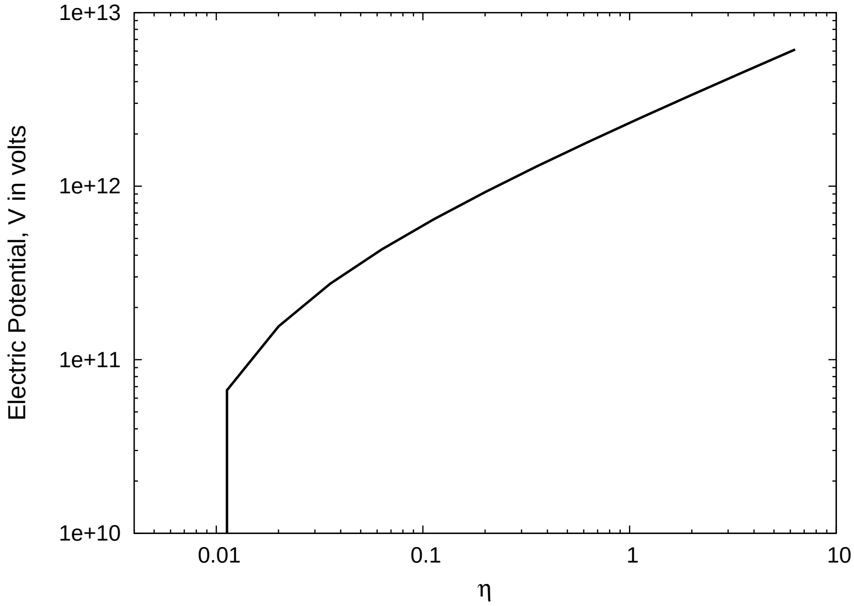

Figure 6.11: Electric field potential (V) as a function of radius (where $\eta = r/R_{\rm lc}$).

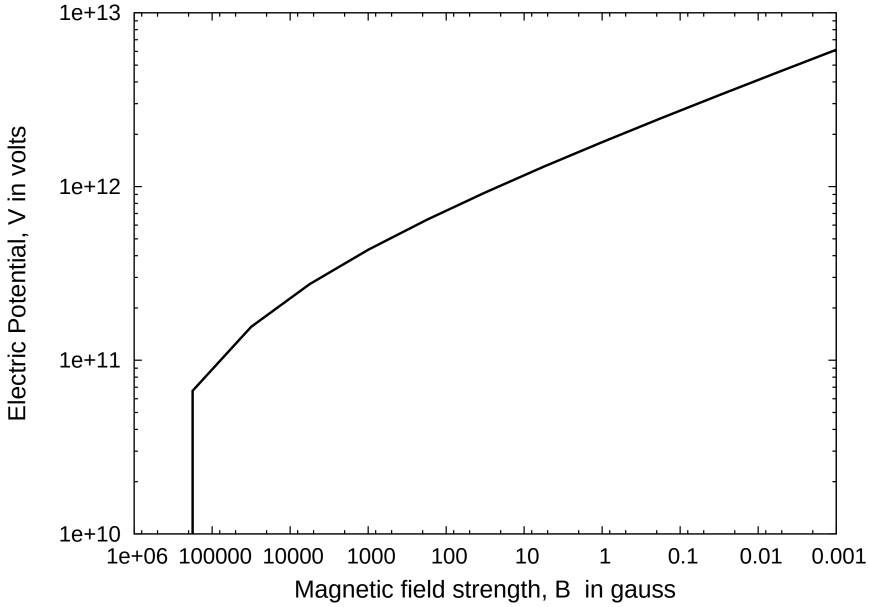

Figure 6.12: Electric field potential as a function of magnetic field strength (B).

$V \geqslant 1$ Tera Volt at distances comparable to $R_{\rm lc}$ and beyond, i.e.

$$
\begin{aligned}
V(R_{\rm lc}) &= 3 \times 10^{11} \left(\frac{P}{33\ \mathrm{s}}\right)^{-5/2} \left(\frac{\mu}{10^{33}\ \mathrm{G\ cm^3}}\right) R_{*,9}^{\frac{1}{2}} \left[\left(\frac{c}{\Omega_* R_*}\right)^{1/2} - 1\right]\ \mathrm{Volt} \\
&= 3 \times 10^{11} \left(\frac{P}{33\ \mathrm{s}}\right)^{-5/2} \left(\frac{\mu}{10^{33}\ \mathrm{G\ cm^3}}\right) R_{*,9}^{\frac{1}{2}} \left[\left(\frac{cP}{2\pi R_*}\right)^{1/2} - 1\right]\ \mathrm{Volt} \\
&\simeq 3 \times 10^{12} \left(\frac{P}{33\ \mathrm{s}}\right)^{-2} \left(\frac{\mu}{10^{33}\ \mathrm{G\ cm^3}}\right)\ \mathrm{Volt}
\end{aligned}
\tag{6.25}
$$

In regions penetrated by the field lines extending beyond the light cylinder, particles can be accelerated (e.g. Usov 1988, and references therein) to energies exceeding 1 TeV. Inside the light cylinder, for an arbitrary r, the energy of an accelerated particle is

$$\begin{aligned}
\varepsilon_{\rm p} &= eV_{\rm pc}(r) \\
&= \frac{1}{2\sqrt{6}}\left(\frac{2\pi}{c}\right)^{5/2} eP^{-5/2}\mu R_*^{1/2}\left[\left(\frac{r}{R_*}\right)^{1/2}-1\right] \\
&= 2\times 10^{11}\left(\frac{P}{33\ {\rm s}}\right)^{-5/2}\left(\frac{\mu}{10^{33}\ {\rm G\ cm^3}}\right)\left(\frac{R_*}{10^9\ {\rm cm}}\right)^{\frac{1}{2}}\left[\left(\frac{r}{R_*}\right)^{1/2}-1\right]\ {\rm eV} \\
&= 0.32\left(\frac{P}{33\ {\rm s}}\right)^{-5/2}\left(\frac{\mu}{10^{33}\ {\rm G\ cm^3}}\right)\left(\frac{R_*}{10^9\ {\rm cm}}\right)^{\frac{1}{2}}\left[\left(\frac{r}{R_*}\right)^{1/2}-1\right]\ {\rm erg}, \qquad (6.26)
\end{aligned}$$

with a Lorentz factor of

$$\gamma_{\rm p} = \frac{\varepsilon_{\rm p}}{m_e c^2} \simeq 4\times 10^5\left(\frac{\mu}{10^{33}\ {\rm G\ cm^3}}\right)\left(\frac{P}{33\ {\rm s}}\right)^{-5/2}\left(\frac{R_*}{10^9\ {\rm cm}}\right)^{\frac{1}{2}}\left[\left(\frac{r}{R_*}\right)^{1/2}-1\right]. \qquad (6.27)$$

The rate at which particles gain energy in the region of the polar cap is given by

$$P_{\rm gain} = \varepsilon_{\rm p}\dot{N}, \qquad (6.28)$$

where $\dot{N}$ is the flux of relativistic particles from the white dwarf:

$$\dot{N} \simeq n(r)c\Delta s, \qquad (6.29)$$

with

$$\Delta s = \pi(\Delta R_{\rm p})^2 = \pi(\Omega R/c)R^2, \qquad (6.30)$$

the area of the polar cap on the surface of the white dwarf about which the particles escape. Then,

$$\begin{aligned}
\dot{N} &= n(r)c\pi(\Omega R/c)R^2 \\
&\simeq 6\times 10^{26} n(r)\left(\frac{R_*}{10^9\ {\rm cm}}\right)^3\left(\frac{P}{33\ {\rm s}}\right)^{-1}\ {\rm s^{-1}}. \qquad (6.31)
\end{aligned}$$

Hence, using Eqs. 6.26 and 6.31 in Eq. 6.28, one can show that

$$P_{\rm gain} \simeq 2\times 10^{26} n(r)\left(\frac{P}{33\ {\rm s}}\right)^{-\frac{7}{2}}\left(\frac{\mu}{10^{33}\ {\rm G\ cm^3}}\right)\left(\frac{R_*}{10^9\ {\rm cm}}\right)^{7/2}\left[\left(\frac{r}{R_*}\right)^{1/2}-1\right]\ {\rm erg\ s^{-1}}. \qquad (6.32)$$

The maximum energy particles (like electrons) can achieve will be limited by energy loss mechanisms. It is considered that during the acceleration process, electrons also experience energy losses due to synchrotron radiation and inverse Compton (IC) scattering (e.g. Bednarek & Pabich 2011). However, in strong magnetospheres, synchrotron radiation is the dominant energy loss mechanism, and the energy radiation rate of an accelerated particle will be given by

$$P_{\rm syn} = \frac{4}{3} c\sigma_{\rm T} U_B \gamma^2, \tag{6.33}$$

where $\sigma_{\rm T} \sim 6.65\times10^{-25}$ cm^2 is the Thomson cross section, and $\gamma = \gamma_{\rm p}$. The magnetic energy density, U_B is given by

$$U_B = \frac{B^2}{8\pi} \simeq 4\times10^{10}\left(\frac{B_*}{10^6\ {\rm G}}\right)^2\left(\frac{R_*}{r}\right)^6\ {\rm erg\ cm^{-3}}. \tag{6.34}$$

The energy radiation rate from the white dwarf can be estimated by

$$L_{\rm rad} = n(r)V' P_{\rm syn}, \tag{6.35}$$

where $n(r)$ is the relativistic particle density and V' is the volume of the emission region, which is probably a cylindrical shell bounded by the light cylinder radius and the radial distance r:

$$\begin{aligned} V' &= \pi(r^2 - R_{\rm lc}^2)h \\ &= \pi(r^2 - R_{\rm lc}^2)(2R_*) \\ &= 2\pi R_{\rm lc}^2 R_*(\eta^2 - 1) \\ &= 2\pi\left(\frac{cP}{2\pi}\right)^2 R_*(\eta^2-1) \\ &\simeq 1.6\times10^{32}(\eta^2-1)\left(\frac{R_*}{10^9\ {\rm cm}}\right)\left(\frac{P}{33\ {\rm s}}\right)^2\ {\rm cm}^3, \end{aligned} \tag{6.36}$$

where $\eta = r/R_{\rm lc}$. The value of V' obtained above is a lower limit. The upper limit can be estimated by considering a spherical shell, i.e.

$$\begin{aligned} V' &= 4\pi r^2 \times r - 4\pi R_{\rm lc}^2 \times R_{\rm lc} \\ &\simeq 5\times10^{34}(\eta^3-1)\left(\frac{P}{33\ {\rm s}}\right)^3\ {\rm cm}^3. \end{aligned} \tag{6.37}$$

Then, using Eqs. 6.27, 6.33, 6.34 and 6.36, the total synchrotron luminosity in Eq. 6.35 can be shown to be,

$$\begin{aligned} L_{\rm rad} &\approx 3\times10^{40} n(r)(\eta^2-1)\left(\frac{P}{33\ {\rm s}}\right)^{-3}\left(\frac{B_*}{10^6\ {\rm G}}\right)^2 \\ &\times\left(\frac{\mu}{10^{33}\ {\rm G\ cm^3}}\right)^2\left(\frac{R_*}{10^9\ {\rm cm}}\right)^2\left(\frac{R_*}{r}\right)^6\left[\left(\frac{r}{R_*}\right)^{1/2} - 1\right]^2\ {\rm erg\ s^{-1}}. \end{aligned} \tag{6.38}$$

In the magnetospheric field closed to the white dwarf, energy losses will inhibit the acceleration process. Effective acceleration is anticipated to occur in regions where the synchrotron losses are less dominant than the acceleration. To constrain the lower boundary of the acceleration zone, the radial distance (r) is determined by equating the power in relativistic particles (Eq. 6.32) to the total synchrotron luminosity of the accelerated particle population (Eq. 6.38). One then obtains,

$$(\eta^2 - 1)\left(\frac{R_*}{r}\right)^6 \left[\left(\frac{r}{R_*}\right)^{1/2} - 1\right] \leqslant 7 \times 10^{-15}. \tag{6.39}$$

Considering that $R_* \ll r$, then

$$\left(\frac{r}{R_{\rm lc}}\right)^2 \left(\frac{R_*}{r}\right)^{\frac{11}{2}} \leqslant 7 \times 10^{-15}. \tag{6.40}$$

Thus, the acceleration dominates synchrotron losses in regions corresponding to $r \geqslant 6{\times}10^{11}$ cm, which leads to $\eta = r/R_{\rm lc} \geqslant 4$. For the model synchrotron power (Eq. 6.38) to match the reported hard X-ray luminosity of $L_{\rm X,hard} \leqslant 5{\times}10^{30}$ erg s^{-1} (e. g. Terada et al. 2008), the number density in the emission region can be shown to be of the order of $n \sim 4{\times}10^3$ cm^{-3}, which is (to order of magnitude) equal to the estimated Goldreich-Julian value (Eq. 6.18) near the white dwarf. The hard X-ray luminosity of $L_{\rm X,hard} \leqslant 5{\times}10^{30}$ erg s^{-1} (above 10 keV) corresponds to $\kappa \sim 0.1$ % of the spin-down power of $L_{\rm s-d} \sim 6 \times 10^{33}$ erg s^{-1}. This places AE Aqr in the same category as young rotation-powered pulsars in the 2-10 keV energy range (e.g. Becker & Trümper 1997).

From Eq. 6.27 and the constrained acceleration zone $r \geqslant 6{\times}10^{11}$ cm, which translates to $\eta \geqslant 4$, the maximum Lorentz factor that electrons can achieve is of the order of $\gamma \sim 10^7$. Thus, the critical frequency (i.e. the frequency where the individual electrons radiate most of their energy) can be shown to be (e.g. Rybicki & Lightman 1979),

$$\begin{aligned} \nu_{\rm c} &= \frac{2\gamma^2 eB}{4\pi m_{\rm e} c} \\ &\approx 2 \times 10^{18} \left(\frac{B(r)}{5 \times 10^{-3}\ {\rm G}}\right)\left(\frac{\gamma}{10^7}\right)^2\ {\rm Hz}, \end{aligned} \tag{6.41}$$

where $B(r) = B_*(R_*/r)^3 \leqslant 0.005$ G, for $r \geqslant 6{\times}10^{11}$ cm. Thus, $\nu_{\rm c}$ satisfactorily explains the energies associated with the non-thermal hard X-ray emission from AE Aqr (e.g. Figure 6.9).

Highly relativistic electrons with $\gamma \sim 10^7$ may provide an interesting possibility for high energy γ-ray production by upscattering soft photons from the K-type secondary star through the inverse

Compton process, which is shown to occur in the Thomson limit for photon frequencies

$$\nu < 1.2 \times 10^{13} \left(\frac{\gamma}{10^7}\right)^{-1} \text{ Hz}, \tag{6.42}$$

which is consistent with the low energy tail from the K3-5 red dwarf, or a circumbinary ring that may orbit the system (e.g. Dubus et al. 2004). An upper limit for γ-ray emission in the Thomson limit is

$$\epsilon_\gamma \leqslant 20 \left(\frac{\gamma}{10^7}\right)^2 \left(\frac{\epsilon_{\rm ph}}{0.05 \text{ eV}}\right) \text{ TeV}, \tag{6.43}$$

which may provide an exciting prospect for follow-up studies using *Fermi* and modern Cerenkov facilities like the High Energy Stereoscopic System (H.E.S.S.) in Namibia.

Chapter 7

Summary and Conclusions

The broad-band multi-wavelength emission in AE Aqr shows characteristics which are both thermal and non-thermal in nature. The system's characteristic emission is the result of different emission processes, of which blackbody radiation, bremsstrahlung and synchrotron radiation were discussed. The near-IR emission, optical emission, UV emission, and soft X-ray ($\epsilon_X \leqslant 10$ keV) emission are the result of thermal blackbody radiation, whereas the radio emission, far-IR emission, hard X-ray emission ($\epsilon_X \geqslant 10$ keV), and the VHE and TeV γ-ray emission are the results of non-thermal rdiation processes. In this thesis, I have presented models to explain the origin of the observed soft and hard X-ray emission from AE Aqr, i.e. the conversion of a fraction of gravitational potential energy at the magnetospheric radius to plasma heating leads to soft X-ray emission, and the non-thermal hard emission is due to a pulsar-like process where electrons are accelerated by a large field aligned potential to relativistic energies and consequently emit synchrotron radiation. In this Chapter, I present a summary of the results.

The analyses of UV and X-ray data observed with Chandra and Swift, showed that AE Aqr is a highly variable source, with flares dominating its light curves. These characteristics have been reported in all wavelengths, from radio to possibly VHE and TeV γ-rays. The fact that AE Aqr is a non-eclipsing binary system means that the variability in the light curves cannot be attributed to the obscuration of either stellar components by the companion, rather the variation in the mass accretion rate. The observed X-ray flares are the result of sudden increase in the emission due to sporadic mass accretion from the companion star. The X-ray spectra of AE Aqr (below 10 keV) are predominantly soft and contain a number of emission lines superimposed on the continuum. The spectra can be fitted with multi-component thermal emission models. These features imply an optically thin emitting plasma, with a continuous temperature distribution.

A period and pulse analysis shows that both UV and X-ray emission are pulsed at a period consistent with the 33 s spin period of the white dwarf. However, the UV pulse profile shows two peaks per cycle, compared with the single broader peak pulse profile of the X-ray emission. This implies that the UV and the X-ray emission originate from different locations in the system. The double peak in the UV pulse profile indicates a location on, or close to both polar caps of the white dwarf. It is shown that the soft thermal X-rays from AE Aqr, with a luminosity of $L_{\mathrm{X}} \sim 10^{31}$ erg s^{-1}, is driven due to dissipation of a fraction ($\alpha \sim 0.01$) of the gravitational potential energy at the magnetospheric radius, with only a small fraction ($\beta \sim 0.03$ %) of the mass transfer being accreted. The broad single-peaked sinusoidal pulsed light curve of the X-ray emission is compatible with the fact that most of the spin-modulated X-ray heating occurs over a broad region $R_X \sim 10^{10}$ cm, which corresponds to the magnetospheric radius.

The recently detected non-thermal hard X-ray emission from AE Aqr (above 10 keV), with a luminosity of $L_{\mathrm{X,hard}} \leqslant 5 \times 10^{30}$ erg s^{-1}, which constitutes a fraction $\kappa \sim 0.1$ % of the spin-down power of the white dwarf, makes AE Aqr unique among the cataclysmic variables, but similar to young rotation-powered pulsars. It is shown that accelerated electrons can attain a Lorentz factor up to the order of $\gamma \sim 10^7$, thus radiating their energy at the critical frequency of $\nu_{\mathrm{c}} \sim 2\times10^{18}$ Hz. This can satisfactorily explain the emission of non-thermal hard X-rays from the system, and a possibility for the production of high-energy γ-rays through inverse Compton scattering of soft photons to VHE and TeV γ-rays. The latter case is not part of this work, and may form the basis for feature research. The number density of particles involved in the non-thermal hard X-ray emission is $n \sim 4 \times 10^3$ cm^{-3}, which is several orders of magnitude lower than the interblob plasma density (10^6 cm$^{-3} \leqslant n_{\mathrm{p}} \leqslant 10^{11}$ cm^{-3}) in the propeller zone, i.e. $r \geqslant 10^{10}$ cm. The low plasma density justifies a pulsar-like model for the non-thermal hard X-ray emission.

It has been shown that the magnetosphere of the white dwarf rotates faster than the accreting mass flow at the Alfvén radius, for mass accretion rates $\dot{M} \leqslant 10^{17}$ g s^{-1}. This means that material cannot penetrate the magnetosphere readily to accrete onto the surface of the white dwarf, instead it is expelled from the system by the fast rotating magnetosphere. Only material attached to the field lines through plasma instabilities (e.g. the K-H instabilities) can gradually drift towards the polar cap regions of the white dwarf. Radiative Cooling results in the UV emission being dominant near the surface.

The non-thermal power-law X-ray emission around $\nu_{\rm c} \sim 10^{18}$ Hz provides interesting possibilities for possible VHE γ-ray emission. Reports of VHE - TeV γ-ray emission made in the 1990's have not been verified by more sophisticated facilities like Magic, H.E.S.S and Vertilas. This can be due to the low duty cycle of pulsed VHE emission (Oruru & Meintjes 2012). More intensive multi-wavelength campaigns in the future may resolve this issue.

Appendix A

Publications/Conference Proceedings

A.1 B. Oruru and P. J. Meintjes, 2012, MNRAS, 421, 1557-1568

Monthly Notices of the ROYAL ASTRONOMICAL SOCIETY

Mon. Not. R. Astron. Soc. **421,** 1557–1568 (2012) doi:10.1111/j.1365-2966.2012.20410.x

X-ray characteristics and the spectral energy distribution of AE Aquarii

B. Oruru and P. J. Meintjes★

Department of Physics, University of the Free State, Bloemfontein 9300, South Africa

Accepted 2011 December 19. Received 2011 November 16; in original form 2011 August 5

ABSTRACT

Using data from contemporaneous observations with *Chandra* and *Swift*, it is shown that the X-ray emission below 10 keV is predominantly thermal, characterized by flares and emission lines and dominated by the soft component. The *Chandra* and *Swift* X-ray spectra ($E_X \leq 10$ keV) can be reproduced by multicomponent thermal emission models with a time-averaged X-ray luminosity of $L_X \sim 10^{31}$ erg s^{-1}. The pulsed 33-s soft X-ray emission below 10 keV is confirmed in both the *Chandra* and *Swift* data sets. The epoch of pulse maximum of the 33-s white dwarf spin period is consistent with the recently derived ephemeris based upon *Suzaku* measurements. The recently detected *Suzaku* hard X-ray component above 10 keV shows a non-thermal power-law nature, with a photon index of $\Gamma \sim 1.2$, possibly the result of synchrotron emission of high-energy electrons in the white dwarf magnetosphere. The hard X-ray luminosity of $L_{X,hard} \leq 5 \times 10^{30}$ erg s^{-1} also constitutes $\kappa \sim 0.1$ per cent of the total spin-down luminosity of the white dwarf. This places AE Aquarii in the same category as young spin-powered pulsars between 2 and 20 keV. Additionally, it is shown that electrons can be accelerated to energies in excess of 10 TeV outside the light cylinder radius, providing interesting possibilities for VHE-TeV follow-up observations. The X-ray emission below $E_X \leq 10$ keV, on the other hand, is explained in terms of plasma heating at the magnetospheric radius, the result of the dissipation of gravitational potential energy. It is found that a conversion efficiency of $\alpha \sim 0.01$ is sufficient to heat the plasma at the magnetospheric boundary to temperatures $kT \leq 10$ keV, sufficient to drive the X-ray emission below 10 keV. Only a small fraction ($\beta \sim 0.3$ per cent) of the mass flow at the magnetospheric radius eventually accretes on to the surface of the white dwarf, emphasizing the very effective magnetospheric propeller process in the system.

Key words: accretion, accretion discs – radiation mechanisms: non-thermal – radiation mechanisms: thermal – binaries: close – white dwarfs.

1 INTRODUCTION

The non-eclipsing close binary system AE Aquarii (hereafter AE Aqr) consists of a magnetic white dwarf orbiting a late-type K3-5 main-sequence companion (e.g. Welsh, Horne & Gomer 1995; Ikhsanov 1997; Choi, Dotani & Agrawal 1999; Itoh et al. 2006), with a binary period of 9.88 h (e.g. Welsh et al. 1993a,b). Estimates of the masses of the companion stars, for an inclination angle, $i = 58^\circ \pm 6^\circ$, have revealed values of $M_1 = 0.79 \pm 0.16\,M_\odot$ and $M_2 = 0.5 \pm 0.1\,M_\odot$, respectively (e.g. Casares et al. 1996; Itoh et al. 2006). The orbital semimajor axis is $a \sim 1.8 \times 10^{11}$ cm.

AE Aqr has traditionally been classified as a nova-like variable (e.g. Joy 1954; Crawford & Craft 1956; de Jager 1991a,b). Based upon this classification, Patterson (1979) modelled the white dwarf as a fast rotating magnetized star accreting matter from a well-developed accretion disc, placing AE Aqr in the DQ Herculis subclass of magnetic cataclysmic variables or intermediate polars (e.g. Warner 1983; Ikhsanov 1997). However, the lack of double-peak emission lines, an indicator of a disc viewed from some inclination, combined with the variation in the line intensities (associated with collisional excitation and high velocity), strongly suggests the absence of a disc (e.g. Eracleous & Horne 1996; Itoh et al. 2006). The current low mass transfer rate from the secondary star, i.e. $\dot{M}_2 \sim 10^{17}$ g s^{-1} (e.g. Wynn, King & Horne 1997), is not able to penetrate the fast rotating magnetosphere deep enough to form a disc, and is most probably ejected from the binary system through a magnetospheric propeller process (e.g. Wynn et al. 1997; Itoh et al. 2006).

AE Aqr has been detected in almost all wavelength bands (e.g. de Jager 1991a,b): in radio (e.g. Bookbinder & Lamb 1987; Bastian, Dulk & Chanmugam 1988; Abada-Simon et al. 1993), in optical (e.g. Zinner 1938; Patterson 1979; Chincarini & Walker 1981; Eracleous & Horne 1996), in X-rays (e.g. Patterson et al. 1980;

★E-mail: MeintjPJ@ufs.ac.za

Clayton & Osborne 1995) and possibly in TeV γ-rays (e.g. Meintjes et al. 1992, 1994; Chadwick et al. 1995). Patterson (1979) observed coherent oscillations at 33 s in the optical light, which were later confirmed in the ultraviolet (UV) and X-ray wavelengths (e.g. Patterson et al. 1980; de Jager et al. 1994; Eracleous et al. 1994). Due to its close proximity of $D \sim 100$ pc (e.g. Welsh et al. 1993), AE Aqr is a relatively bright X-ray source with luminosity $L_X \sim 10^{31}$ erg s^{-1} (e.g. Itoh et al. 2006) and has therefore been observed on a regular basis (e.g. Patterson et al. 1980; Choi et al. 1999; Itoh et al. 2006; Mauche 2006; Terada et al. 2008a,b). Most studies have reported a predominantly thermal soft X-ray component (below 10 keV), but a recent detection using the *Suzaku* satellite revealed a non-thermal hard X-ray component above 10 keV (e.g. Terada et al. 2008). The *Suzaku* data above 10 keV reveal a non-thermal power-law photon index of $\Gamma \approx 1.2$, similar to the observed $\Gamma \approx 1.4$ photon index seen in most young spin-powered pulsars (Gotthelf 2003). The hard X-ray luminosity of $L_{X,\mathrm{hard}} \leq 5 \times 10^{30}$ erg s^{-1} also constitutes approximately $\kappa \leq 0.1$ per cent of the spin-down power of the white dwarf, which is approximately $P_{\text{s-d}} \sim 10^{34}$ erg s^{-1}, similar to that observed in young spin-powered pulsars (e.g. Becker & Trümper 1997). Qualitative models are presented to explain the nature of the soft ($\leq$10 keV) and hard ($\geq$10 keV) X-ray emission in AE Aqr.

This paper is organized as follows. In Section 2, observations of AE Aqr with the *Chandra* and the *Swift* are presented with a brief description of each of the satellites. Data reduction procedures are described in Section 3 and results of the analyses are presented in Section 4. Since the nature of the X-ray emission can best be understood within the framework of the magnetospheric propeller process, a qualitative discussion of the magnetospheric propeller process is presented in Section 5. The proposed models of the soft and hard X-ray emission in AE Aqr are presented in Section 6. In Section 7, the spectral energy distribution (SED) of AE Aqr is presented. Finally, a summary is presented in Section 8.

2 X-RAY OBSERVATIONS: *CHANDRA* AND *SWIFT*

The *Chandra X-ray Observatory* (*CXO*; e.g. Brissenden 2001; Weisskopf et al. 2002; Weisskopf 2003) consists of a high-resolution X-ray telescope, the principal elements of which are the High-Resolution Mirror Assembly (HRMA), designed to maximize reflection of X-rays, and the Optical Bench Assembly (OBA) that provides mounts for the *Chandra*'s two objective transmission gratings, i.e. the Low-Energy Transmission Grating (LETG) and the High-Energy Transmission Grating (HETG). The observatory also contains a complementary set of imaging (I) and spectroscopic (S) instruments, the High-Resolution Camera (HRC) and the Advanced CCD Imaging Spectrometer (ACIS), which are the primary readout detectors for LETG and HETG, respectively.

AE Aqr was observed by *Chandra* (Obs ID 5431; PI, C. Mauche) on 2005 August 30 at 06:37 UT for ~80 ks (e.g. Mauche 2006, 2009), using the ACIS detector and the HETG. Data were archived and standard processing was done at the Chandra X-ray Center (CXC), becoming public on 2006 September 7. Eventually, data were acquired through the High Energy Astrophysics Science Archive Research Center (HEASARC) online service, provided by the NASA's Goddard Space Flight Center (GSFC).

The *Swift* gamma-ray burst explorer (e.g. Gehrels et al. 2004) contains three instruments: the Burst Alert Telescope (BAT; e.g. Barthelmy et al. 2005), the X-ray Telescope (XRT; e.g. Burrows et al. 2005) and the Ultraviolet/Optical Telescope (UVOT; e.g. Roming et al. 2005). These instruments combine to form a powerful multiwavelength observatory capable of rapid position determination of gamma-ray bursts (GRBs) and their corresponding afterglows (e.g. Burrows et al. 2005), as well as the ability to measure both their light curves and redshifts. The BAT is a highly sensitive, large field-of-view (FoV), coded aperture instrument designed to search for new GRBs in the sky, upon which an automatic spacecraft slew is triggered to bring the bursts in the FoVs of the XRT and the UVOT, respectively. The XRT is a flexible and an autonomous X-ray imaging spectrometer designed to measure fluxes, spectra and light curves over a wide dynamic range covering more than seven orders of magnitude in flux. It uses a grazing incidence Wolter I telescope to focus X-rays on to a CCD detector, which is thermoelectrically cooled (e.g. Burrows et al. 2005; Capalbi et al. 2005; Gehrels et al. 2004). The XRT can operate in four science (or readout) modes, i.e. photodiode (PD), image (IM), windowed timing (WT) and photon counting (PC) modes, respectively. Detailed descriptions of each of these modes are given in Burrows et al. (2005) and Capalbi et al. (2005). The XRT is designed for autonomous operation, switching between the different readout modes, depending on the source intensity (e.g. Hill et al. 2004; Evans et al. 2007).

Swift observed AE Aqr (target ID: 30295) between 2005 August 30 and September 2 for a total on-source duration of ~10.5 ks, either as a pre-planned target (e.g. Evans et al. 2009) or a target of opportunity (ToO). Data were archived in 2005 September. Standard data processing was done later at the UK Swift Science Data Centre (UK SDC) in 2007 April. The results presented in this paper are based on data collected when the XRT was operating in the PC mode, in which full imaging and spectroscopic resolutions are retained, but timing resolution is limited to 2.5 s (e.g. Burrows et al. 2005; Capalbi et al. 2005).

3 DATA REDUCTION

3.1 *Chandra* data

To generate light curves and spectra, the level 2 event file was used, processed at the CXC from the level 1 event list, and archived together with other data products which shall be mentioned later. The *Chandra* Interactive Analysis of Observations software (CIAO version 4.2) was used to process the light curves and spectra, respectively.

For the light curves, the event times in the level 2 event file were converted from terrestrial time (TT) to barycentric dynamical time (TDB) by running the AXBARY tool with the orbit ephemeris file. Then, energy filtering was applied to the barycentre corrected data. For each of the filtered data, a source region and a background region were created in ds9, then the chip (CCD_ID) being used was determined. From these, background-subtracted binned light curves were created.

For the spectra, a spectrum file (pha2.fits) was extracted from the level 2 event file and then split into single spectrum files with respect to the order of the spectrum (diffraction order) and the spectral component (grating arm), which were determined from the spectrum block of the pha2 file. Then, for each of the single spectra, a response matrix file (RMF) was created and used alongside the event file, pha2 file and other data product files, for example, the bad pixels file (bpix1.fits), the aspect solution file (asol1.fits) and the parameter block file (pbk0.fits), to create the corresponding ancillary response file (ARF). The additional product files enabled the exclusion of bad pixels and accurate determination of celestial position of the events.

3.2 *Swift*-XRT data

Data reduction and analyses were done using the High-Energy Astrophysics software (HEASOFT version 6.11). For the light curves, level 2 event files were used for each of the scheduled observations. A barycentric correction was applied to each of these files. The multimission barycentric correction tool (barycorr) was run with the ASCII version of the clock file (swco.dat) and the orbit file for the particular observation. Then, using xselect, grade filtering (0–12) was applied to the corrected event data, and the data were combined. Using the combined data, source and background regions were determined in ds9, from which source and background events were generated. Then, energy filtering was applied to the source and background events, and finally binned background-subtracted light curves were created.

For the spectra, the on-demand software was used (developed by the *Swift* team). These were acquired by manually registering the information of AE Aqr since it is a ToO. The detail of how the spectral data files are generally created by the software for most sources is presented in Evans et al. (2009). In summary, combined source and background spectra from all the observations were created using the software, as well as the ARF. The RMF, however, was obtained from the calibration data base (CALDB; http://swift.gsfc.nasa.gov/docs/heasarc/caldb/swift/).

4 RESULTS

4.1 Light curves

Figs 1 and 2 show the background-subtracted light curves of AE Aqr from *Chandra* and *Swift*-XRT data, created with bin times of 1800 s and 600 s, respectively. The gaps in the XRT data correspond to different exposures since *Swift* is a low-Earth orbit satellite. From these figures, the characteristic highly variable nature of the source is revealed, with the light curves dominated by flaring.

Both *Chandra* and *Swift* data sets have been divided into soft $E_X = (0.3\text{–}2)$ keV and hard $E_X = (2\text{–}10)$ keV sets. The hardness ratio, defined as HR = (hard count rate)/(soft count rate), has been plotted for both data sets (Figs 3 and 4). It can be seen that the X-ray data below 10 keV are dominated by the soft component, i.e. HR < 1.

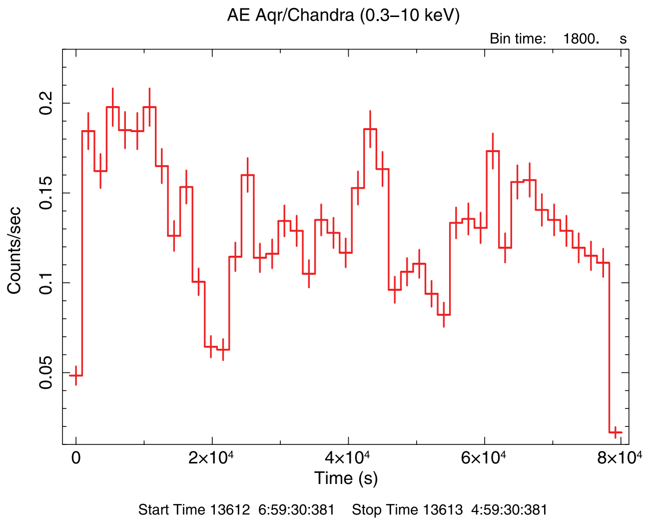

Figure 1. Background-subtracted light curves of AE Aqr from the *Chandra* data.

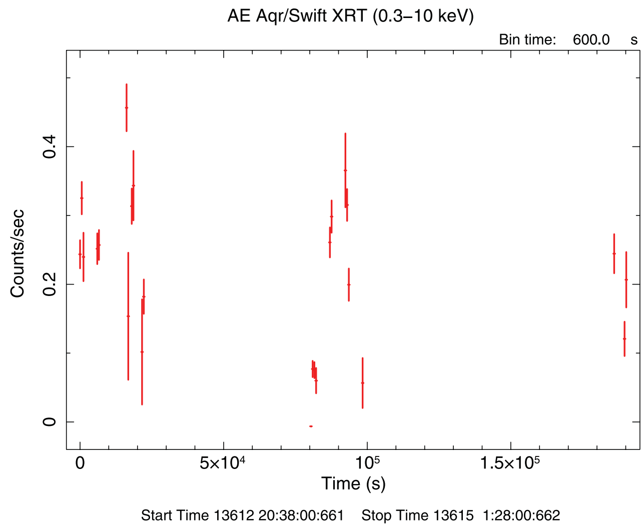

Figure 2. Background-subtracted light curves of AE Aqr from the *Swift*-XRT data.

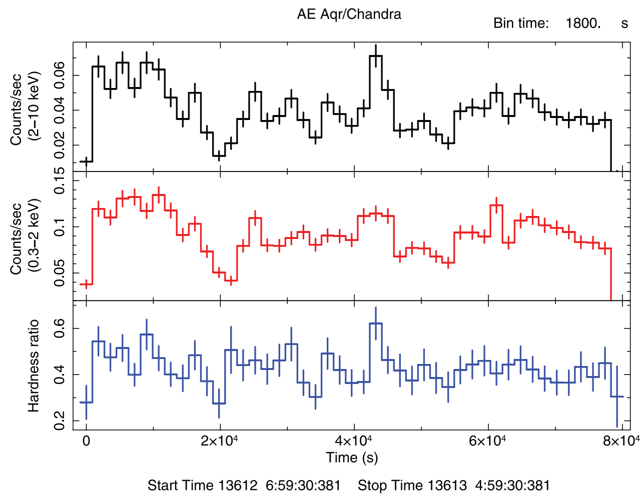

Figure 3. Hardness ratio for the *Chandra* data.

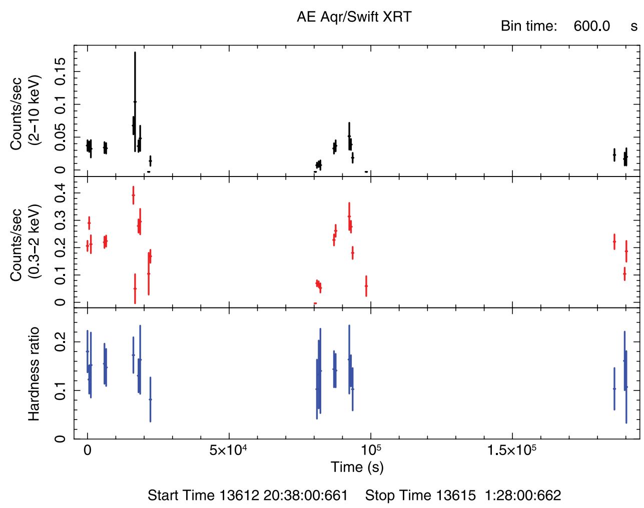

Figure 4. Hardness ratio for the *Swift*-XRT data.

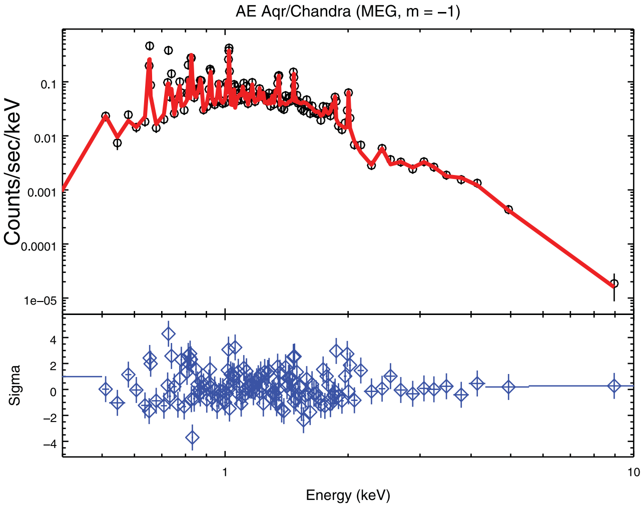

Figure 5. MEG energy spectrum for the diffraction order $m = -1$, fitted with a three-temperature VMEKAL model.

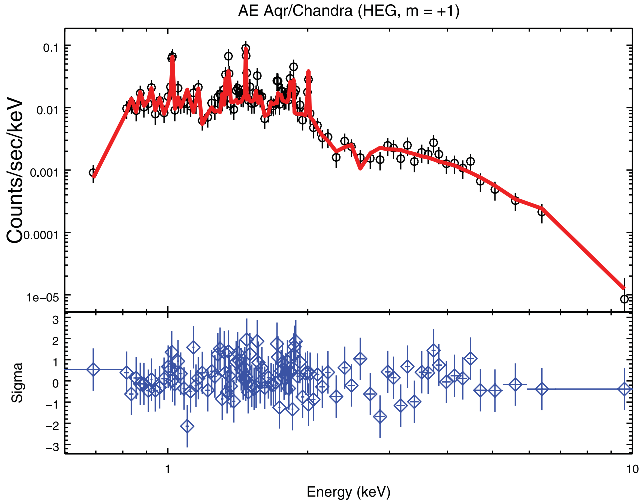

Figure 7. HEG energy spectrum for the diffraction order $m = +1$, fitted with a two-temperature VMEKAL model.

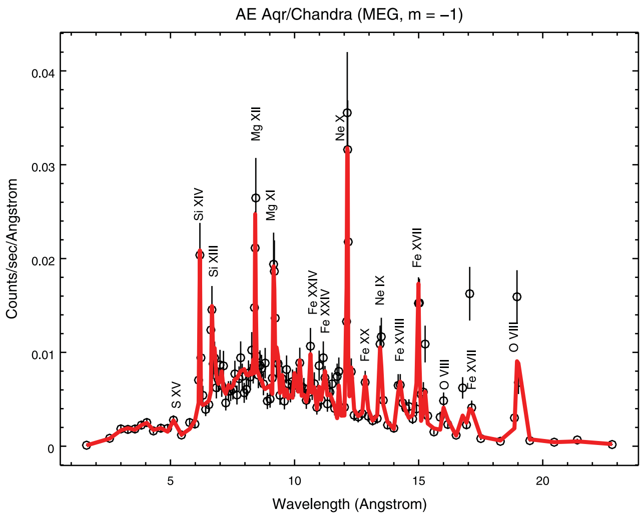

Figure 6. MEG wavelength spectrum for the diffraction order $m = -1$, fitted with a three-temperature VMEKAL model.

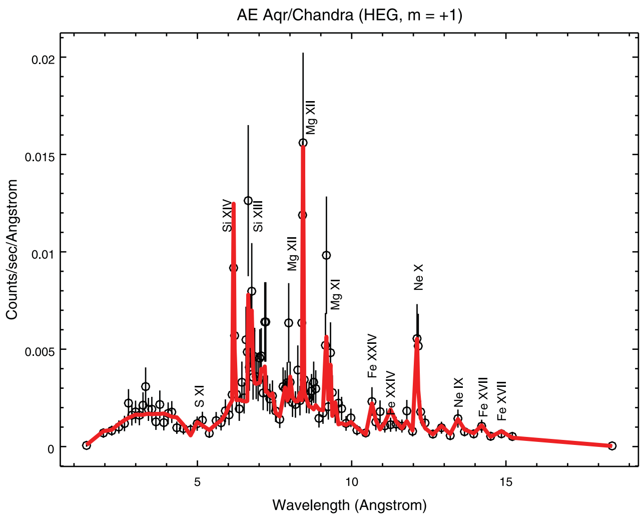

Figure 8. HEG wavelength spectrum for the diffraction order $m = +1$, fitted with a two-temperature VMEKAL model.

4.2 Spectra

4.2.1 Chandra spectra

For each diffraction order and grating arm, a background-subtracted spectrum was plotted and models fitted using SHERPA, a package in the CIAO software. Figs 5 and 6 show the medium-energy grating (MEG) energy and wavelength spectra for the diffraction orders $m = -1$, fitted with a three-temperature VMEKAL model of temperatures (kT): $0.19^{+0.05}_{-0.04}$, $0.64^{+0.02}_{-0.02}$ and $3.14^{+0.35}_{-0.33}$ keV, respectively. Figs 7 and 8 are the corresponding high-energy grating (HEG) spectra for the diffraction order $m = +1$, fitted with a two-temperature VMEKAL model of temperatures (kT): $0.62^{+0.05}_{-0.05}$ and $3.05^{+0.51}_{-0.37}$ keV, respectively. Table 1 summarizes the best-fitting parameters for the two grating arms and diffraction orders, respectively. Noticeable from the figures are the emission lines in the lower energy range of the spectrum, with some of the prominent lines labelled (e.g. Mauche 2009). The energy fluxes at these lines are given in Table 2, for each grating arm and diffraction order, respectively.

4.2.2 Swift-XRT spectra

Figs 9 and 10 show the folded and unfolded spectra of AE Aqr from *Swift*-XRT data, fitted with a three-temperature VMEKAL model. The fitting was performed in XSPEC using C-statistic, and the parameters were obtained with 90 per cent confidence for which the statistic had worsened by 2.706 compared with the best-fitting value. The model temperatures obtained in this analysis are $0.4^{+0.07}_{-0.07}$, $0.92^{+0.12}_{-0.10}$ and $3.95^{+0.94}_{-0.42}$ keV, respectively. Elemental abundances were also fixed to those obtained by Itoh et al. (2006), as presented in the caption of Table 1. The spectrum shows similar characteristics, i.e. characterized by emission-line features in the lower energy part. The unabsorbed X-ray flux obtained in the range 0.5–10 keV is $7.98^{+0.29}_{-0.44} \times 10^{-12}$ erg cm^{-2} s^{-1}, which, for an estimated source distance of 100 pc (e.g. Welsh et al. 1993), translates to a luminosity of $L_X \sim 9 \times 10^{30}$ erg s^{-1}, consistent with the time-averaged soft X-ray luminosity ($L_X \sim 10^{31}$ erg s^{-1}) reported from previous observations (e.g. Itoh et al. 2006), and higher than the hard ($E_X \geq 10$ keV) X-ray luminosity of $L_{X,\mathrm{hard}} \leq 5 \times 10^{30}$ erg s^{-1} (e.g. Terada et al. 2008).

Table 1. Best-fitting parameters from the *Chandra* data. Elemental abundances are fixed to those obtained by Itoh et al. (2006); see also Choi & Dotani (2006): N = 3.51, O = 0.74, Ne = 0.43, Mg = 0.70, Si = 0.81, S = 0.73, Ar = 0.21, Ca = 0.19, Fe = 0.47 and Ni = 1.27.

	Best-fitting values			
Parameter	MEG ($m = -1$)	MEG ($m = +1$)	HEG ($m = -1$)	HEG ($m = +1$)
N_H (10^{20} cm^{-2})	3.59 (fixed)	3.59 (fixed)	3.59 (fixed)	3.59 (fixed)
kT_1 (keV)	$0.19^{+0.05}_{-0.04}$	$0.17^{+0.06}_{-0.06}$	–	–
Norm$_1$ (10^{-3})	0.87 ± 0.26	1.37 ± 1.00	–	–
kT_2 (keV)	$0.64^{+0.02}_{-0.02}$	$0.61^{+0.05}_{-0.01}$	$0.63^{+0.04}_{-0.04}$	$0.62^{+0.05}_{-0.05}$
Norm$_2$ (10^{-3})	2.15 ± 0.16	2.07 ± 0.18	2.54 ± 0.33	$2.28^{+0.35}_{-0.36}$
kT_3 (keV)	$3.14^{+0.35}_{-0.33}$	$3.10^{+0.32}_{-0.27}$	$3.19^{+0.51}_{-0.44}$	$3.05^{+0.51}_{-0.37}$
Norm$_3$ (10^{-3})	3.70 ± 0.20	3.84 ± 0.20	3.44 ± 0.34	3.57 ± 0.36
χ^2_ν (dof)	2.23 (137)	1.83 (123)	0.90 (130)	0.68 (107)
	Absorbed flux (10^{-12} erg cm^{-2} s^{-1})			
0.5–1.0 keV	3.45	3.70	2.80	2.62
1.0–2.0 keV	2.28	2.27	2.29	2.24
2.0–4.0 keV	1.50	1.52	1.42	1.43
4.0–8.0 keV	1.02	1.04	0.97	0.94
0.5–10 keV	8.40	8.67	7.61	7.36

Table 2. Energy fluxes determined for the prominent emission line from the *Chandra* spectra.

		MEG		HEG	
		$m = -1$	$m = +1$	$m = -1$	$m = +1$
Line	Peak (Å)	Flux $\times 10^{-13}$ erg cm^{-2} s^{-1}			
Si XIV	6.2	1.2	1.2	1.1	1.1
Si XIII	6.7	1.4	1.3	1.4	1.4
Mg XII	8.4	1.1	1.1	1.1	1.0
Mg XI	9.2	1.0	1.0	1.0	1.0
Ne X	12.1	1.5	1.5	1.7	1.6
Ne IX	13.5	1.7	1.6	1.8	1.6
Fe XVII	15.0	2.2	2.3	2.5	–
O VIII	19.0	3.8	–	–	–

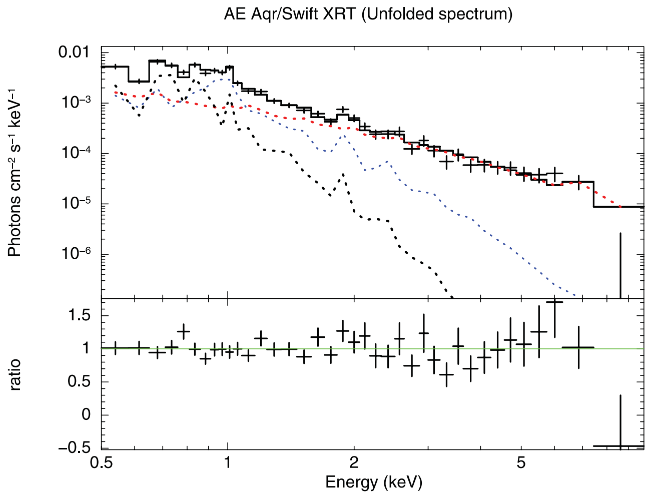

Figure 10. Unfolded spectrum of AE Aqr from *Swift*-XRT fitted with a three-temperature VMEKAL model.

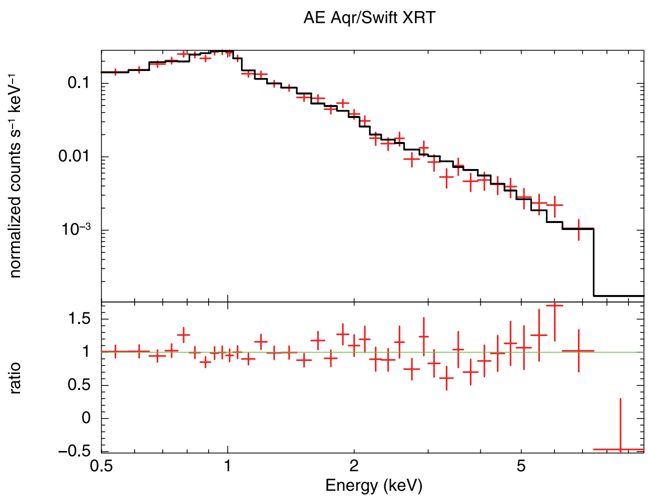

Figure 9. Folded spectrum of AE Aqr from *Swift*-XRT fitted with a three-temperature VMEKAL model.

4.3 Pulse timing

A search for periodicity using an epoch-folding method was carried out on the barycentric corrected *Chandra* and *Swift* data. The light curves were folded with a large number of periods using the ephemeris for the pulsed emission, obtained for a 14-yr baseline of optical observations (e.g. de Jager et al. 1994), and the best periods found by chi-squared maximization. Fig. 11 shows the pulse period determined for the *Chandra* data. The Fourier period resolution (FPR) is $P^2/2T \sim 6.75 \times 10^{-3}$ s, where P is the folding period and T is the length of the observation (∼80 ks). The resulting peak was fitted with a Gaussian which was used to determine the actual pulse period of $P_{\rm pulse} = 33.0767 \pm 0.0068$ s. Similarly, the pulse period obtained for the *Swift*-XRT data is 33.0767 ± 0.0030 s (from Fig. 12), with corresponding resolution $P^2/2T \sim 3 \times 10^{-3}$ s. In the latter case, the data gaps introduced aliases which are noticeable in

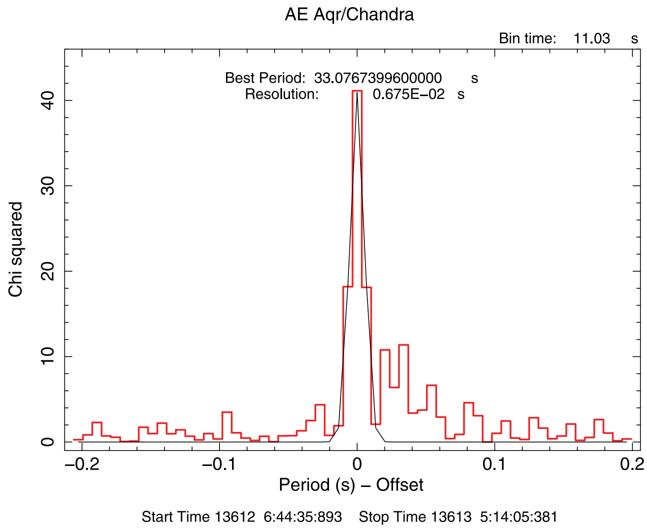

Figure 11. Pulse period determination from the *Chandra* data.

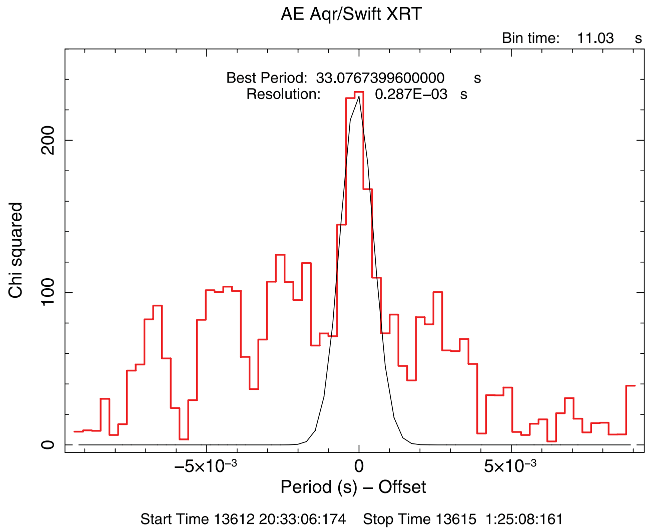

Figure 12. Pulse period determination from the *Swift*-XRT data.

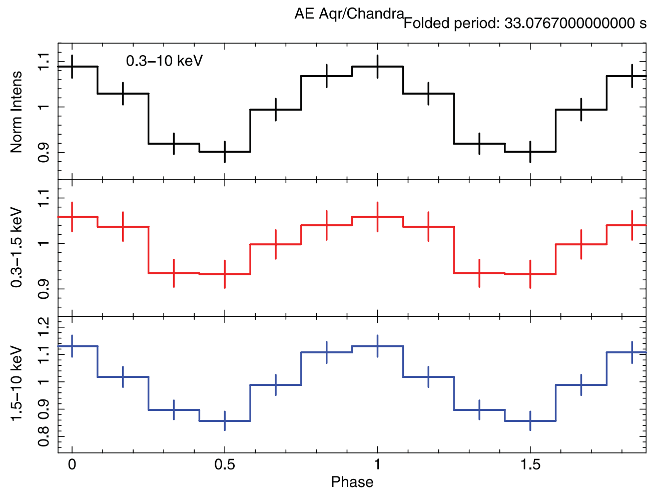

Figure 13. Pulse profile of AE Aqr from the *Chandra* data. Phase 0 corresponds to BJD 245 3673.5.

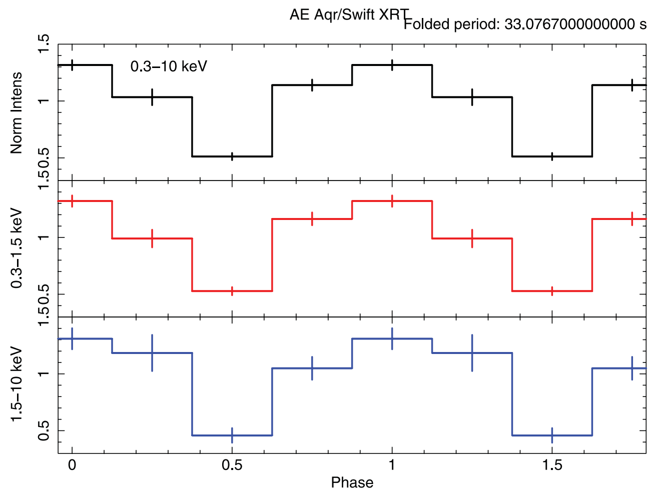

Figure 14. Pulse profile of AE Aqr from the *Swift*-XRT data. Phase 0 corresponds to BJD 245 3673.5.

the power spectrum. The pulse periods obtained for both data sets (i.e. *Chandra* and *Swift*-XRT data) are perfectly reconcilable with the previously determined spin period of the white dwarf (de Jager et al. 1994; Mauche 2006), as well as the recent *Suzaku* result (Terada et al. 2008). Using the period obtained above, the pulse profiles were determined using the epoch of BJD 245 3673.5 (Terada et al. 2008). The profiles are shown in Figs 13 and 14 for *Chandra* and *Swift*-XRT data, respectively.

5 MAGNETOSPHERIC PROPELLER

The nature of the soft ($E_X \leq 10$ keV) and hard ($E_X \geq 10$ keV) X-ray emission can best be understood within the framework of a very effective magnetospheric propeller process in the system. It has been shown (Meintjes 2002; Schenker et al. 2002) that AE Aqr went through a phase of very high thermal time-scale mass transfer more than 10^7 years ago, resulting in the white dwarf being spun-up to a period of $\sim$30 s over a time-scale comparable to the thermal time-scale. It has been shown (Meintjes 2002; Schenker et al. 2002) that the white dwarf probably accreted at a rate $M_{\mathrm{i},*} \sim 10^{19}$ g s^{-1} that could have sustained stable nuclear burning on its surface, resulting in supersoft X-ray (SSS) emission. It has been shown that the runaway mass transfer and high accretion shut down when a critical binary q-ratio was reached, i.e. $q = (M_2/M_1) \approx 0.73$ (Meintjes 2002). Since then, the mass transfer dropped considerably.

It can be shown that the current thermal time-scale mass transfer rate from the secondary star is

$$\dot{M}_2 \sim 4 \times 10^{17} \left(\frac{M_2}{0.6\,\mathrm{M}_\odot}\right) \left(\frac{\tau_{\mathrm{th}}}{10^7\,\mathrm{yr}}\right)^{-1} \mathrm{g\ s^{-1}}. \tag{1}$$

If this is representative of the accretion rate, it would drive an accretion luminosity of $\sim$afew $\times\ 10^3\ L_X$, with $L_X \sim 10^{31}$ erg s^{-1} being the expected luminosity associated with the mass accretion on to the surface of the white dwarf (Eracleous & Horne 1996). It has been shown (Eracleous & Horne 1996; Wynn et al. 1997; Meintjes & de Jager 2000) that magnetohydrodynamics (MHD) propellering occurs in the proximity of the magnetospheric radius (i.e. the Alfvén radius), where the field starts to dominate the mass flow dynamics. This is of the order of

$$R_{\mathrm{M}} = 10^{10} \left(\frac{M_*}{\mathrm{M}_\odot}\right)^{-1/7} \left(\frac{\dot{M}_{2,17}}{4}\right)^{-2/7} \mu_{33}^{4/7}\ \mathrm{cm}, \tag{2}$$

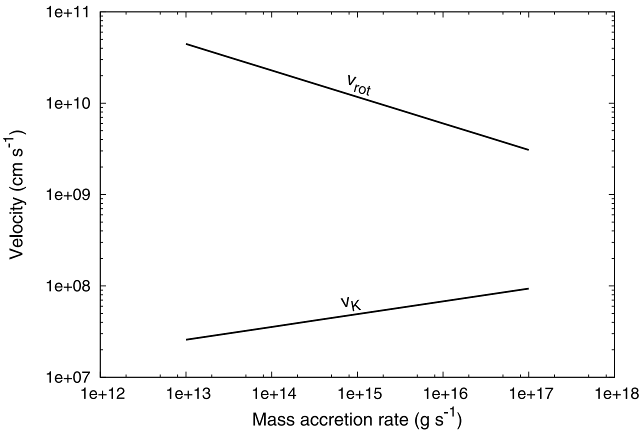

Figure 15. A comparison between the rotational velocity of the magnetosphere and the Keplerian flow of the gas at the magnetospheric radius.

where μ_{33} is the magnetic moment of the white dwarf in the units of $10^{33}\,\mathrm{G\,cm^3}$ and $\dot{M}_{2,17}$ represents the mass transfer rate in units of 10^{17} g s^{-1}. At the Alfvén radius, the magnetosphere rotates with a velocity of

$$v_{\mathrm{rot}} \simeq 2\times10^9\left(\frac{M_*}{\mathrm{M_\odot}}\right)^{-1/7}\dot{M}_{2,17}^{-2/7}P_{33}^{-1}\mu_{33}^{4/7}\ \mathrm{cm\ s^{-1}}. \tag{3}$$

The Keplerian velocity of the orbiting matter at this distance from the white dwarf is

$$v_{\mathrm{K}} \simeq 10^8\left(\frac{M_*}{\mathrm{M_\odot}}\right)^{4/7}\dot{M}_{2,17}^{1/7}\mu_{33}^{-2/7}\ \mathrm{cm\ s^{-1}}. \tag{4}$$

For $\dot{M}_2 \lesssim 10^{17}\,\mathrm{g\,s^{-1}}$, $v_{\mathrm{rot}} > v_{\mathrm{K}}$ as shown in Fig. 15. The high rotational velocity of the magnetosphere, with respect to orbiting gas, drives the centrifugal expulsion of material from the binary system.

If the mass transfer flow is converted into radiation in the propeller zone, the resultant luminosity is

$$L_{\mathrm{mag}} \sim 5\times10^{33}\left(\frac{M_1}{\mathrm{M_\odot}}\right)\left(\frac{\dot{M}_{2,17}}{4}\right)\left(\frac{R}{R_{\mathrm{mag}}}\right)^{-1}\ \mathrm{erg\ s^{-1}}, \tag{5}$$

for the current thermal time-scale mass transfer rate. This is sufficient to drive optical emission associated with flares (Eracleous & Horne 1996). Observations seem to suggest that the accretion luminosity inferred from UV–X-ray data is approximately $L_{\mathrm{acc}} \sim 10^{31}$ erg s^{-1}, which implies an accretion rate of

$$\dot{M}_* \sim 10^{14}\left(\frac{L}{L_{\mathrm{acc}}}\right)\left(\frac{R_*}{10^9\,\mathrm{cm}}\right)\left(\frac{M_*}{\mathrm{M_\odot}}\right)^{-1}\ \mathrm{g\ s^{-1}}, \tag{6}$$

significantly lower than the inferred mass transfer rate. This suggests that the majority of the mass flow from the secondary star is ejected from the binary system. This accretion rate constitutes only ($\beta \approx 0.03$ per cent) of the mass transfer flow from the secondary star.

The total MHD power transmitted to the orbiting gas stream is of the order of (Meintjes & Venter 2005)

$$P_{\mathrm{mhd}} \approx 10^{34}\left(\frac{v_{\mathrm{rel},\perp}}{2\times10^9\,\mathrm{cm\ s^{-1}}}\right)\left(\frac{B_{\mathrm{circ}}}{300\,\mathrm{G}}\right)^2 \times\left(\frac{A_{\mathrm{stream}}}{5\times10^{20}\,\mathrm{cm^2}}\right)\ \mathrm{erg\ s^{-1}}. \tag{7}$$

The dissipated magnetospheric power is consistent with the spin-down power of the white dwarf inferred from the spin-down rate (de Jager et al. 1994; Mauche 2006), exceeding the accretion luminosity by several orders of magnitude, i.e. $P_{s-d} \sim 10^3 L_{\mathrm{X}}$. The spin-down power provides a substantial reservoir of energy that may be channelled into particle acceleration and non-thermal emission (e.g. de Jager et al. 1994; Meintjes & de Jager 2000). A recent study of the X-ray emission from AE Aqr (Terada et al. 2008) using the *Suzaku* satellite showed indications of a non-thermal pulsed hard X-ray component, a telltale signature of particle acceleration in the system.

6 X-RAY EMISSION IN AE AQR

The observed X-ray features of AE Aqr tend to distinguish it from most cataclysmic variables which are mainly accretion driven (e.g. Warner 1995). For example, the spectra are mainly soft (e.g. Clayton & Osborne 1995; Choi et al. 1999; Ikhsanov & Biermann 2006), and the inferred plasma density of $n_{\mathrm{e}} \sim 10^{11}\,\mathrm{cm^{-3}}$ (e.g. Itoh et al. 2006) is a few orders less than the estimated density in the post-shock accretion column of cataclysmic variables (e.g. Ikhsanov & Biermann 2006). The inferred linear scale of $l_{\mathrm{p}} \geq 2\times10^{10}$ cm (e.g. Ikhsanov & Biermann 2006; Itoh et al. 2006) implies that the bulk of the emission is probably not coming from the surface of the white dwarf, but from a radial distance corresponding to the magnetospheric radius, from where the bulk of the matter is ejected from the binary system. The non-thermal nature of the observed hard X-ray component could indicate a different mechanism, possibly driven by the loss of rotational kinetic energy from the fast rotating white dwarf (e.g. Cheng, Gil & Zhang 1998). In this section, possible scenarios are investigated to constrain the observed thermal and non-thermal characteristics.

6.1 Soft X-ray emission: gravitational heating

The accretion scenario in AE Aqr may be compared to those in X-ray pulsars, where rapidly rotating magnetized neutron stars accrete gas from their companions (e.g. Bildsten et al. 1997 and references therein). Lipunov (1992) suggested that the system can be either in an accretor phase or in a propeller phase, depending on the rotational period and the surface magnetic field of the compact object. In the accretor phase, most of the matter is channelled by the magnetic fields on to the magnetic poles, creating heated regions where energy is radiated (e.g. Becker & Wolff 2007). However, for AE Aqr the bulk of the material is ejected at a radial distance comparable to the magnetospheric radius, casting doubt whether shock heated gas at the polar caps of the white dwarf is responsible for the bulk of the X-ray emission. For typical mass accretion rates of $\dot{M}_* \sim 10^{17}$ g s^{-1}, associated with magnetic cataclysmic variables, the accretion luminosity is given by

$$L_{\mathrm{acc}} = \frac{GM_*\dot{M}_*}{R} \simeq 10^{34}\left(\frac{M_*}{\mathrm{M_\odot}}\right)\dot{M}_{*,17}R_9\ \mathrm{erg\,s^{-1}}, \tag{8}$$

where M_* is the mass of the white dwarf, R_9 is its radius in the units of 10^9 cm and $\dot{M}_{*,17}$ is the mass accretion rate in the units of $10^{17}\,\mathrm{g\,s^{-1}}$. The observed soft X-ray luminosity of AE Aqr is $L_{\mathrm{X}} \sim 10^{31}\,\mathrm{erg\,s^{-1}}$, approximately three orders of magnitude less than L_{acc}. Besides, the inferred $T_{\mathrm{X}} > 10^6$ K associated with the observed X-ray emission in AE Aqr is probably not reconcilable with the inferred low accretion rate of approximately $\dot{M}_* \sim 10^{14}$ g s^{-1}. An alternative source of heating and associated X-ray emission may be the conversion of gravitational potential energy to heat energy of

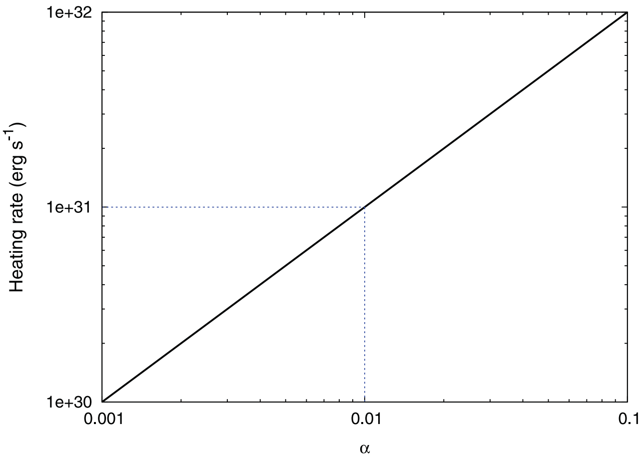

Figure 16. $\dot{E}_{\rm th}$ calculated for different values of α at the Alfvén radius for $\dot{M}_2 = 10^{17}$ g s^{-1} and $B_* = 10^6$ G.

the ballistic stream plunging into the Roche lobe of the white dwarf from the inner Lagrangian point. A qualitative discussion, aiming to illustrate the energetics involved, is presented below.

If a fraction α of the accretion power liberated at the Alfvén radius is converted into plasma heating, the resultant heating rate is

$$\dot{E}_{\rm th} = \frac{\alpha G M_* \dot{M}_2}{R_{\rm M}} \simeq 10^{31}\left(\frac{\alpha}{0.01}\right)\left(\frac{M_*}{{\rm M}_\odot}\right)^{8/7} \dot{M}_{2,17}^{9/7}\mu_{33}^{-4/7}\ {\rm erg\,s^{-1}}, \tag{9}$$

where $R_{\rm M}$ is the Alfvén radius and μ_{33} is the magnetic moment of the white dwarf in the units of 10^{33} G cm^3 for the surface magnetic field of the order of 10^6 G (Meintjes & de Jager 2000). Hence, for $\alpha \sim 0.01$, $\dot{E}_{\rm th} \sim L_{\rm X}$, as illustrated in Fig. 16. It can be shown that this dissipation rate of gravitational potential energy at the magnetospheric radius, over the free-fall time-scale, which is of the order of $t_{\rm ff} \sim 1000$ s, results in an increase in the thermal energy of the order of

$$\Delta E_{\rm th} \approx 10^{34}\left(\frac{\dot{E}_{\rm th}}{10^{31}\ {\rm erg\ s^{-1}}}\right)\left(\frac{t_{\rm ff}}{1000\ {\rm s}}\right)\ {\rm erg}. \tag{10}$$

The total thermal energy density at the magnetospheric radius as a result of the dissipation of gravitational potential energy is of the order of

$$\Delta u_{\rm th} \approx \left(\frac{\Delta E_{\rm th}}{r^3}\right) \approx 1500\left(\frac{\Delta E_{\rm th}}{10^{34}\ {\rm erg}}\right)\left(\frac{r}{R_{\rm M}}\right)^{-3}\ {\rm erg\ cm^{-3}}. \tag{11}$$

The increase in energy density as a result of the dissipation of gravitational potential energy is sufficient to heat the plasma with density $n_{\rm p}$ to temperatures

$$kT = \left(\frac{\Delta u_{\rm th}}{n_{\rm p}}\right) \le 10\left(\frac{\Delta u_{\rm th}}{1500\,{\rm erg\ cm^{-3}}}\right)\left(\frac{n_{\rm p}}{10^{11}\ {\rm cm^{-3}}}\right)^{-1}\ {\rm keV}, \tag{12}$$

which is sufficient to explain the X-ray emission in AE Aqr below 10 keV, assuming a conversion of gravitational potential energy to thermal energy of the order of $\alpha \sim 0.01$ (e.g. Choi et al. 1999).

6.2 Hard X-ray emission: pulsar model

The recent *Suzaku* observations reveal a pulsed hard X-ray component $\epsilon_{\rm X} \ge 10$ keV, with a photon power-law index of $\Gamma = 1.16$, compatible with the photon power-law index of $\Gamma \sim 1.4$ of young rotation-powered pulsars (Gotthelf 2003). It has been shown (e.g. Cheng, Taam & Wang 2006) that non-thermal X-ray emission in pulsars can usually be associated with synchrotron radiation of accelerated electrons within the magnetosphere. Since AE Aqr contains a rapidly rotating, highly magnetic white dwarf, the key factors behind the energetics of pulsar emission (e.g. Ikhsanov 1998), a pulsar-like process may be attractive to explain the origin of the observed non-thermal hard X-ray emission. Additionally, the ratio of the observed hard X-ray luminosity to the spin-down luminosity of the white dwarf in AE Aqr lies in the range of 0.01–0.1 per cent, which is the same as observed from young rotation-powered pulsars in the 2–10 keV range (e.g. Becker & Trümper 1997; Terada et al. 2008).

The process of particle acceleration in rapidly rotating magnetospheres, and the accompanying radiation, have been discussed extensively (e.g. Usov 1988, 1993; Leung, Cheng & Fung 1993; Ikhsanov & Biermann 2006). The lack of substantial mass accretion on to the surface of the white dwarf in AE Aqr (e.g. Wynn et al. 1997) may result in the white dwarf rotating in a region of low particle density. As a result, an electric field $E_\parallel$ is introduced along the magnetic field, i.e. $E_\parallel = (\boldsymbol{E}\cdot\boldsymbol{B})/B$. Close to the surface, the electric field force ($e\boldsymbol{E}$) will cause charged particles to flow away, forming a magnetosphere whose particle density is given by

$$n_{\rm GJ} = \frac{\boldsymbol{\Omega}_*\cdot\boldsymbol{B}}{2\pi c e} \simeq 2\times 10^3\left(\frac{R_*}{r}\right)^3 B_{*,6}P_{33}^{-1}\ {\rm cm^{-3}}, \tag{13}$$

where $n_{\rm GJ}$ is the so-called Goldreich–Julian particle density (e.g. Goldreich & Julian 1969), B is the magnetic field strength at a distance of $r > R_*$ (B scales as r^{-3}) and $B_{*,6}$ is the field strength at the surface of the white dwarf in the units of 10^6 G. The electric field component $E_\parallel$ can be evaluated for $s > R_*$, where $r = R_* + s$ (e.g. Arons & Scharlemann 1979):

$$E_\parallel = E_{\rm AS}^{\parallel}\sqrt{2R_*/r} \simeq 10^3 P_{33}^{-5/2}\mu_{33}r_{l,11}^{-1/2}\ \ {\rm V\ m^{-1}}, \tag{14}$$

where

$$E_{\rm AS}^{\parallel} = \frac{1}{8\sqrt{3}}\left(\frac{\Omega_* R_*}{c}\right)^{5/2} B_*, \tag{15}$$

with the field being evaluated in the vicinity of the light cylinder radius ($R_{\rm lc} \sim 1.6\times 10^{11}$ cm). A thermal plasma exposed to an electric field in excess of the so-called Dreicer field, $E_{\rm D} \sim 2\times 10^{-10}(n_{\rm e}/T_{\rm eff})$ statvolt cm^{-1} (e.g. Dreicer 1959; Meintjes & de Jager 2000), will accelerate freely without experiencing the obstructive effect introduced by particle–particle collisions. For AE Aqr,

$$E_{\rm D} \sim 0.1 n_{{\rm e},11}T_{\rm eff,7}^{-1}\ \ {\rm V\ m^{-1}}, \tag{16}$$

where the particle density and temperature are expressed in units of 10^{11} cm^{-3} and 10^7 K, respectively. One can see that $\delta = (E_\parallel/E_{\rm D}) \sim 10^4$. Thus, the electric fields along the magnetic fields are large enough to effectively accelerate the electrons to high energies, determined by the dominant energy loss mechanisms, which in the case of AE Aqr is most probably synchrotron radiation.

The electric potential in the region of the polar cap is given by

$$V_{\rm pc}(r) = \int_R^r E_\parallel\,{\rm d}s \simeq 2\times 10^{11} P_{33}^{-5/2}\mu_{33}R_9^{1/2}\left[\left(\frac{r}{R}\right)^{1/2} - 1\right]\ \ {\rm V}, \tag{17}$$

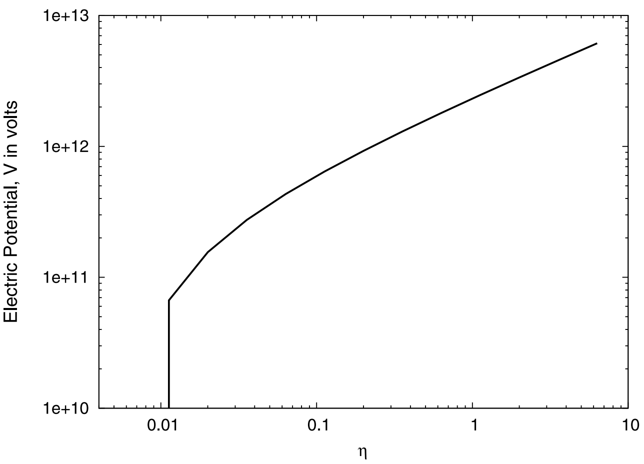

Figure 17. Electric field potential as a function of radius ($\eta = r/R_{\rm lc}$). Close to the surface of the white dwarf, $V \approx 0$.

and close to the light cylinder radius, i.e. $r \sim R_{\rm lc} \simeq c/\Omega_*$,

$$V(R_{\rm lc}) \simeq 3 \times 10^{12} P_{33}^{-2} \mu_{33} \ \ {\rm V}. \tag{18}$$

Fig. 17 shows the variation of electric potential with distance (r), expressed in terms of a fraction $\eta = (r/R_{\rm lc})$ of the light cylinder radius. Noticeable is the increase in potential difference with increasing distance, reaching large values in excess of 1 teravolt (TV) outside the light cylinder radius, approximately $R_{\rm lc} \approx 5$ ls (ls = lightseconds) from the white dwarf.

The energy of a particle accelerated in the potential $V_{\rm pc}(r)$ is given by

$$\begin{aligned}\varepsilon_{\rm p} &= eV_{\rm pc}(r)\\ &\simeq 2 \times 10^{11} P_{33}^{-5/2} \mu_{33} R_9^{1/2} \left[\left(\frac{r}{R}\right)^{1/2} - 1\right] \ \ {\rm eV},\end{aligned} \tag{19}$$

with a Lorentz factor of

$$\begin{aligned}\gamma_{\rm p} &= \frac{\varepsilon_{\rm p}}{m_{\rm e}c^2}\\ &\simeq 4 \times 10^5 P_{33}^{-5/2} \mu_{33} R_9^{1/2} \left[\left(\frac{r}{R}\right)^{1/2} - 1\right].\end{aligned} \tag{20}$$

Accelerated electrons also experience energy losses due to synchrotron radiation and inverse Compton (IC) scattering (e.g. Bednarek & Pabich 2011). In strong magnetospheres, synchrotron radiation is the dominant loss mechanism, and the energy radiation rate of an accelerated electron is then

$$L_{\rm syn} = \frac{4}{3} c \sigma_{\rm T} U_{\rm B} \gamma_{\rm p}^2, \tag{21}$$

where $\sigma_{\rm T} \sim 6.65 \times 10^{-25}\ {\rm cm}^2$ is the Thomson cross-section and $U_{\rm B}$ is the magnetospheric energy density, given by

$$\begin{aligned}U_{\rm B} &= \frac{B^2}{8\pi}\\ &\simeq 10^{12} \left(\frac{B_*}{10^6\ {\rm G}}\right)^2 \left(\frac{R_*}{r}\right)^6 \ \ {\rm erg\ cm^{-3}},\end{aligned} \tag{22}$$

where $B = B_*(R_*/r)^3$ is the magnetic field at radial distance r from the centre of the white dwarf. The energy radiation rate from the white dwarf magnetosphere is then

$$L_{\rm rad} = n(r) V' P_{\rm syn}, \tag{23}$$

where $n(r)$ is the particle density and V' is the volume of the emission region, which is probably a cylindrical shell bounded by the light cylinder radius and the radial distance r, i.e.

$$\begin{aligned}V' &= \pi \left(r^2 - R_{\rm lc}^2\right)(2R_*)\\ &\simeq 1.6 \times 10^{32} (\eta^2 - 1) R_{*,9} \left(\frac{P}{33\,s}\right)^2 \ \ {\rm cm}^3,\end{aligned} \tag{24}$$

where $\eta = r/R_{\rm lc}$. The volume V' obtained above is a lower limit, and the upper limit is obtained by considering a spherical shell. It can then be shown that

$$\begin{aligned}L_{\rm rad} &\approx 3 \times 10^{40} n(r)(\eta^2 - 1) P_{33}^{-3} B_{*,6}^2 \mu_{33}^2 R_{*,9}^2\\ &\quad \times \left(\frac{R_*}{r}\right)^6 \left[\left(\frac{r}{R_*}\right)^{1/2} - 1\right]^2 \ \ {\rm erg\ s^{-1}}.\end{aligned} \tag{25}$$

It can also be shown that the energy gain rate of particles ($P_{\rm gain} = \varepsilon_{\rm p} \dot{N}$), in the polar cap region, is

$$\begin{aligned}P_{\rm gain} &\simeq 2 \times 10^{26} n(r) P_{33}^{-7/2} \mu_{33} R_{*,9}^{7/2}\\ &\quad \times \left[\left(\frac{r}{R_*}\right)^{1/2} - 1\right] \ \ {\rm erg\ s^{-1}},\end{aligned} \tag{26}$$

where $\dot{N} \simeq n(r) c \Delta s$ is the flux of relativistic particles, with $\Delta s = \pi(\Omega R_*/c) R_*^2$, the area of the polar cap limiting the outflow of particles along open magnetic field lines.

In the magnetospheric field near the white dwarf, synchrotron losses will inhibit particle acceleration. It can be shown that synchrotron losses in the magnetosphere, inside the propeller zone, limit electron energies to

$$\gamma_{\rm e} = 10^5 \left(\frac{R_{\rm prop}}{10^{10}\ {\rm cm}}\right)^{-1} \left(\frac{B_{\rm p}}{130\,{\rm G}}\right)^{-2}, \tag{27}$$

where $B_{\rm p}$ is the value of the magnetospheric field in the propeller zone. The frequency at which individual electrons with energies $\gamma \sim 10^5$ radiate most of their energy is then

$$\nu_{\rm c} = 5 \times 10^{18} \left(\frac{B_{\rm p}}{130\,{\rm G}}\right) \left(\frac{\gamma_{\rm e}}{10^5}\right)^2 \ {\rm Hz}, \tag{28}$$

consistent with the hard X-ray emission detected with the *Suzaku* satellite reported by Terada et al. (2008). The reported hard ($\geq$10 keV) X-ray luminosity of $L_{\rm X,hard} \leq 5 \times 10^{30}\ {\rm erg\ s^{-1}}$ (Terada et al. 2008) corresponds to $\kappa \sim 0.1$ per cent of the spin-down power, putting AE Aqr in the same category as young rotation-powered pulsars in the 2–10 keV energy range (Becker & Trümper 1997).

Effective acceleration to VHE energies is anticipated to occur in regions where the synchrotron losses are less dominant than the acceleration. The lower boundary of the acceleration zone can be constrained, i.e. when the power in relativistic particles (equation 26) is compared to the total synchrotron luminosity (equation 25). One then obtains

$$(\eta^2 - 1) \left(\frac{R_*}{r}\right)^6 \left[\left(\frac{r}{R_*}\right)^{1/2} - 1\right] \leq 7 \times 10^{-15}. \tag{29}$$

Considering that $R \ll r$, it can be shown that the acceleration dominates synchrotron losses in regions corresponding to $r \geq 6 \times 10^{11}$ cm, translating to $\eta = r/R_{\rm lc} \geq 4$. This implies that effective acceleration to VHE energies ($\gamma \sim 10^7$) occurs outside the light cylinder radius.

Highly relativistic electrons with energies $\gamma \sim 10^7$ provide an interesting possibility for high-energy gamma-ray production by upscattering soft photons from the K-type companion star, or propeller ejected outflow, to high energies, i.e. the inverse Compton process. It can be shown that the inverse Compton process occurs in the Thomson limit for photon frequencies

$$\nu < 1.2 \times 10^{13} \left(\frac{\gamma}{10^7}\right)^{-1} \text{Hz}, \tag{30}$$

which are consistent with the photon frequencies associated with the low-energy tail of the K3-5 secondary star, or a circumbinary ring that may orbit the system (Dubus et al. 2004). An upper limit for gamma-ray energies produced in the Thomson limit is

$$\epsilon_\gamma \leq 20 \left(\frac{\gamma}{10^7}\right)^2 \left(\frac{\epsilon_{\rm ph}}{0.05\,\text{eV}}\right) \text{TeV}, \tag{31}$$

which provides an interesting prospect for follow-up studies using *Fermi* and modern Cerenkov facilities like the High-Energy Stereoscopic System (HESS) in Namibia.

7 SPECTRAL ENERGY DISTRIBUTION OF AE AQR

The peculiar nova-like variable AE Aqr has been observed from radio to possibly VHE and TeV energies (e.g. Patterson 1979; Bastian et al. 1988; Meintjes et al. 1992, 1994; Chadwick et al. 1995; Dubus et al. 2004). The peculiar multiwavelength characteristics of the source are illustrated clearly by constructing the SED from radio to the reported, but still unconfirmed, VHE and TeV gamma-ray emission. Two sets of data were used to construct the SED for AE Aqr, i.e. archive data and analysed data (*Swift* and *Chandra*). For the archive data, the Vizier online service was used and the energy fluxes obtained are shown in Table 3. For the analysed data, the data from *Swift* UVOT and *Chandra* were used (Table 4) and combined with additional published results. For example, the radio to optical data were taken from Abada-Simon et al. (2005) and Dubus et al. (2004) and references therein. The hard X-ray data were taken from Terada et al. (2008). These data were combined with the unconfirmed reports of transient burst-like VHE and TeV gamma-ray emission (Meintjes et al. 1992, 1994; Chadwick et al. 1995). The reported TeV gamma-ray emission also showed pulsations corresponding to the 33-s rotation period of the white dwarf (Meintjes et al. 1992, 1994). The derived duty cycle for the burst-like emission was approximately $\delta_{\rm burst} \sim 0.024$ per cent, while the duty cycle for strong pulsed emission close to the spin period of the white dwarf, above the 99.999 per cent confidence level, was $\delta_{\rm pulsed} \sim 1$ per cent. However, weak pulsed emission at the spin period, above the 95 per cent significance level, was detected more often with a duty cycle of approximately $\delta_{\rm weak} \sim 30$ per cent in all the observations between 1988 and 1991 (Meintjes et al. 1992, 1994). It has been shown (Meintjes & de Jager 2000) that the burst-like VHE and TeV gamma-ray emission is most probably the result of burst-like particle acceleration events associated with the magnetospheric propeller process, i.e. exploding double layers and magnetic reconnection. It has been shown that the associated TeV gamma-ray flux levels measured during short burst-like episodes (Meintjes et al. 1994; Meintjes & de Jager 2000) correspond to the entire spin-down luminosity ($L_{\rm s-d} \sim 10^{34}$ erg s^{-1}) of the white dwarf being converted into VHE and TeV gamma-ray emission over time-scale of approximately 1 min. The multiwavelength SED is displayed in Fig. 18.

Table 3. Radio to X-ray data for AE Aqr, taken from published results obtained from the Vizier online catalogue. The online magnitude-to-flux conversion tool was used to calculate fluxes for IR and optical data. For the X-ray data, the satellites' conversion factors were used to calculate fluxes from count rates.

Radio to near-IR		Optical to X-rays	
Frequency (Hz)	Energy flux (erg cm^{-2} s^{-1})	Frequency (Hz)	Energy flux (erg cm^{-2} s^{-1})
1.4×10^9	8.4×10^{-17}	3.3×10^{14}	6.1×10^{-10}
2.5×10^{11}	6.0×10^{-14}	4.3×10^{14}	6.3×10^{-10}
1.4×10^{14}	2.6×10^{-10}	5.5×10^{14}	5.9×10^{-10}
1.8×10^{14}	4.8×10^{-10}	2.4×10^{17}	1.2×10^{-11}
2.4×10^{14}	6.0×10^{-10}	4.8×10^{17}	6.7×10^{-12}

Table 4. Near-UV and X-ray fluxes obtained from *Swift* UVOT and *Chandra* data.

UV data		X-ray data	
Frequency (Hz)	Energy flux (erg cm^{-2} s^{-1})	Frequency (Hz)	Energy flux (erg cm^{-2} s^{-1})
1.00×10^{15}	1.70×10^{-10}	3.63×10^{17}	3.16×10^{-12}
1.10×10^{15}	8.96×10^{-11}	6.05×10^{17}	1.18×10^{-12}
1.20×10^{15}	4.50×10^{-11}	1.09×10^{18}	4.88×10^{-13}
1.30×10^{15}	2.21×10^{-11}	1.57×10^{18}	5.78×10^{-13}
1.40×10^{15}	1.05×10^{-11}	1.81×10^{18}	2.68×10^{-13}

The radio-to-far-IR data have been fitted with a power-law model (po). The emission in this wavelength band is attributed to synchrotron radiation of expanding magnetized blobs of electrons (e.g. Bastian et al. 1988; Meintjes & Venter 2003; Venter & Meintjes 2006) which become optically thin (and hence the electrons follow a power-law distribution), and subsequently emit the observed non-thermal radiation. The near-IR, optical and near-UV data are fitted with a thermal blackbody model (bb) of temperature of $T_{\rm bb} \simeq 4.65 \times 10^3$ K, associated with the secondary star companion.

The non-thermal nature of the transient radio emission (e.g. Bastian et al. 1988), combined with the possible non-thermal nature of the hard X-ray emission above 10 keV (Terada et al. 2008) and the VHE and TeV gamma-ray emission reported in the 1990s (e.g. Meintjes et al. 1992, 1994; Chadwick et al. 1995), clearly shows that AE Aqr possibly hosts sites of particle acceleration with associated non-thermal emission over 18 decades in frequency.

8 SUMMARY

The X-ray light curves of AE Aqr reveal that the source is highly variable and characterized by flaring. The observed flares in the light curves could be the result of a sudden increase in the emission due to sporadic mass accretion. The spectra (below 10 keV) are mainly soft, characterized by emission lines, and can be fitted with multicomponent thermal emission models. A period and pulse analysis shows that the X-ray emission is pulsed at a period consistent with the spin period of the white dwarf. It is shown that the soft thermal X-ray emission in AE Aqr is produced as a result of the dissipation of some fraction ($\alpha \sim 0.01$) of the gravitational potential energy at the magnetospheric radius with only a small fraction ($\beta \sim 0.03$ per cent) of the mass transfer flow being accreted. This is sufficient to explain the pulsed nature and luminosity associated with the soft X-ray emission in AE Aqr below 10 keV. The hard X-ray emission above 10 keV exhibits a non-thermal power law with a photon index of $\Gamma \approx 1.2$, similar to young rotation-powered pulsars. The hard X-ray luminosity also constitutes a fraction of $\kappa \sim 0.1$ per cent of the spin-down luminosity, also observed in young pulsars. This makes AE Aqr unique among the cataclysmic variables. The SED reveals multiwavelength emission over 18 decades in

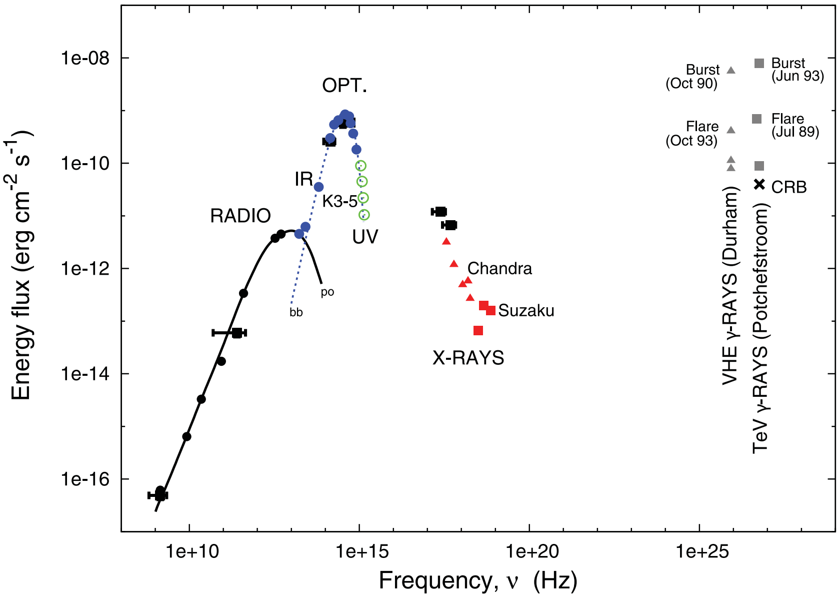

Figure 18. SED of AE Aqr. Catalogue data are the black filled squares with error bars and the analysed data are the rest of the points. States of bursts and flares are indicated in the VHE γ-ray and TeV γ-ray regimes.

frequency, of which a large fraction is non-thermal emission associated with particle acceleration. It is likely that most of the emission processes occur in the propeller zone, where a significant amount of the spin-down power of the white dwarf is converted into propeller-driven mass outflow and radiation. The unconfirmed reports of pulsed VHE and TeV gamma-ray emission, albeit with a low duty cycle, justify follow-up observational campaigns with modern Cerenkov facilities.

ACKNOWLEDGMENTS

This research has made use of data obtained from three Chandra Data Archive and the Chandra Source Catalog, and software provided by the Chandra X-ray Center (CXC) in the application packages CIAO, ChIPS, and Sherpa. The research has also made use of data supplied by the UK Swift Science Data Centre at the University of Leicester, and the VizieR catalogue access tool, CDS, Strasbourg, France (http://vizier.u-strasbg.fr/viz-bin/VizieR). One of the authors, BO, was funded by the South African Square Kilometre Array Project and the National Research Foundation (NRF) of South Africa. A special word of thanks to Dr Chris Mauche for several very enlightening discussions related to the X-ray emission from AE Aquarii.

REFERENCES

Abada-Simon M., Lecacheux A., Bastian T. M., Bookbinder J. A., Dulk G. A., 1993, ApJ, 406, 692
Abada-Simon M. et al., 2005, A&A, 433, 1063
Arons J., Scharlemann E. T., 1979, ApJ, 231, 854
Barthelmy S. D. et al., 2005, Space Sci. Rev., 120, 143
Bastian T. S., Dulk G. A., Chanmugam G., 1988, ApJ, 324, 431
Becker W., Trümper J., 1997, A&A, 326, 682
Becker P. A., Wolff M. T., 2007, ApJ, 654, 435
Bednarek W., Pabich J., 2011, MNRAS, 411, 1701
Bildsten L. et al., 1997, ApJS, 113, 367
Bookbinder J. A., Lamb D. Q., 1987, ApJ, 323, 131
Brissenden R. J., 2001, in Harnden F. R., Jr, Primini F. A., Payne H. E., eds, ASP Conf. Ser. Vol. 238, Astronomical Data Analysis Software and Systems X. Astron. Soc. Pac., San Francisco, p. 22
Burrows D. N. et al., 2005, Space Sci. Rev., 120, 165
Capalbi M., Perri M., Saija B., Tamburelli F., Angelini L., 2005. The *Swift* X-Ray Telescope Data Reduction Guide. ASI Science Data Center. Available online: http://heasarc.nasa.gov/docs/swift/analysis/xrt_swguide_v1_2.pdf
Casares J., Mouchet M., Martinez-Pais I. G., Harlaftis E. T., 1996, MNRAS, 282, 182
Chadwick P. M. et al., 1995, Astropart. Phys., 4, 99
Cheng K. S., Gil J., Zhang L., 1998, ApJ, 493, 35
Cheng K. S., Taam R. E., Wang W., 2006, ApJ, 641, 427
Chincarini G., Walker M. F., 1981, A&A, 104, 24
Choi C.-S., Dotani T., 2006, ApJ, 646, 1149
Choi C.-S., Dotani T., Agrawal P. C., 1999, ApJ, 525, 399
Clayton K. L., Osborne J. P., 1995, in Buckley D. A. H., Warner B., eds, ASP Conf. Ser. Vol. 85. Cape Workshop on Magnetic Cataclysmic Variables Astron. Soc. Pac., San Francisco, p. 379
Crawford J. A., Craft R. P., 1956, ApJ, 123, 44
de Jager O. C., 1991a, ApJ, 378, 286
de Jager O. C., 1991b, Int. Cosmic Ray Conf., 2, 463
de Jager O. C., 1994, ApJS, 90, 775
de Jager O. C., Meintjes P. J., O'Donoghue D., Robinson E. L., 1994, MNRAS, 267, 577
Dreicer H., 1959, Phys. Rev., 115, 242
Dubus G., Campbell R., Kern B., Taam R. E., Spruit H. C., 2004, MNRAS, 349, 869
Eracleous M., Horne K., 1996, ApJ, 471, 427
Eracleous M., Horne K., Robinson E. L., Zhang E., Marsh T. R., Wood J. H., 1994, ApJ, 433, 313
Evans P. A. et al., 2007, A&A, 469, 379
Evans P. A. et al., 2009, MNRAS, 397, 1177
Gehrels N. et al., 2004, ApJ, 611, 1005
Goldreich P., Julian W., 1969, ApJ, 175, 869
Gotthelf E. V., 2003, ApJ, 591, 361
Hill J. E. et al., 2004, in Flanagan K. A., Siegmund O. H. W., eds, Proc. SPIE Vol. 5165, X-Ray and Gamma-Ray Instrumentation for Astronomy XIII. SPIE, Bellingham, p. 217
Ikhsanov N. K., 1997, A&A, 325, 1045
Ikhsanov N. K., 1998, A&A, 338, 521
Ikhsanov N. K., Biermann P. L., 2006, A&A, 445, 305
Itoh K., Okada S., Ishida M., Kunieda H., 2006, ApJ, 639, 397
Joy A. H., 1954, ApJ, 120, 377
Leung P. P., Cheng K. S., Fung P. C. W., 1993, ApJ, 410, 309

Lipunov V. M., 1992, Astrophysics of Neutron Stars. Springer-Verlag, Berlin, p. 83
Mauche C. W., 2006, MNRAS, 369, 1983
Mauche C. W., 2009, ApJ, 706, 130
Meintjes P. J., 2002, MNRAS, 336, 265
Meintjes P. J., de Jager O. C., 2000, MNRAS, 311, 611
Meintjes P. J., Venter L. A., 2003, MNRAS, 341, 891
Meintjes P. J., Venter L. A., 2005, MNRAS, 360, 573
Meintjes P. J., Raubenheimer B. C., de Jager O. C., Brink C., Nel H. I., North A. R., van Urk G., Visser B., 1992, ApJ, 401, 325
Meintjes P. J., de Jager O. C., Raubenheimer B. C., Nel H. I., North A. R., Buckley D. A. H., Koen C., 1994, ApJ, 434, 292
Patterson J., 1979, ApJ, 234, 978
Patterson J., Branch D., Chincarini G., Robinson E. L., 1980, ApJ, 240, L133
Roming P. W. A. et al., 2005, Space Sci. Rev., 120, 95
Schenker K., King A. R., Kolb U., Wynn G. A., Zhang Z., 2002, MNRAS, 337, 1105
Terada Y. et al., 2008a, PASJ, 60, 387
Terada Y. et al., 2008b, Adv. Space Res., 41, 512
Usov V. V., 1988, Pis'ma Astron. Zh., 14, 606
Usov V. V., 1993, ApJ, 410, 761
Venter L. A., Meintjes P. J., 2006, MNRAS, 366, 557
Warner B., 1983, in Livio M., Shaviv G., eds, Cataclysmic Variables and Related Objects. Reidel, Dordrecht, p. 155
Warner B., 1995, Cataclysmic Variable Stars. Cambridge Univ. Press, Cambridge, p. 417
Weisskopf M. C., 2003, Adv. Space Res., 32, 2005
Weisskopf M. C., Brinkman B., Canizares C., Garmire G., Murray S., van Speybroeck L. P., 2002, PASP, 114, 1
Welsh W. F., Horne K., Oke J. B., 1993a, ApJ, 406, 229
Welsh W. F., Horne K., Gomer R., 1993b, ApJ, 410, L39
Welsh W. F., Horne K., Gomer R., 1995, MNRAS, 275, 649
Wynn G. A., King R. A., Horne K., 1997, MNRAS, 286, 436
Zinner E., 1938, Astron. Nachr., 265, 345

This paper has been typeset from a TEX/LATEX file prepared by the author.

A.2 B Oruru and P J Meintjes, 2011, Proceedings of SAIP 2011, ISBN: 978-1-86888-688-3, 501-506

Pulsar-like hard X-ray emission in AE Aquarii

B Oruru and P J Meintjes

Department of Physics, University of the Free State, P. O. Box 339, Bloemfontein 9300, ZA

E-mail: OruruB@ufs.ac.za, MeintjPJ@ufs.ac.za

Abstract. Spectral analyses have revealed that the X-ray emission in AE Aquarii displays both thermal and non-thermal characteristics. The recently detected non-thermal hard X-ray component above 10 keV is pulsed with the 33 s spin period of the white dwarf, and displays the tell-tale signature of synchrotron emission of high energy electrons in the white dwarf magnetosphere. It is proposed that these electrons are accelerated by large field aligned potentials of $V > 10^{12}$ V, a process common in the environments of fast rotating neutron stars, or pulsars. This places AE Aquarii in a unique category with respect to other members of the cataclysmic variables.

1. Introduction

The low-mass non-eclipsing close binary system AE Aquarii (hereafter AE Aqr) has traditionally been classified as a nova-like variable [1, 2, 3]. The peculiar high variability has been explained in terms of a magnetic white dwarf accreting gas from an orbiting disc surrounding it, which is fed from the mass transfer from the orbiting secondary star. Based upon most of the observable properties, AE Aqr was then considered as a member of the DQ Herculis sub-class of magnetic cataclysmic variables, where a fast rotating magnetized white dwarf is accreting material from an accretion disc [4]. However, the lack of double-peak emission lines, the tell-tale signature of emission originating in a disc, combined with the high line variability, suggest the absence of a disc. The current mass transfer rate $\dot{M} \sim 10^{17}\,\mathrm{g\ s^{-1}}$ [5] from the secondary star is also not able to penetrate the fast rotating magnetosphere deep enough to form a disc, and is most probably ejected from the binary system through a magnetospheric propeller process [5, 6].

AE Aqr shows orbital modulation at a period of 9.88 h [1, 4], which is rather long for a typical cataclysmic variable. The white dwarf is spinning at ~ 33 s [7, 8] and has a surface magnetic field of $B_* \sim 10^6$ G [10]. The white dwarf is reportedly spinning down at a period rate of $\dot{P} \geqslant 5.642\times10^{-14}\ \mathrm{s\ s^{-1}}$ [7, 9], resulting in an inferred spin-down power of the order of $P_{\rm sd} \sim 10^{34}\,\mathrm{erg\ s^{-1}}$, believed to be the driving mechanism behind the magnetospheric propeller process, as well as particle acceleration and non-thermal emission [5, 10].

AE Aqr has been detected in almost the entire electromagnetic spectrum, in which coherent oscillations at the white dwarf spin period have been observed [4, 11, 7, 12, 13]. The most unique characteristic of AE Aqr is perhaps its rapid flaring in almost all wavelengths [14]. In radio and TeV γ-rays, AE Aqr shows up as a transient non-thermal source, and could rather be compared with Cyg X-3 (a microquasar) than with any of the presently known cataclysmic variables [8]. In the remaining parts of the spectrum, the emission is predominantly thermal. However, the recent Suzaku X-ray detection [15, 16] has shown that the high energy component of the X-ray emission ($E_\gamma \geq 10\,\mathrm{keV}$) displays a non-thermal spectral nature, with a photon power-law index of $\Gamma = 1.16$ similar to the photon power-law index observed in young rotation-powered pulsars in the energy range between 2-10 keV [16]. Based on the observed characteristics of the hard X-ray emission (listed in §2), a model is proposed to explain it within the framework of a pulsar-like mechanism, driven by the spin-down power released in the propeller process. This would place AE Aqr in the same category as rotation-powered pulsars driven by the loss of rotational kinetic energy of a rapidly rotating, highly magnetized neutron star.

2. Possible models for X-ray emission

The observed X-ray features of AE Aqr make it quite different from most cataclysmic variables, which are mainly accretion driven. The spectrum are mainly soft [17, 18], the inferred plasma density of $n_e \sim 10^{11}$ cm^{-3} [6] is a few orders less than the estimate in the postshock accretion column of cataclysmic variables [18], and the inferred linear scale of $l_{\rm p} \geqslant 2\times 10^{10}$ cm [6, 18] implies that the emission is probably not coming from the surface of the white dwarf. The non-thermal nature of the observed hard X-ray component could indicate a different mechanism, driven by the loss of rotational kinetic energy from the fast rotating white dwarf [19]. In this section, possible emission models are investigated to constrain the observed thermal and non-thermal X-ray emission in AE Aqr.

2.1. Soft X-rays: Magnetospheric accretion

Accretion in AE Aqr may be compared to those in X-ray pulsars, where rapidly rotating magnetized neutron stars accrete from their companions [20]. This can occur either in the accretor or propeller phases, depending on the rotational period and surface magnetic field of the primary star [21]. In the accretor phase, most of the matter is channeled onto the magnetic poles and falls onto the surface creating small heated regions where energy is radiated [22]. The scenario corresponds to the flow of a mixture of gas and radiation inside a magnetic pipe, sealed with respect to the gas but transparent to the radiation [23]. The typical accretion luminosity applicable to most white dwarfs in cataclysmic variables in general, is given by

$$L_{\rm acc} = \frac{GM_*\dot{M}}{R_*} \simeq 1.3\times 10^{34}\left(\frac{M_*}{M_\odot}\right)\dot{M}_{17}R_{*,9}^{-1}\ {\rm erg\ s^{-1}}, \tag{1}$$

where M_* is the mass of the white dwarf in Solar mass units, $R_{*,9}$ its radius in the units of 10^9 cm, and $\dot{M}_{17}$ is the typical mass accretion rate in the units of 10^{17} g s^{-1} respectively. The estimate of the temperature of a black body radiating this luminosity is

$$T_{\rm eff} = \left(\frac{L_{\rm acc}}{A_{\rm cap}\sigma_{\rm SB}}\right)^{1/4} \simeq 3.27\times 10^5\left(\frac{M_*}{M_\odot}\right)^{1/4}\dot{M}_{17}^{\frac{1}{4}}R_{*,9}^{-1}P_{33}^{\frac{1}{4}}\ {\rm K}, \tag{2}$$

where $A_{\rm cap} = \pi(\Omega_* R_*/{\rm c})R_*^2$, is the area of the polar cap, Ω_* is the angular frequency of the white dwarf, $\sigma_{\rm SB}$ is the Stefan-Boltzmann constant, and P_{33} is the spin period, normalized to the 33 s spin period of the white dwarf in AE Aqr. However, the observed X-ray luminosity of AE Aqr is $L_{\rm X} \sim 10^{31}$ erg s^{-1} [12, 17], 3 orders of magnitude less than $L_{\rm acc}$, and the observed temperature of $T_{\rm X} > 10^6$ K [11] is an order of magnitude greater than $T_{\rm eff}$. Therefore, it is unlikely that the X-ray emission is the result of accretion onto the surface of the white dwarf.

If a fraction α of the accretion power liberated at the magnetospheric radius, i.e. the Alfvén radius, is converted to plasma heating, the resultant heating rate is

$$\dot{E}_{\rm th} = \frac{\alpha GM_*\dot{M}}{R_{\rm M}} \simeq 10^{31}\left(\frac{\alpha}{0.01}\right)\left(\frac{M_*}{M_\odot}\right)^{8/7}\dot{M}_{17}^{\frac{9}{7}}\mu_{33}^{-\frac{4}{7}}\ {\rm erg\ s^{-1}}, \tag{3}$$

where $R_{\rm M}$ is the Alfvén radius,

$$R_{\rm M} = \left(\frac{\mu^2}{2\dot{M}(2GM_*)^{1/2}}\right)^{2/7} \simeq 2\times 10^{10}\left(\frac{M_*}{M_\odot}\right)^{-1/7} \dot{M}_{17}^{-\frac{2}{7}}\mu_{33}^{\frac{4}{7}} \text{ cm}, \tag{4}$$

with μ_{33} the magnetic moment of the white dwarf in the units of 10^{33} G cm^3 and mass transfer rates of the order of $\sim 10^{17}$ g s^{-1}, applicable to AE Aqr and most cataclysmic variables. Hence, $\dot{E}_{\rm th} \rightarrow L_{\rm X}$ for $\alpha \rightarrow 0.01$. It can be shown that this dissipation rate of gravitational potential energy at the magnetospheric radius, i.e. the propeller zone, will heat the plasma to temperatures $kT_{\rm X} \leq 10\,$keV, sufficient to explain the soft X-ray emission in AE Aqr [17].

2.2. *Hard X-rays: Pulsar model*

The energetics of particle acceleration and accompanying synchrotron emission of accelerated electrons are investigated as a possible model to explain the non-thermal power-law nature of the hard X-ray emission (above 10 keV) in AE Aqr. Non-thermal X-ray emission in pulsars has been associated with synchrotron radiation from relativistic electrons accelerated within the magnetosphere of the fast rotating neutron star [24]. This pulsar-like process is particularly attractive for AE Aqr since it contains a rapidly rotating, highly magnetic white dwarf, the key factors behind the energetics of pulsar emission [25]. Also, for AE Aqr, the ratio of the observed hard X-ray luminosity to the spin-down power lies in the range 0.01-0.1 %, which is the same as observed from young rotation-powered neutron stars in the 2-10 KeV range [16, 26].

The process of particle acceleration in rapidly rotating magnetospheres have been discussed extensively [28, 29, 30, 18]. The lack of substantial accretion onto the surface of the white dwarf may result in the white dwarf rotating in a region of low particle density, which is required to support the production of electric fields directed along the rotating magnetic fields. Close to the surface, the electric field force $(e\vec{E})$ will cause charged particles to flow away, forming a magnetosphere whose particle density is given by

$$n_{\rm GJ} = \frac{\mathbf{\Omega}_* \cdot \mathbf{B}}{2\pi ec} \simeq 2\times 10^3\left(\frac{R_*}{r}\right)^3 B_{*,6}P_{33}^{-1} \text{ cm}^{-3}, \tag{5}$$

where $n_{\rm GJ}$ is the so-called Goldreich-Julian particle density allowing the existence of electric fields in a plasma [27], B is the magnetic field strength at a distance $r > R_*$ (B scales as r^{-3}), and $B_{*,6}$ is the field strength at the surface of the white dwarf in the units of 10^6 G. The electric field component $E_{||}$ can be evaluated for $s > R_*$, where $r = R_* + s$ [31]:

$$E_{||} = E_{\rm AS}^{||}\sqrt{2R_*/r} \simeq 10^3 P_{33}^{-\frac{5}{2}}\mu_{33} r_{l,11}^{-1/2} \text{ V m}^{-1}, \tag{6}$$

where

$$E_{\rm AS}^{||} = \frac{1}{8\sqrt{3}}\left(\frac{\Omega_* R_*}{c}\right)^{5/2} B_*, \tag{7}$$

with the field being evaluated in the vicinity of the light cylinder radius ($R_{\rm lc} \sim 1.6\times 10^{11}$ cm). A thermal plasma exposed to an electric field in excess of the so-called Dreicer field, $E_{\rm D}$ $\sim 2\times 10^{-10}(n_{\rm e}/T_{\rm eff})$ statvolts cm^{-1} [32, 10], will accelerate freely without being hindered by particle-particle collisions. For AE Aqr,

$$E_{\rm D} \sim 0.1 n_{e,11} T_{eff,7}^{-1} \text{ V m}^{-1}, \tag{8}$$

where the particle density and temperature are expressed in units of $10^{11}\,$cm^{-3} and $10^7\,$K respectively. One can see that $\delta = \frac{E_{||}}{E_D} \sim 10^4$. Thus, the electric fields along the magnetic fields are large enough to effectively accelerate the electrons to high energy.

In the region of the polar cap, the electric potential is

$$V_{\rm pc}(r) = \int_{R_*}^{r} E_{\|} ds \simeq 2 \times 10^{11} P_{33}^{-\frac{5}{2}} \mu_{33} R_{*,9}^{1/2} \left[\left(\frac{r}{R_*} \right)^{1/2} - 1 \right] \ {\rm V}, \tag{9}$$

and close to the light cylinder radius where $r \sim R_{\rm lc} \simeq c/\Omega_*$,

$$V(R_{\rm lc}) \simeq 3 \times 10^{12} P_{33}^{-2} \mu_{33} \ {\rm V}. \tag{10}$$

Figure 1 shows the variation of electric potential with radius. Close to the surface of the white dwarf, $V = 0$ and particle acceleration is not possible. Far outside, the electric potential is large

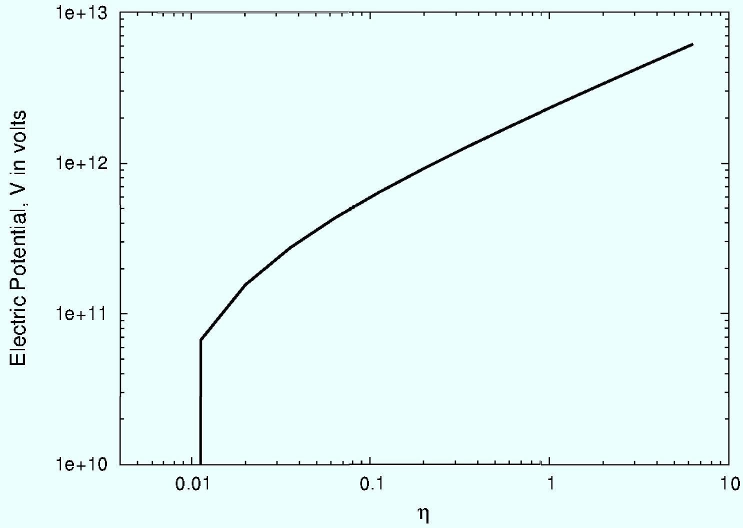

Figure 1. Electric field potential (V) as a function of radius (where $\eta = r/R_{\rm lc}$).

enough to accelerate the electron population. A particle accelerated in $V_{\rm pc}(r)$ has energy,

$$\varepsilon_{\rm p} = eV_{\rm pc}(r) \simeq 2 \times 10^{11} P_{33}^{-\frac{5}{2}} \mu_{33} R_{*,9}^{1/2} \left[\left(\frac{r}{R_*} \right)^{1/2} - 1 \right] \ {\rm eV}, \tag{11}$$

hence a Lorentz factor of

$$\gamma_{\rm p} = \frac{\varepsilon_{\rm p}}{m_e c^2} \simeq 4 \times 10^{5} P_{33}^{-\frac{5}{2}} \mu_{33} R_{*,9}^{1/2} \left[\left(\frac{r}{R_*} \right)^{1/2} - 1 \right]. \tag{12}$$

As the electrons are accelerated, they also experience energy losses due to synchrotron radiation and inverse Compton (IC) scattering [33]. In strong magnetospheres, synchrotron radiation dominates significantly, and the energy loss rate of an accelerated electron is

$$L_{\rm syn} = \frac{4}{3} c \sigma_{\rm T} U_{\rm B} \gamma_{\rm p}^2, \tag{13}$$

where $\sigma_{\rm T} \sim 6.65 \times 10^{-25}$ cm^2, is the Thomson cross section, and the magnetospheric energy density $U_{\rm B}$ is given by

$$U_{\rm B} = \frac{B^2}{8\pi} \simeq 10^{12} \left(\frac{B_*}{10^6 \ {\rm G}} \right)^2 \left(\frac{R_*}{r} \right)^6 \ {\rm erg \ cm^{-3}}, \tag{14}$$

where $B = B_*(R_*/r)^3$, is the magnetic field at radial distance r from the centre of the white dwarf. The energy radiation rate from the white dwarf magnetosphere is then

$$L_{\rm rad} = n(r)V'P_{\rm syn}, \tag{15}$$

where $n(r)$ is the accelerated particle density and V' is the volume of the emission region, which is the cylindrical shell bounded by the light cylinder radius and the radial distance r:

$$V' = \pi(r^2 - R_{\rm lc}^2)(2R_*) \simeq 1.6 \times 10^{32}(\eta^2 - 1)R_{*,9}\left(\frac{P}{33\ {\rm s}}\right)^2\ {\rm cm}^3, \tag{16}$$

where $\eta = r/R_{\rm lc}$. The volume V' obtained above is a lower limit, the upper limit is obtained by considering a spherical shell. It can then be shown that

$$L_{\rm rad} \approx 3 \times 10^{40} n(r)(\eta^2 - 1)P_{33}^{-3}B_{*,6}^2\mu_{33}^2R_{*,9}^2\left(\frac{R_*}{r}\right)^6\left[\left(\frac{r}{R_*}\right)^{1/2} - 1\right]^2\ {\rm erg\ s^{-1}}. \tag{17}$$

It can also be shown that, in the region of the polar cap, particles gain energy at the rate,

$$P_{\rm gain} = \varepsilon_{\rm p}\dot{N} \simeq 2 \times 10^{26} n(r)P_{33}^{-\frac{7}{2}}\mu_{33}R_{*,9}^{\frac{7}{2}}\left[\left(\frac{r}{R_*}\right)^{1/2} - 1\right]\ {\rm erg\ s^{-1}}, \tag{18}$$

where $\dot{N} \simeq n(r)c\Delta s$, is the flux of relativistic particles, and $\Delta s = \pi(\Omega R/c)R^2$, is the area of the polar cap on the surface of the white dwarf about which the particles escape.

In the magnetospheric field closed to the white dwarf, energy losses will inhibit the acceleration process. Effective acceleration is anticipated to occur in regions where the synchrotron losses are less dominant than the acceleration. To constrain the lower boundary of the acceleration zone, the radial distance (r) is determined by equating the power in relativistic particles (Eq. 18) to the total synchrotron luminosity (Eq. 17). One then obtains,

$$(\eta^2 - 1)\left(\frac{R_*}{r}\right)^6\left[\left(\frac{r}{R_*}\right)^{1/2} - 1\right] \leqslant 7 \times 10^{-15}. \tag{19}$$

Considering that $R \ll r$, it can be shown that the acceleration dominates synchrotron losses in regions corresponding to $r \geqslant 6\times10^{11}$ cm, which translates to $\eta = r/R_{\rm lc} \geqslant 4$. This implies that effective acceleration occurs at distances significantly outside the propeller zone.

Using Hubble Space Telescope (HST) UV spectroscopic measurements, the interblob plasma density in the propeller zone, i.e. $r \sim 10^{10}$ cm [5, 10], has been constrained between 10^6 cm^{-3} $\leqslant n_{\rm p} \leqslant 10^{11}$ cm^{-3} [34, 10]. For the model synchrotron power (Eq. 17) to match the observed hard X-ray luminosity of $L_{\rm HX} \leqslant 5\times10^{30}$ erg s^{-1} [15, 16], the relativistic electron number density in the emission region is $n(r) \sim 4\times10^3$ cm^{-3}, which is comparable to the estimated Goldreich-Julian value (Eq. 5) and orders of magnitude below the plasma density in the propeller zone closer to the white dwarf. It is encouraging to note that only a minute fraction $\eta \to 0.004$ of the lower limit of the thermal plasma density in the propeller zone, closer to the white dwarf, accelerated to high energy, is sufficient to explain the non-thermal hard X-ray synchrotron emission in AE Aqr.

3. Summary

It was shown that the thermal X-ray emission in AE Aqr is not the result of accretion onto the surface of the white dwarf but possibly the dissipation rate of gravitational potential energy in the propeller zone. The non-thermal hard X-ray emission has been accounted for in terms of a pulsar-like mechanism, for which synchrotron radiation of accelerated electrons takes place just outside the radius of the light cylinder of the white dwarf. The pulsar-like process will explain successfully the pulsed nature of the hard X-ray emission, as well as the observed power-law spectrum, which is also associated with the synchrotron X-ray emission from fast rotation-powered pulsars. This makes AE Aqr unique among the cataclysmic variables.

Acknowledgments

This study has been funded by the African Square Kilometre Array Project, and the National Research Foundation of South Africa. The authors would like to thank the anonymous referees for the suggestions and positive criticism.

References

[1] Joy A H 1954 *Astrophys. J.* **120** 377–83
[2] Crawford J A and Craft R P 1956 *Astrophys. J.* **123** 44–54
[3] de Jager O C 1991 *Astrophys. J.* **378** 286–92
[4] Patterson J 1979 *Astrophys. J.* **234** 978–92
[5] Wynn G A, King R A and Horne K 1997 *Mon. Not. R. Astron. Soc.* **286** 436–46
[6] Itoh K, Okada S, Ishida M and Kunieda H 2006 *Astrophys. J.* **639** 397–04
[7] de Jager O C, Meintjes P J, O'Donoghue D and Robinson E L 1994 *Mon. Not. R. Astron. Soc.* **267** 577–88
[8] Ikhsanov N K 1997 *Astron. Astrophys.* **325** 1045–54
[9] Mauche C W 2006 *Mon. Not. R. Astron. Soc.* **369** 1983–87
[10] Meintjes P J and de Jager O C 2000 *Mon. Not. R. Astron. Soc.* **311** 611–20
[11] Patterson J, Branch D, Chincarini G and Robinson E L 1980 *Astrophys. J. Lett.* **240** 133–36
[12] Eracleous M, Horne K, Robinson E L, Zhang E, Marsh T R and Wood J H 1994 *Astrophys. J.* **433** 313–31
[13] Meintjes P J, de Jager O C, Raubenheimer B C, Nel H I, North A R, Buckley D A H and Koen C 1994 *Astrophys. J.* **434** 292–05
[14] Ikhsanov N K, Neustroev V V and Beskrovnaya N G 2004 *Astron. Astrophys.* **421** 1131–42
[15] Terada Y, Ishida M, Mukai K, Dotani T, Makishima K, Naik S, Hayashi T, Okada S, Nakamura R and Enoto T 2008 *Advances in Space Research* **41** 512–17
[16] Terada Y, Hayashi T, Ishida M, Mukai K, Dotani T, Okada S, Nakamura R, Naik S, Bamba A and Makishima K 2008 *Publ. Astron. Soc. Japan* **60** 387–97
[17] Choi C-S, Dotani T and Agrawal P C 1999 *Astrophys. J.* **525** 399–06
[18] Ikhsanov N K and Biermann P L 2006 *Astron. Astrophys.* **445** 305–12
[19] Cheng K S, Gil J and Zhang L 1998 *Astrophys. J. Lett.* **493** 35–38
[20] Bildsten L *et al.* 1997, *Astrophys. J. Suppl. Ser.* **113** 367–08
[21] Lipunov V M 1992 *Astrophysics of Neutron Stars* (Berlin: Springer-Verlag) p 82
[22] Becker P A and Wolff M T 2007 *Astrophys. J.* **654** 435–57
[23] Bednarek W 2009 *Astron. Astrophys.* **495** 919–29
[24] Cheng K S, Taam R E and Wang W 2006 *Astrophys. J.* **641** 427–37
[25] Ikhsanov N K 1998 *Astron. Astrophys.* **338** 521–26
[26] Becker W and Trümper J 1997 *Astron. Astrophys.* **326** 682–92
[27] Goldreich P and Julian W 1969 *Astrophys. J.* **175** 869–80
[28] Leung P P, Cheng K S and Fung P C W 1993 *Astrophys. J.* **410** 309–14
[29] Usov V V 1988 *Pis'ma Astron. Zh.* **14** 606–09
[30] Usov V V 1993 *Astrophys. J.* **410** 761–63
[31] Arons J and Scharlemann E T 1979 *Astrophys. J.* **231** 854–79
[32] Dreicer H 1959 *Phys. Rev.* **115** 238–49
[33] Bednarek W and Pabich J 2011 *Mon. Not. R. Astron. Soc.* **411** 1701–06
[34] Eracleous M and Horne K 1996 *Astrophys. J.* **471** 427–46

A.3 B Oruru and P J Meintjes, 2011, Proceedings of SAIP 2011, ISBN: 978-1-86888-688-3, 507-512

X-ray timing and spectral analyses of the unusual magnetic cataclysmic variable AE Aquarii

B Oruru and P J Meintjes

Department of Physics, University of the Free State, P. O. Box 339, Bloemfontein 9300, ZA

E-mail: OruruB@ufs.ac.za, MeintjPJ@ufs.ac.za

Abstract. Analyses of the X-ray light curves and spectra of AE Aquarii from data observed contemporaneously with Chandra and Swift X-ray satellites are presented. The X-ray emission in the 0.3-10 keV range is predominantly soft and characterised by flares and emission lines, contrary to the hard X-ray emission above 10 keV, which shows a non-thermal nature, possible synchrotron emission of high energy electrons. The soft X-ray spectra, below 10 keV, can be reproduced by multi-component thermal emission models, and the time-averaged X-ray luminosity is calculated to be $\sim 10^{31}$ erg s^{-1}. It is shown that the X-ray emission is pulsed at a period consistent with the 33 s spin period of the white dwarf, and its source is linked with the interaction between the white dwarf magnetosphere and the accretion flow from the red star (or secondary) companion.

1. Introduction

AE Aquarii (AE Aqr) consists of a fast rotating magnetized white dwarf orbiting a late-type K3-5 main sequence companion [1, 2, 3]. The binary period is 9.88 h [4, 6]. Although the system has been classified as a DQ Her-type cataclysmic variable, usually associated with the presence of an accretion disc, the observed properties of the system do not conform to this [7, 3]. The absence of double-peaked emission lines, usually associated with the presence of an accretion disc, combined with the rapid variation in the line intensities forthcoming from Hubble Space Telescope (HST) UV spectroscopy, associated with collisional excitation and high velocity, cast serious doubt whether an accretion disc is present in the system [5]. These phenomena have been explained successfully in terms of the fast rotating white dwarf expelling the mass flow from the secondary star from the system, i.e. the so-called magnetospheric propeller effect [7].

AE Aqr has been detected in almost all wavelength bands [8], from radio, through optical to TeV γ-rays [9, 1, 10, 11]. Coherent oscillations at 33 s were first observed by Patterson in the optical light [1], and later confirmed in UV and X-ray wavelengths [12, 13, 14]. AE Aqr is a relatively bright X-ray source ($L_X \sim 10^{31}$ erg s^{-1} [3]), and coupled with its close proximity to the Earth ($D \sim 100$ pc [4, 6]), it has been observed on a regular basis [12, 15, 3, 16, 17]. Previous analyses have reported that the soft X-ray emission below 10 keV is predominantly thermal, but a recent detection using the Suzaku satellite has reported a non-thermal hard X-ray power-law component above 10 keV [17], probably the result of synchrotron radiation from high energy electrons accelerated by huge potentials in the fast rotating white dwarf magnetosphere, i.e. a pulsar-like process. The reported photon index of $\Gamma = 1.16$ correlates well with the observed photon power-law indices observed in young rotation-powered pulsars at similar energies [17].

This paper will focus on the soft X-ray ($E_X \leq 10$ keV) characteristics of AE Aqr based on the analyses of data from recent observations with Chandra and Swift.

2. Observations of AE Aqr

The Chandra X-ray satellite [18] observed AE Aqr on August 30, 2005 for ~ 80 ks (ObsID 5431 [16]), using the Advanced CCD Imaging Spectrometer (ACIS) detector and the High Energy Transmission Grating. Standard data processing was done at the Chandra X-ray Center, and

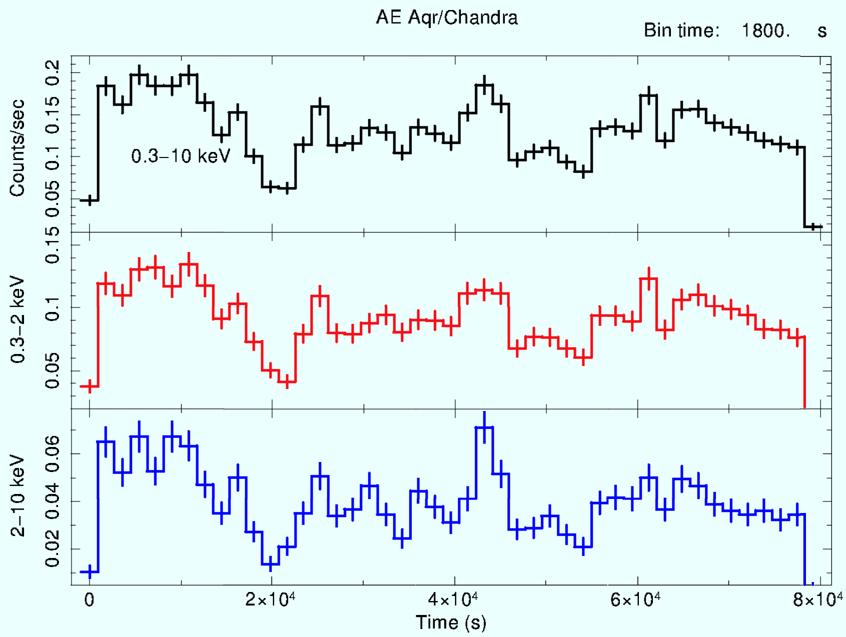

Figure 1. Background subtracted light curve of AE Aquarii from Chandra.

data was acquired through the High Energy Astrophysics Science Archive Research Center (HEASARC) on-line service, provided by the NASA's Goddard Space Flight Center (GSFC). Data reduction and analyses were done using the Chandra Interactive Analysis of Observations software (ciao version 4.2).

The Swift gamma-ray burst explorer [19] observed AE Aqr (target ID = 30295) between August 30 and September 2, 2005 for a total duration of ~ 10.5 ks, as a pre-planned target [20]. Data were archived in September 2005, and standard processing was done later at the UK Swift Science Data Centre. The results presented in this paper are based on data collected when the X-ray telescope (XRT) on-board Swift was operating in the photon counting mode, in which full imaging and spectroscopic resolutions are retained, but timing resolution is limited to 2.5 s [21]. Data was acquired through the HEASARC on-line service. Data reduction and analyses were done using the High-energy Astrophysics software (heasoft version 6.11). The spectra were created using the on-demand software, developed by the Swift team [20].

3. Results

3.1. Light curves

Figures 1 shows the background subtracted light curves of AE Aqr from Chandra data. The figure reveals the well established highly variable nature of the source (i.e. seen in almost all wavelengths), which is also characterised by flares [9, 1]. Most of the X-ray counts are obtained in the lower energy range (0.3-2 keV). Similar characteristics were also seen in the light curves obtained from Swift XRT data.

3.2. Spectra
Figure 2 shows the unfolded spectrum of AE Aqr from Swift XRT data, fitted with a three-temperature vmekal model. The model temperatures obtained are $0.4^{+0.07}_{-0.07}$ keV, $0.92^{+0.12}_{-0.10}$ keV and $3.95^{+0.94}_{-0.42}$ keV respectively. The spectrum shows emission line features, most of which are in the lower energy range (0.3-2 keV). The unabsorbed X-ray flux obtained in the 0.5-10 keV

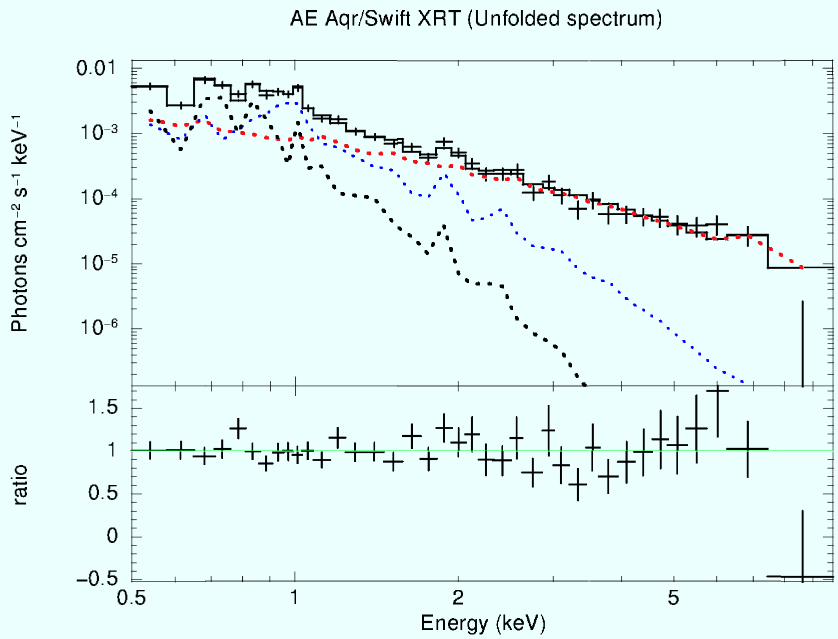

Figure 2. Spectrum of AE Aqr from Swift XRT fitted with a three-temperature vmekal model.

is $7.98^{+0.29}_{-0.44}\times 10^{-12}$ erg cm^{-2} s^{-1}, which, for an approximate source distance of 100 pc [4, 6], translates to a luminosity of $L_X = 9.03^{+0.23}_{-0.50} \times 10^{30}$ erg s^{-1}.

Figure 3 shows the background subtracted spectrum of AE Aqr from Chandra data, for the medium energy grating (MEG) and diffraction order m = -1. The spectrum was fitted with a three-temperature vmekal model. The model temperatures are $0.24^{+0.02}_{-0.06}$ keV, $0.73^{+0.02}_{-0.07}$ keV and $3.85^{+0.20}_{-0.17}$ keV respectively. Noticeable are the emission lines in the lower energy range of the spectrum, with some of the prominent lines labeled. Similar features were also seen in the spectra (not included in this paper) for the diffraction order $m = +1$, and for the high energy grating (HEG) arm respectively. It has been shown that the conversion of gravitational potential energy of the mass transfer flow from the secondary star towards the region of closest approach, where the plasma is ejected by the propeller, can comfortably drive the total X-ray luminosity assuming a conversion efficiency of only ~ 1 % [15]. This process can also heat the plasma up to temperatures $E_{\rm th} \leq 10$ keV, which is sufficient to drive the emission line spectrum [15].

3.3. Pulse timing
A search for periodicities in the barycentric corrected light curves was carried out using epoch folding method, where the light curves were folded with large number of periods around a guess value (period), and the best period found by chi squared maximization. In this analysis, the

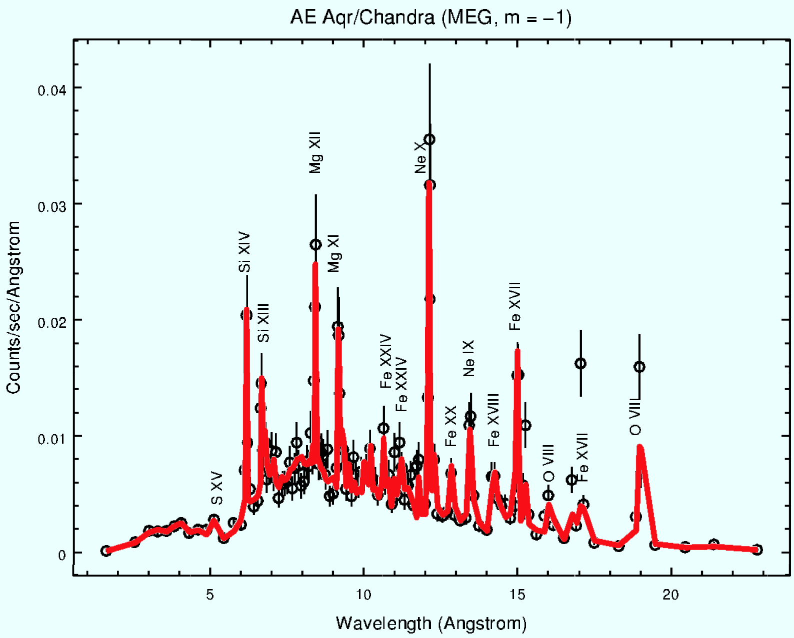

Figure 3. Spectrum of AE Aqr from Chandra fitted with a three-temperature vmekal model.

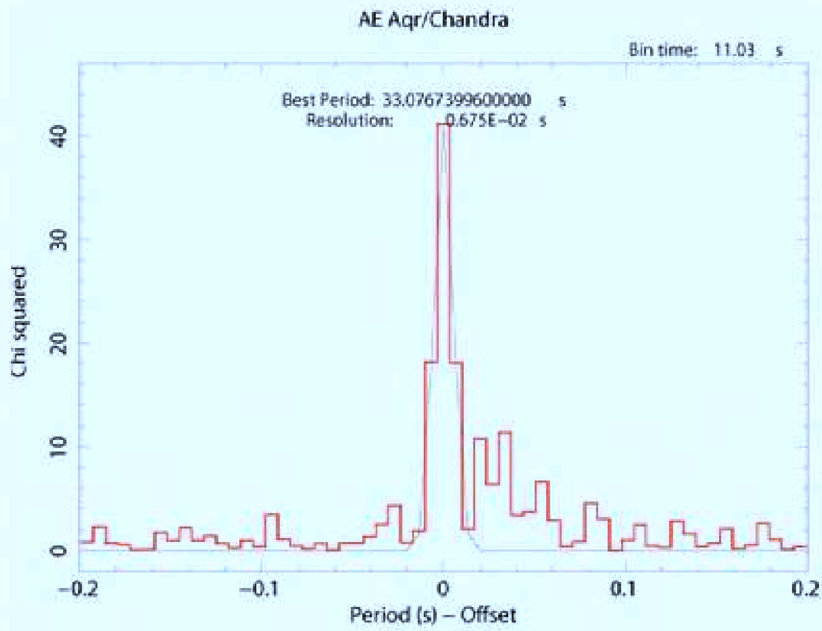

Figure 4. X-ray pulse period determination from Chandra data. Details in the text.

ephemeris for the pulsed emission, obtained from a 14 year baseline of optical observations [13], were used to fold the data. Figure 4 shows the pulse period determined for the Chandra data. The default Fourier period resolution (FPR), $P^2/2T \sim 6.75 \times 10^{-3}$ s was used, where P is the

 ISBN: 978-1-86888-688-3

folding period and T is the length of observation ($\sim$ 80 ks). The resulting peak was fitted with a gaussian, which was used to determine the actual pulse period, $P_{\rm pulse} = 33.0767 \pm 0.0068$ s. Similarly, the pulse period obtained for the Swift XRT data is 33.076 ± 0.052 s. The pulse periods obtained for both data sets (i.e. Chandra and Swift XRT) are perfectly reconcilable with the spin period of the white dwarf determined earlier [13]. Using the period obtained from the longer Chandra data set, the pulse profiles were determined using the epoch of BJD 2453673.5 [17]. These profiles are shown in Figures 5 and 6 for Chandra and Swift XRT data respectively.

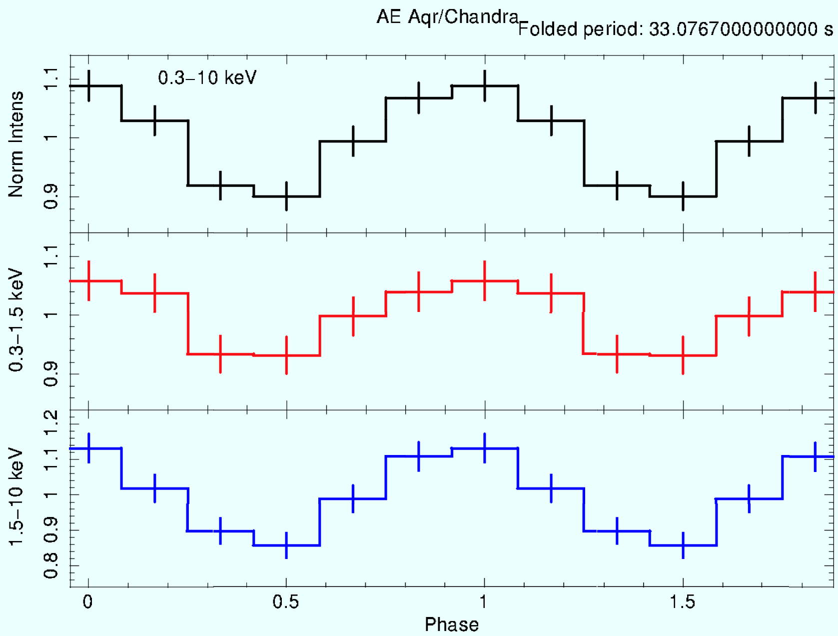

Figure 5. Pulse profile of AE Aqr from Chandra data. Phase 0 corresponds to BJD 2453673.5.

4. Discussion

The light curves of AE Aqr show that the source is highly variable and characterised by flares. Since AE Aqr is a non-eclipsing binary system, the variability is most likely the result of the interaction between the mass transfer from the secondary star a very efficient magnetospheric propeller process. Flares could be the result of sudden increase in the emission due to sporadic mass accretion onto the surface of the white dwarf. The spectra show a number of emission line features, and can be fitted with multi-component thermal emission models, suggesting temperatures in the X-ray emission region below 10 keV. A period and pulse analyses show that the X-ray emission is pulsed at the spin period of the white dwarf.

Acknowledgments

This work made use of data supplied by the Chandra X-ray Center, and the UK Swift Science Data Centre at the University of Leicester. The research has been funded by the African Square Kilometre Array Project, and the National Research Foundation of South Africa. The authors would like to thank the anonymous referees for constructive criticism.

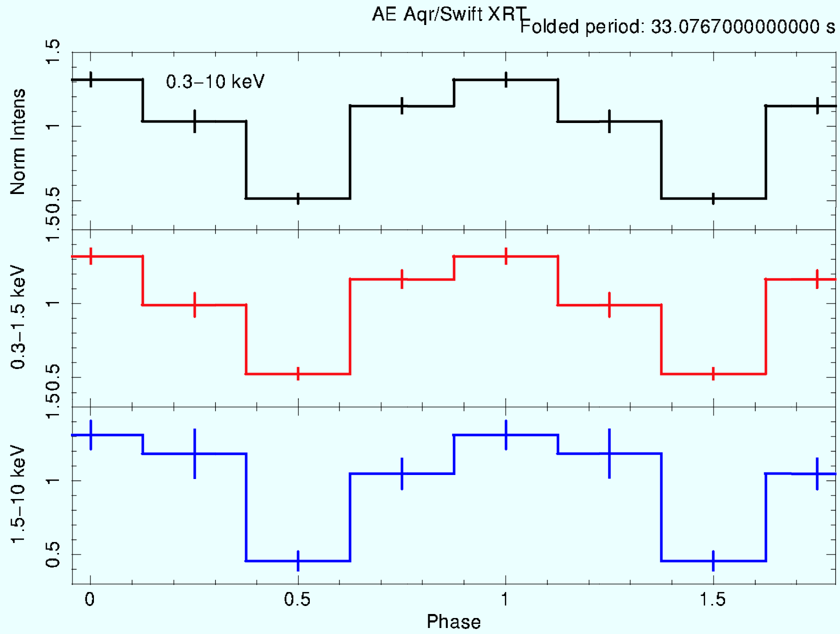

Figure 6. Pulse profile of AE Aqr from Swift XRT data. Phase 0 corresponds to BJD 2453673.5.

References

[1] Patterson J 1979 *Astrophys. J.* **234** 978–92
[2] Welsh W F, Horne K and Gomer R 1995 *Mon. Not. R. Astron. Soc.* **275** 649–70
[3] Itoh K, Okada S, Ishida M and Kunieda H 2006 *Astrophys. J.* **639** 397–04
[4] Welsh W F, Horne K and Gomer R 1993 *Astrophys. J. Lett.* **410** 39–42
[5] Eracleous M and Horne K 1996 *Astrophys. J.* **471** 427–46
[6] Welsh W F, Horne K and Oke J B 1993 *Astrophys. J.* **406** 229–39
[7] Wynn G A, King R A and Horne K 1997 *Mon. Not. R. Astron. Soc.* **286** 436–46
[8] de Jager O C 1991 *Astrophys. J.* **378** 286–92
[9] Bookbinder J A and Lamb D Q 1987 *Astrophys. J. Lett.* **323** 131–35
[10] Chadwick P M *et al.* 1995 *Astroparticle Physics* **4** 99–11
[11] Meintjes P J, de Jager O C, Raubenheimer B C, Nel H I, North A R, Buckley D A H and Koen C 1994 *Astrophys. J.* **434** 292–05
[12] Patterson J, Branch D, Chincarini G and Robinson E L 1980 *Astrophys. J. Lett.* **240** 133–36
[13] de Jager O C, Meintjes P J, O'Donoghue D and Robinson E L 1994 *Mon. Not. R. Astron. Soc.* **267** 577–88
[14] Eracleous M, Horne K, Robinson E L, Zhang E, Marsh T R and Wood J H 1994 *Astrophys. J.* **433** 313–31
[15] Choi C-S, Dotani T and Agrawal P C 1999 *Astrophys. J.* **525** 399–06
[16] Mauche C W 2006 *Mon. Not. R. Astron. Soc.* **369** 1983–87
[17] Terada Y, Hayashi T, Ishida M, Mukai K, Dotani T, Okada S, Nakamura R, Naik S, Bamba A and Makishima K 2008 *Publ. Astron. Soc. Japan* **60** 387–97
[18] Brissenden R J 2001 *Astron. Soc. Pac. Conf. Ser.* **238** 22–31
[19] Gehrels N *et al.* 2004 *Astrophys. J.* **611** 1005–20
[20] Evans P A *et al.* 2009 *Mon. Not. R. Astron. Soc.* **397** 1177–01
[21] Burrows D N *et al.* 2005 *Space Sci. Rev.* **120** 165–95

A.4 Bosco Oruru and P. J. Meintjes, 2011, Proceedings of Science, PoS (HTRS 2011) 063 (http://pos.sissa.it/cgi-bin/reader/conf.cgi?confid=122)

PROCEEDINGS OF SCIENCE

Spectroscopy of the Pulsar-like White Dwarf AE Aquarii from Chandra and Swift XRT Data

Bosco Oruru[*†]
University of the Free State
E-mail: `OruruB@ufs.ac.za`

P. J. Meintjes
University of the Free State
E-mail: `MeintjPJ@ufs.ac.za`

The multi-wavelength properties of the highly transient novalike variable AE Aqr makes it an ideal laboratory for the study of accretion related astrophysical fluid dynamics. It consists of a fast rotating highly magnetic white dwarf (WD) orbiting, and accreting mass, from a low-mass main sequence companion. The WD is spinning down at a rate $\dot{p} \sim 5.64\times10^{-14}$ s s^{-1}, corresponding to a spin-down luminosity of $L_{\rm sd} \sim 6 \times 10^{33}$ erg s^{-1}. The system is in a propeller state, and most of its emission properties are associated with the propeller process. It has been detected in almost all wavelengths, with the optical emission dominated by emission from the companion. We have analysed its X-ray spectra using contemporanous Chandra and Swift X-ray data. The results of this study show that the X-ray emission has both thermal and non-thermal characteristics. The associated energy (kT) range is $\sim$ 0.2-3.8 keV and power-law index for the non-thermal part is $p \sim 2.2$. In this paper, results related to the Chandra and Swift X-ray spectroscopy, based on the constraints of the thermal and non-thermal emission mechanisms, will be presented.

Keywords: Binary stars: individual (AE Aquarii) - Stars: White dwarf - Accretion: Magnetic

Fast X-ray timing and spectroscopy at extreme count rates
February 7-11, 2011
Champéry, Switzerland

[*]Speaker.

[†]The content of this paper is part of the work intended for the author's PhD thesis under the supervision of the co-author, Prof P. J. Meintjes.

PoS(HTRS 2011)063

1. Introduction

AE Aquarii (hereafter AE Aqr) is a low mass non-eclipsing close binary system consisting of a magnetic white dwarf, accreting matter from a late-type main sequence companion (e.g. Welsh et al. 1995; Ikhsanov 1997; Choi et al. 1999). The orbital period is 9.88 h (e.g. Welsh et al. 1993). It has traditionally been classified as a novalike variable (e.g. Joy 1954; Crawford & Craft 1956; de Jager 1991). Based on this classification, Patterson (1979) adopted the oblique rotator model and explained the system in terms of a magnetized white dwarf ($P_{\rm spin} \sim 33$ s) accreting matter from a well developed accretion disc, which placed AE Aqr in the intermediate polar subclass of the cataclysmic variables (e.g. Warner 1983; Ikhsanov 1997). However, the observed spectral profile of the H_α emission line is single-peaked and the spectral widths of the Balmer emission lines are highly variable (e.g. Itoh et al. 2006, and references therein), seriously questioning the presence of an accretion disc.

AE Aqr has been detected in almost all wavelengths (e.g. de Jager 1991); in radio (e.g. Bookbinder & Lamb 1987), in optical (e.g. Zinner 1938; Patterson 1979), in X-rays (e.g. Patterson et al. 1980; Clayton & Osborne 1995) and possibly in TeV γ-rays (e.g. Meintjes et al. 1992, 1994). In radio and TeV γ-rays, the emission is reportedly of non-thermal nature (e.g. Ikhsanov 1997), and the rest of the emission is predominantly thermal. Coherent oscillations at 33 s were first detected in the optical light (e.g. Patterson 1979), and later in other wavelengths (e.g. Patterson et al. 1980; de Jager et al. 1994; Eracleous et al. 1994; Meintjes et al. 1994).

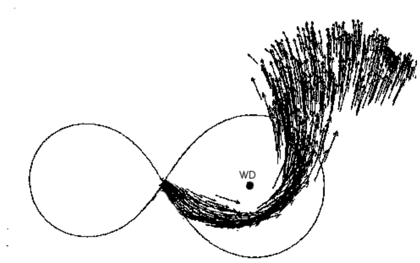

Recent studies (e.g. Wynn et al. 1997; Meintjes & de Jager 2000) have shown that the properties of the emission lines can be explained satisfactorily within the magnetic propeller model. These authors have shown that the fast rotating white dwarf will most probably act as a magnetospheric propeller, ejecting the bulk of the mass transfer flow from the binary system (see figure on the right; adapted from Wynn et al. 1997). For an effective propeller, no accretion disc is formed, a characteristic that makes AE Aquarii quite unique. The propeller model has been widely considered to account for the spin-down of the WD (de Jager et al. 1994; Mauche 2006) at $\dot{P} \sim 5.64\times10^{-14}$ s s^{-1}. On the other hand, Meintjes & de Jager (2000) have suggested that a fraction of the spin-down energy is channeled into particle acceleration and non-thermal emission.

This paper is organized as follows. In §2, observations of AE Aqr with Chandra and Swift are presented. A brief description of data reduction procedures, with respect to the spectra, are presented. The spectral properties are presented in §3, with a discussion of possible X-ray emission models presented in §4.

2. Observations and Data Reduction

AE Aqr was observed by Chandra (ObsID 5431) on August 30, 2005 at 06:37 UT for ~ 80 ks (e.g. Mauche 2006), using the ACIS-S detector and HETG. Standard processing was done at the

Chandra X-ray Center (CXC), and data was acquired through HEASARC on-line service, provided by the NASA's Goddard Space Flight Center. To generate spectra, CIAO software was used, where the level 2 event file was used as input to create a spectrum file (pha2.fits) that was then split into single spectrum files with respect to the diffraction order and the grating arm. Then, for each of the single spectra, a response matrix file (RMF) was created and used alongside other data files to create the corresponding ancilliary response file (ARF).

Swift observed AE Aqr (target ID = 30295) between August 30 and September 2, 2005 for $\sim$ 10.5 ks, as a pre-planned target (PPT; Evans et al. 2009). The data were processed at the UK Swift Science Data Centre (UKSSDC) in April 2007. The X-Ray Telescope (XRT; Burrows et al. 2005) is one of the three science instruments on-board Swift. It is a sensitive, flexible and autonomous X-ray imaging spectrometer designed to measure fluxes, spectra and lightcurves over a wide dynamic range covering more than 7 orders of magnitude in flux. It is designed for an autonomous operation, switching between four different readout modes, depending on the source intensity (Hill et al. 2004; Evans et al. 2007). The results presented in this paper are based on data collected when the XRT was operating in the Photon Counting (PC) mode, in which full imaging and spectroscopic resolutions are retained, but timing resolution is limited to 2.5 s (Burrows et al. 2005). The data used to generate the spectra were obtained using the on-demand software through the HEASARC on-line service. These were acquired by mannually registering the information of AE Aqr. Detailed description is given in the original paper by Evans et al. (2009).

3. Results

3.1 Chandra Spectra

Figure 1 shows the background subtracted energy spectra of the HEG arm for the diffraction orders m = -1 (left) and m = +1 (right) respectively. Each of the spectra was generated using sherpa and fitted with a two-temperature vmekal (thermal emission) model, $kT \sim 0.65$, 3.37 keV for m = -1 and $kT \sim 0.67$, 3.32 keV for m = +1 respectively. In Figure 2, the corresponding MEG spectra are shown. Each spectrum is fitted with a three-temperature vmekal model, $kT \sim 0.20$, 0.68, 3.82 keV for m = -1 and $kT \sim 0.40$, 0.82, 3.83 keV for m = +1 respectively. From the figures, a number of emission lines are seen superimposed on the continuum emission, and most of which are prominent in the soft X-ray regime.

The average fluxes of X-ray emission for the energy range 0.3-10 keV were found to be $\sim 8.09\times10^{-12}$ ergs cm^{-2} s^{-1} and 1.04×10^{-11} ergs cm^{-2} s^{-1} for HEG and MEG respectively. For an estimated source distance of 100 pc (e.g. Welsh et al. 1993), then it can be shown that the X-ray luminosities are $\sim 9.71\times10^{30}$ erg s^{-1} and 1.25×10^{31} erg s^{-1} for HEG and MEG respectively.

3.2 Swift-XRT Spectra

Figure 3 (left) shows the spectrum of AE Aqr from Swift-XRT data, generated in XSPEC. Fitting was performed using the C-statistic, and the resulting parameters were obtained with 90 % confidence for which the fit was repeatedly done until the C-statistic had worsened by 2.706 compared with the best fitting value. The spectrum was fitted with a combination of an absorbed power-law ($p \sim 2.19\pm0.16$) and a two-temperature vmekal emission model ($kT_1 \sim 0.44\pm0.10$ keV

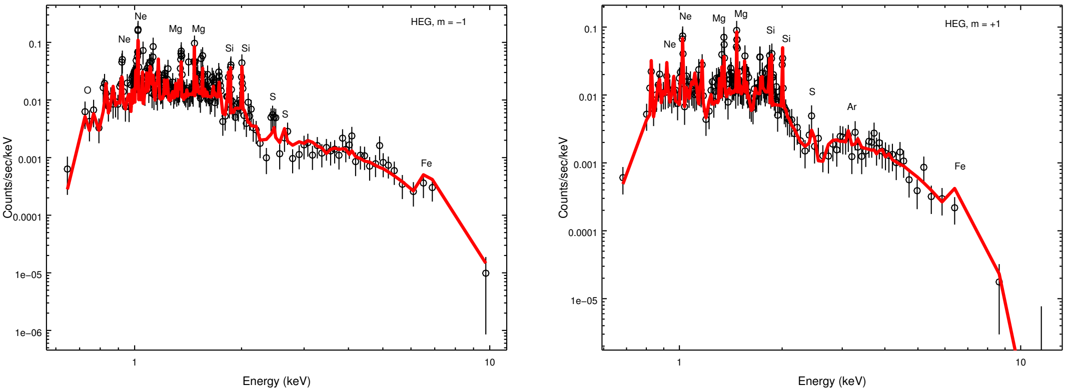

Figure 1: *Left*: HEG spectrum for the diffraction order m = -1. *Right*: HEG spectrum for the diffraction order m = +1.

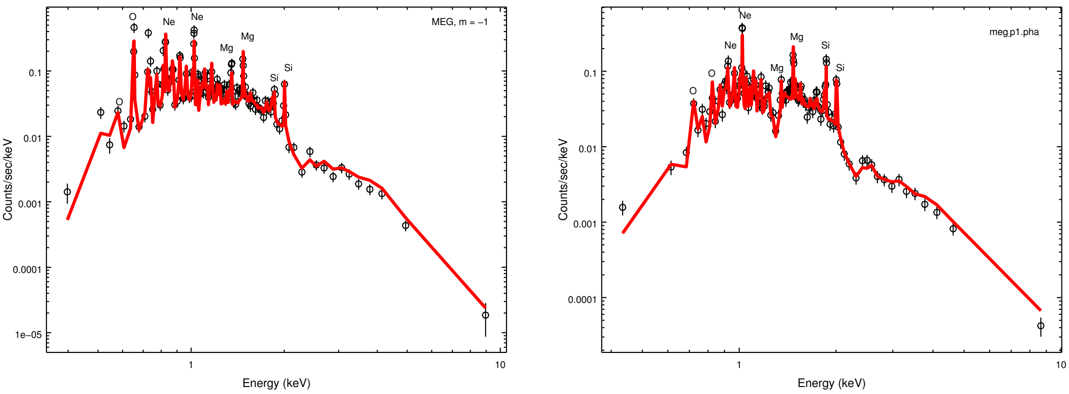

Figure 2: *Left*: MEG spectrum for the diffraction order m = -1. *Right*: MEG spectrum for the diffraction order m = +1.

and $kT_2 \sim 0.96{\pm}0.11$ keV respectively), suggesting that the X-ray emission has both thermal and non-thermal characteristics. On the right is the unfolded models plotted with the data. The blue and red dotted lines are the vmekal models, showing emission lines prominent at lower X-ray energies ($\lesssim$ 2.5 keV). The power-law model (green dashed line) provides a satisfactory fit for data in the hard energy range (kT $>$ 2 keV). Plots of photon and energy fluxes (Figure 4) also show that the hard X-ray data can be fitted with a power-law ($p \sim 2.01$).

The average flux obtained for the default Swift-XRT soft energy range (0.3-1.5 keV) was $\sim$ $6.22\times\ 10^{-12}$ erg cm^{-2} s^{-1}, and the corresponding default hard X-ray (1.5-10 keV) flux was 4.68×10^{-12} erg cm^{-2} s^{-1} . Then, the luminosities in the soft and hard energy bands are 7.46×10^{30} erg s^{-1} and 5.62×10^{30} erg s^{-1} respectively. Thus, the total X-ray luminosity is $\sim 1.31\times10^{31}$ erg s^{-1}.

4. Discussions

The spectral analyses of both Chandra and Swift-XRT data show that the X-ray emission is predominantly soft and contains a number of emission lines. These characteristics are associated

PoS(HTRS 2011)063

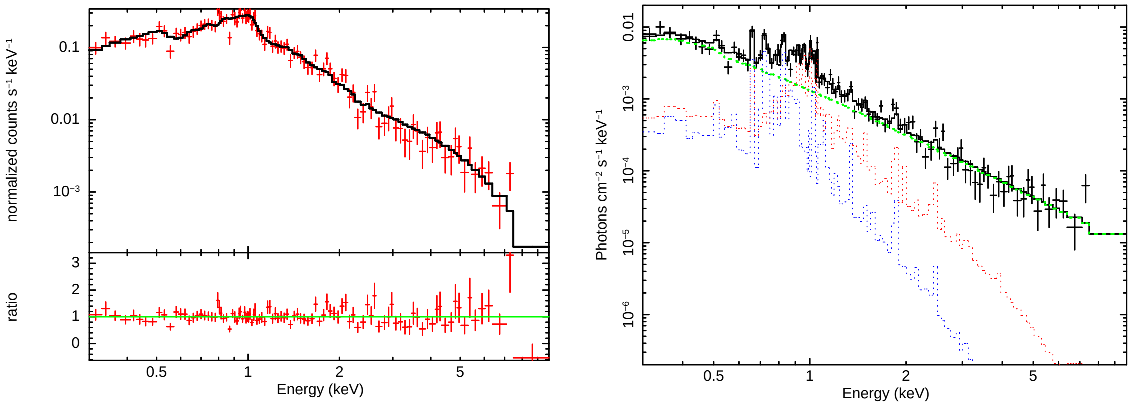

Figure 3: *Left*: Spectrum of AE Aquarii with the best fitting models. *Right*: Unfolded models plotted with data.

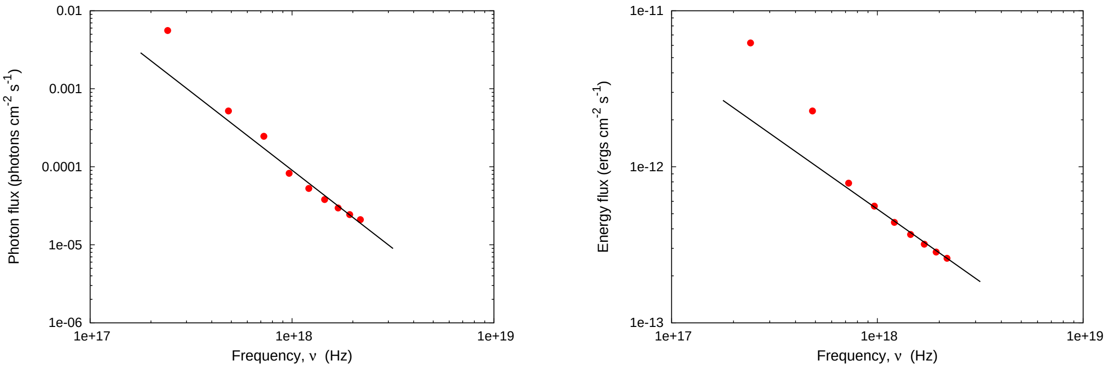

Figure 4: Photon flux (left) and energy flux (right), fitted with a power-law of index, $p \sim 2.01$.

with an optically thin emission region with a continuous temperature distribution. The vmekal emission model (with $T > 10^6$ K) means that a thermal emission process is one of the components of the X-ray emission of AE Aqr. Black body emission is unlikely because the observed luminosity ($\sim 10^{31}$ erg s^{-1}) is much less than $\sim 10^{34}$ erg s^{-1}, which is the expected value for accretion onto the surface of the white dwarf. For AE Aqr, the very effective propeller process greatly hinders the accretion onto the surface, and most likely then, bremsstrahlung (from heated mass outflow) could be the thermal emission process responsible for most of the X-rays (e.g. Oruru & Meintjes, in preparation). With a temperature, $T > 10^6$ K, it would require that the X-ray emitting region is well above the polar cap region (e.g. Patterson et al. 1980).

The power-law model, used alongside the vmekal model in fitting the Swift-XRT data, suggests a non-thermal emission, possibly arising from synchrotron radiation of accelerated particles (e.g. Terada et al. 2008). This is suggested for the hard X-ray emission which is modelled to have a different emission region from the soft X-ray emission, although both components are pulsed (e.g. Oruru & Meintjes, in preparation). It is proposed that the hard X-ray emission should be from a region in the vicinity of the light cylinder radius (e.g. Oruru & Meintjes, in preparation).

The spectral characteristics of AE Aqr discussed above make it similar to accretion-driven X-ray pulsars, but with properties of the white dwarf (e.g. spin period and surface magnetic field) much different compared with those of neutron stars. Hence, the hard X-ray emission in AE Aqr is not strong enough to be detected by most X-ray observatories.

Acknowledgements: This work made use of data supplied by the Chandra X-ray Center, and the UK Swift Science Data Centre at the University of Leicester. The research has been funded by the African Square Kilometre Array Project, and the National Research Foundation of South Africa.

References

[1] Bookbinder J. A., Lamb D. Q., 1987, ApJ, 323, 131

[2] Burrows D. N., Hill J. E., Nousek J. A. et al., 2005, Space Sci. Rev., 120, 165

[3] Choi C-S., Dotani T., Agrawal P. C., 1999, ApJ, 525, 399

[4] Clayton K. L., Osborne J. P., 1995, ASPC, 85, 379C

[5] Crawford J. A., Craft R. P., 1956, ApJ, 123, 44

[6] de Jager O. C., 1991a, ApJ, 378, 286

[7] de Jager O. C., 1991b, ICRC, 2, 463

[8] de Jager O. C., Meintjes P. J., O'Donoghue D., Robinson E. L., 1994, MNRAS, 267, 577

[9] Eracleous M., Horne K., Robinson E.L., Zhang E., Marsh T.R. & Wood J.H., 1994, ApJ, 433, 313

[10] Evans P. A., Beardmore A. P., Page K. L., Osborne J. P. et al., 2007, A&A, 469, 379

[11] Evans P. A., Beardmore A. P., Page K. L., Osborne J. P., et al., 2009, MNRAS, **397**, 1177

[12] Hill J. E., Burrows D. N., Nousek J. A., et al. 2004, SPIE, 5165, 217

[13] Ikhsanov N. K., 1997, A&A, 325, 1045

[14] Itoh K., Okada S., Ishida M., Kunieda H., 2006, ApJ, 639, 397

[15] Mauche C. W., 2006, MNRAS, 369, 1983

[16] Meintjes P. J., de Jager O. C., 2000, MNRAS, 311, 611

[17] Meintjes P. J., de Jager O. C., Raubenheimer B. C., Nel H. I., et al., 1994, ApJ, 434, 292

[18] Meintjes P.J., Raubenheimer B.C., de Jager O.C., Brink C., et al., 1992, ApJ, 401, 325

[19] Oruru B., Meintjes P. J., 2011, in preparation, MNRAS

[20] Patterson J., 1979, ApJ, 234, 978

[21] Patterson J., Branch D., Chincarini G., Robinson E. L., 1980, ApJ, 240, L133

[22] Terada Y., Ishida M., Mukai K., Dotani T., et al., 2008, Adv. Space Research, 41, 512

[23] Warner B., 1983, in Livio M., and Shaviv G. (eds.), Cataclysmic Variables and Related Objects, Dordrecht: Reidel, p. 155

[24] Welsh W. F., Horne K., Gomer R., 1993, ApJ, 410, L39

[25] Welsh W. F., Horne K., Oke J.B., 1993, ApJ, 406, 229

[26] Welsh W. F., Horne K., Gomer R., 1995, MNRAS, 275, 649

[27] Wynn G. A., King R. A., Horne K., 1997, MNRAS, 286, 436

[28] Zinner E., 1938, Astron.Nach., 265, 345

PoS(HTRS 2011)063

Appendix B

The Basics of Spectroscopy

There are many different mechanisms producing electromagnetic radiation in astronomical sources. Each mechanism has a characteristic spectrum, distinguished from the rest, and generally the observed spectrum is a result of one or more mechanisms. Extracting scientific information from the observed spectrum would require detailed understanding of various emission mechanisms, the physical conditions surrounding them, as well as the knowledge of the instrument used to record the spectrum.

A spectrometer cannot measure the spectrum of a source directly, rather it obtains photon counts (C) within specified instrument channels (I). The actual spectrum, $f(E)$, relates with the observed spectrum, $C(I)$, by

$$C(I) = \int_0^\infty f(E)R(I,E)dE, \tag{B.1}$$

where $R(I,E)$ is the instrument response, which is proportional to the probability that a photon of energy E will be detected in channel I (e.g. Arnaud et al. 2008). It is not possible to obtain the actual spectrum directly from Eq. 5.3 (e.g. Arnaud et al. 2008). However, the actual spectrum is obtained indirectly by choosing a model spectrum and matching (or fitting) it to the data, from which a predicted count spectrum is calculated and compared with the observed data.

An interactive X-ray spectral-fitting program, the so-called xspec, uses both data (source) and background files to obtain the observed spectrum, i.e. the background subtracted spectrum. In particular, the data file provides xspec with information regarding the total number of photons detected by the instrument in a given channel. It is indeed the observed spectrum, generated in xspec, to which the model spectrum can be fitted. The model spectrum is calculated within xspec using energy ranges defined by the response file. Composite models can be constructed in xspec, consisting of additive and multiplicative components. These models when convolved and/or mixed can perform sophisticated model fits on the observed spectrum. Detailed descriptions of the various xspec models can be found in xspec user's guide (e.g. Arnaud et al. 2008).

Bibliography

[1] Abada-Simon M., Bastian T. S., Bookbinder A. J., Aubier M., Bromage G., Dulk G. A., Lecacheux A., 1995b. Extension of the Radio Spectrum of AE Aquarii to the Sub-millimetric Range. *Lecture Notes in Physics, Berlin Springer Verlag*, **454**, 268

[2] Abada-Simon M., Bastian T. S., Horne K., Bookbinder A. J., 1995a. The Radio and Optical Flares of AE Aquarii, in Cape Workshop on Magnetic Cataclysmic Variables, Buckley D. A. H. & Warner B., eds. *ASP Conf. Ser.*, **85**, 355

[3] Abada-Simon M., Casares J., Evans A., Eyres S., Fender R., Garrington S., de Jager et al., 2005. First detections of the cataclysmic variable AE Aquarii in the near to far infrared with ISO and IRAS: Investigating the various possible thermal and non-thermal contributions. *Astron. Astrophys.*, **433**, 1063

[4] Abada-Simon M., Lecacheux A., Bastian T. M., Bookbinder J. A., Dulk G. A., 1993. The spectrum and variability of radio emission from AE Aquarii. *Astrophys. J.*, **406**, 692

[5] Abada-Simon M., Mouchet M., Aubier et al., 1999. First detection of the cataclysmic variable AE Aquarii at 90 μm. *ESASP*, **427**, 257

[6] Abbey, A. F., Carpenter, J., Read et al., 2005. Micrometeroid Damage to CCDs in XMM-Newton and Swift and its Significance for Future X-ray Missions, *in ESA-SP 604, The X-ray Universe* 2005, 943

[7] Altenhoff W. J., Thum C., Wendker H. J., 1994. Radio emission from stars: A survey at 250 GHz. *Astron. Astrophys.*, **281**, 161

[8] Arnaud K., Dorman B., Gordon C., 2008. XSPEC User's Guide. HEASARC, NASA GSFC

[9] Arnaud M., Rothenflug R., 1985. An updated evaluation of recombination and ionization rates. *Astron. Astrophys. Suppl. Ser.*, **60**, 425

[10] Arons J., Scharlemann E. T., 1979. Pair formation above pulsar polar caps - Structure of the low altitude acceleration zone. *Astrophys. J.*, **231**, 854

[11] Arons J., Tavani M., 1993. High-energy Emission from the Eclipsing Millisecond Pulsar PSR 1957+20. *Astrophys. J.*, **403**, 249

[12] Aungwerojwit A., Gänsicke B. T., Rodríguez-Gil et al., 2005. HS 0139+0559, HS 0229+8016, HS 0506+7725, and HS 0642+5049: four new long-period cataclysmic variables. *Astron. Astrophys.*, **443**, 995

[13] Backer D. C., Kulkarni S. R., Heiles et al., 1982. A millisecond pulsar. *Nature*, **300**, 615

[14] Barthelmy S. D., Barbier L. M., Cummings et al. 2005. The Burst Alert Telescope (BAT) on the Swift Midex Mission. *Space Sci. Rev.*, **120**, 143

[15] Bastian T. S., Dulk G. A., Chanmugam G., 1988. Radio flares from AE Aquarii: A low-power analog to Cygnus X-3? *Astrophys. J.*, **324**, 431

[16] Beardmore A. P., Osborne J. P., 1997. Simultaneous rapid hard X-ray and optical variability in AM Herculis: measurement of blob parameters. *Mon. Not. R. Astron. Soc.*, **290**, 145

[17] Becker W., Trümper J., 1997. The X-ray luminosity of rotation-powered neutron stars. *Astron. Astrophys.*, **326**, 682

[18] Becker P. A., Wolff M. T., 2007. Thermal and Bulk Comptonization in Accretion-powered X-Ray Pulsars. *Astrophys. J.*, **654**, 435

[19] Bednarek W., 2009. Gamma-rays from the vicinity of accreting neutron stars inside compact high-mass X-ray binaries. *Astron. Astrophys.*, **495**, 919

[20] Bednarek W., Pabich J., 2011. X-rays and Gamma-rays from Cataclysmic Variables: The example case of Intermediate Polar V1223 Sgr. *Mon. Not. R. Astron. Soc.*, **411**, 1701

[21] Beskrovnaya N. G., Ikhsanov N. R., Bruch A., Shakhovskoy N. M., 1996. Photometric and polarimetric analysis of the flaring activity in AE Aqr. *Astron. Astrophys.*, **307**, 840

[22] Bildsten L., Chakrabarty D., Chiu et al., 1997. Observations of Accreting Pulsars. *Astrophys. J. Suppl.*, **113**, 367

[23] Bookbinder J. A, Lamb D. Q., 1987. Discovery of radio emission from AE Aquarii. *Astrophys. J.*, **323**, 131

[24] Bowden C. C. G., Bradbury S. M., Brazier K. T. S., Carriminana et al., 1991. 400 GeV Gamma Rays From AE Aquarii. *Proc 22nd Int. Cosmic Ray Conf., M. Cawley et al. (eds.)*, Dublin Inst. Adv. Stud., Dublin, **1**, 356

[25] Bowden C. C. G., Bradbury S. M., Chadwick P. M., Dickinson et al., 1992. 350 GeV gamma rays from AE Aqr. *Astropart. Phys.*, **1**, 47

[26] Brissenden R. J., 2001. Chandra X-ray Observatory Operations. *ASP Conf. Ser.*, **238**, 22

[27] Bruch A., 1991. Multicolour photometry of the unusual cataclysmic variable AE Aquarii. *Astron. Astrophys.*, **251**, 59

[28] Burnard D. J., Lea S. M., Arons J., 1983. Accretion onto magnetized neutron stars - X-ray pulsars with intermediate rotation rates. *Astrophys. J.*, **266**, 175

[29] Burrows D. N., Hill J. E., Nousek et al. 2005. The Swift X-Ray Telescope. *Space Sci. Rev.*, **120**, 165

[30] Burstein D., Jones C., Forman et al., 1997. An EINSTEIN X-ray Survey of Optically Selected Galaxies. I. Data. *Astrophys. J. Suppl. Ser.*, **111**, 163

[31] Capalbi M., Perri M., Saija B., Tamburelli F., Angelini L., 2005. The Swift X-Ray Telescope Data Reduction Guide. ASI Science Data Center. Available online:

http://heasarc.nasa.gov/docs/swift/analysis/xrt_swiftguide_v1_pdf

[32] Carroll B. W., Ostlie D. A., 2007. An Introduction to Modern Astrophysics (2nd Ed). Addison-Wesley Publishing, San Francisco, CA, page 241

[33] Casares J., Mouchet M., Martinez-Pais I. G., Harlaftis E. T., 1996. A coordinated campaign of the intermediate polar AE aqr. 1: The system parameters. *Mon. Not. R. Astron. Soc.*, **282**, 182

[34] Chadwick P. M., Dickinson J. E., Dickinson M. R., Dipper N. A. et al., 1995. A burst of pulsed VHE gamma rays from AE Aquarii. *Astropart. Phys.*, **4**, 99

[35] Cheng K. S., Gil J., Zhang L., 1998. Nonthermal Origin of X-rays from Rotation-powered Neutron Stars. *Astrophys. J.*, **493**, L38

[36] Cheng K. S., Ho C., Ruderman M., 1986a. Energetic radiation from rapidly spinning pulsars. I - Outer magnetosphere gaps. II - VELA and Crab. *Astrophys. J.*, **300**, 500

[37] Cheng K. S., Ho C., Ruderman M., 1986b. Energetic Radiation from Rapidly Spinning Pulsars. II. VELA and Crab. *Astrophys. J.*, **300**, 522

[38] Cheng, A, Ruderman, M., Sutherland P., 1976. Current Flow in Pulsar Magnetospheres. *Astrophys. J.*, **203**, 209

[39] Cheng K. S., Taam R. E., Wang W., 2006. Pulsar Wind Nebulae and the Nonthermal X-Ray Emission of Millisecond Pulsars. *Astrophys. J.*, **641**, 427

[40] Chincarini G., Walker M. F., 1981. Image tube spectroscopic studies of rapid variables. IV - Spectroscopic and photometric observations of AE Aquarii. *Astron. Astrophys.*, **104**, 24

[41] Chisholm J. R., Harnden et al., 1999. ROSAT High Resolution Imager Identifications of Suspected Stellar Sources from the EINSTEIN Slew Survey. *Astron. J.*, **117**, 1845

[42] Choi C-S., Dotani T., 2006. A Flare of AE Aquarii Observed with XMM-Newton. Astrophys. J., *646*, 1149

[43] Choi C-S., Dotani T., Agrawal P. C., 1999. A Study of the X-ray Emission of the Magnetic Cataclysmic Variable AE Aquarii. *Astrophys. J.*, **525**, 399

[44] Clayton K. L., Osborne J. P., 1995. ROSAT Observations of AE Aqr Made During the Whole Earth Telescope and World Astronomy Day Campaign. *ASP Conf. Ser.*, **85**, 379C

[45] Condon J. J., Cotton W. D., Greisen et al., 1998. The NRAO VLA Sky Survey. *Astron. J.*, **115**, 1693

[46] Crawford J. A., Kraft R. P., 1956. An Interpretation of AE Aquarii. *Astrophys. J.*, **123**, 44

[47] Cropper M. S., 1990. The Polars. *Space Sci. Rev.*, **54**, 195

[48] Davidson K., Ostriker J. P., 1973. Neutron-Star Accretion in a Stellar Wind: Model for a Pulsed X-Ray Source. *Astrophys. J.*, **179**, 585

[49] Del Zanna L., Volpi D., Amato E., Bucciantini N., 2006. Simulated synchrotron emission from pulsar wind nebulae. *Astron. Astrophys.*, **453**, 621

[50] de Jager O. C., 1991a. The unusual X-ray pulse timing of AE Aquarii. *Astrophys. J.*, **378**, 286

[51] de Jager O. C., 1991b. Evidence for particle acceleration in AE AQR from radio and X-ray observations. *Int. Cosmic Ray Conf.*, **2**, 463

[52] de Jager O.C., 1994. Evidence for particle acceleration in a magnetized white dwarf from radio and gamma-ray observations. *Astrophys. J. Suppl. Ser.*, **90**, 775

[53] de Jager O. C., Meintjes P. J., O'Donoghue D., Robinson E. L., 1994. The discovery of a brake on the white dwarf in AE Aquarii. *Mon. Not. R. Astron. Soc.*, **267**, 577

[54] Dreicer H., 1959. Electron and Ion Runaway in a Fully Ionized Gas. I. *Phys. Rev.*, **115**, 238

[55] Dubus G., Campbell R, Kern et al., 2004. Excess mid-infrared emission in cataclysmic variables. *Mon. Not. R. Astron. Soc.*, **349**, 869

[56] Eracleous M., 1999. Constraints on the Accretion Flow in AE Aquarii from its X-ray Properties as Observed by ASCA. *ASP Conf. Ser.*, **157**, 343

[57] Eracleous M., Halpern J. P., Patterson J., 1991a. X-ray spectra of cataclysmic variables from the Einstein Observatory. *Astrophys. J.*, **382**, 290.

[58] Eracleous M., Halpern J. P., Patterson J., 1991b. A search for periodicities in the X-ray emission from cataclysmic variables. *Astrophys. J.*, **370**, 330.

[59] Eracleous M., Horne K., 1996. The Speedy Magnetic Propeller in the Cataclysmic Variable AE Aquarii. *Astrophys. J.*, **471**, 427

[60] Eracleous M., Horne K., Robinson E. L., Zhang E., Marsh T. R., Wood J. H., 1994. The ultraviolet pulsations of the cataclysmic variable AE Aquarii as observed with the Hubble Space Telescope. *Astrophys. J.*, **433**, 313

[61] Eracleous M., Horne K., Robinson E. L., Zhang E., Marsh T. R., Wood J. H., 1994. The ultraviolet pulsations of AE Aquarii as observed with the Hubble Space Telescope. *ASP Conf. Ser.*, **56**, 330

[62] Eracleous M., Horne K., Osborne J. P., Clayton K. L., 1995. HST Observations of AE Aquarii During the 1993 WAD Campaign. *ASP Conf. Ser.*, **85**, 392

[63] Evans P. A., Beardmore A. P., Page K. L., Osborne et al. 2007. An Online Repository of Swift/XRT Light Curves of Gamma-Ray Bursts. *Astron. Astrophys.*, **469**, 379

[64] Evans P. A., Beardmore A. P., Page K. L., Osborne et al., 2009. Methods and Results of An Automatic Analysis of A Complete Sample of Swift-XRT Observations of GRBs. *Mon. Not. R. Astron. Soc.*, **397**, 1177

[65] Frank J., King A., Raine D., 1992. Accretion power in Astrophysics. Cambridge University Press, Cambridge, page 46

[66] Frank J., King A., Raine D., 2002. Accretion power in Astrophysics. Cambridge University Press, Cambridge, page 48

[67] Friedman H., Lichtman S. W., Byram E. T., 1951. Photon Counter Measurements of Solar X-Rays and Extreme Ultraviolet Light. *Phys. Rev.*, **83**, 1025.

[68] Froning C. S., Long K. S., Gänsicke B., Szkody P., 2012. A Survey of Far Ultraviolet Spectroscopic Explorer Observations of Cataclysmic Variables. *Astrophys. J. Suppl. Ser.*, **199**, 7

[69] Giacconi R., 2003. Nobel Lecture: The dawn of x-ray astronomy. *Rev. Mod. Phys.*, **75**, 995

[70] Giacconi R., Branduardi G., Briel U., Epstein et al., 1979. The Einstein (HEAO 2) X-ray Observatory. *Astrophys. J.*, **230**, 540

[71] Giacconi R., Gursky H., Paolini F. R., Rossi B. B., 1962. Evidence for X-rays from Sources Outside the Solar System. *Phys. Rev. Lett.*, **9**, 439

[72] Giacconi R., Kellogg E., Gorenstein et al., 1971. An X-Ray Scan of the Galactic Plane from UHURU. *Astrophys. J.*, **165**, 27

[73] Gehrels N., Chincarini G., Giommi et al. 2004. The Swift Gamma-Ray Burst Mission. *Astrophys. J.*, **611**, 1005

[74] Goad M. R., Tyler L. G., Beardmore A. P., Evans et al. 2007. Accurate Early Positions for Swift GRBs: Enhancing X-ray Positions with UVOT Astrometry. *arXiv:0708.0986v1 [astro-ph] 7 Aug 2007*

[75] Goldreich P., Julian W. H., 1969. Pulsar Electrodynamics. *Astrophys. J.*, **157**, 869

[76] Hameury J. M., King A. R., Lasota J. -P., 1986a. A model for soft X-ray transients. *Astron. Astrophys.*, **162**, 71

[77] Harris D. E., Forman W., Gioa et al., 1994, VizieR On-line Data Catalog: IX/13

[78] Harrison T. E., Campbell R. K., Howell S. B., Cordova F. A., Schwope A. D. Spitzer IRS spectroscopy of intermediate polars: Constraints on mid-infrared cyclotron emission. *arXiv:astro-ph/0611026v1 1 Nov 2006*

[79] Hellier C., 2001. Cataclysmic Variable Stars. Praxis Publ. Ltd., Chichester, UK, page 1

[80] Hill J. E., Burrows D. N., Nousek et al. 2004. Readout Modes and Automated Operation of the Swift X-Ray Telescope. *SPIE*, **5165**, 217

[81] Holloway N. J., 1973. Pulsars-p-n junctions in pulsar magnetospheres. *Nature Phys. Sci.*, **246**, 6

[82] Hoshino M., Arons J., Gallant Y. A., Langdon A. B., 1992. Relativistic magnetosonic shock waves in synchrotron sources - Shock structure and nonthermal acceleration of positrons. *Astrophys. J.*, 390, 454

[83] Ikhsanov N. K., 1997. Spindown of the primary in AE Aquarii. *Astron. Astrophys.*, **325**, 1045

[84] Ikhsanov N. R., Neustroev V. V., Beskrovnaya N. G., 2004. A White Dwarf in the State of an Ejector. *Astron. Letters*, **30**, 675

[85] Ikhsanov N. K., Biermann P. L., 2006. High-energy emission of fast rotating white dwarfs. *Astron. Astrophys.*, **445**, 305

[86] Immler S., Still M., Boyd et al. 2008. The Swift UVOT Software Guide. NASA, GSFC

[87] Itoh K., Okada S., Ishida M., Kunieda H., 2006. Density Diagnostics of the Hot Plasma in AE Aquarii with XMM-Newton. *Astrophys. J.*, 639, 397

[88] Jackson J. D., 1999. Classical Elecrodynamics. John Wiley, New York, page 240

[89] Joy A. H., 1954. Spectroscopic observations of AE Aquarii. *Astrophys. J.*, **120**, 377

[90] Katz J. I., Smith I. A., 1988. Particle Acceleration in Accreting Magnetospheres. *Astrophys. J.*, **326**, 733

[91] Kennel C. F., Coroniti F. V., 1984. Confinement of the Crab Pulsar's Wind by its Supernova Remnant. *Astrophys. J.*, **283**, 694

[92] Kennel C. F., Coroniti F. V., 1984. Magnetohydrodynamic Model of Crab Nebula Radiation. *Astrophys. J.*, **283**, 710

[93] King A. R., 1991. Spin evolution in wind-fed X-ray binaries. *Mon. Not. R. Astron. Soc.*, **250**, 3

[94] King A.R., 1993. The accretion of diamagnetic blobs by a rotating magnetosphere. *Mon. Not. R. Astron. Soc.*, **261**, 144

[95] King A., Cominsky L., 1994. X-ray emission of the pulsar-Be star binary PSR 1259-63. *Astrophys. J.*, **435**, 411

[96] Klebesadel R. W., Strong I. B., Olson R. A. 1973. Observations of Gamma-Ray Bursts of Cosmic Origin. *Astrophys. J.*, **182**, 85

[97] Knigge C., Baraffe I., Patterson J., 2011. The Evolution of Cataclysmic Variables as Revised by their Donor Stars. *arXiv:1102.2440v2 [astro-ph.SR] 3 April 2011*

[98] Kuijpers J., Fletcher L., Abada-Simon et al., 1997. Magnetic pumping in the cataclysmic variable AE Aquarii. *Astron. Astrophys.*, **322**, 242

[99] Lamb F. K., Aly J. -J., Cook M.C., Lamb D. Q., 1983. Synchronization of magnetic stars in binary systems. *Astrophys. J.*, **274**, 71

[100] LaValley M. P., 2008. Logistic Regression. *Journal of the American Heart Association*, **117**, 2395

[101] Larsson S., 1996. Parameter estimation in epoch folding analysis. *Astron. Astrophys. Suppl. Ser.*, **117**, 197

[102] Lerche I., 1972. Pulsed and Continuous Radiation from White Dwarfs. *Astrophys. Space Sci.*, 17, 117

[103] Leung P. P., Cheng K. S., Fung P. C. W., 1993. A model of nonthermal radiation from accreting X-ray pulsars. *Astrophys. J.*, **410**, 309

[104] Lipunov V. M., 1992. Astrophysics of Neutron Stars. Springer-Verlag, Berlin

[105] Longair M. S., 1992. High Energy Astrophysics - Vol. 1. Cambridge Univ. Press, Cambridge

[106] Longair M. S., 1994. High Energy Astrophysics - Vol. 2. Cambridge Univ. Press, Cambridge

[107] Longair M. S., 2011. High Energy Astrophysics (3rd Ed). Cambridge Univ. Press, Cambridge

[108] Mandel'Štam S. L., 1965. X-ray Emission of the Sun. *Space Sci. Rev.*, **4**, 587

[109] Mauche C. W., 2006. The white dwarf in AE Aqr brakes harder. *Mon. Not. R. Astron. Soc.*, **369**, 1983

[110] Mauche C. W., 2009. Chandra High Energy Transmission Grating Spectrum of AE Aquarii. *arXiv:0910.0084v1 [astro-ph.SR] 1 Oct 2009*

[111] Meegan C. A., Pendleton G. N., Briggs et al. 1996. The Third BATSE Gamma-Ray Burst Catalog. *Astrophys. J. Suppl. Ser.*, **106**, 65

[112] Meintjes P. J., 2002. On the evolution of the nova-like variable AE Aquarii. *Mon. Not. R. Astron. Soc.*, **366**, 265

[113] Meintjes P. J., de Jager O. C., 2000. Propeller spin-down and the non-thermal emission from AE Aquarii. *Mon. Not. R. Astron. Soc.*, **311**, 611

[114] Meintjes P. J., de Jager O. C., Raubenheimer B. C., Nel H. I., North A. R., Buckley D. A. H., Koen C., 1994. Simultaneous optical and TeV gamma-ray observations of the cataclysmic variable AE Aquarii. *Astrophys. J.*, **434**, 292

[115] Meintjes P. J., Raubenheimer B. C., de Jager O. C., Brink C., Nel H. I., North A. R., van Urk G., Visser B., 1992. AE Aquarii - an emitter of pulsed TeV gamma rays resembling optical emission during flares. *Astrophys. J.*, **401**, 325

[116] Meintjes P. J., Venter L. A., 2003. Modelling the continuous radio outbursts in AE Aquarii.

Mon. Not. R. Astron. Soc., **341**, 891

[117] Meintjes P. J., Venter L. A., 2005. The diamagnetic blob propeller in AE Aquarii and non-thermal radio to mid-infrared emission. *Mon. Not. R. Astron. Soc.*, **360**, 573

[118] Mészáros P., Nagel W., Ventura J., 1980. Exact and approximate solutions for the one-dimensional transfer of polarized radiation, and applications to X-ray pulsars. *Astrophys. J.*, **238**, 1066

[119] Mészáros P., Rees M. J., 1992. Tidal heating and mass loss in neutron star binaries - Implications for gamma-ray burst models. *Astrophys. J.*, **397**, 570

[120] Mewe R., Gronenschild E. H. B. M., van den Oord G. H. J., 1985. Calculated X-radiation from optically thin plasmas. V..., Astron. Astrophys. Suppl. Ser., **62**, 197

[121] Mewe R., Lemen J. R., van den Oord G. H. J., 1986. Calculated X-radiation from optically thin plasmas. VI... Astron. Astrophys. Suppl. Ser., **65**, 511

[122] Moretti A., Campana S., Mineo et al., 2005. In-flight Calibration of the Swift XRT Point Spread Function. *SPIE*, **5898**, 360

[123] Mouchet M., Casares J., Harlaftis E. T., Emannelsen I. G., Martinez-Pais P.-I., Olsen O., 1995. The Complex H-alpha Profile of AE AQR. *ASP Conf. Ser.*, **85**, 359

[124] Murray S. S., Austin G. K., Chappell J. H., Gomes et al., 2000. In-flight performance of the Chandra high-resolution camera. *SPIE*, **4012**, 68

[125] Oruru B., Meintjes P. J., 2012. X-ray characteristics and the spectral energy distribution of AE Aquarii. *Mon. Not. R. Astron. Soc.*, **421**, 1557

[126] Osborne J. P., 1990, in Accretion-Powered Compact Binaries, ed. C. W. Mauche, Cambridge University Press, Cambridge, p. 215

[127] Osborne J. P., Clayton K. L., O'Donoghue D., Eracleous M., Horne K., Kanaan A., 1995. Simultaneous X-ray, UV and Optical Observations of Flaring in AE Aquarii. *ASP Conf.*

Ser., **85**, 368

[128] Pagani C., Morris D. C., Kobayashi et al., 2006. The Swift X-ray Flaring Afterglow of GRB 050607. *Astrophys. J.*, **645**, 1315

[129] Patterson J., 1979. Rapid Oscillations in Cataclysmic Variables. III - An Oblique Rotator in AE Aquarii. *Astrophys. J.*, **234**, 978

[130] Patterson J., Branch D., Chincarini G., Robinson E. L., 1980. 33 Second X-ray Pulsations in AE Aquarii. *Astrophys. J.*, **240**, L133

[131] Pringle J. E., Rees M. J., 1972. Accretion Disc Models for Compact X-Ray Sources. *Astron. Astrophys.*, **21**, 1

[132] Rees M. J., Gunn J. E., 1974. The origin of the magnetic field and relativistic particles in the Crab Nebula. *Mon. Not. R. Astron. Soc.*, **167**, 1

[133] Reinsch K., Beuermann K., Hanusch H., Thomas H. -C., 1995. ROSAT Observations of Intermediate Polars: AE AQR and YY DRA. In "Magnetic Cataclysmic Variables", Eds. D. Buckley and B. Warner, *ASP Conf. Ser.*, **85**, 115

[134] Richmond M. W., Droege, T. F., Gombert et al., 2000. TASS Mark III Photometric Survey of the Celestial Equator. *Publ. Astron. Soc. of the Pacific*, **112**, 397

[135] Roming P. W. A., Kennedy T. E., Mason et al. 2005. The Swift Ultra-Violet/Optical Telescope. *Space Sci. Rev.*, **120**, 95

[136] Rybicki G.B. & Lightman A.P., 1979. Radiative Processes in Astrophysics. Wiley, New York

[137] Rybicki G. B., Lightman A. P., 2004. Radiative Processes in Astrophysics. WILEY-VCH Verlag GmbH & Co. KGaA, Weinheim, page 1

[138] Safi-Harb S., Dubner G., Petre et al., 2004. Chandra Spatially Resolved Spectroscopic Study and Multi-Wavelength Imaging of the Supernova Remnant 3C 397 (G41.1-0.3).

Astrophys. J., **321**, 338

[139] Schenker K., King A. R., 2002. A new evolution future for CVs and LMXRBs II. The impact of thermal-timescale mass transfer. *ASP Conf. Ser.*, **261**, 242

[140] Schenker K., King A. R., Kolb U., Wynn G. A., Zhang Z., 2002. AE Aquarii: how cataclysmic variables descend from supersoft binaries. *Mon. Not. R. Astron. Soc.*, **337**, 1105

[141] Schneider D.P., Young P., 1980a. The magnetic maw of 2A 0311-227. *Astrophys. J.*, **238**, 946

[142] Schneider D.P., Young P., 1980b. VV Puppis and an Ursae Majoris - A radial velocity study. *Astrophys. J.*, **240**, 871

[143] Skinner M. A., Jordan S. P., 1997. AXAF: the Science Instrument Module. *Proc. SPIE*, **3114**, 2

[144] Skrutskie M. F., Cutri R. M., Steining et al., 2006. The Two Micron All Sky Survey (2MASS). *Astron. J.*, **131**, 1163

[145] Tanzi E. G., Chincarini G., Tarenghi M., 1981. Infrared Observations of AE Aquarii. *Publ. Astron. Soc. Pac.*, **93**, 68

[146] Tavani M., 1991. "Hidden" Millisecond Pulsars. *Astrophys. J.*, **379**, 69

[147] Tavani M., 1995. Binary Pulsar Shock Emission As Galactic Gamma-Ray Source. *astro-ph/9502058*

[148] Tavani M., Arons J., 1997. Theory of High-energy Emission from the Pulsar/Be Star System PSR 1259-63. I. Radiation Mechanisms and Interaction Geommetry. *Astrophys. J.*, **477**, 439

[149] Terada Y., Ishida M., Mukai K., Dotani et al., 2008a. Possible Suzaku detection of non-thermal X-ray signals from a rotating magnetized white dwarf. *Adv. Space Research*, **41**,

512

[150] Terada Y., Hayashi T., Ishida M., Mukai K., Dotani T., Okada S., Nakamura R., Naik S., Bamba A., Makishima K., 2008b. Suzaku Discovery of Hard X-Ray Pulsations from a Rotating Magnetized White Dwarf, AE Aquarii. *Publ. Astron. Soc. Japan*, **60**, 387

[151] Usov V. V., 1988. Generation of gamma rays by a rotating magnetic white dwarf. *Pis'ma Astron. Zh.*, 14, 606

[152] Usov V. V., 1993. High-frequency Emission of X-ray Pulsar 1E 2259+586. *Astrophys. J.*, **410**, 761

[153] van Paradijs J., Kraakman H., van Amerongen S., 1989. Five-colour optical photometry of AE Aquarii. *Astron. Astrophys.*, **79**, 20

[154] Venter L. A., Meintjes P. J., 2007. A tenous X-ray corona enveloping AE Aquarii. *Mon. Not. R. Astron. Soc.*, **378**, 681

[155] Vietri M., 2008. Foundations of High-Energy Astrophysics. The University of Chicago Press, Ltd., London, page 131

[156] Voges W., Aschenbach B., Boller et al., 1999. The ROSAT all-sky survey bright source catalogue. *Astron. Astrophys.*, **349**, 389 (VizieR On-line Data Catalog: IX/10A)

[157] Wang Y. -M., 1987. Disc accretion by magnetized neutron stars - A reassessment of the torque. *Astron. Astrophys.*, **183**, 257

[158] Wang Y. -M., Robertson J. A., 1985. Propeller action by rotating neutron stars. *Astron. Astrophys.*, **151**, 361

[159] Warner B., 1983, in Livio M., and Shaviv G. (eds.), Cataclysmic Variables and Related Objects, Dordrecht: Reidel, p. 155

[160] Warner B., 1995. Cataclymic Variable Stars. Cambridge Univ. Press, Cambridge, page 27

[161] Waters L. B. F. M., van den Heuvel E. P. J., Taylor et al., 1988. Evidence for low-velocity winds in Be/X-ray binaries. *Astron. Astrophys.*, **198**, 200

[162] Weisskopf M. C., 2003. The Chandra X-ray Observatory: An Overview. *Adv. Space Res.*, **32**, 2005

[163] Weisskopf M. C., Brinkman B., Canizares C., Garmire G., Murray S., van Speybroeck L. P., 2002. An Overview of the Performance and Scientific Results from the Chandra X-ray Observatory. *Publ. Astron. Soc. of the Pacific*, **114**, 1

[164] Welsh W. F., Horne K., Gomer R., 1993. On the location of the oscillations in AE Aquarii. *Astrophys. J.*, **410**, 39

[165] Welsh W. F., Horne K., Gomer R., 1998. Doppler signatures of H flares in AE Aquarii. *Mon. Not. R. Astron. Soc.*, **298**, 285

[166] Welsh W. F., Horne K., Oke J. B., 1993. Optical spectrophotometry of oscillations and flickering in AE Aquarii. *Astrophys. J.*, **406**, 229.

[167] White N. E., Swank J. H., Holt S. S., 1983. Accretion powered X-ray pulsars. *Astrophys. J.*, **270**, 711

[168] Wynn G. A., King R. A., 1995. Diamagnetic accretion in intermediate polars - I. Blob orbits and spin evolution. *Mon. Not. R. Astron. Soc.*, **275**, 9

[169] Wynn G. A., King R. A., Horne K., 1997. A magnetic propeller in the cataclysmic variable AE Aquarii. *Mon. Not. R. Astron. Soc.*, **286**, 436

[170] Zinner E., 1938. Mitteilungen uber veranderliche und verdachtige Sterne. *Astron. Nach.*, **265**, 345

[171] http://chandra.harvard.edu/resources/illustrations/teleSchem.html

[172] http://cxc.harvard.edu/proposer/POG/

[173] http://heasarc.nasa.gov/docs/swift/about_swift/uvot_desc.html

[174] http://home.cc.umanitoba.ca/∼umbarkm4/swift_telescope.html

[175] http://no.wikipedia.org/wiki/Fil:Nasa_swift_satellite.jpg

[176] http://swift.gsfc.nasa.gov/docs/heasarc/caldb/swift/

[177] http://www.astro.utu.fi/∼cflynn/astroII/l3.html

[178] http://www.astro.utu.fi/∼cflynn/astroII/l4.html

[179] http://www.astro.wisc.edu/∼bank/index.html

[180] http://www.daviddarling.info/encyclopedia/C/close_binary.html

[181] http://www.swift.psu.edu/xrt/techDescription.html